LASER-INDUCED PHOTODISSOCIATION OF HALOGENATED MOLECULES IN GAS PHASE: DYNAMICS OF OH & X (Cl, Br) FORMATION

By

ANKUR SAHA

CHEM01201004004

Bhabha Atomic Research Centre, Mumbai

A thesis submitted to the

Board of Studies in Chemical Sciences

In partial fulfillment of requirements

for the Degree of

DOCTOR OF PHILOSOPHY

of

HOMI BHABHA NATIONAL INSTITUTE

April, 2015

Recommendations of the Viva Voce Committee

As members of the Viva Voce Committee, we certify that we have read the dissertation prepared by Mr. Ankur Saha entitled "Laser-induced photodissociation of halogenated molecules in gas phase: Dynamics of OH & X(Cl, Br) formation." and recommend that it may be accepted as fulfilling the thesis requirement for the award of Degree of Doctor of Philosophy.

Chairman - Dr. S. K. Sarkar **Date:** 08.10.2015

Guide / Convener – Dr. Awadhesh Kumar Awadhesh Kumar **Date:** 08.10.2015

External Examiner- Prof. T. Chakraborty T. Chakraborty **Date:** 08.10.2015

Member 1- Dr. P. D. Naik PDNaik **Date:** 08.10.2015

Member 2 – Dr. R. K. Vatsa RKVatsa **Date:** 08.10.2015

Member 3- Dr. H. P. Upadhyaya **Date:** 08.10.2015

Final approval and acceptance of this thesis is contingent upon the candidate's submission of the final copies of the thesis to HBNI.

I hereby certify that I have read this thesis prepared under my direction and recommend that it may be accepted as fulfilling the thesis requirement.

Date: 08.10.2015

Place: Mumbai

Awadhesh Kumar

Guide: Dr. Awadhesh Kumar

STATEMENT BY AUTHOR

Ankur Saha

DECLARATION

I, hereby, declare that the investigation presented in the thesis has been carried out by me. The work is original and has not been submitted earlier as a whole or in part for a degree / diploma at this or any other Institution / University.

Ankur Saha

List of Publications arising from the thesis

1. "Photodissociation dynamics of benzoyl chloride at 235 nm: Resonance-enhanced multiphoton ionization detection of Cl and HCl." **Ankur Saha**, Monali Kawade, Sumana SenGupta, Hari P. Upadhyaya, Awadhesh Kumar and Prakash D. Naik, *J. Phys. Chem. A*, **2014**, *118*, 1185-1195.

2. "Resonance enhanced multiphoton ionization time-of-flight (REMPI-TOF) study of tetrachloroethylene photodissociation at 235 nm: Role of bound π-$\sigma^*_{C\text{-}Cl}$ state." **Ankur Saha**, Hari P. Upadhyaya, Awadhesh Kumar and Prakash D. Naik, *Chem. Phys.*, **2014**, *428*, 127-136.

3. "Photoexcitation of 2-bromo-2-chloro-1,1,1-trifluoroethane (halothane) to repulsive surface $n\sigma^*$(C-Br) at 234 nm: Dynamics of C-Br and C-Cl bond rupture." **Ankur Saha**, Monali N. Kawade, Hari P. Upadhyaya, Awadhesh Kumar and Prakash D. Naik, *Chem. Phys.*, **2013**, *416*, 1-10.

4. "Dynamics of C-Cl bond fission in photodissociation of 2-furoyl chloride at 235 nm." **Ankur Saha**, Hari P. Upadhyaya, Awadhesh Kumar, Prakash D. Naik and Parma Nand Bajaj, *Chem. Phys.*, **2012**, *402*, 74-82.

5. "Laser-induced UV photodissociation of 2-bromo-2-nitropropane: Dynamics of OH and Br formation." **Ankur Saha**, Monali Kawade, Hari P. Upadhyaya, Awadhesh Kumar and Prakash D. Naik, *J. Chem. Phys.*, **2011**, *134*, 044316/1-13.

Ankur Saha

List of other publications (not included in the thesis)

1. "Photodissociation dynamics of 2-chloro-6-nitrotoluene and nitrocyclopentane in gas phase: Laser-induced fluorescence detection of OH." Monali Kawade, **Ankur Saha**, Hari P. Upadhyaya, Awadhesh Kumar and Prakash D. Naik, *Chem. Phys.*, **2014**, *443*, 123-132.

2. "Photodissociation dynamics of enolic 1,2-cyclohexanedione at 266, 248, and 193 nm: Mechanism and nascent state product distribution of OH." Monali Kawade, **Ankur Saha**, Hari P. Upadhyaya, Awadhesh Kumar and Prakash D. Naik, *J. Phys. Chem. A*, **2013**, *117*, 2415-2426.

3. "Photodissociation dynamics of halogenated thiophenes at 235 nm: A resonance enhanced multiphoton ionization-time-of-flight (REMPI-TOF) study." Monali Kawade, **Ankur Saha**, Hari P. Upadhyaya, Awadhesh Kumar, Prakash D. Naik, and P.N. Bajaj, *J. Phys. Chem. A*, **2012**, *116*, 10656-10667.

4. "Resonance enhanced multiphoton ionization time-of-flight (REMPI-TOF) study of phosphorous oxychloride ($POCl_3$) dissociation at 235 nm: Dynamics of $Cl(^2P_j)$ formation." **Ankur Saha**, Monali N. Kawade, Hari P. Upadhyaya, Awadhesh Kumar, Prakash D. Naik and P.N. Bajaj, *Chem. Phys.*, ***2012***, *407*, 83-91.

5. "Ultraviolet photodissociation dynamics of trichloroethylene at 235 nm." Hari P. Upadhyaya, **Ankur Saha**, Awadhesh Kumar and Prakash D. Naik, *Ind. J. Phys.*, ***2012***, *86*, 165-171.

6. "Photodissociation dynamics of 3-bromo-1,1,1-trifluoro-2-propanol and 2-(bromomethyl) hexafluoro-2-propanol at 234 nm: Resonance-enhanced multiphoton ionization (REMPI) detection of $Br(^2P_j)$." Y. N. Indulkar, **Ankur**

Saha, Hari P. Upadhyaya, Awadhesh Kumar, Prakash D. Naik and P.N. Bajaj, *J. Chem. Phys.*, **2011**, *134*, 194313/1-10.

7. Dynamics of Cl (^2P_j) atom formation in the photodissociation of fumaryl chloride (ClCO − CH = CH − COCl) at 235 nm: A resonance enhanced multiphoton ionization (REMPI) time-of-flight (TOF) study. Monali Kawade, **Ankur Saha**, Hari P. Upadhyaya, Awadhesh Kumar, Prakash D. Naik, and P.N. Bajaj, *J. Phys. Chem. A*, **2011**, *115*, 1538-1546.

8. "Dynamics of N-OH bond dissociation in cyclopentanone and cyclohexanone oxime at 193 nm: Laser-induced fluorescence detection of nascent OH (v'', J'')." Monali Kawade, **Ankur Saha**, Hari P. Upadhyaya, Awadhesh Kumar and Prakash D. Naik, *J. Phys. Chem. A*, **2010**, *114*, 12369-12377.

9. "Photodissociation dynamics of phosphorous tri-chloride (PCl_3) at 235 nm using resonance enhanced multiphoton ionization (REMPI) with time-of-flight (TOF) mass spectrometry." Hari P. Upadhyaya, Ankur Saha, Awadhesh Kumar, T. Bandyopadhyay, Prakash. D. Naik and P.N. Bajaj, *J. Phys. Chem. A*, **2010**, *114*, 5271-5278.

Ankur Saha

DEDICATIONS

My Parents: To whom I owe existence of my life

My Teachers: To whom I owe direction of my life

My Wife: To whom I owe meaning of my life

and

My Daughter: To whom I owe perpetuity of my life

ACKNOWLEDGMENTS

I am grateful to so many people who have directly and indirectly made it possible for me to write this today. First of all, I wish to record my most sincere gratitude towards my guide, Dr. Awadhesh Kumar of Bhabha Atomic Research Centre (BARC), for his guidance with superior scientific knowledge and generous co-operation throughout the execution of this thesis. I am indebted to Dr. Hari P. Upadhyaya, for his deep involvement, guidance, and enthusiastic support in realization of my Ph.D. project. This thesis would not have been possible without support, critical analysis and valuable suggestions from Dr. Prakash D. Naik, Head, CDS. A sincere thanks to my ex-lab mates Monali Kawade and Yogesh Indulkar for their great support during my experimental research. Three of us shared a great time together. I am also thankful to Dr. Sumana SenGupta and Dr. Dhanya Suresh, for sharing their excellent knowledge and scientific understanding with me. I also appreciate the help from Dr. K.K. Pushpa, Asmita Sharma, Mohini Walavalkar, Hariprasad Alwe and D. Srinivas. Special thanks to Mr. silay Basu for his technical help and Mr. S. A. Nadkarni, Mr. R. Manimaran and Mrs. K. G. Girija for their support related to electronics problems.

The members (Dr. P. N. Bajaj, Dr. P. D. Naik, Dr. Awadhesh Kuma, Dr. R. K. Vatsa and Dr. Hari P. Upadhyaya) and the chairman of the doctoral committee, Prof. S. K. Sarkar, are gratefully acknowledged for their critical review and suggestions during the progress review and pre-synopsis viva-voce.

I sincerely acknowledge the support and encouragement rendered to me during my research work by Dr. D. K. Palit, Head, RPCD and Dr. B. N. Jagatap, Director, Chemistry Group.

At last, but not the least, I like to thank my family, especially my wife and my daughter. Their love and encouragement support me to go through the highs and lows of my Ph. D. program. I also take this opportunity to thank all my friends and well-wishers, who redefined the word family to me. Their good wishes paved my path throughout this journey.

CONTENTS

SYNOPSIS

INTRODUCTION:

Photodissociation, often termed as second half of a full collision, is the formation of two (or more) fragments following absorption of light by a molecule. Upon photoexcitation, a molecule can undergo several photophysical and photochemical processes. Among them, in gas phase, perhaps the most investigated process is the unimolecular photodissociation of polyatomic molecules [1], as this is the initiation of many chemical reactions in the atmosphere. In recent times the gas phase photodissociation of halogenated polyatomic molecules has attracted immense interest mainly due to their active role in stratospheric ozone depletion. Several experimental and theoretical studies have been devoted to understand these molecular dissociation processes. Measurement of different microscopic details, like partitioning of the available energy among different states of a photofragment often point to the mechanism of the reaction. Combining the experimentally obtained information with the results of theoretical calculations can help in fundamental level understanding of a photodissociation process.

The nature of chromophore present and the initially prepared excited state often dictate the fate of the photodissociation dynamics and product state distribution. For example, the UV excitation of the $\sigma^*(C\text{-}X) \leftarrow n(X)$ transition of monohalogenated alkanes generally leads to impulsive C-X bond cleavage, producing the halogen radical in both its ground state $X(^2P_{3/2})$ and spin orbit excited state $X^*(^2P_{1/2})$ with different branching ratios and recoil anisotropy. However for alkyl halides with multichromophores, various additional dissociation channels can operate with different branching ratios, depending on the nature of excitation and the presence of a functional group. Therefore, the studies on photodissociation dynamics of alkyl halides with multihalogen atoms and other functional groups are being pursued actively [2]. In this thesis we have investigated the UV-photodissociation of halogenated compounds with various functional groups to understand the role of chemical environment and nature of the initial excited state, on the C-X and N-OH bond dissociation dynamics. The thesis consists of seven chapters for a clear presentation of the work and explained briefly in the following paragraphs.

CHAPTER 1

This is an introductory chapter giving a general overview of photodissociation dynamics and its importance. The methods of photoexcitation, followed by the fate of the excited molecule, are discussed with a focus on photodissociation processes. A brief discussion on the essence of photodissociation dynamics study and its development is also highlighted. Various aspects of a photodissociation process, like potential energy surfaces of reactants and products, partitioning of the available energy into internal states of the nascent products, and the models available for explaining this distribution, are discussed. Since, theoretical calculation is employed to aid interpretation of the experimental results, a brief on the computational chemistry, *ab initio* molecular orbital calculations and semi-empirical calculations employing Gaussian 03 programme [3], is also discussed.

CHAPTER 2

This chapter gives a brief account of the experimental techniques and instrumentation employed to execute the work. Two very sensitive and selective, Molecular Beam-Resonance Enhanced Multiphoton Ionisation-Time of Flight Mass

Spectrometry (MB-REMPI-TOFMS) and Laser Photolysis-Laser Induced Fluorescence (LP-LIF) techniques have been used to detect transient species and to obtain the dynamical information. The LP-LIF experiments were carried out in a flow system, and REMPI experiments in a molecular beam environment.

REMPI was used to detect the halogen atoms, Cl/Br ($^2P_{3/2}$) and Cl*/Br* ($^2P_{1/2}$), and HCl in their nascent states. A single laser beam near 235 nm was employed for photodissociation of parent molecules as well as ionization of the photoproducts. The OH fragment was probed by exciting its $A^2\Sigma \leftarrow X^2\Pi$ system (306-309 nm), using a tunable dye laser and monitoring the subsequent A→X fluorescence.

CHAPTER 3

In this chapter the photodissociation dynamics of 2-bromo-2-chloro-1,1,1-trifluoroethane (halothane) on excitation of the σ*(C-Br)←n(Br) transition near 234 nm is reported [4]. These studies are aimed at investigating the effect of the Cl atom on the dynamics of the expected C-Br bond scission in halothane. In addition, we were interested in exploring the possibility of the stronger C-Cl bond cleavage. The experiment was carried out in a molecular beam environment, employing REMPI-TOF-MS setup. Analogous to saturated alkyl halide dissociation, the C-Br bond scission is observed predominantly due to direct σ*(C-Br)←n(Br) transition. However, the formation of chlorine atom with a considerable value of recoil anisotropy parameter β is interesting, since it signifies intramolecular energy transfer from one repulsive state [n,σ*(C-Br)] to another [n,σ*(C-Cl)]. The details of the chlorine (bromine) atom formation channel and the effect of bromine (chlorine) atom on the overall dynamics of halothane dissociation are discussed in this chapter. The velocity distribution of bromine atom has one component, however, that of chlorine atom is bimodal. Both fast and slow chlorine atom channels, with the β value of 0.3±0.1, are produced impulsively from the [n,σ*(C-Cl)] repulsive surface, indicating a fast energy transfer to the C-Cl channel from the initial excited state.

CHAPTER 4

This chapter deals with the details of the UV-photodissociation of tetra chloroethylene in a supersonic molecular beam at ~235 nm [5]. The principal objective of the work was to understand the dynamics of the C-X bond scission in an unsaturated alkyl halide, which has many low energy excited states. Tetrachloroethylene was selected as a representative molecule to investigate the C-Cl bond dissociation.

UV excitation of saturated alkyl halides, e.g. halothane discussed in chapter 3, generally leads to the C-X (X=Cl / Br) bond fission from a repulsive state [n,σ*(C-X)] with an impulsive mechanism, producing X and X* with an anisotropic angular distribution. However, the dynamics of the C-X bond fission in unsaturated alkyl halides is totally different, and depends upon the nature of the excited state. In this regard dissociation dynamics of chloroethylenes are interesting due to the presence of multiple pathways, which can get altered depending on the excitation wavelength, including simple bond cleavage, molecular eliminations and three body dissociation processes. In this work we have determined the center-of-mass photofragment speed distribution, recoil anisotropy parameter (β), and the spin-orbit branching ratio for chlorine atom elimination channels. Two components, namely, the fast and the slow, are observed in the translational energy distributions of Cl and Cl*. The average translational energies for the Cl and Cl* channels for the fast components are 17.6±1.9 and 14.0±1.7 kcal/mol, while that for the slow components are 2.2±1.0 and 3.2±1.0

kcal/mol, respectively. Detailed theoretical calculations are performed using Time-dependent Density Functional Theory (TD-DFT) method to understand the nature of the dissociative potential energy surface involved in the chlorine atom formation channel. Here, the bound nature of the πσ*(C-Cl) state in chloroethylenes is reported. Finally, it is concluded that the high translational energy component of the chlorine atom channel is coming from the [π,σ*(C-Cl)] surface. Whereas, the lower energy component is mainly due to internal conversion from the [π,σ*(C-Cl)] state to the ground state, that dissociates statistically.

CHAPTER 5

This chapter provides the details on photodissociation dynamics of 2-furoyl chloride [6] and benzoyl chloride [7] in a supersonic molecular beam at around 235 nm. These two molecules are selected as representative aromatic acyl halides, which have COCl moiety in their side chain, to investigate the dynamics of the C(O)-Cl bond dissociation. In general the gas-phase dissociation of acyl halides in the UV region is dominated by the C-Cl bond cleavage through the diabatic interactions between the initially excited [n,π*(CO)] or [π,π*(CO)] state and [n,σ*(C-Cl)] repulsive state. Fast diabatic interactions between [n,π*(CO)] and [n,σ*(C-Cl)] have been reported, which lead to chlorine atom generations with high kinetic energy and non-zero value of recoil anisotropy parameter, β. However, in the present work on 2-furoyl chloride and benzoyl chloride, chlorine atoms were formed isotropically (β=0) in both their ground and the spin orbit excited states with bimodal translational energy distributions. The observed branching ratio of the high to low energy chlorine component in benzoyl chloride (0.72/0.28) is slightly different from that in 2-furoyl chloride (0.78/0.22). The results suggest that the electronic relaxation to the vibrationally excited ground state in benzoyl chloride is more efficient than that in 2-furoyl chloride. One major difference in the dissociation dynamics of these two compounds is the presence of the molecular HCl elimination channel in benzoyl chloride. Apart from the HCl channel, the overall dynamics of dissociation of benzoyl chloride and 2-furoyl chloride are similar, and the dissociation takes place only in the side chain. On excitation at 235 nm benzoyl chloride and 2-furoyl chloride are initially excited to the S_3 ($^1\pi,\pi^*$) and S_2 ($^1\pi,\pi^*$) states, respectively, from where a major fraction relaxes to the S_1 ($^1n,\pi^*$) state to produce the high kinetic energy chlorine atom channel, and a minor fraction relaxes to the ground (S_0) state to produce the slow chlorine channel.

CHAPTER 6

In this chapter the details of UV-photodissociation of 2-bromo-2-nitropropane (BNP) is discussed [8]. The previous chapters in this thesis were focused on the dynamics of halogen atom formation on UV excitation of different halogenated molecules, and the role played by the nature of initial excited states in controlling the overall dynamics of the C-X bond dissociation. However, the presence of a halogen atom itself can significantly alter the dynamics of dissociation of a polyatomic organic molecule by changing the nature of excitation of the molecule, and providing various low energy dissociation pathways. Our interest was to investigate the effect of a halogen substituent on the dissociation dynamics of a nitrocompound, for which BNP is selected.

Photoexcitation of BNP at 248 and 193 nm generates OH, Br and NO_2 among other products. The OH fragment is detected by laser-induced fluorescence spectroscopy, and its translational and internal state distributions are probed. At both 248 and 193 nm, the OH fragment is produced translationally hot with the energy of

10.8 and 17.2 kcal/mol, respectively. However, it is produced vibrationally cold ($v''=0$) at 248 nm, and excited ($v''=1$) at 193 nm with a vibrational temperature of 1870±150 K. It is also generated with rotational excitation, rotational populations of OH($v''=0$) being characterized by a temperature of 550±50 and 925±100 K at 248 and 193 nm excitation of BNP, respectively. The NO_2 product is produced electronically excited at 193 nm, as detected by measuring UV-visible fluorescence, and mostly in the ground electronic state at 248 nm. The Br product is detected employing resonance-enhanced multiphoton ionization with time-of-flight mass spectrometer. The average translational energies for the Br and Br* channels are 5.0±1.0 and 6.0±1.5 kcal/mol. No recoil anisotropies were observed for these products. Most plausible mechanisms of OH and Br formation are discussed based on both the experimental and the theoretical results. The electronically excited BNP molecules at 248 and 234 nm relax to the ground state, and subsequently dissociate to produce OH and Br through different channels. The mechanism of OH formation from BNP on excitation at 193 nm is also discussed.

CHAPTER 7

This chapter provides a summary to the work carried out in this thesis, and a future direction to this work to acquire assistive knowledge. The thesis presents details on dynamics of UV dissociation of several halogenated molecules with atmospheric relevance. The effect of various substituents on photodissociation has been investigated by probing the nascent photoproducts (mostly halogen atom and OH), employing LIF and REMPI techniques in a collision-free condition. Various scalar and vector quantities of dissociation have been measured, and corroborated by theoretical modelling and molecular orbital calculations.

Halothane, a saturated alkyl halide, undergoes the impulsive C-Br bond cleavage, as expected, on excitation of the σ*(C-Br)←n(Br) transition at 235 nm. However, unexpectedly the stronger C-Cl bond also cleaves due to the energy transfer from the [n,σ*(C-Br)] state to the [n,σ*(C-Cl)] state. The presence of the bromine atom has a pronounced effect on the C-Cl bond dissociation dynamics. The energy transfer between these two modes is fast enough to produce anisotropic distribution of the chlorine atoms. In case of tetrachloroethylene, however, presence of unsaturation modifies the initial transition at 235 nm to the [π,σ*(C-Cl)] state, from where fast chlorine is produced. In addition, a slow chlorine atom channel is observed from the ground state of tetrachloroethylene, formed after fast internal conversion. Both chlorine atom channels are associated with a slow dissociation. In halogenated molecules of benzoyl and 2-furoyl chlorides, with carbonyl group and extended conjugation, the initial excitation at ~235 nm leads to the ($^1\pi,\pi^*$) state with the initial excitation localized in the carbonyl group. The initially excited state produces mainly the high kinetic energy chlorine atom channel, and a minor fraction relaxes to the ground state (S_0) to produce the slow chlorine atom channel. The overall C-Cl bond dissociation dynamics is similar in both the molecules. However, in benzoyl chloride a molecular HCl elimination channel was observed, which is not feasible energetically in 2-furoyl chloride. For a halogenated molecule with a nitro group, such as 2-bromo-2-nitropropane (BNP), the dynamics of dissociation is very much different. At 248 nm the BNP molecule is excited to the (n,π^*) state from where it relaxes to the ground state, and subsequently dissociates to produce OH and Br through different channels. At 193 nm the initial excitation is located at C-Br bond (n,σ* state), from where BNP molecules can undergo repulsive C-Br bond scission, and subsequently the co-fragment of Br can dissociate producing OH after intramolecular re-arrangement. Alternatively, the mechanism of OH formation can remain similar as that proposed for the dissociation of BNP at 248 nm excitation.

FUTURE DIRECTIONS

The work reported in the thesis employing REMPI technique has been carried out by single laser beam. Better information about the excited PESs, and their interaction can be deduced by performing experiments at different frequencies of the pump laser, and using velocity map imaging. Our main objective was to measure the scalar dynamical quantities like, internal energy distribution, spin-orbit ratio, doublet ratio, etc. associated with OH formation for understanding OH formation dynamics in photodissociation of polyatomic molecules. One may obtain additional information on the dynamics by performing polarization experiments and detecting the vector quantities, like angular distribution of the OH photofragment etc.

We have explained our experimental results satisfactorily with theoretical calculations at relatively lower level, because of computation resource constraints. The associated error level in energy calculations can be further reduced by performing calculations at higher level with larger basis sets.

List of Figures

List of Tables

furoyl chloride at 235 nm, leading to Cl and its co-fragment radical. All energies are in kcal/mol.

Table 5.2: The excitation energy (hν), dissociation energy of the C-Cl bond (D_0), available energy (E_{avl}), the average translational energy, $\langle E_T \rangle$ value, the relative quantum yield (Φ) and the recoil anisotropy parameter (β) for photodissociation of benzoyl chloride at 235 nm, leading to Cl and its co-fragment radical. The values in parentheses pertain to the slow chlorine atom channels. All energies are in kcal/mol.

Table 5.3: A comparison between experimental UV absorption and theoretically calculated vertical excitation energy (VEE), oscillator strengths (OS) and characters of lower singlet excited electronic states of benzoyl chloride, 2-furoyl chloride and benzoic acid.

CHAPTER 1

Introduction

One of the challenging dreams to a chemist is to have a control over the route of chemical reactions by driving them in the desired directions. To achieve this, one must have exact knowledge about the true nature of chemical reactions at molecular level. Chemical dynamics is the branch of chemistry which deals with the study of microscopic details of the chemical reactions, at the molecular level. It deals with both intramolecular motion and intermolecular collisions [9]. Bond dissociation being a fundamental chemical process, its investigation induced by a laser provides valuable information both on basic understanding of a chemical process and its important applications. It also provides a great deal of information regarding potential energy surfaces upon which the fragments fly apart [10,11]. The photochemical approach for studying bond dissociation is preferable over the thermal bond dissociation process. In thermal dissociation the given heat energy gets distributed statistically throughout all degrees of freedom and eventually the weakest bond gets broken [12]. However, due to the bond selective nature of photochemical dissociation, high degree of selectivity can be obtained in reaction channels by this route. Particularly, the application of lasers has given a new dimension to photodissociation studies under non-thermal equilibrium conditions in the time scale extending up to picoseconds and femtoseconds. In recent times several laser spectroscopic techniques have emerged as primary tools to obtain detailed information on structure and intramolecular dynamics of the molecules. The spectroscopic studies, which basically furnish the information on the microscopic details of reactants and products states, measure the dependence of physical quantities on frequency and rely primarily on the interaction of radiation (more precisely electromagnetic radiation) with matter. When an electromagnetic radiation falls on a molecule or an atom, the oscillating electric field induces an oscillating dipole to the molecule or atom. This oscillating dipole now acts as a source of electromagnetic radiation with the same frequency as the frequency of the incident radiation, propagating in all direction. However, when the frequency of the incident radiation matches with the natural frequency of the molecule or atom, as given by its energy states, a resonant condition is established between these two (i.e., the photon and the molecule or atom). Consequently, the molecule or atom absorbs a quantum of radiation (i.e., a photon) and gets promoted to a higher energy state.

1.1 Different methods of photoexcitation

The excited state of a species can be prepared by various methods using electromagnetic radiation as an excitation source, e.g. one photon excitation, multiphoton excitation, vibration mediated photoexcitation, etc. The work described in this thesis deals with one photon excitation of polyatomic molecules to initiate the photodissociation process, and one or multiphoton excitation to probe the resulting photoproducts.

1.1.1 One photon excitation

In one photon excitation the species of interest absorbs a single photon to get excited from its ground state to an upper energy state. The selection rules [13] governing that kind of excitations, for diatomic molecules or linear polyatomic molecules, are

(i) $\Delta\Lambda = 0, \pm 1$: allowed changes in the projection of total orbital angular momentum in the direction of molecular axis.

(ii) $\Delta\Omega = 0, \pm 1$: allowed changes in the projection of total angular momentum (orbital and spin) in the direction of molecular axis (where, $\Omega = \Lambda + \Sigma$).

(iii) $\Delta S = 0$: total spin is conserved

(iv) Symmetry properties of the states must be conserved.

As symmetry is more and more reduced, the quantum numbers in non linear polyatomic molecules become less important. In this case, only the rule (iii) $\Delta S = 0$ is valid, and the total spin S remains important; at least for molecules without atoms of highly charged nuclei, where spin-orbit-interaction occurs.

1.1.2 Multiphoton excitation

In multiphoton excitation two or more photons are simultaneously absorbed by the species (molecule or atom) to get excited. The probability of an absorption process is often described by the term absorption cross-section, and for *n* number of simultaneous photon absorption process it can be defined as:

(*n* photon transition probability) = (*n* photon absorption cross-section) X (light intensity)^n. The absorption cross-section for single-photon absorption is several orders of magnitude greater than that for multiphoton absorption, e.g. typical values for one and two photon absorption cross-sections are in the order of 10^{-18}cm^2 molecule^{-1}and 10^{-48}cm^4 s molecule^{-1} photon^{-1}, respectively [14].

The important point regarding the multiphoton excitation is that, the same selection rules are valid for each step of all these processes [14]. It implies that two photon transitions can only be observed between two states that are both connected to an intermediate level (a virtual state) by allowed single photon transitions. Here the overall transition can occur with no change in parity, and hence $g \rightarrow g\ and\ u \rightarrow u$ transitions are observed for molecules having center of symmetry. It is therefore possible to reach atomic/molecular states, using two photon excitation, which cannot be populated by single photon excitation from the ground state.

1.2 Fate of the electronically excited molecule

A molecule in the electronic excited state can behave as a completely different chemical species because of the different charge density, excess energy and weaker bonds with respect to its ground state entity. The excited molecule, subsequently, can undergo different photophysical processes for returning to the ground state or photochemical processes to lose its identity.

1.2.1 Photophysical processes at the excited state

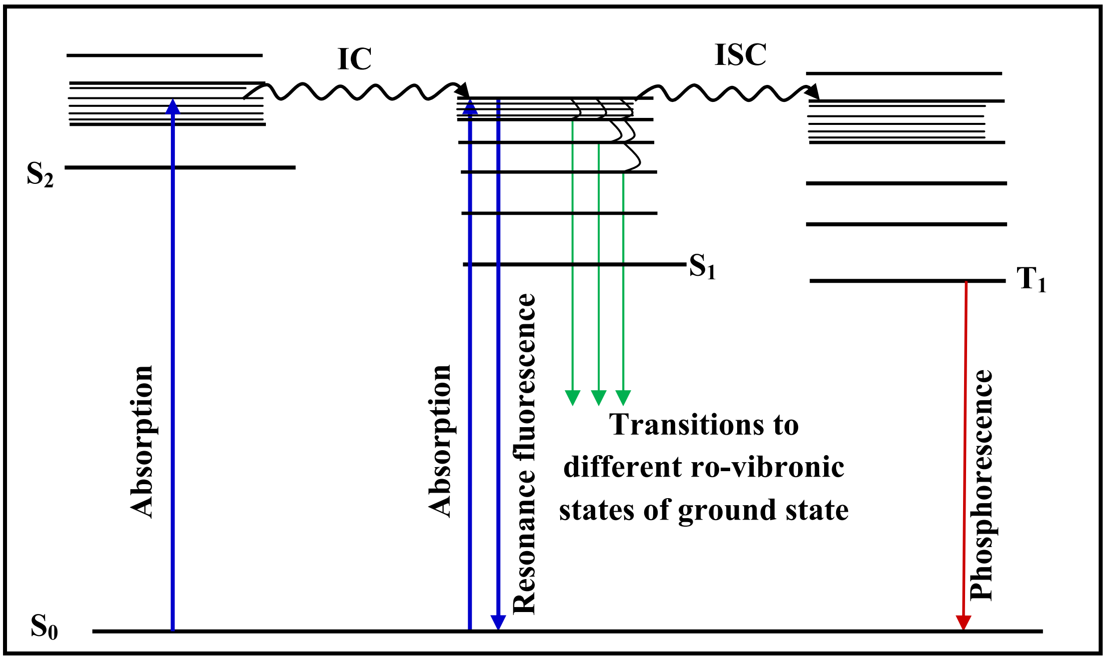

FIG. 1.1: *Photophysical processes of an excited polyatomic molecule in gas phase. Vertical straight lines represent radiative transitions, wavy lines represent non-radiative transitions.*

Once a molecule absorbs energy in the form of electromagnetic radiation, there are a number of photophysical routes by which it can return to the ground state (statistically the most common energy state for chemical species at room temperature). In monoatomic gases at low pressure and temperatures, resonant emission is likely to be the only mode of return. However, in condensed systems and in polyatomic molecules in gases at reasonable pressure, there are more than one pathways available for the excited molecule to revert back to the ground state. In the condensed phase, the Jablonski diagram best illustrates the photophysical process of electronically excited molecules that has been prepared by UV or visible light irradiation. But, in the gas phase at low pressure, the collision-induced processes are less efficient and hence Jablonski diagram should be accordingly modified to understand the fate of an excited molecule in the gas phase. For diatomic species, like OH radical, the fluorescence mostly occurs from the same ro-vibronic level (resonance fluorescence) of higher state to which the molecule was initially excited. For polyatomic molecules the most common method to denote the energy states is simply by their spin multiplicity, defined as $2S+1$, where S is the spin quantum number. Electronic states with all its electrons spin-paired are referred as the singlet states and denoted by the symbol '*S*'. While electronic states with two electrons with parallel spin called triplet states and are represented by '*T*'. Each one of these electronic levels has a number of vibrational levels and each vibrational level in turn has a set of rotational levels. The photophysical processes for gas-phase (in low pressure, where collision deactivation is negligible) are shown in FIG. 1.1, where S_0, S_1 and S_2 denote, respectively, the ground, first and second excited singlet electronic states of a molecule, and T_1, T_2 etc. represent the triplet states of that system. If the photon emission occurs between states of the same spin state (e.g. $S_1 \rightarrow S_0$) this is termed fluorescence. If the spin states of the initial and final energy levels are different (e.g. $T_1 \rightarrow S_0$), the emission is called phosphorescence. Since fluorescence is statistically much more likely than phosphorescence for most molecules, the lifetimes of fluorescent states are very short (nano seconds) compared to phosphorescence (micro seconds) to minutes or even hours). Internal conversion (IC), is the radiationless transition between energy states of the same spin states, and intersystem crossing (ISC) is a radiationless transition between different spin states. Vibrational relaxation is another type of radiationless transition, which is most common among the three radiationless transitions in condensed phase (or even in gas phase at high pressure), occurs very quickly ($<1 \times 10^{-12}$ s) and is enhanced by physical contact of an excited molecule with other particles. In a polyatomic molecule with 3n-6 (n is number of atoms in the molecule) modes of vibrations, radiatonless transitions are observed even in vapor phase at very low pressures. Here the rate of collisions (typically 10^4 collisions s^{-1} at 1 mtorr pressure and room temperature) is likely to be less than the rate for radiationless conversion (typically 10^{12} s^{-1} at state density of 25 states /cm^{-1}) [15]. It indicates that non-radiative conversion is an intrinsic property of polyatomic molecule [13].

1.2.2 Photochemical processes at the excited state

The nature of the excited state often dictates the fate of the excited molecule, e.g. a transition from a bonding to an anti-bonding orbital can cause a single bond to break or lowering the bond order of a multiple bond. Excited state processes that result in changes in bonding are known as photochemical processes. An electronically excited molecule can undergo various photochemical processes, such as photodissociation, photo-isomerism or photo-rearrangement, electron transfer etc. In the following section, the photodissociation process is discussed in detail, as the work in this thesis is based on the photodissociation dynamics of polyatomic molecules in gas phase.

1.2.2.1 Photodissociation and its types

Photodissociation involves the fragmentation of a bound molecule through absorption of one or more photons [1]. The molecule will irreversibly break apart when the internal energy of the molecule, gained from conversion of the electromagnetic energy of the light beam, exceeds the binding energy of its weakest bond. However, it is worth mentioning here that, mode selective dissociation can be achieved using a laser light source with selective wavelength and proper pulse width or using vibrationally mediated photoexcitation.

A typical photodissociation reaction can be written as

$$\mathrm{AX}+\mathrm{N\ photon}\ (h\nu) \rightarrow (\mathrm{AX})^* \rightarrow \mathrm{A}(\alpha) + \mathrm{X}(\beta). \quad (1.1)$$

Here, in the first step the parent molecule AX absorbs N number of photons with frequency ν and gets excited to form $(AX)^*$. The second step represents the fragmentation of the excited complex into products A and X, where A and X represent either structure less atoms or molecules with internal degrees of freedom of their own, and the labels α and β specify the particular internal quantum states of the nascent products. The dissociation energies may vary from a few kcal/mol for physically bound van der Waals molecules to hundred of kcal/mol for chemically bound molecules. The extremely wide range of possible dissociation energies necessitates the use of different kinds of light source to break molecular bonds. Vander Waals molecules can be fragmented with single infrared (IR) photons whereas the fission of a chemical bond requires either a single ultraviolet (UV) or many IR photons.

Photodissociation, initiated by single photon absorption, can be roughly categorized as either direct or indirect dissociation. Electronic transitions bring the molecule to the PES of a particular excited electronic state from that of the electronic ground state. The shape of every PES is different from all others. Because of the instantaneous nature of the electronic transition i.e., much faster than the nuclear motion, the molecule does not change its shape during the transition (Frank-Condon principle). Therefore, just after the transition, the shape of the molecule is, in general, not the equilibrium one of that particular excited state, to which the molecule brought on to. In other words, the molecule is not at the bottom of the PES of the excited electronic state. Very often the molecule finds itself on the steep slope of a repulsive PES, which can lead to instantaneous (i.e. in less than 10^{-13} s) dissociation (as in Figure 1.2 a). This process is known as direct dissociation.

In case of indirect photodissociation (FIG. 1.2(b), (c) and (d)) a dynamical constraint like potential barrier obstructs the immediate dissociation of the molecule.

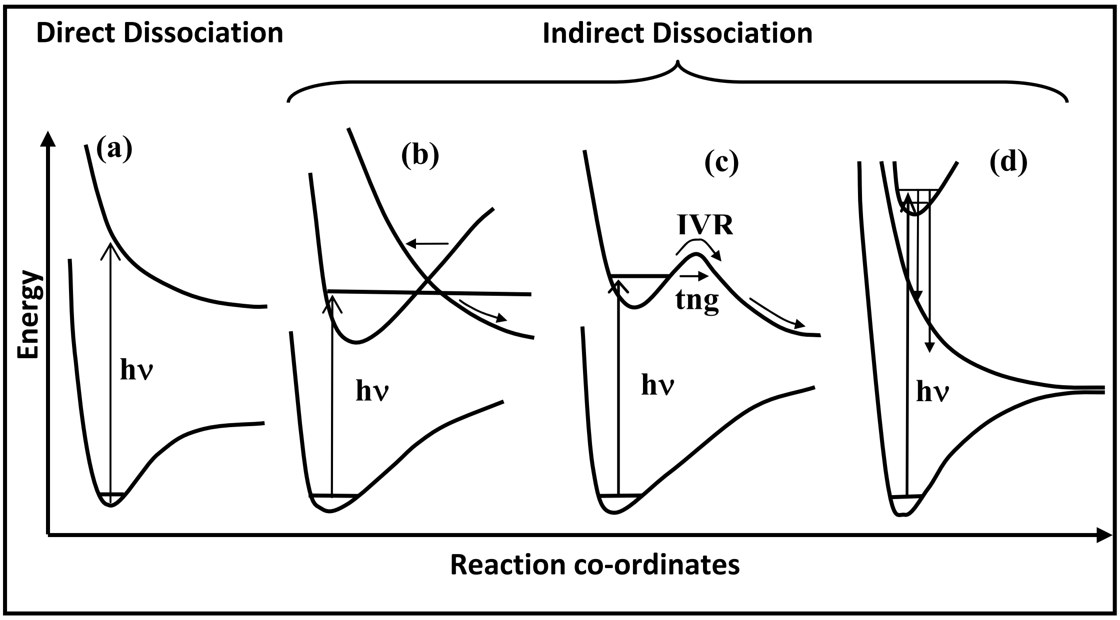

FIG. 1.2: *Direct and indirect photodissociation processes of diatomic molecules.*

In the process 1.2 (b) the photon excites the molecule AX to a bound electronic state where it cannot break apart. However, if the molecule undergoes a transition from the bound state to a repulsive state (the diabatic representation, through an intersection of two excited state), the molecule will ultimately decay. The rate of such process depends on the coupling between the two electronic states, and final fragmentation takes place in a different electronic state than the originally excited state. This process is called electronic predissociation [1]. The word "predissociation" means that the molecule dissociates before it can decay to the electronic ground state by emission of a photon.

In other type of predissociation (FIG. 1.2(c)) there is a potential well at a close distance to the excited state and a barrier that blocks the dissociation channel. The barrier might be considered to be the result of an avoided crossing with another electronic state (the adiabatic representation). In this situation, excitation of the molecules is to quasi-stable (known as “resonance”) states inside the well, and immediate dissociation is prevented by the potential barrier. These excited molecules can dissociate either by tunneling (tng) through the barrier, or by intramolecular vibrational energy redistribution (IVR) between the various vibrational degrees of freedom in a polyatomic molecule. The rate here depends on the rate of tunneling and/or the efficiency of vibrational energy transfer. This predissociaton is termed as vibrational predissociation. Apart from above mentioned predissociation, the excited bound states can dissociate through the spontaneous radiative dissociation (FIG. 1.2(d)), in which the emission of photons populates the continuum of a low-lying repulsive state or the vibrational continuum of ground electronic state. The efficiency of the above process is determined by the competition with spontaneous emission into low-lying bound states [1,15]. Figure 1.3 shows two additional types of photodissociation processes [1]. In (a) the photon excites first a bound electronic state which subsequently decays following a radiation-less transition to a lower electronic state. This produces a highly excited vibrational-rotational quantum level above the dissociation threshold of the electronic ground state which eventually breaks apart. Alternatively, in (b) a highly excited quantum state above the dissociation threshold is created directly by pumping a large amount of energy into the molecule by single-photon excitation of overtone vibrations.

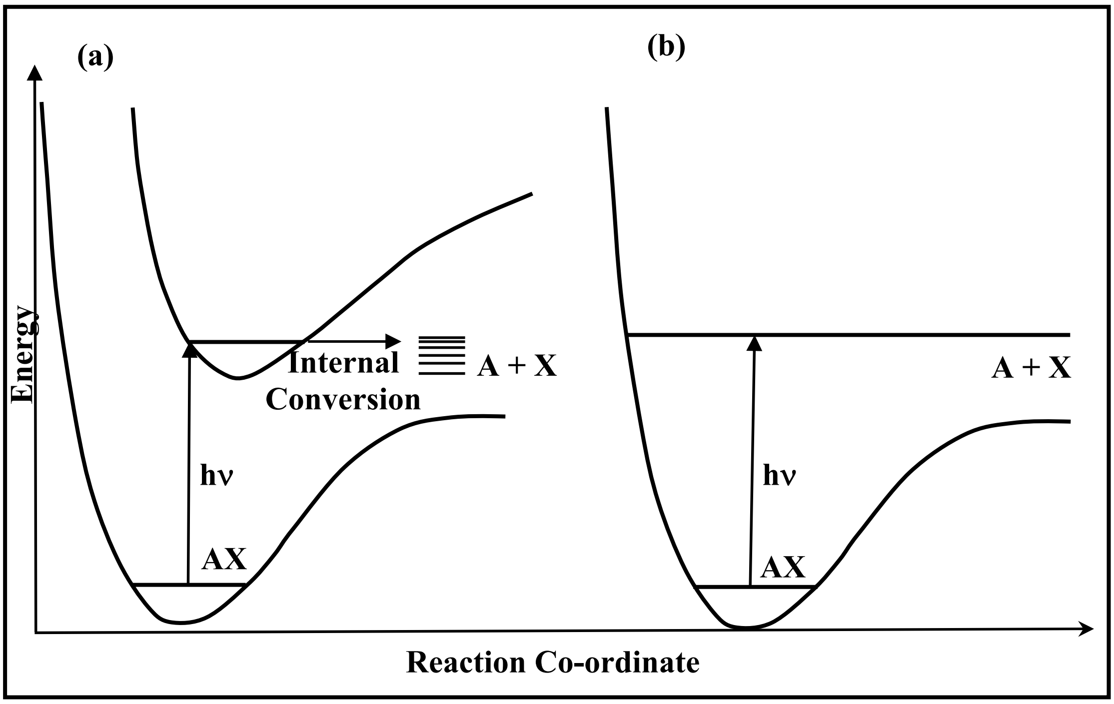

FIG. 1.3: *Two additional types of photodissociation processes of diatomic molecules.*

1.3 Photodissociation dynamics

The principal aim of photodissociation studies is to obtain a clear picture of the molecular dynamics in the excited electronic state as the molecule leaves the Frank Condon region, traverses the ‘transition state’ (i.e., the barrier, if there is any), and finally reaches the asymptotic channel(s), where the fragments are formed. Studying photodissociation dynamics in gas phase provides the simplest view of unimolecular reaction and correlation between the nature of potential energy surfaces and mechanism of dissociation. These microscopic knowledge, ultimately, may able to answer the fundamental questions like [1]: What is the lifetime of the molecule in the upper state and how does this lifetime depend on the excitation energy? Which bonds break and what is the branching ratio for the possible chemical channels? If more than one bond breaks, does this occur in a concerted or a sequential process? Is the dissociation governed by one and only one electronic state or does the fragmentation take place on several potential energy surfaces? How is the total available energy, E_{avl}: $= E_{photon} - D_o$ (i.e., the photon energy minus the dissociation energy) distributed among the translational and internal degrees of freedom of the fragments? What are the probabilities for filling the various electronic, vibrational, and rotational states of the fragments after the bond is broken?

Photodissociation induced by the single photon absorption facilitates the detailed study of molecular dynamics such as the breaking of bonds, internal energy transfer, radiationless transitions, etc. These microscopic informations obtained are not only of fundamental interest, but are also valuable in different branches of chemistry. In recent times the availability of powerful tunable lasers has stimulated rapid development of new experimental techniques, in the field of photodissociation dynamics, which make it possible to analyze photodissociation processes in minute detail. At the same time, theoretical support to treat this fundamental process, at least for small molecules, paved the way for better understanding of molecular motion in excited electronic states.

1.3.1 Experimental methods

With the advent of tunable dye lasers in early 70’s the field of reaction dynamics got a major boost. The hitherto impossible experiments, which could not be performed due to lack of intensity or insufficient resolution, get successfully pursued by virtue of the special properties of lasers like, high intensity, monochromaticity, low divergence etc. Applications of lasers have been very useful to the studies of photodissociation dynamics for a variety of reasons [16].

(1) The narrow line width of laser light can be exploited for preparation of reactant molecules in a well-defined vibronic and ro-vibronic level. Subsequently, these molecules can be probed to understand their fate in a collision-free condition of the gas phase.

(2) Tunable dye lasers have played a major role in studying , and the implementation of techniques like laser induced fluorescence (LIF) [17,18], coherent anti-Stokes Raman spectroscopy (CARS) [19] and resonance enhanced multiphoton ionization (REMPI) [20]. These laser based techniques allow detailed investigation of the internal quantum state population distributions (e.g. rotation, vibration, spin–orbit, lambda doublet, etc.) within a wide range of products from both unimolecular (i.e. photofragmentation) and bimolecular reactions.

(3) A reaction can be followed in real time by carrying out a time domain experiment using pico- or femtosecond pulsed lasers.

(4) Use of polarized laser light gives us a wealth of information on vectorial characteristics of photodissociation mechanisms, such as **E-μ-v** correlation, **E-μ-J** correlation and **v-J** correlation, where **μ** is transition moment of the parent, **v** and **J**

are the velocity and rotational angular momentum of the recoiling fragments, respectively, and **E** is the polarization of the laser.

(5) Novel laser-based techniques, for example, cavity ring-down spectroscopy, offer high sensitive and selective detection tools in addition to LIF and REMPI.

In this thesis, different dynamical parameters like partitioning of the available energy in the product states, branching ratio of different possible channels etc. are probed by employing two state selective and sensitive techniques mentioned above, i.e., LIF and REMPI. The details of the experimental setup are provided in the 2nd chapter of this thesis; however, a brief introduction to these techniques is given as follows.

1.3.1.1 Laser induced fluorescence (LIF)

The LIF method, based on the fluorescence phenomenon, is one of the most widely used laser based diagnostics in various research fields [14,21]. LIF involves the absorption of radiation by the species of interest, and monitoring of the subsequent emission from the excited state. In UV-visible LIF in a gaseous medium, it is possible to transfer the population of molecules from a ro-vibrational state in the ground electronic state to a rovibrational state in the excited electronic state, using a laser with proper wavelength (provided, the spectral bandwidth of the laser employed is less than the rotational state spacing). The intensity of the fluorescence signal I_{lif} , is proportional to the population of the species in the excited state, which is related to the initial ground state population before laser excitation. The schematic of laser photolysis-LIF is shown in FIG. 1.4. In the first step the photodissociation laser ($h\nu_d$) forms the photofragment of interest in different ro-vibrational states. By scanning the probe laser ($h\nu_p$), after a suitable time delay with respect to the pump or dissociating laser, photofragments in a specific ro-vibrational level (*v″, J″*) are excited to a particular ro-vibrational level (*v′, J′*) in the electronic excited state, when the energy of the laser light coincides with the energy separation between the two levels. Then the total fluorescence from the excited level to various ground state levels (hν_f) is collected without energy dispersion. This fluorescence excitation spectrum corresponds to the absorption spectrum [17], but is advantageous over the latter due to less interference from the scattered photons. In principle, the technique is very useful and can be used for detecting single molecular species. One may obtain sensitivity of 10^6 particles cm^{-3}. However, there are certain requirements to use LIF technique as a probe, such as, the species should be fluorescence with high quantum yield, the band system to be accessed by LIF technique should be spectroscopically well characterized and tunable laser system should be available to access the band system.

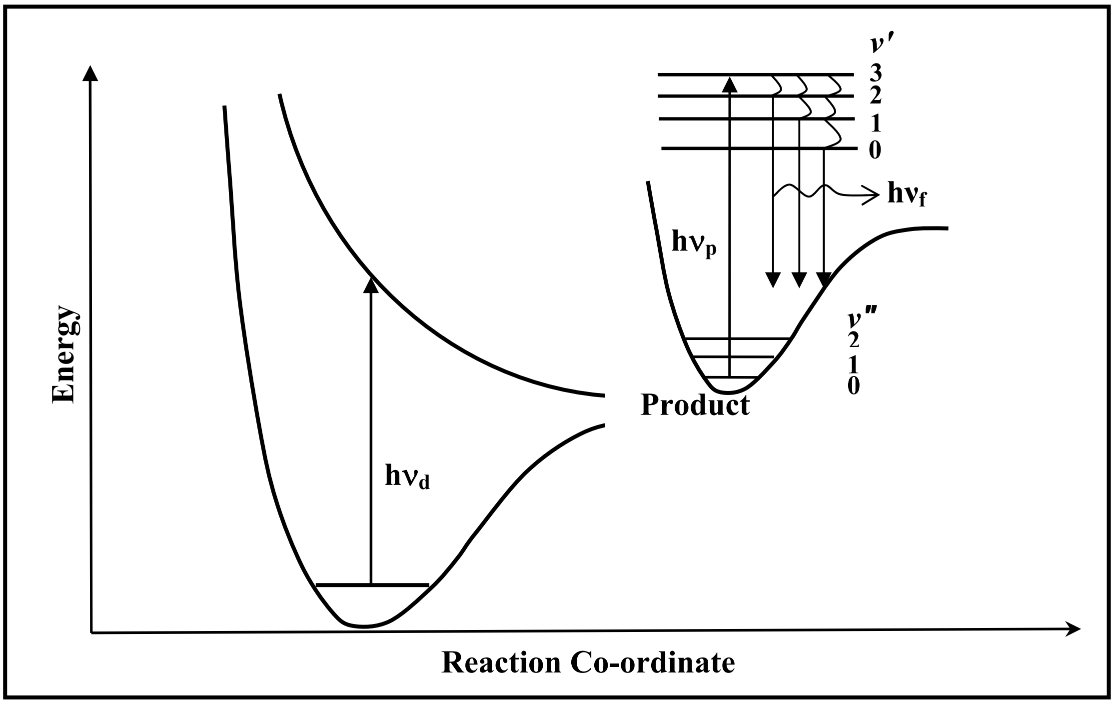

FIG. 1.4: *Schematic of laser photolysis-laser induced fluorescence technique.*

1.3.1.2 Resonance enhanced multiphoton ionization (REMPI)

The REMPI technique typically involves a resonant single or multiphoton excitation of a molecule or an atom to an electronically excited intermediate state followed by absorption of another photon or more than one photon, which ionizes the species. The basic difference between a multi photon ionization (MPI) process and REMPI is that the latter involves simultaneous absorption of m number (m can be one or greater) of photons in resonance with a particular excited state of the molecule. Therefore, the efficiency of MPI is enhanced by several orders of magnitude. This process, aptly called resonance enhanced multiphoton ionization (REMPI), is a highly sensitive and (because only those molecules preselected in the intermediate state can be ionized) highly state-selective method. A REMPI scheme involving m number of simultaneous photon absorption to an excited electronic state followed by n number of photon absorption for ionization purpose, is designated as "(m+n) REMPI".

For example, REMPI process, in which two photons are used for resonant formation of the excited state, and the other for pumping the prepared state into the ionization continuum, is designated as (2+1) REMPI. In the above processes, the second-step transition i.e. ionization is saturated at the typical intensity of about 10^{26} photons cm^2/s obtained from nanosecond pulsed laser system. FIG 1.5 represents various REMPI schemes with different m and n values, where a solid line (denoted by S_i or S_f) represents a real state and a dotted line represents an intermediate virtual state. REMPI technique is, in general, more sensitive than the LIF technique, as in case of the former highly sensitive mass analyzed detection of photofragments can be done and detection of the ion-current is much easier than the measurement of fluorescence photons. However, an experimental setup for REMPI is relatively more

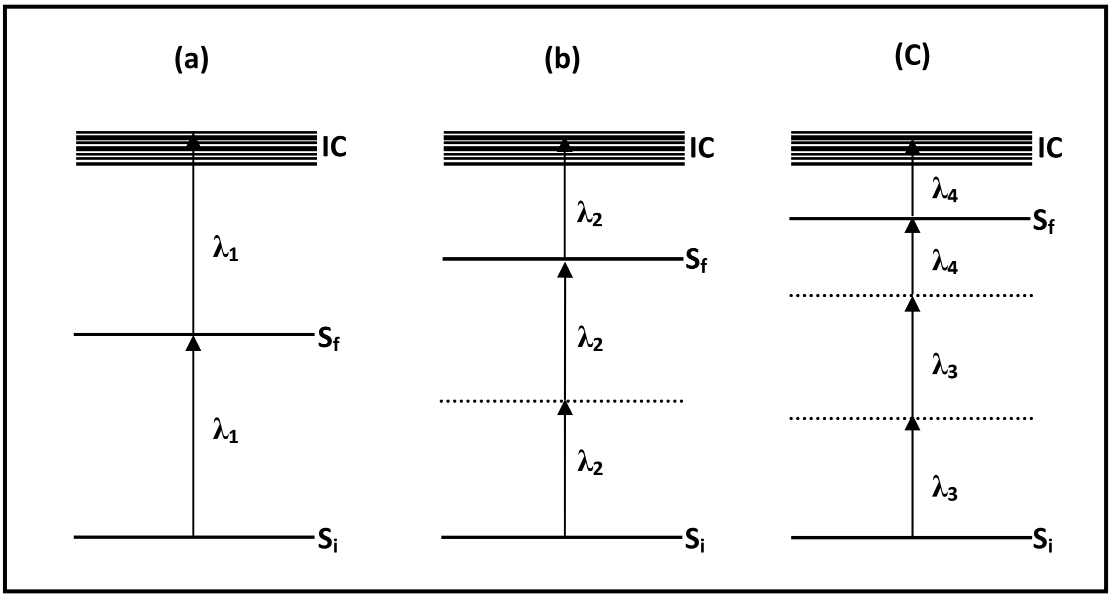

FIG. 1.5: *Schematic of REMPI schemes: a) One color (1+1) REMPI; b) One color (2+1) REMPI; and c) Two color (3+1) REMPI.* S_i, S_f, *and IC denote the initial ground state, resonant excited state and the ionization continuum, respectively.*

complicated than the LIF setup, since the former often required integrated molecular beam setup for sample insertion and mass spectrometry setup for ion detection.

1.3.2 Experimental observables and their importance in understanding dynamics

Photodissociation process is often termed as the second half of a full collision [1]. In a full collision, the reacting particles approach each other from large separation having no interaction between them. During the collision they form an intermediate complex, which subsequently decays to all possible product channels. However, in photodissociation the initially bound parent molecule AX is electronically excited to generate the excited complex (shown in equation 1.1). The photon promoted AX dissociates from the higher electronic state either immediately or after a delay depending on whether the potential is repulsive or has a barrier to fragmentation. Since the second step of photodissociation is equivalent to the second step of a full collision, the terminology "half collision" is justified. The whole process of photodissociation can be understood by determining the scalar, (e.g. kinetic energy distribution, internal energy distribution, branching ratio, etc.) and vector properties (e.g. recoil anisotropy parameter, β etc.) of the photofragments formed. In the following section some experimental observables of a photodissociation process are discussed which help to understand the overall dynamics of the photodissociation process.

1.3.2.1 Partitioning of available energy

The photodissociation reaction event occurs under the constraint of energy and angular momentum conservation. Let a photodissociation event is initiated by the absorption of single photon, having energy hν. When the bond dissociation energy is D, the available energy (neglecting small internal energy of the parent molecule)

$$E_{avl} = h\nu - D \qquad (1.2)$$

is distributed among the translational energy (E_T) and internal energy (E_{int}) of the fragments, where, the latter consist of electronic, vibrational, and rotational energy (E_{el}, E_V, and E_R, respectively) of the photofragments. The fractions of E_{avl} among these energies are denoted as f_T, f_{int}, f_{el}, f_V, and f_R, respectively ($f_T + f_{el} + f_V + f_R = 1$), where $f_i = E_i/E_{avl}$. The way in which the available energy is distributed among the degrees of freedom is called energy disposal. In gas phase dynamics studies use of ultrasensitive and fast detection methods, in a collision less condition, enables the measurement of energy distribution among the photofragments in their nascent state. The measurement of such nascent internal energy state distribution has been one of the major areas of experimental research in chemical dynamics. Vibrational and rotational energy distribution is usually obtained in chemiluminescent and LIF experiments, whereas the translational energy distribution is obtained from time-of-flight – mass spectrometer (TOF-MS) and Doppler shift studies. A detailed procedure to obtain the available energy distribution in different internal and translational energy modes using LIF and REMPI-TOF-MS is discussed in the next chapter.

The partitioning of the available energy into various degrees of freedom of the photofragments is mainly governed by the nature of transition state, and its location on the dissociative potential energy surface. Different models are often employed to explain the experimentally obtained energy partitioning data. These models range between the statistical model at one end and the impulsive model at the other end. A statistical prior distribution, and thus the statistical model, is often the starting model to understand any dissociating event. In this model the available energy (E_{avl}) is distributed among all the accessible states with equal probabilities under the constraint of conservation of energy. In those cases where, the photo-excited parent molecule is so long-lived that the excess energy is partitioned statistically among the available degrees of freedom of the products, the statistical dissociation process occurs predominantly. These long lived processes include dissociation from the ground state or a rapid internal conversion to the ground electronic state followed by the subsequent slow dissociation. Under such cases, in a large molecule, with many low-frequency modes, a relatively small amount of the excess energy is partitioned into translational motion of the products. For this statistical dissociation process, a priori calculations [22-24] were adopted, along with a simple analytical expression established by Klots [25], relating the mean translational energy release, E_T, and the E_{avl}, for a statistical barrierless dissociation process. The impulsive model [26], on the other hand, best describes the energy partitioning for a dissociative event on a repulsive surface. In this case, the distribution of energy among product states is governed by the dissociative event, i.e., by the repulsive force acting during the breaking of the parent molecule into the products. This treatment conserves the energy and both the linear and the angular momenta but provides only single-point energies, and not a distribution. The impulsive model assumes that all the available energy is stored within the breaking bond, i.e., when the bond breaks, the impulse transfers the energy to the photofragments, conserving the linear and the angular momenta. In general, the impulse is not along the center of mass of the separating fragments and thus imparts rotational angular momentum to the departing fragments. Apart from the two types of dissociation processes, described above, there are cases where considerable energy barrier is there in the exit channel of a dissociation event. Here,

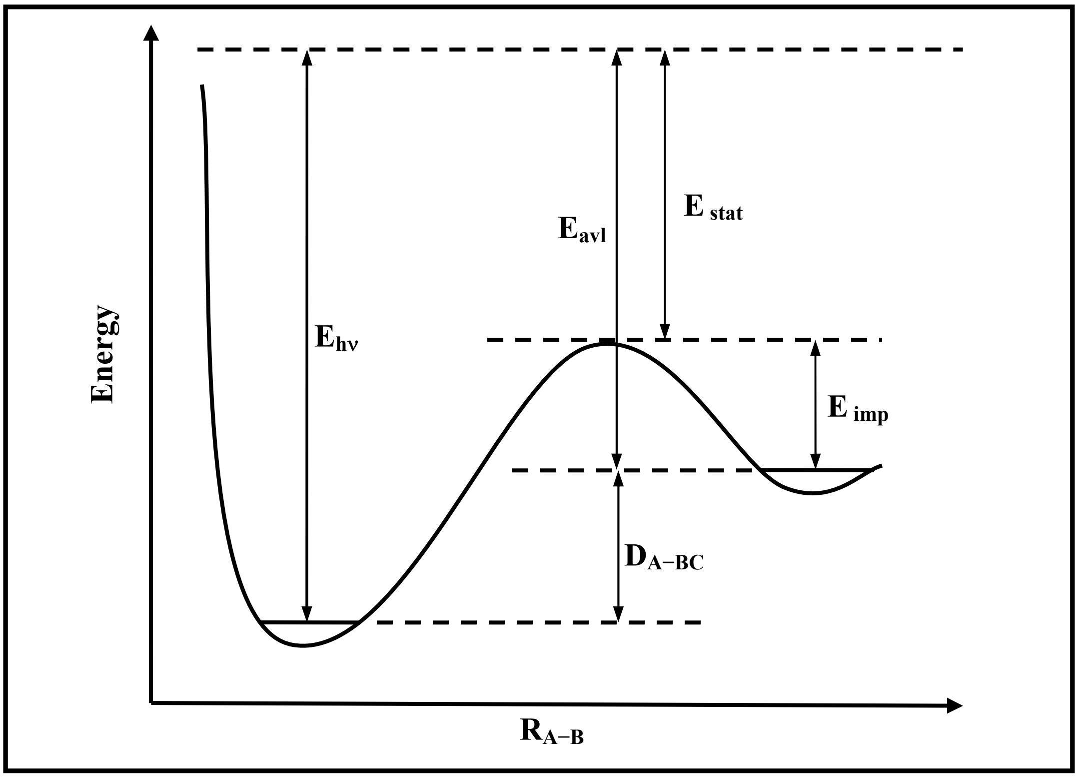

FIG. 1.6: *Energy partitioning, using hybrid model, for the dissociation process* $A{-}BC \xrightarrow{h\nu} A + BC$.

neither statistical nor impulsive model is appropriate to calculate the energy partitioning, and the hybrid model [27], a combination of statistical and impulsive model is usually applicable to explain the energy partitioning data. FIG. 1.6 describes the energy partitioning using hybrid model. In this model, the available energy (E_{avl}) for the products is divided into the excess energy above the exit barrier (E_{stat}) and the exit barrier energy (E_{imp}). The partitioning of E_{stat} and E_{imp} is treated respectively by the statistical and modified impulsive models. The energy partitioned into each fragment is then obtained by adding contributions from each of these two models.

1.3.2.2 Branching ratio

Upon excitation to a particular well defined excited state, the photodissociation of a polyatomic molecule is expected to correlate with a particular product state. However, possibilities of multiple product channels and thus branching ratio arises, due to curve crossing and interaction of the initial excited state with other dissociative surfaces, which correlates with other products. In the photodissociation of polyatomic molecules two or more dissociation channels can compete with each other. This different dissociation channels can even correlate to the same product species but with different quantum state, e.g. spin orbit ground ($^2X_{3/2}$) and excited state ($^2X_{1/2}$) of halogen atom, spin orbit ground ($^2\Pi_{3/2}$) and excited state ($^2\Pi_{1/2}$) of the OH radical etc. The branching ratio can be experimentally obtained by observing the quantum yields of each of the products, using state selective and sensitive techniques like LIF, REMPI, etc. The value of the quantum yield often indicates the position of curve crossing with respect to the exit channel [28-30]. The effect of curve crossing on relative yield of two different photoproducts is discussed in detail in chapter 3 with reference to photodissociation of bromochloro alkanes.

1.3.2.3 Vector quantities in photodissociation dynamics

Vector quantities have an important role in the elucidation of both molecular dynamics in general and photodissociation dynamics in particular. The importance of vector correlation between a molecule and its fragments was recognized as early as 1928 [31]. However, influence of these correlations on the dynamics of photodissociation was realized in the 60's [32]. These vector quantities, in combination with scalar quantities like energy partitioning, branching ratio, etc., help in elucidating the photodissociation event. When an event is probed using a linearly polarized laser source with a polarization vector defined as **E**, several other vectors of interest can be measured in correlation with that. The vectors of interest due to the vector correlations are:

E: the polarization vector of the laser light.

μ: the transition dipole moment vector of the parent compound.

v: the recoil velocity vector of the fragments.

J: the rotational angular momentum of the photofragment.

Analysis of the correlations of **μ**, **v**, and **J** with **E** and among each other is necessary for a better understanding of photodissociation dynamics, particularly for polyatomic molecules with more than three atoms. The vector correlation between **E** and **μ** can be considered as the most preliminary one, as under the electric dipole approximation [1] the probability for absorbing the photon, by the molecule of interest, is proportional to $\cos^2\theta$, where θ is the angle between **μ** and **E.** Thus, the photon preferentially excites those molecules with their dipole moments parallel to the polarization vector. This leads to an alignment of the excited molecule in the laboratory system, immediately after the absorption. The direction of fragment departure, the recoil velocity **v**, mostly bears a fixed angular relationship with **μ** in the laboratory frame. For example, in a diatomic molecule **v** will be either parallel or perpendicular to **μ**, and **μ** is already aligned in the laboratory frame with the dissociating laser. Consequently, **v** will also be aligned in the laboratory frame, provided that the dissociation is rapid enough so that the alignment of **μ** is not lost before the moment of fragmentation [32]. This situation finally results to an overall **E-μ-v** correlation.

The vector correlation between **μ** and **v** often leads to an anisotropic distribution of the photofragments, which is quantified in terms of recoil anisotropy parameter β, and is given by,

$$\beta=2\langle P_2(\cos\theta_m)\rangle \qquad (1.3)$$

where, θ_m is the molecular frame angle between **μ** and **v,** and $P_2(x) = 3x^2/2-1/2$ is the second order Legendre polynomial. Thus, limiting values of β are 2 and -1 for θ_m of 0° and 90°, respectively, and the β value determine the angular distribution of the photofragments, I(θ). For example, if an excited diatomic molecule dissociates immediately after the absorption of the photon, the angular distribution of the photofragments would be $I(\theta) \sim \cos^2\theta$ for an anisotropy parameter $\beta = 2$. On the other hand $\beta = -1$ would yield $I(\theta) \sim \sin^2\theta$. If the parent molecules are excited from a state, for example, Λ(or Ω)=0, then in the former case they dissociate from a state Λ(or Ω)=0 (referred as parallel transition) and in the latter case from a state with Λ(or Ω)=1(referred as perpendicular transition). Thus knowing the β ($-1\leq \beta \leq 2$) parameter can provide information concerning the alignment of the transition dipole moment **μ** in the molecular frame of the parent molecule and can depict the symmetry of the upper state, if that of the lower state is known.

Another consequence of the alignment of parent molecules by the dissociating photon is that a laboratory frame alignment may be induced in the rotational angular momentum **J** of the photofragment. Similar in case of the recoil anisotropy, this alignment is strongest when the dissociation takes place in a timescale short compared to the rotational time period of the parent compound. It arises because there is usually an angular correlation between the transition dipole moment **μ** and the plane of fragment rotation. Now, since **μ** is aligned in the laboratory frame by **E**, **J** will also be aligned, thus give rise to **E-μ-J** correlation. Consequences of this correlation is that, if the fragment is born in its ground state, it will preferentially absorb light of a specific polarization [33] whereas if the fragment is formed in an excited state, its emission will be polarized [34]. Since both **v** and **J** are correlated with **μ**, they must also be correlated with each other (FIG. 1.7 [32]). However, there is one basic difference between the correlations discussed above and the **v**-**J** correlation. While the **E-v** and the **E-J** correlations relate to the laboratory frame, the correlation between the recoil velocity **v** and the fragment angular momentum **J** is in the molecular frame and eventually, completely independent of the laboratory system. This has very important consequences on the dynamics of dissociation. As already mentioned above the

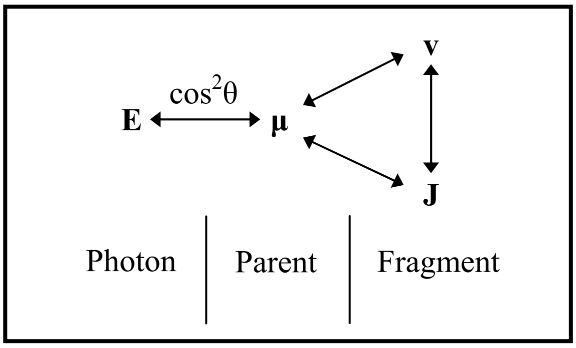

FIG. 1.7: *Different vector correlations in photodissociation dynamics. The transition dipole vector,* **μ,** *is correlated both with* **v** *and with* **J.** *Consequently,* **v** *and* **J** *are correlated even there is no* **E-v** *or* **E-J** *correlation.*

alignment of **v** and **J** with respect to the space-fixed z-axis (let the polarization vector **E** is along z axis in laboratory frame) is diminished by overall rotation before the excited complex dissociates. A long lifetime destroys the alignment. The correlation of **J** with **v**, on the other hand, is completely independent of the laboratory frame and not established until the bond breaks and the two fragments recoil. Thus, rotation of the parent molecule prior to dissociation is irrelevant in this case. The **v**-**J** correlation represents a new observable which can provide additional information about the bond rupture and the exit channel dynamics other than the final state distributions [1].

Knowing the experimentally determined dynamical parameter like nascent state distribution of available energy, branching ratio of different possible channels, recoil anisotropy parameter etc. can give an overall idea of the dissociation process at molecular level. However, a variety of theoretical calculations can be helpful in explaining not only the experimental results, but also predicting the outcome of photodissociation reactions. In the following section a brief on the theoretical calculations is given, which is used in this work to obtain a correlation between the dynamics of dissociation and features of potential energy surfaces.

1.3.3 Computational methods in understanding photodissociation dynamics

It is really necessary to compare the experimental results with theoretical predictions to get a real insight into the heart of a photodissociation event. The theoretical studies related to photodissociation dynamics can be broadly classified as: (a) studies on reaction rates and the energy disposal under statistical or other assumptions (as discussed in section 1.3.2.1) and (b) studies on molecular PESs by ab initio and other methods. The work carried out in this thesis is mostly supported by *ab initio* molecular electronic structure theories. Where, Gaussian 03 [3] program is employed to investigate energetic of different atomic and molecular channels like formation of Br, Cl, OH, HCl etc. The ground state geometries of the parent molecule, along with other fragments and the transition state involved, were optimized mostly at the B3LYP/6-311++G(d,p) level of theory, and energies of these geometries were calculated at the QCISD(T) level with the same basis sets. A common practice was to employ the molecular geometry obtained by optimization at the low level of theory for a single computation, and at a higher level for the energy accuracy. The harmonic vibrational frequencies are also calculated for ensuring the stationary points on the potential energy surface to be true minima, and also for zero point energy correction. Excited electronic state calculations are performed at the time dependent density functional theory (TD-DFT) level, using aug-cc-pVTZ basis sets (in most cases), and the electronic states of the parent molecule, accessible at the photolysis wavelength, are predicted from the vertical excitation energies and the molecular orbital analysis. The structure of an excited electronic state and a transition state have been optimized at CIS level of theory using various basis set. Intrinsic reaction coordinate (IRC) analysis has been performed to characterize a TS structure. The detail of the theoretical methods employed for different system is discussed in the corresponding chapter of this thesis. Some of the keywords for the methods, which are used in this work, are listed in TABLE 1.1. The representation of the molecular orbitals within a molecule is given by the basis set. It can be interpreted as restricting each electron to a particular region of space. Table 1.2 lists the commonly used basis functions. Larger basis sets impose lesser constraints on electrons and more accurately approximate exact molecular orbital. Thus, one can systematically increase the size of the basis set until the results converge to within some desired limits of accuracy.

Table 1.1: *Commonly used methods in Gaussian calculation.*

Keyword	**Methods**
HF	Hartree-Fock Self-Consistent Field
MP2	2nd Order Møller-Plesset Perturbation Theory
QCISD	Quadratic Configuration Interaction (Singles and Doubles)
CIS	Configuration Interaction (Singles)
MP3	3nd Order Møller-Plesset Perturbation Theory
MP4	4nd Order Møller-Plesset Perturbation Theory
QCISD(T)	Quadratic CI (Singles, Doubles and Triples)

Table1.2: *Commonly used basis functions and their description.*

Basis set	**Description**	**No. of basis function**	
		heavy atom[#]	**hydrogen**
STO-3G	Minimal basis set: Used for more qualitative results for big systems	5	1
3-21G	2 sets of functions in the valance region: Used when 6-31G is too expensive	9	2
6-31G(d)	Adds polarization functions to heavy atoms: Used for most jobs up to medium size systems	15	2
6-31G(d,p)	Adds polarization functions to hydrogen as well: Used when hydrogen atoms are the site of interest	15	5
6-31+G(d)	Adds diffuse functions: Most important for systems with lone pairs, anions, excited states	19	2
6-31+G(d,p)	Adds p functions to hydrogen as well: Used when diffuse functions are needed over 6-31G(d,p)	19	5
6-311+G(d,p)	Adds extra valance functions (3 sizes of s and p functions) to 6-31+G(d,p)	22	6
6-311+G(2d,2p)	Puts 2d and 1f functions (and diffuse functions) on heavy atoms and 2p functions on hydrogen atoms.	27	9
6-311++G(2df,2pd)	Puts 2d and 1f functions (and diffuse functions) on heavy atoms and 2p and 1d functions on hydrogen atoms.	34	14
6-311++G(3df,3pd)	Puts 3d and 1f functions (and diffuse functions) on heavy atoms and 3p and 1d functions on hydrogen atoms.	39	18

[#] *Lithium through Neon.*

1.4 Motivation and outline of the thesis

This thesis deals with the UV photodissociation of halogen containing organic molecules in the gas phase. Photodissociation dynamics of these molecules is important because of their important role in atmospheric chemistry, particularly in ozone depletion, and industry. At the same time these molecules have attracted a lot of experimental and theoretical studies, mainly because the C-X bond dissociation is generally observed from a repulsive state, and the curve crossing plays an important role in determining the fine-structure branching ratio of the halogen atom (X). Moreover, number and type of halogen atoms present in a molecule govern the dynamics of the C-X bond dissociation on UV excitation. The UV excitation of the $\sigma^*(C\text{-}X) \leftarrow n(X)$ transition of monohalogenated alkanes produces the halogen radical in both its ground state $X(^2P_{3/2})$ and spin orbit excited state $X^*(^2P_{1/2})$ with different branching ratios and recoil anisotropy, generally involving an impulsive C-X bond scission. But, for alkyl halides having multichromophores, several additional dissociation channels can be observed with different branching ratios, depending on the presence of a functional group and the nature of excitation. Thus it implies that, the nature of chromophore present and the initially prepared excited state of the parent molecule dictate the nature of the photodissociation dynamics and the product state distribution.

In the present thesis we have studied the UV photodissociation of halogenated compounds with various functional groups to investigate the role of chemical environment and nature of the initial excited state on the C-X and N-OH bond dissociation dynamics. The experiments are carried out in collision free condition of the gas phase, using state selective and sensitive state-of-the-art techniques, such as laser photolysis - laser induced fluorescence (LP-LIF) and resonance enhanced multiphoton ionization – time-of-flight (REMPI-TOF). Both the stable and the transient photoproducts are detected, and the nascent state distributions of reaction transients are measured to map the fraction of the available energy partitioned to relative translation, rotation and vibration of the fragments. In addition, the time-evolution of a transient is followed to know the reaction time of a chemical event. Finally theoretical calculations are employed to aid interpretation of the experimental results and to obtain a correlation between the dynamics of dissociation and features of potential energy surfaces.

The thesis consists of total seven chapters for a clear presentation of the work. **Chapter 1** is an introductory chapter providing a general overview of photodissociation dynamics and its importance. **Chapter 2** gives a brief account of the experimental techniques and instrumentation employed to execute the work. In **chapter 3** the photodissociation dynamics of 2-bromo-2-chloro-1,1,1-trifluoroethane (halothane) on excitation of the σ*(C-Br)←n(Br) transition near 234 nm is reported. The details of the chlorine (bromine) atom formation channel and the effect of bromine (chlorine) atom on the overall dynamics of halothane dissociation are discussed in this chapter. Diabetic curve crossing is reported to play an important role in the formation of Chlorine atom channel. **Chapter 4** deals with the UV photodissociation of tetra chloroethylene in a supersonic molecular beam at ~235 nm, with the principal objective to understand the dynamics of the C-Cl bond scission in an unsaturated alkyl halide, which has many low energy excited states. In the next chapter, **chapter 5**, photodissociation dynamics of 2-furoyl chloride and benzoyl chloride in a supersonic molecular beam at around 235 nm is discussed. These two cyclic molecules, served as representative aromatic acyl halides having COCl moiety in their side chain, are selected to investigate the dynamics of the C(O)-Cl bond dissociation. The work described up to chapter 5 is focused on the dynamics of halogen atom formation on UV excitation of different halogenated molecules, and the role played by the nature of initial excited states in controlling the overall dynamics of the C-X bond dissociation. However, the presence of a halogen atom itself can significantly alter the dynamics of dissociation of a polyatomic organic molecule by changing the nature of excitation of the molecule, and providing various low energy dissociation pathways. Therefore UV photodissociation of 2-bromo-2-nitropropane (BNP) is studied and discussed in **chapter 6**. In this work BNP was selected with the aim to investigate the effect of a halogen substituent on the dissociation dynamics of a nitrocompound. The experiment was carried out at different photolysis wavelengths, 193, 234 and 248 nm, and OH, Br and NO_2 were detected in their nascent states to get a holistic picture of the dissociation dynamics. Finally in **chapter 7**, conclusions drawn from all these studies have been summarized and future scope of the present work is discussed.

CHAPTER 2

Experimental methods

2.1 Introduction

It is evident from the title that the work in this thesis has been carried out in gas phase. In all the work described here, photodissociation of a polyatomic molecule is initiated by a laser source, and the process was ensured to be monophotonic in nature. Two very sensitive and state selective pump-probe techniques, REMPI and LIF were employed to detect the nascent photoproducts, and to extract desired dynamical information of the photodissociation event. The major work in this thesis involves the use of REMPI technique, to probe Cl, Br, and HCl photoproducts. Whereas, LIF technique was used to probe the OH radical, produced during the UV-photodissociation of BNP (described in chapter 6). In case of LP-LIF technique, the experiment was done in a flow cell, while in REMPI it was done in a molecular beam environment (*vide infra*).To ensure the detection of the photoproducts in their nascent state, the experiments were performed at low pressure, and sufficiently short delay was kept between pump and probe laser pulses. That was to ensure that the desired photoproduct has not undergone any collision before its detection. In this chapter experimental details of the two techniques along with the analysis of the experimental data are discussed.

2.2 Laser photolysis-laser induced fluorescence

The experimental details of the LP-LIF technique are discussed in this chapter, with its basic principle explained in the previous chapter. The work carried out using this technique is described in chapter 6. The photolysis was effected by an excimer laser (Lambda Physik, Model Compex-102, Fluorine version), and the product OH was probed by a dye laser, with frequency doubling and the mixing module (Quantel TDL 90), pumped by a seeded Nd:YAG laser (Quantel model, YG980 E-20). The overall process of investigating photodissociation dynamics of a polyatomic molecule, using LP-LIF, can be described by the following experimental steps:

1. Photodissociation of the parent molecule,
2. LIF detection of the desired photofragments, and
3. Extracting the dynamical information from the LIF spectra.

2.2.1 Photodissociation of the parent molecule

The first step of a LP-LIF technique involves the photodissociation of the parent molecule, and creation of the photofragments. The excitation of the parent molecule is initiated by a suitable pump laser source, such that the molecule has a high absorption cross-section at the output wavelength of the laser. An excimer laser is used for the photodissociation in the present work. The dissociation dynamics of BNP (chapter 6) was studied at two different photolysis wavelengths of 193 nm (ArF laser) and 248 nm (KrF laser). The pulse width of the laser is 20 ns and its maximum energy is ~200 mJ per pulse for ArF and ~350 mJ per pulse for KrF. The time Jitter is less than 5 ns. For experiments the photolysis laser flux was kept low (< 5 mJ cm^{-2}), to avoid multi photon processes and it was achieved by using an aperture, filters and by lowering the high voltage to the laser system. FIG. 2.1 depicts the experimental set up for LP-LIF study. The experiment was done in a collision free condition in a flow cell. The reaction chamber was made of pyrex glass with crossed arms at right angles provided for the entrance of the pump and the probe laser beams, which intersect at the center of the reaction chamber. The crossed arms are provided with MgF_2 windows for photolysis laser and quartz windows for probe laser, at the Brewster angle to facilitate transmission with reduced scattering. The reactor is also equipped with three other ports for the gas inlet, pressure transducer and the vacuum pump. The detection system was attached to the bottom window to capture fluorescence.

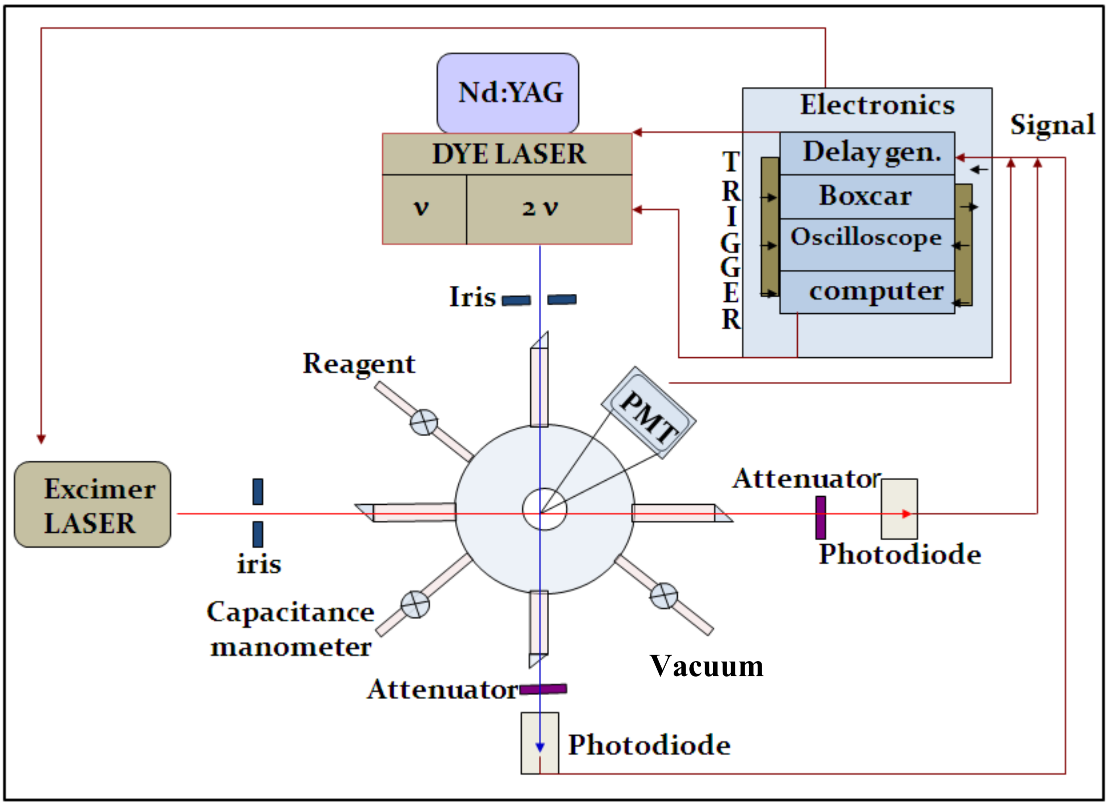

FIG. 2.1: Schematic of experimental setup of laser photolysis laser induced fluorescence technique.

2.2.2 LIF detection of the desired photofragments

In the present work the OH fragment is probed state selectively by exciting the $A^2\Sigma^+ \leftarrow X^2\Pi$ (0,0) transition of OH (306-309 nm), and monitoring the subsequent A→X fluorescence. Similarly, the product OH (v''=1,J″) was detected by exciting the A-X(1,1) transition. The OH radical can be probed very efficiently using LIF technique, as it fulfills all the conditions (discussed in section 1.3.1.1, chapter 1) required for LIF detection, e.g. it has a high absorption cross-section (~10^{-17}cm^2 molecule^{-1}), high fluorescence quantum yield (~80%), and well studied spectral features of the $A^2\Sigma^+ \leftarrow X\,^2\Pi$ band system at ~308 nm [35]. The probe laser employed here is a Quantel dye laser operated with DCM special dye pumped by a 532 nm laser beam from the second harmonic of the Nd:YAG laser, and provides the fundamental wavelength tuning range of 600-640 nm. The fundamental dye laser output is frequency doubled in a KDP crystal to obtain the laser output in the range of 300-320 nm, and was used for probing the OH radical. The pulse width of the laser is ≤ 8 ns and the fluence used is < 20 μJ cm^{-2}. The fluorescence is collected by 38-mm diameter lens of focal length 50 mm, attached to the bottom window of the flow reactor, and detected by a photomultiplier tube (PMT, Hamamatsu, model R 928P). A band-pass filter (λ_{center} = 310 nm, FWHM = ±10 nm, Transmission at 310 nm = 10%) is placed between the collecting lens and the PMT to cut-off the scattering from the photolysis laser. The laser frequency is calibrated, using an optogalvanic cell (Fe-Ne), with an accuracy of ±0.3 cm^{-1}. The laser intensity fluctuations associated with the pump and probe lasers are corrected by monitoring those using photodiodes, and normalizing the fluorescence intensities during the analysis. The spectral resolution of the probe laser is 0.06 cm^{-1}. The fluorescence signal from the PMT is sampled with a boxcar integrator (SRS250). During the LIF experiments, the gate width of the boxcar integrator was ∼100 ns, and the signal is averaged over 30 laser shots for a good signal to noise ratio, and fed to an interface (SRS245) for A/D conversion. A Pentium PC is used to control the scan of the dye laser via a RS232 interface and to collect data through a GPIB interface using a control and data acquisition program. A digital delay/pulse generator, with pulse resolution of 20 ps, was employed as the master to trigger all the instruments for time synchronization.

The LIF signal obtained is often associated with some uncertainties e.g. the intensity fluctuations of the excitation laser may propagate into the measured signal. Uncertainty may also arises from the detection system, if the number of detected photons is small, as the signal precision is affected by the so-called photon shot noise; this noise decreases with square root of the number of detected photons. However, for gaseous system at high pressure, the most common cause for measurement in uncertainty is from variation in collision quenching. Furthermore, competing fluorescence (from other species) also can cause degradation of the measurements. During the experiment certain precautions are taken to keep the uncertainties associated with the LIF data as low as possible.

1) The spectral band width of the probe laser was ensured to be less than the rotational line spacing of the OH photofragment. So that, state selective excitation of a molecule (OH radical) is possible from a particular ro-vibrational state of the ground electronic state to a particular ro-vibrational state of the excited electronic state.

2) To minimize any contribution from window florescence, impurity free window material was used. Window reflection was reduced using light baffles and keeping entrance and exit windows at the Brewster angle.

3) To avoid any saturation in LIF signal the laser probe beam was unfocused and attenuated. This was verified by plotting LIF signal versus laser intensity, which was found to be linear, for both photolysis and probe lasers. For further confirmation, the line intensities of main and satellite branches of OH were measured and fond to be in ratio of their corresponding Einstein coefficients. Since a main branch and the

adjacent satellite branch lines probe the population of the same state, and if there is no saturation in the LIF intensities, the ratio of their LIF intensities should be equal to the ratio of their Einstein coefficients.

4) To maintain a collision less condition, the pressure maintained inside the flow cell was maintained under 100 mTorr and an optimum time delay (as there is a certain formation time of the OH fragment) of ~ 50 ns was kept between the pump and the probe laser. The LIF spectra were measured at pump-probe delays of 50 and 100 ns, and found to be identical, thereby ensuring negligible collision relaxation of the nascent OH radical. The LIF intensities were also measured as a function of the substrate pressure, and found to be linear within the pressure range used.

The rotationally resolved LIF spectra collected under collision less condition were used to extract important dynamic information of the photodissociation process. In absence of other non-radiative process, the intensity of the LIF signal is directly proportional to the population of the product in the different ro-vibrational levels at the ground states. The following section describes the analysis of the LIF spectra to obtain the dynamical information like, nascent state internal energy distribution, spin-orbit and Λ doublet ratio etc. associated with the OH channel.

2.2.3 Extracting the dynamical information from the LIF spectra

2.2.3.1 Electronic spectroscopy of OH

Before entering the analysis procedure of the LIF data, it is necessary to have a brief knowledge on the spectroscopy of OH. Unlike in an atomic system, in a diatomic molecule like OH, the motion of the electron takes place in a reduced symmetry of the field. Here the electron does not move in a spherically symmetrical field and there is only symmetry of field about the internuclear axis, due to the electrostatic field of the two nuclei. The precession of the orbital angular momentum vector, about the field directed along the internuclear axis, gives the component $M_L(h/2\pi)$, where M_L has values from -L to +L. Due to the electrostatic nature of the field, the states with the same M_L values but different sign are degenerate. These different values of M_L are represented by Λ, which is given by

$$\Lambda = | M_L | \tag{2.1}$$

Thus for a given value of L, there are L+1 values of Λ, corresponds to L+1 distinct states with different energies. According to the international nomenclature, Λ=0, 1, 2, 3,…are designated as Σ, Π, Δ, Φ,….states.

The spins of the individual electrons in the molecule give the resultant spin S. In the case of the Λ= 0, Σ state, the resultant spin is oriented in a fixed space, as long as the molecule does not rotate. In other cases when Λ≠ 0, the internal magnetic field in the internal nuclear axis resultant from the orbital angular motion causes the precession of S about it. It is designated as Σ, and has 2S+1 different values for it.

The algebraic addition of Λ, the orbital angular momentum along the internuclear axis, and Σ, the electronic spin angular momentum along the internuclear axis, gives the total electronic angular momentum, Ω, about the internuclear axis, where

$$\Omega = |\Lambda + \Sigma| \tag{2.2}$$

and the electronic term symbol of the diatomic species is designated as $^{2S+1}\Lambda_{\Omega}$.

According to this nomenclature, the ground electronic state of OH is $^2\Pi$ and the first excited electronic state is $^2\Sigma$. The interaction of electron spin and orbital angular momentum splits each rotation state with $\Lambda \neq 0$ into two spin-orbit states. Thus, for the ground state of OH, the two spin-orbit states are $^2\Pi_{1/2}$ and $^2\Pi_{3/2}$. At high rotational quantum number, the rotational angular momentum interacts strongly with the electronic angular momentum and lifts the degeneracy of the $\Lambda \neq 0$ states, which are doubly degenerate, and gives the two components $\Lambda^+(A')$ and $\Lambda^-(A'')$. Relative populations of these two spin-orbit states and Λ doublet states provide important information on dynamics of dissociation.

2.2.3.2 Analysis of the experimental results

Typical LIF spectra, with appropriate assignments, are shown in FIG. 6.1 for the (0,0) band of the A-X system of OH, produced from BNP on photodissociation at 193 nm. The P, Q, and R branches refer to rotational transitions with $\Delta N= -1, 0$, and 1, respectively. The subscripts 1 and 2 represent the transitions $\Sigma_{J=N+1/2} \leftarrow \Sigma_{J=N+1/2}$ and $\Sigma_{J=N-1/2} \leftarrow \Sigma_{J=N-1/2}$, respectively and known as main branch. Whereas, the subscripts 21 and 12 represent the transitions $\Sigma_{J=N-1/2} \leftarrow \Sigma_{J=N+1/2}$ and $\Sigma_{J=N+1/2} \leftarrow \Sigma_{J=N-1/2}$, respectively and are known as satellite branch. Thus, the transitions represented by subscript 1 and 21 originate from $\Pi_{3/2}$, whereas those represented by 2 and 12 originate from the $\Pi_{1/2}$ spin orbit state. According to the parity selection rule ($+ \leftrightarrow -$), the Q branch arises from the Π^- (A'') state, while the P and R branches originate from the Π^+ (A') state. Relative populations of the OH fragment were determined by normalizing the respective peak area of the rotational lines with respect to pump and probe laser intensities, pressure change, if any, and the respective Einstein absorption coefficients B_{ij} [36]. The spin-orbit and the Λ doublet ratios were calculated from the relative populations of different states. The translational energy associated with the OH fragment was calculated from the Doppler profiles of the rotational lines. The rotational populations of the ground state P(J″), obtained after normalization as mentioned above, of the nascent OH fragment generated by photodissociation, were plotted against energy (ε) of rotational levels J″, to construct a Boltzmann plot given by the equation,

$$\ln(P(J''/(2J''+1)) = -\ \varepsilon\ hc/kT_R + \text{constant}. \qquad (2.3)$$

A typical Boltzmann plot is shown in Fig. 6.2 for BNP photodissociation at 193 and 248 nm.

Similarly assuming a Boltzmann distribution, a vibrational temperature can be obtained from the ratio of the LIF intensities of the same rotational line of the (0, 0) and (1, 1) transitions by

$$I\ (R_{1,2}\ (N''); v'' = 1)\ /\ I\ (R_{1,2}\ (N''); v'' = 0)\ =\ \exp\ (-\Delta\varepsilon_v\ hc\ /\ kT_V), \qquad (2.4)$$

where $\Delta\varepsilon_v$ is the energy difference between $v'' = 1$ and $v'' = 0$ for a given spin-orbit state and N″, and T_V is the vibrational temperature. The constants h, c and k have their usual meanings.

The spin-orbit ratio, generally known as the F_1/F_2 ratio, which gives the relative population in $\Pi_{3/2}$ and $\Pi_{1/2}$ states, was obtained from the ratio of population $P_1(N'')/P_2(N'')$, $Q_1(N'')/Q_2(N'')$, etc. For $F_1(N'')$ and $F_2(N'')$, since the J″ values are not the same, the population was normalized with a statistical weighting factor, i.e., 2J″+1.

The Λ-doublets arise from the orientation of the π-lobes of OH with respect to the plane of rotation. In the Π^+ (A') state, the π-lobe lies in the plane of rotation, while in the Π^- (A″) state, the π-lobe is perpendicular to the plane of rotation [1]. The Λ doublet ratio was obtained from $Q_1(N'')/P_1(N'')$ or $Q_1(N'')/R_1(N'')$. For $Q_1(N'')$ or $P_1(N'')$ or $R_1(N'')$, normalization of populations is not required, since the J″ values are the same. The relative populations of the spin orbit and Λ doublet states provide information about the exit channel dynamics during the breaking of the chemical bond. For example, preferential population of $\Pi_{3/2}$ state often indicates the interaction of initial prepared state with nearby triplet state. Similarly, preferential population of Π^- (A″) state indicates some geometrical constraint, like H-bonding etc., at the transition state.

The widths of the LIF lines have contributions from different line-broadening factors, like thermal motion of the parent molecule, molecular velocity of the fragments, finite probe laser width and vector correlations. Among these, molecular velocity of the fragments leads to Doppler broadening of LIF lines. Hence, the width of a rotational line, corrected for the probe laser line-width, can be used for calculating the velocity component $f(v_z)$ of the absorbing species along the propagation direction of the probe laser beam. If the velocity distribution $f(v)$ is isotropic, i.e., $f(v_x)=f(v_y)=f(v_z)$, then the average translational energy in the laboratory frame is given by,

$$E_T^{lab}(OH) = \frac{3}{2} m_{OH} < v_z^2 >_{OH} \quad (2.5)$$

where $<v_z^2>_{OH}$ represents the second moment of laboratory velocity distribution of the OH radical. Details on the translation energy estimation, associated with OH radical in lab frame are given in chapter 6. A flow chart given in FIG. 2.2 shows the overall procedure of obtaining dynamical information from LIF experiment.

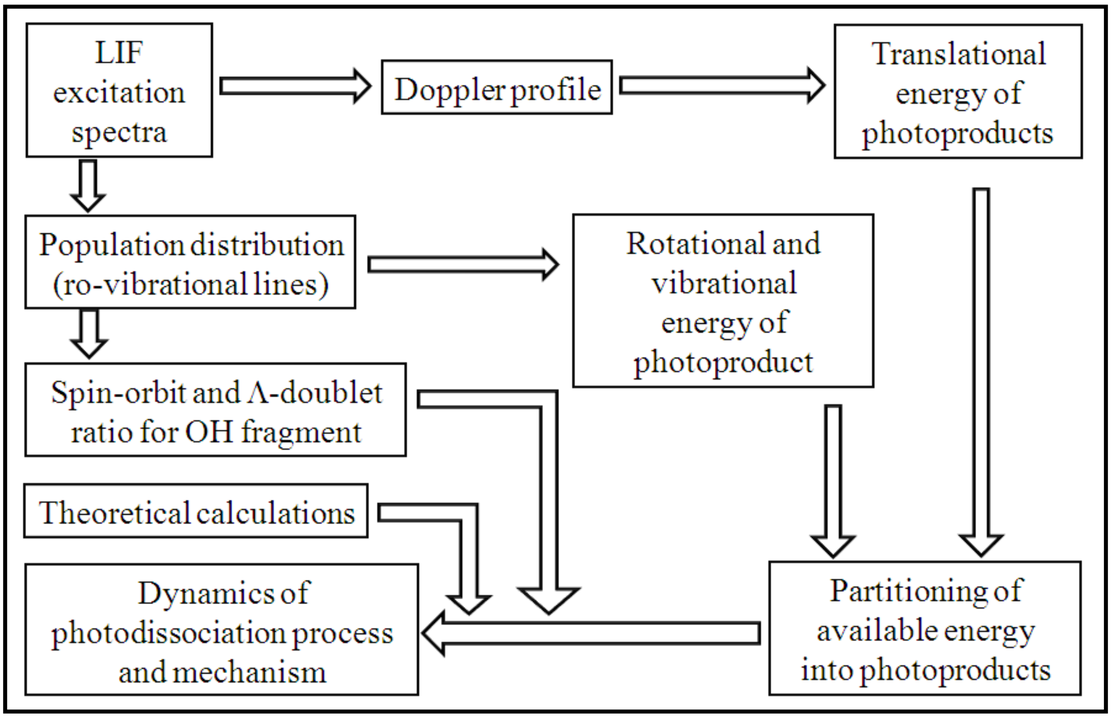

FIG. 2.2: *Flow chart for obtaining the dynamics of photodissociation process from LIF data.*

2.3 Resonance enhanced multiphoton ionization

The major part of the work described in this thesis involves REMPI detection of the halogen photofragments in their nascent states. In gas phase at the room temperature, detection of a chemical species by the REMPI technique involves only a small fraction of the total available molecules to the excitation process. This is due to a broad population distribution (Boltzmann distribution) in the ro-vibrational states. Thus, in order to improve the REMPI sensitivity, and to make the transitions sharp, the population in the ground state has to be enhanced. At the same time, the collisions of sample molecules between themselves and with the background gas molecules have to be minimized. Both these objectives can be fulfilled by employing supersonic beam of the parent molecules, as it can provide an intense source of molecules traveling with a fixed velocity in a given direction in vacuum, having a very narrow velocity distribution. These molecules are cooled to such an extent that the excited rotational and vibrational levels are almost depopulated. The supersonic molecular beams also enable to prepare molecular reactants in well-defined quantum states, with known translational energy. Thus, the halogen atom detection was performed using a molecular beam time of flight mass spectrometer system (MB-TOF-MS) consisting of a supersonic beam source and an ionization (beam - laser interaction) region. To maintain the desired vacuum the system is differentially pumped, using two similar 9-inch turbomolecular pumps (TMP), backed by rotary pumps. An additional 4-inch TMP was used to pump the TOF tube located at the end, near the detector. A schematic diagram of the system is shown in FIG. 2.3.

The overall process of investigating photodissociation dynamics of a polyatomic molecule, using MB-REMPI-TOF-MS technique, can be described by the following experimental steps:

1. Photodissociation of the parent molecule,
2. REMPI tagging of the desired photofragment,
3. Detection of the ion sphere,
4. Recovery of the dynamical information.

2.3.1 Photodissociation of the parent molecule

Similar to the LP-LIF or any other technique for studying photodissociation dynamics, the first step of REMPI is the creation of the photofragment i.e. the photodissociation of the parent molecule. In all the experiments reported in this thesis, using REMPI technique, the same laser beam was employed as a pump as well as probe, i.e., for both photodissociation of the parent molecule and ionization of the photoproducts like, Cl($^2P_{3/2}$), Cl*($^2P_{1/2}$), Br($^2P_{3/2}$), Br*($^2P_{1/2}$) and HCl. The laser pulses were generated by a dye laser (TDL 90, Quantel), using rhodamine 101 dye. The dye laser was pumped by 532 nm light from the second harmonic of a Nd:YAG laser (YG-981-C, Quantel), operating at 20 Hz. The fundamental dye laser output was frequency-doubled in a KDP crystal, and mixed with the fundamental output of the Nd:YAG

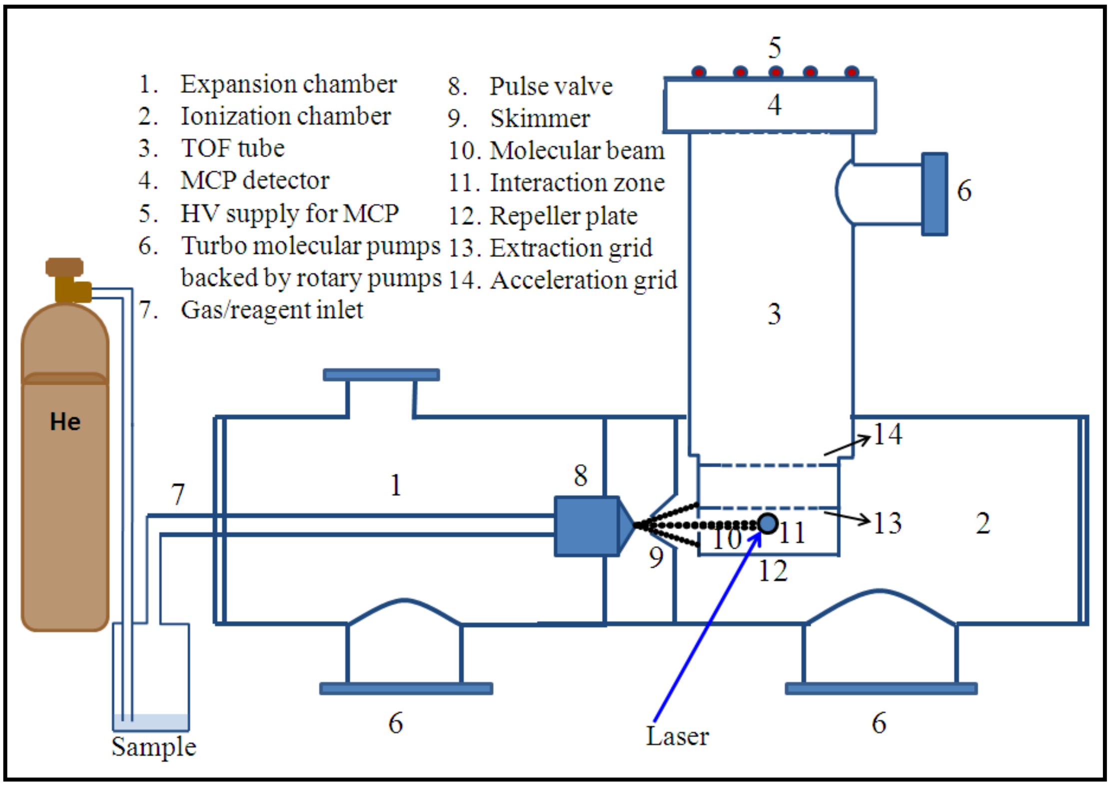

FIG. 2.3: Schematic of molecular beam-resonance enhanced multiphoton ionization-time of flight mass spectrometry (MB-REMPI-TOF-MS) setup.

laser, to obtain an output in the range 230-236 nm. The resultant light had a bandwidth of ~0.14 cm^{-1}, and was calibrated, using a Fe/Ne optogalvanic (OG) cell and a wavemeter. The above laser output was separated from the rest of laser beams, using a set of four Pellin-Broca prisms. The laser beam was focused by a lens, and the distance of the lens from the center of the molecular beam axis was varied, to obtain the best ratio of on- and off-resonant signals.

For sample insertion helium was bubbled through the sample maintained at room temperature, and the mixture was expanded through the nozzle at a stagnation pressure of 1500 Torr of He. Typical operating pressures for the source and the ionization regions were in the order of 10^{-5} and 10^{-7} Torr, respectively. A pulsed supersonic molecular beam was generated using a solenoid valve with a 0.8 mm nozzle and 500 μs opening time. A 1.9 mm diameter conical skimmer was used to skim off the molecular beam to the interaction region. The pulsed valve was located ~ 2 cm from the skimmer and 7.5 cm from the interaction region. In the interaction region the laser beam interacts with the sample molecular beam, and the dissociation of the parent molecule as well as REMPI tagging of the photofragments take place within the laser pulse width of 10 ns. The precautions taken in this step are as follows:

1) It was ensured that any interference to the measurements due to cluster photofragmentation was negligible by operating at a low stagnation pressure, and using only the rising part of the molecular beam pulse.

2) The velocity spread of the parent molecular beam parallel to the detector axis is minimized by taking a MB direction perpendicular to the detector axis. It is because the velocity spread of the parent molecule, in the detection axis, will propagate to the fragment velocity distribution.

3) Internal energy of the parent molecule is minimized, by employing the supersonic expansion. Since, those can contribute to the angular distribution as well as translational energy of the photofragments.

4) The use of excessive laser flux is avoided as it can result in multiphoton processes and saturation of signal. To ensure the monophotonic nature of the dissociation, power dependence measurements were performed by measuring the integrated chlorine/bromine atom REMPI signal, i.e., measuring boxcar gated signal/output on the *m*/*z* 35 and *m*/*z* 37 or *m*/*z* 79 and *m*/*z* 81 peaks in the TOF spectrum. Similar power dependence study was also performed for the HCl fragment, formed during photodissociation of benzoyl chloride shown in FIG. 2.4. The ln-ln plot of REMPI signal intensity vs. laser intensity shows a slope of ~3, which ensures the monophotonic dissociation of the parent molecule followed by the (2+1) REMPI

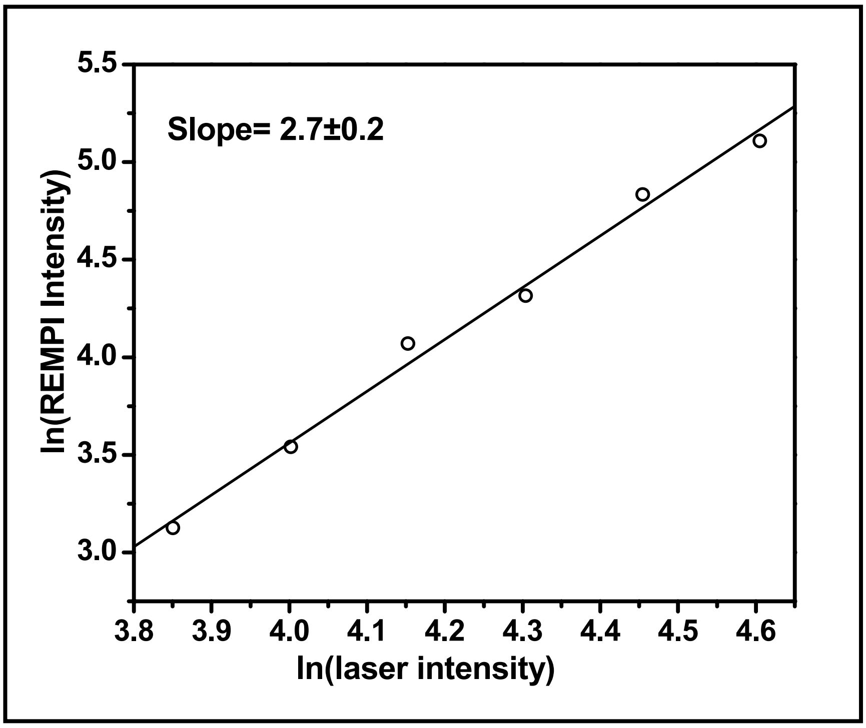

FIG. 2.4: *Dependence of the REMPI signal of HCl, formed during photolysis of benzoyl chloride, on the laser intensity.*

detection of the photo fragment. The ionization step is saturated in nature and does not contribute to the power dependence.

2.3.2 REMPI tagging of the desired photofragment

A (2+1) REMPI scheme was employed to detect the chlorine, bromine and the HCl photofragments. HCl was detected using (2+1) REMPI in the wavelength range 236-237 nm (details given in chapter 6) for the Q(J) branch of the V $^1\Sigma^+$ $(0^+)\leftarrow\leftarrow$ X $^1\Sigma^+$ (0^+) (12,0) band. The spin-orbit ratio of Cl/Cl* or Br/Br* can be calculated from the ion intensities for corresponding transitions, after correction due to their two-photon oscillator strengths. For this purpose, two REMPI lines each of Cl and Br are chosen. For chlorine atom peaks at 235.336 nm (42492.5 cm^{-1}) and 235.205 nm (42516.1 cm^{-1}), corresponding to 4p $^2D_{3/2}$ ← 3p $^2P_{3/2}$ and 4p $^2P_{1/2}$ ← 3p $^2P_{1/2}$ transitions, respectively, and for bromine atom peaks at 233.700 nm (42789.9 cm^{-1}) and 234.040 nm (42727.7 cm^{-1}), corresponding to 6p $^4P_{3/2}$ ← 4p $^2P_{3/2}$ and 6p $^2S_{1/2}$ ← 4p $^2P_{1/2}$, respectively, were selected. FIG 2.5 and 2.6 show the (2+1) REMPI scheme of Cl, Cl* and Br, Br* respectively. The TOF spectra of Cl and Cl* were measured with three different geometries of horizontal (laser polarization perpendicular to the detection axis), vertical (laser polarization parallel to the detection axis) and magic angle (54.7° to the detection axis) to estimate the recoil anisotropies of these products. The laser beam, having a typical energy of ~50 μJ/pulse, was partially focused by a converging lens (focal length = 280 mm). The following facts are worth mentioning on REMPI measurements.

1) Ionization can introduce recoil to the photofragment, i.e. excess energy over the ionization threshold. This can lead to inaccuracy in measurement of the photofragment translational energy. Since, most of this energy is taken away by e$^-$ as its mass is

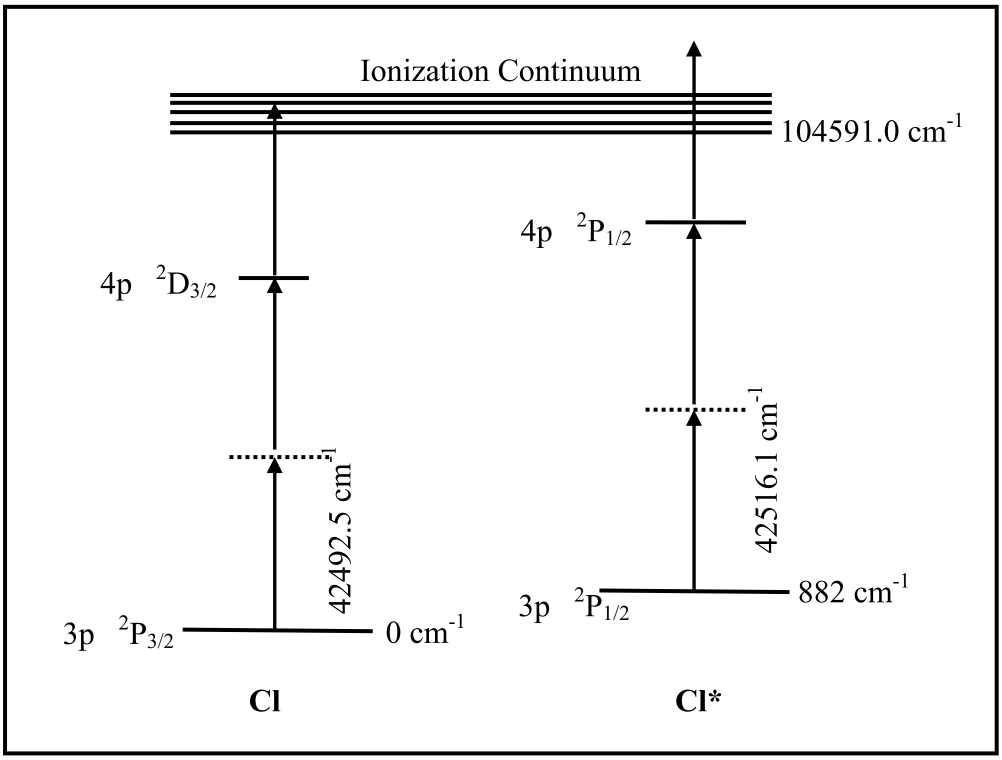

FIG. ***2.5:*** *(2+1) REMPI scheme for Cl and Cl* detection.*

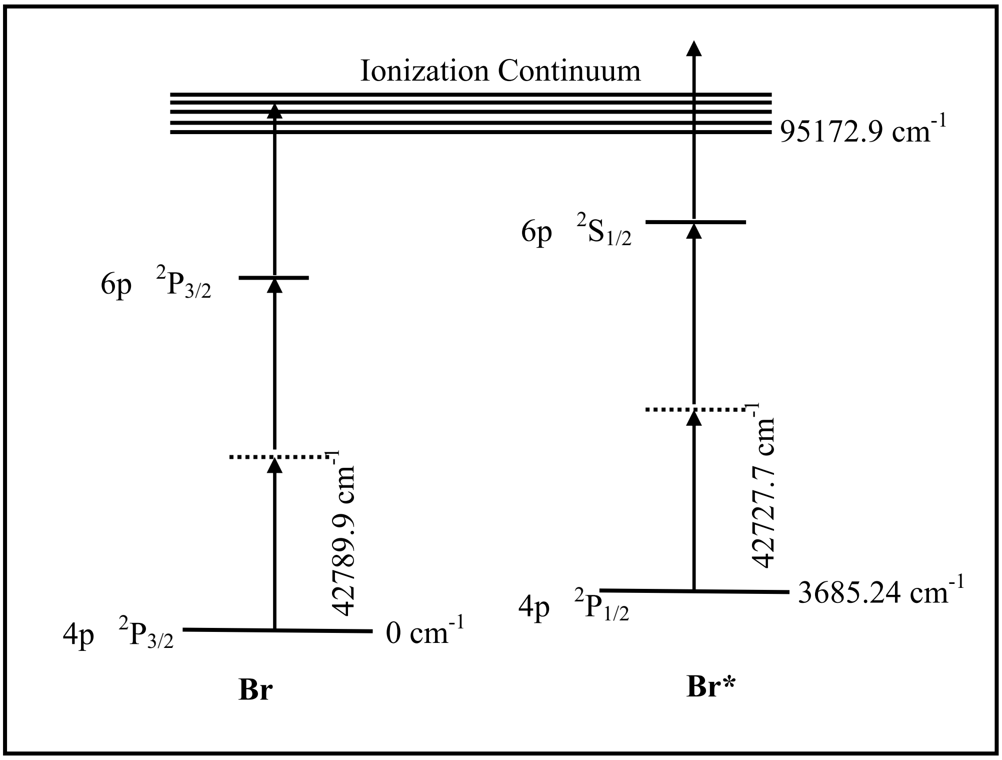

FIG. ***2.6:*** *(2+1) REMPI scheme for Br and Br* detection.*

much less compared to the photofragments (Cl, Br and HCl) probed in this work, this problem is avoided.

2) State selective ionization requires a resonant bound transition. This implies that, each fragment would show a velocity dependent Doppler shift. Thus, a broadened line width (> 1.5 cm^{-1}) of the laser output was employed in all the REMPI experiments to excite and ionize a fragment with all the velocities. To broaden the line width, the Nd:YAG laser was operated without an injection seeder, and the dye laser was operated without a set of prisms (NBP prisms) in the laser cavity, used to narrow the line width. The laser line width was always greater than the Doppler profile of the recoiling fragment.

2.3.3 Detection of the ion sphere

After the state selective ionization of the desired photofragments by a (2+1) REMPI scheme, the next step is their mass selective detection. In the present system, the TOFMS assembly, similar to Lubman and Jordan design, is used [37]. It consists of three distinct parts, an ion source, an analyzer (the TOF tube) and a detector. In the first part of the ion source, the ions are produced, extracted, accelerated and directed into the analyzer. The detector system consists of a two-stage Wiley–McLaren [38] time-of-flight mass spectrometer (TOF-MS), with an extraction and an acceleration region, mounted vertically perpendicular to the horizontal MB (FIG. 2.3).

2.3.3.1 The ion source

The extraction region consists of a repeller electrode (a solid plate of stainless steel) of 5 cm × 5 cm dimension and an extractor grid mounted 1cm above the repeller plate. The acceleration region is defined by an extractor electrode and an acceleration grid held at ground potential, separated from each other by 1cm. Both these grids, with dimensions 5 cm × 5 cm, are constructed from stainless steel mesh, with 90% transmission. In order to collect the total ion signal, the extraction region was held at ~300 V/cm, and the acceleration region was held at ~3900 V/cm. A schematic of the ion source is provided in FIG. 2.7.

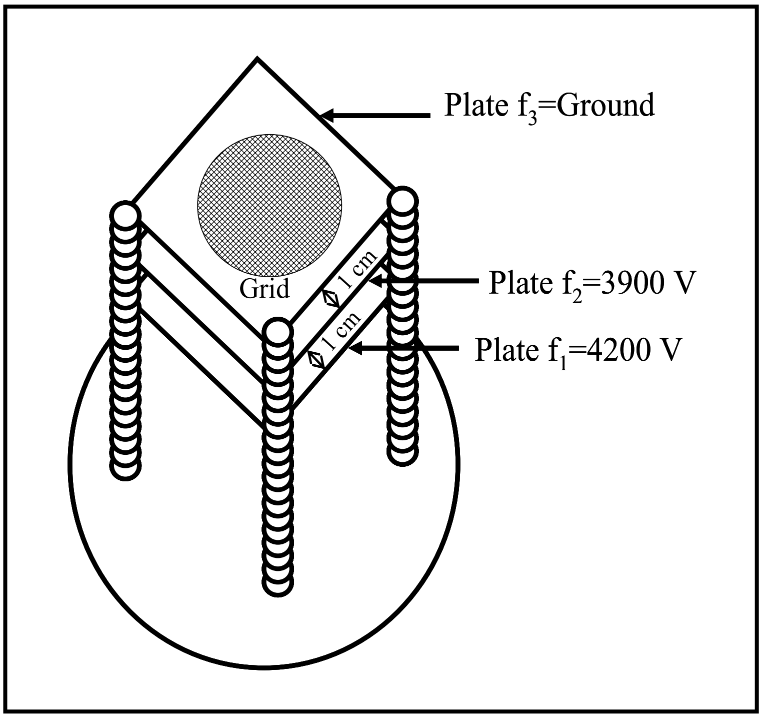

FIG. 2.7: *Schematic of the ion source. Plates f_1, f_2 and f_3 stands for the repeller plate, extraction and acceleration grid, respectively.*

2.3.3.2 The TOF analyzer

After passing through the acceleration region, the ion packet passes through a 1035 mm long field-free flight tube to the detector. Two deflector plates placed perpendicular to the detector axis (*z* axis) directed the ion packet in the *(x,y)* plane of the flight tube to center it on the detector. Typical field strength for the deflector plates was 2–6 V/cm. The ions, after passing through the acceleration region, are accelerated to very high energy, and thus reduced in the spread in the initial energy. The kinetic energy of all the ions in a given ion pulse coming out of the ion source is almost the same, and, therefore, the velocity of each ion depends on its mass to charge ratio. The analyzer is a field-free drift tube, also called flight tube, wherein the ions travel under field-free conditions, with the velocity obtained in the acceleration region. Here, the ions are spatially dispersed, depending on their m/z. Lastly, at the end of the flight the ions are detected by a dual micro-channel plate (MCP). In each pulse/cycle, TOF analyzer allows all the ions to pass through, thus the complete mass spectrum of the sample can be obtained from a single pulse.

In TOFMS, identification of the ions is made on the basis of their flight time from the region of generation to the detector. If the length of the field-free flight tube is very much longer than the acceleration region, then m/z of the ion is related to its flight time‘t’ by an expression of type,

$$t^2=a\ m/z + b, \tag{2.6}$$

where a and b are constants. The above expression is generally used for calibrating m/z of ions with respect to their flight times. For the mass calibration, in our case, a multiphoton ionization (MPI) time-of-flight spectrum of tetrachloroethylene (TCE) was recorded and the REMPI lines for ^{35}Cl and ^{37}Cl in this spectrum were confirmed by scanning the probe laser. Then this spectrum was compared with the mass spectrum of TCE reported by NIST. A calibration curve was then drawn for m/z against time (t), and shown in FIG. 2.8.

The mass resolution (R) of the set-up was estimated from the arrival time (t) and FWHM (Δt) of aniline ion to be 400, using the following relation (equation 2.7)

$$R = t/\Delta t. \tag{2.7}$$

This relation can be obtained from a more general expression for TOF-MS, which relates the difference in the masses of the species (ΔM), and the average mass of the two ions (M). Assuming a single charge on the ion this relation is given as (equation 2.8),

$$R = M/\Delta M. \tag{2.8}$$

In fact, the resolution provides a measure of the highest mass (M) that can be completely separated from its adjacent masses (M±1).

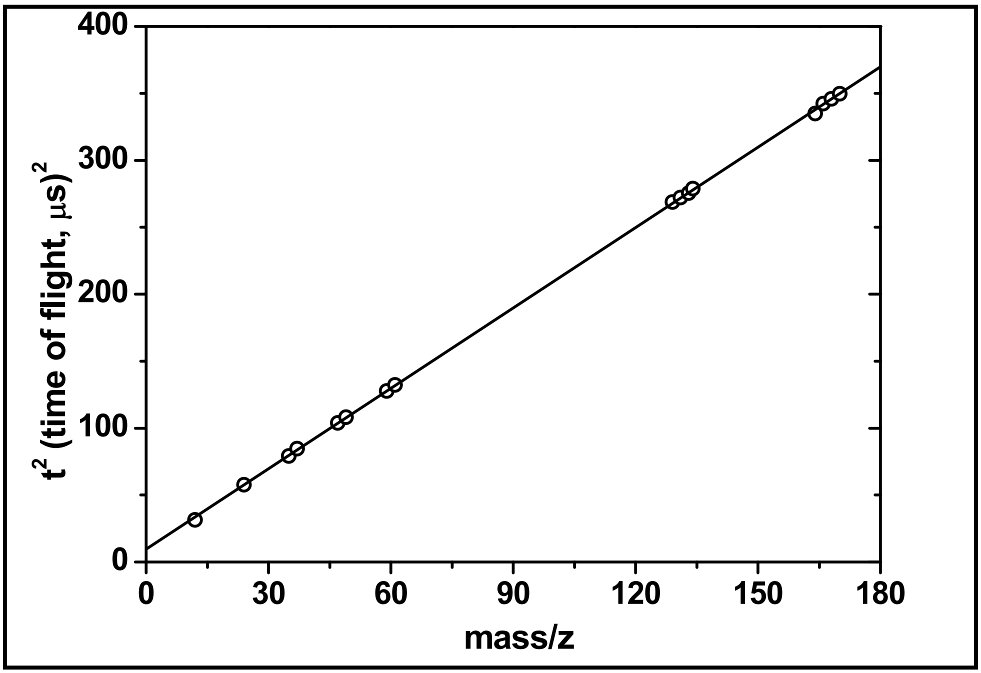

FIG. 2.8: *Plot of arrival time (μs) for various fragments (m/z) for TCE for mass calibration.*

2.3.3.3 The Detector system

The detector is a dual microchannel plate (MCP), having an active area of 18 mm and sub-nanosecond rise time. A single compact voltage generator, having multiple output voltage ports, was employed to power the TOF ion optics, the deflection plates and the MCP detector (FIG. 2.9). The specification of the MCP detector employed is given in Table 2.1.

In order to obtain a TOF spectrum, the signal was sent to a 400 MHz digital oscilloscope (LeCroy 9310A), which was interfaced to a Pentium PC. The off-resonant signal was subtracted from on-resonant signal to effectively remove the minor pump-oil related background contribution to the TOF spectra and also the contribution from the multiphotonic process. The same digital delay/pulse generator employed in LIF experiments with pulse resolution of 20 ps, was employed as the master to trigger all the instruments for time synchronization.

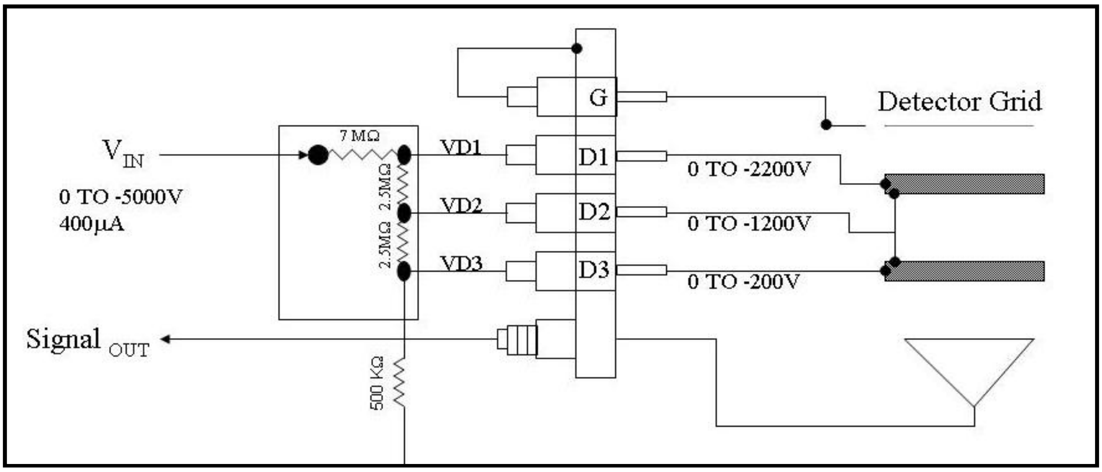

FIG. 2.9: *The voltage divider for supplying the requisite power to the MCP.*

The time delay between the trigger pulse applied to the pulsed valve and the valve opening was obtained by measuring the delay between the trigger pulse and the fast ionization gauge (FIG) signal, employing a digital oscilloscope. This delay is the sum of the time required to open the pulsed valve from its trigger input and that for the molecular pulse to reach FIG from its generation, i.e., the nozzle exit. By measuring these time delays for different FIG positions with respect to the skimmer, the flow velocity of the molecular beam was estimated, and used to obtain the time required for the molecular beam to reach the extraction region of the TOFMS. The ion signal was gate integrated by a boxcar, averaged for 30 laser shots, and fed into an interface (SRS 245), for A/D conversion. A PC was used to control the scan of the dye laser via an RS232 interface, and to collect data from SRS 245, through a GPIB interface, using a control and data acquisition program.

Table 2.1: *Mechanical and electrical specifications of microchannel plate.*

S.No.	Parts	Dimension/specification
1	Ground plane grid diameter (input aperture)	0.75 inches
2	Grid transmission	90%
3	Active surface area diameter	0.75 inches
4	Distance from input grid to the face of vacuum flange	1.3 inches
5	Maximum protrusion from the flange face into vacuum system	1.75 inches
6	Minimum tube I.D. for vacuum housing	2.75 inches
7	Maximum voltage across each plate	1000 V
8	Gain per plate at 1000 V	1000

2.3.4 Recovery of the dynamical information

The last step of the REMPI experiment involves the analysis of the experimental data to extract the required dynamical information. The relative quantum yields for the halogen atom (chlorine or bromine) fragments, formed in different spin-orbit states, were determined using normalized integrated intensity, i.e., peak areas S(X) and S(X*), of the respective (2+1) REMPI transitions. The integrated REMPI intensity was normalized with respect to the laser intensity, and the ratio of the two-photon absorption coefficients (details are given in respective chapters). The major dynamical information, such as speed distribution $g(v)$, translational energy distribution and the recoil anisotropy parameter (β), is obtained by analyzing the observed TOF profiles of Br, Br*, Cl and Cl*, using a forward convolution method.

First, the experimental TOF profiles, I(t,χ), at a particular geometry χ (the angle between the laser polarization and the detection axis), are transformed into the velocity domain, I(v_Z,χ). Under space focusing conditions, a simple linear relation [39],

$$v_z = \frac{qV_{ex}(t - t_0)}{m}, \tag{2.9}$$

is used for this transformation, where *q* and *m* are the charge and mass of the photofragment X (Br or Cl), V_{ex} is the electric field in the extraction region, and t(t_0) is the TOF(mean TOF). The distribution of v_Z, f(v_Z, χ), generates the observed velocity domain TOF signal, I(v_Z, χ), on convolution with an instrument response function. The function f(v_Z, χ) is described by an equation [40-43],

$$f(v_z,\chi) = \int_{|v_z|}^{\infty} \frac{g(v)}{2v}\left[1+\beta P_2(\cos\chi)P_2\left(\frac{v_z}{v}\right)\right]dv \tag{2.10}$$

where v_Z is the velocity component along the *z* axis, v is the recoil speed of the fragments, β is the anisotropy parameter, $P_2(\cos\chi)$ is the second-order Legendre polynomial, and Cos(χ)=**ε.z** , implying the projection of the pump laser electric field **ε** on the detection axis **z**. The anisotropy parameter β is defined as,

$$\beta = 2\langle P_2(\cos\theta_m)\rangle = 3\cos^2\theta_m - 1, \tag{2.11}$$

where θ_m is the molecular frame angle between the molecular transition dipole moment, **μ**, and the fragment recoil direction, **v** (the bond dissociation co-ordinate). We determined the instrument response function by measuring the (1+1) REMPI of aniline beam at 34029 cm^{-1} (293.77 nm). The function was found to be Gaussian in the time domain, with FWHM of 27 ns [44]. Thus, under space focusing conditions it generates a convolution function in the velocity domain, which depends linearly on the electric field in the extraction region. In present work, we have employed a procedure of non-core sampling data [41], with an assumption that the nature and the shape of the TOF profiles for the X fragment are independent of the probe polarization. But, this assumption can only be approximate because of the presence of atomic **v.j** correlations. However, these correlations are generally weak, and can be neglected [45,46].

We assumed an initial center-of-mass photofragment speed distribution $g_i(v)$ for each active decay channel i, to extract the photofragment speed distribution, $g_i(v)$, and anisotropy, β_i, of each decay channel i contributing to the experimental TOF profiles, $I(v_Z, \chi)$. The dependence of $f(v_z, \chi)$ on β can be eliminated by either measuring data at the magic angle ($\chi = 54.7°$), where $P_2(\cos\chi)$ is zero or by co-adding normalized profiles with $\chi = 90°$ and $\chi = 0°$, in a 2:1 ratio. Both the approaches yield isotropic $f(v_z, \chi)$ profiles and the total center of mass (c.m.) speed distribution is obtained by differentiation of equation 2.10 at $\chi = 54.7°$

$$g(v_z) = -2v\frac{d}{dv_z} f(v, 54.7^{\circ})|_{v_z = v} \tag{2.12}$$

Thus, the TOF profile at the magic angle, $I(v_Z, 54.7°)$, gives an estimate of the total center-of-mass speed distribution $g(v)$, and provides an indication of the form of the individual speed distributions $g_i(v)$. These are usually modeled with the functional form [47,48]

$$g_i(v) = (f_T)_i^{a_i}\left[1-(f_T)_i\right]^{b_i} \tag{2.13}$$

where $(f_T)_i$ is the fraction of the available energy channeled into translation, a_i and b_i are adjustable parameters. The function $f(v_Z, \chi)$ is calculated simultaneously for all three geometries $\chi = 0°$, 54.7° and 90°, using an adjustable anisotropy parameter β_i

and weight for each decay channel. Then, this function is convoluted with the instrument response function to simulate TOF profiles, which are compared with the experimental results, I(v_Z, χ). The adjustable parameters are then varied to achieve a satisfactory agreement with the experimental data. The determined photofragment speed distributions are transformed into center-of-mass translational energy distributions $P(E_T)$, using the following equation,

$$P(E_T) = g(v)\frac{dv}{dE_T} \quad . \tag{2.14}$$

The analysis procedure can be summarized in the following flow chart (FIG. 2.10).

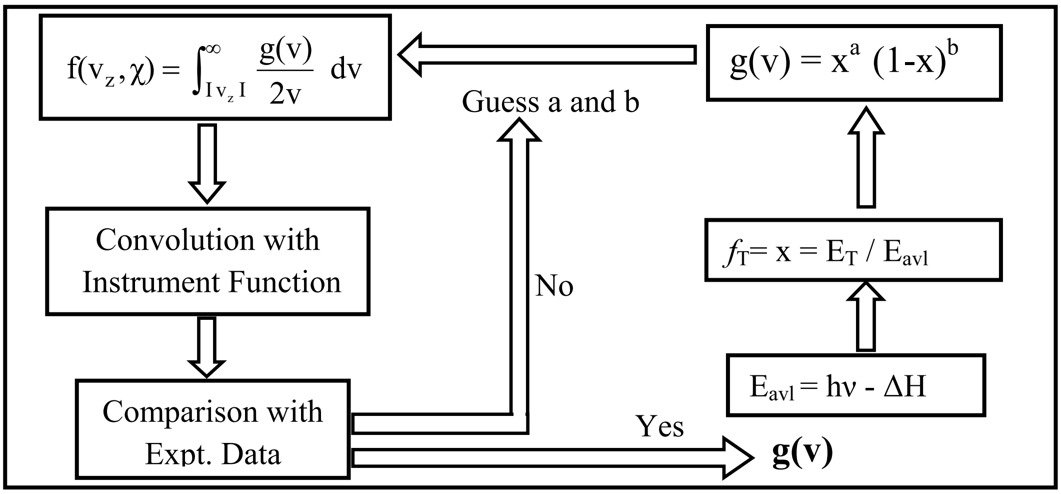

FIG. 2.10: *Flow chart of analysis procedure of REMPI data.*

CHAPTER 3

UV-Photodissociation of 2-bromo-2-chloro-1,1,1-trifluoroethane (halothane): Dynamics of C─Br and C─Cl bond rupture

3.1 Introduction

The gas-phase photodissociation of volatile halogenated compounds is currently a topic of strong interest, not only for fundamental knowledge of how atomic eliminations occur from a dissociative surface adiabatically, or non-adiabatically after curve crossing , but also for its relevance to processes taking place in the atmosphere and in plasmas. Halothane (2-bromo-2-chloro-1,1,1-trifluoroethane), which contains three different halogens as substituent on a simple ethane skeleton, is a widely used general inhalation anesthetic and one of the major man-made bromine-containing species found in the free troposphere [49]. Since Br atom is predicted to have several times more efficiency in depletion of ozone in stratosphere than Cl atom [50,51], photodissociation studies on bromohalides are of importance. The fine-structure branching ratio and the recoil velocity anisotropy parameter of a halogen atom (X) have been measured in the photodissociation of halogens (X_2), hydrogen halides (HX) and several simple alkyl halides (RX), with an aim to locate the point of the curve crossing and to ascertain the nature of the excited state. CH_3I has been investigated extensively, both experimentally and theoretically [52,53], and the dynamical features of this molecule are well understood to serve as a model for dissociation dynamics of other alkyl halides.

On UV excitation of CH_3Br via σ*(C-Br)←n(Br), the C-Br bond dissociation leads to formation of Br and CH_3, with the latter having a vibrational distribution [54]. Br is produced with only one velocity component, for CH_3 in a particular vibrational state. On similar σ*←n excitation in CH_2BrCl at 234 nm [55], and CF_2BrCl at 267 nm [56], the Br fragment formed has two velocity components. The fast Br channels in both have been suggested to originate from the repulsive σ*(C-Br) surface with high translational energy. The slow Br component in CF_2BrCl has been assigned to dissociation from the ground electronic state, whereas that in CH_2BrCl is suggested to originate from the crossing seam of σ*(C-Br) and σ*(C-Cl), but with a little vibrational excitation. In contrast, on similar σ*←n excitation in CF_2BrCl at 234 nm [57], the Br fragment formed has only one velocity component from the repulsive σ*(C-Br) surface, but the Cl fragment has a bimodal velocity distribution. The Cl channel is suggested to result from the crossing of the excitation from σ*(C-Br) to σ*(C-Cl) surface. However, three-body dissociation to CF_2+Br+Cl and CH_2+Br+Cl is not observed in CF_2BrCl and CH_2BrCl, respectively, at 234 nm because of energy constraints. But, this high energy channel is reported, in both experimental [58] and theoretical work [30], from excitation of CF_2BrCl at 157 nm. Even the 210 nm excitation of CH_2BrI has sufficient energy to open up a three-body dissociation channel [2]. Similar three-body dissociation is reported even in larger alkyl halides, such as $CF_3CHBrCl$ (2-bromo-2-chloro-1,1,1-trifluoroethane, popularly known as halothane) [29], on excitation at 157 nm. In this work the calculated energetics for all the possible dissociation channels of halothane have also been reported. The UV photodissociation of halothane is important not only for basic understanding of the C-Br and C-Cl bond cleavage dynamics, but also from its atmospheric [49,59], synthetic

[60,61] and medical implications, particularly for application as an inhalational general anesthetic [62,63]. Although it is not classified as a human carcinogen, its acute human exposure, by inhalation or dermal contact during its production or surgical procedures, produces several side effects, such as hepatitis, respiratory and gastrointestinal problems, etc. [63]. Its production and use as an anesthetic may result in its release to the environment through various waste streams. It exists solely as a vapor in the ambient atmosphere, and degraded by reaction (atmospheric lifetime of ~7 years) with photochemically produced hydroxyl radicals [59,64]. Due to its long atmospheric lifetime, about 12 to 21% of halothane is expected to diffuse slowly into the stratosphere [64], where it will undergo direct UV photolysis, releasing radicals that contribute to damage of the ozone layer.

UV irradiation of halothane produces various dissociation channels, following its σ*(C-Cl)←n(Cl) transition at 157 nm [29]. In addition to the C-Cl bond dissociation, the C-Br bond was also reported to cleave as a result of transition from the initially excited nσ*(C-Cl) diabatic surface to the nσ*(C-Br) diabatic surface. In this chapter, we present the UV photodissociation dynamics of halothane from a different excited state, σ*(C-Br), following its σ*(C-Br)←n(Br) transition at 234 nm, to examine the possibility of diabatic crossing from the nσ*(C-Br) surface to the nσ*(C-Cl) diabatic surface, and examine the effect of such crossing on the relative branching ratio of the C-Cl and C-Br bond scission, translational energy distribution and the anisotropy parameter. The measured dynamical features of halothane at 234 nm are compared with that at 157 nm, and also with CF_2BrCl at 234 nm.

3.2 Experimental

The photodissociation dynamics of halothane has been studied in a molecular beam (MB), using resonance-enhanced multiphoton ionization (REMPI) with time-of-flight (TOF) mass spectrometer, and the photoproducts, Br(4P $^2P_{3/2}$), Br*(4P $^2P_{1/2}$), Cl(3P $^2P_{3/2}$) and Cl*(3P $^2P_{1/2}$) atoms, detected state-selectively. Details of the experimental set up are discussed in chapter 2. The halothane sample (Aldrich, 99% purity) was used as supplied, after degassing and purifying by several freeze-pump-thaw cycles.

The REMPI spectra of Br, Br*, Cl and Cl* were measured by scanning the laser frequencies through their absorption transitions, and feeding the REMPI signal to a gated boxcar integrator. The relative quantum yields of Br and Br* were extracted from the relative integrated REMPI peaks at 233.700 nm (42789.9 cm^{-1}, 6p $^4P_{3/2} \leftarrow$ 4p $^2P_{3/2}$) and 234.040 nm (42727.7 cm^{-1}, 6p $^2S_{1/2} \leftarrow$ 4p $^2P_{1/2}$), and their corresponding two-photon transition probabilities [65]. Similarly, the relative integrated REMPI intensities of Cl and Cl*, respectively, at 235.336 nm (42492.5 cm^{-1}, 4p $^2D_{3/2} \leftarrow$ 3p $^2P_{3/2}$) and 235.205 nm (42516.1 cm^{-1}, 4p $^2P_{1/2} \leftarrow$ 3p $^2P_{1/2}$), were used to extract their relative quantum yields using two-photon transition probabilities [66] of the transitions involved.

3.3 Computational details

Ab initio molecular electronic structure theories were employed to investigate the Br and Cl formation channels in halothane, using Gaussian 03 program [3]. The ground state geometries of halothane, along with other fragments, were optimized at the B3LYP/6-311++G(d,p) level of theory, and energies of these geometries were calculated at the QCISD(T) level with the same basis sets. The harmonic vibrational frequencies were calculated for ensuring the stationary points on the potential energy surface to be true minima, and also for zero point energy correction. All the energy values reported are corrected with zero point energy. The most stable geometry for the ground state halothane has a staggered conformation. The calculated bond dissociation energies of the C-Br and the C-Cl bonds are 60.5 and 73.2 kcal/mol, respectively. Our calculated C-Br bond dissociation energy (60.5 kcal/mol) is intermediate between the reported values of 56.7 [29] and 65.7 [67] kcal/mol, respectively. Hence, we have used our calculated values of the bond dissociation energies of the C-Br and the C-Cl bonds for estimation of the available energies.

Excited electronic state calculations were performed at the time dependent density functional theory (TD-DFT) level, using aug-cc-pVTZ basis sets, and the electronic states of halothane, accessible at 234 nm, were predicted from the vertical excitation energies and the molecular orbital analysis. The lower singlet excited states S_1, S_2, S_3 and S_4 have vertical excitation energies of 5.79 eV (214.1 nm), 5.83 eV (212.7 nm), 6.72 eV (184.6 nm) and 7.01 eV (177.0 nm) with the oscillator strengths of 0.0018, 0.0104, 0.0013 and 0.0556, respectively. Molecular orbital calculations predict that both the S_1 and S_2 states originate from the $\sigma^*(\text{C-Br})\leftarrow n(\text{Br})$ excitation, involving the non-bonding electrons on Br. Both these states are nearly degenerate, and have different ratios of in-plane and out-of-plane non-bonding orbitals. The S_1 and S_2 states have relatively greater contributions of out-of-plane and in-plane non-bonding orbital, respectively. The lowest two triplet states T_1 and T_2 have similar nature as S_2 and S_1 states, respectively. The higher singlet states S_3 and S_4 originate from mixed transitions, comprising of the $\sigma^*(\text{C-Br})\leftarrow n(\text{Cl})$ and $\sigma^*(\text{C-Cl})\leftarrow n(\text{Cl})$ transitions. Like S_1 and S_2 states, the S_3 and S_4 states also have relatively greater contributions of out-of-plane (with respect to the plane containing C-Br and C-Cl bonds) and in-plane non-bonding orbital, respectively. Our calculated oscillator strengths suggest the dominant contributions of the in-plane transitions. Thus, these calculations predict that the excitation of halothane at 234 nm to the S_1 and S_2 states is due to the $\sigma^*(C\text{-}Br)\leftarrow n(Br)$ transition. For these assignments of the transitions to be true, the C-Br bond lengths in the S_1 and S_2 states, and the C-Cl bond lengths in the S_3 and S_4 states should be greatly extended. Thus, to further validate these assignments, we optimized the structures of the S_1-S_4 states of halothane at the configuration interaction with single electronic excitation (CIS) level with the 6-311++G(d,p) basis sets. As expected, the C-Br bond lengths are much elongated in the S_1 and S_2 states from 1.955 Å in the ground state to 2.786 and 2.806 Å, respectively. Similarly, the C-Cl bond lengths are much elongated in the S_3 and S_4 states from 1.78 Å in the ground state to 2.84 and 2.80 Å, respectively.

3.4 Experimental results

Photodissociation of halothane at ~234 nm generates Br and Cl, in both the ground ($^2P_{3/2}$) and the excited ($^2P_{1/2}$) spin orbit states, which were detected using (2+1)-REMPI and TOF mass spectrometer. The observed TOF profiles of Br, Br*, Cl and Cl* were analyzed, using a forward convolution method, described in detail in chapter 2. The (2+1)-REMPI signal at *m/e*= 36(HCl) could not be observed in the wavelength range 230-237 nm; suggesting that the HCl molecular elimination channel is either not taking place, or it is too small in yield to be detected.

3.4.1 REMPI detection of bromine and chlorine atom

The laser power dependence of the REMPI intensity, for both Br and Cl, has a linear log-log plot with a slope of ~3.0, implying one photon for photolysis and two for REMPI detection, in the range of the laser power used. Thus, the result suggests (2+1)-REMPI detection of chlorine and bromine atoms (REMPI spectra are given later) produced in a single photon process, assuming the ionization step is saturated. Additional experiments were performed to verify that the halogen atoms are produced in a single photon process. The shape and the width of TOF profiles of halogen atoms are systematically measured at various laser energies, and observed to be independent of laser energies used. All the measurements were performed in the low energy region, ensuring that the single photon dissociation condition was maintained.

3.4.1.1 Anisotropy parameters (β) and translational energy distributions of Br, Br*, Cl and Cl*

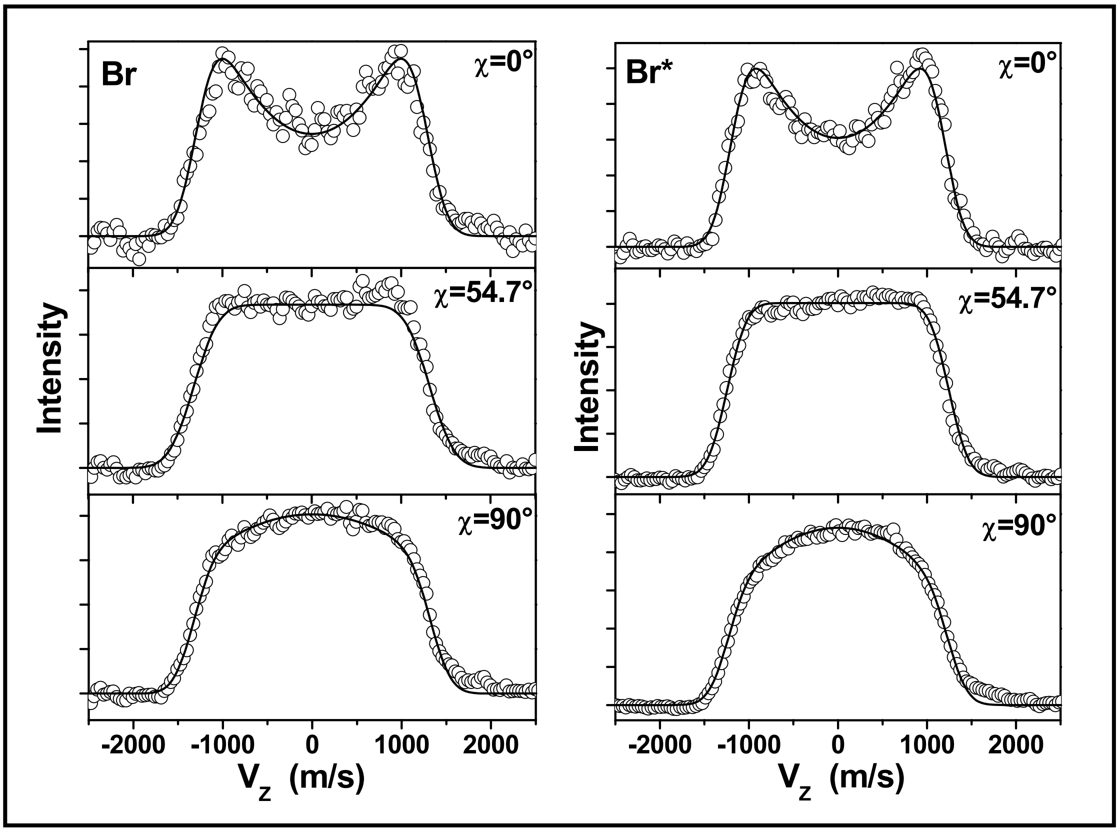

FIG. 3.1: *REMPI-TOF profiles of Br($^2P_{3/2}$) and Br*($^2P_{1/2}$) produced from the 234 nm photodissociation of halothane. The circles are the experimental data and the solid line is a forward convolution fit.*

The measured time of flight profiles of Br($^2P_{3/2}$), Br*($^2P_{1/2}$) and Cl($^2P_{3/2}$), Cl*($^2P_{1/2}$) with different laser polarizations, at the χ values (the angle between the laser polarization and the detection axis) of 0°, 54.7° (the magic angle) and 90° are depicted in FIG. 3.1 and 3.2, respectively. The TOF profiles of Br* and Cl* are similar to that of Br and Cl, respectively. The laser polarization dependence of TOF profiles implies non-zero β values. The analysis of TOF spectra results in the β values of 0.6±0.2 for Br and Br*, and 0.3±0.1 for Cl and Cl* fragments. The β values, along with other observables, are given in Table 3.1. The non-zero β values imply an anisotropic angular distribution of the fragments, suggesting fast (with respect to the rotational period of halothane) formation of Br and Br*, and also probably for Cl and

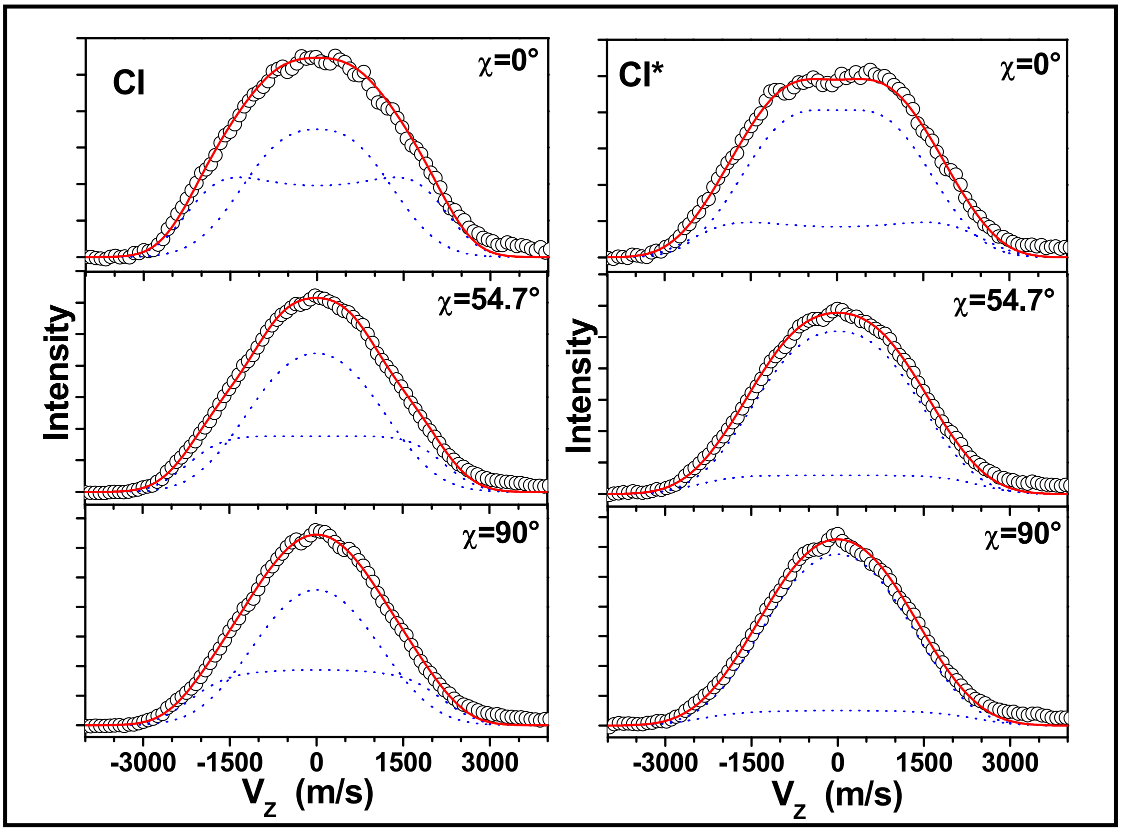

FIG. 3.2: *REMPI-TOF profiles of Cl($^2P_{3/2}$) and Cl*($^2P_{1/2}$) produced from the 234 nm photodissociation of halothane. The circles are the experimental data, the dashed lines are forward convolution fit for two different channels and the solid line shows the sum.*

Cl*. Thus, halothane mostly dissociates from an initially electronically excited state or other excited state(s) or the ground state, which is populated after fast relaxation of an excited state.

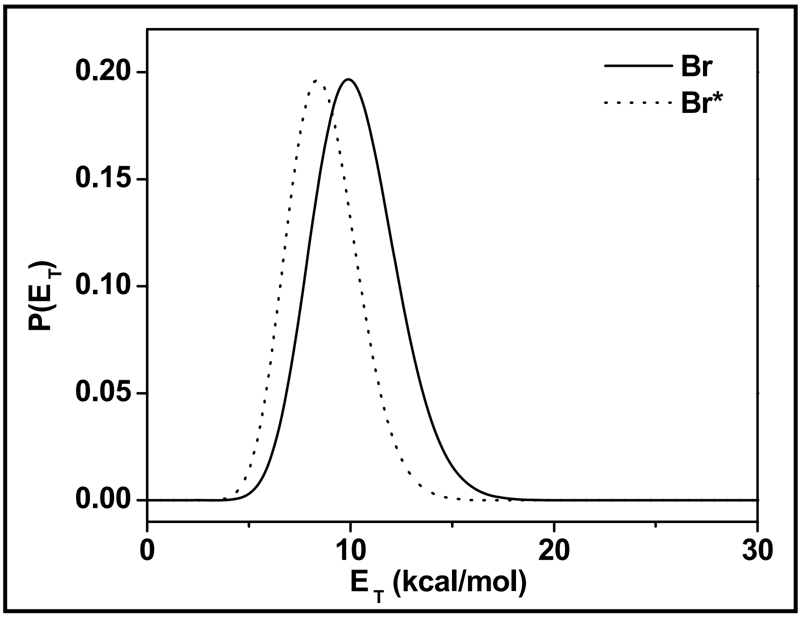

FIG. 3.3: *Photofragment center-of-mass translational energy distribution for the 234 nm dissociation of halothane for Br elimination channel. The solid lines indicate the translational energy distributions for the Br($^2P_{3/2}$) and dotted line for Br*($^2P_{1/2}$) atom, respectively.*

Using the forward convolution analysis of the TOF profiles, we also obtained photofragment speed distribution of Br, Br*, Cl and Cl*. The analyses reveal only one velocity component (fast) in the distribution of both Br and Br*, but two components (fast and slow) in the distribution of both Cl and Cl*. Thus, each of two bromine channels (Br or Br*) originates from a single pathway, whereas each of two chlorine channels (Cl or Cl*) originates from two different dissociation pathways. Using the speed distributions, photofragment translational energy distributions [P(E$_T$)] of Br, Br*, Cl and Cl* are determined.

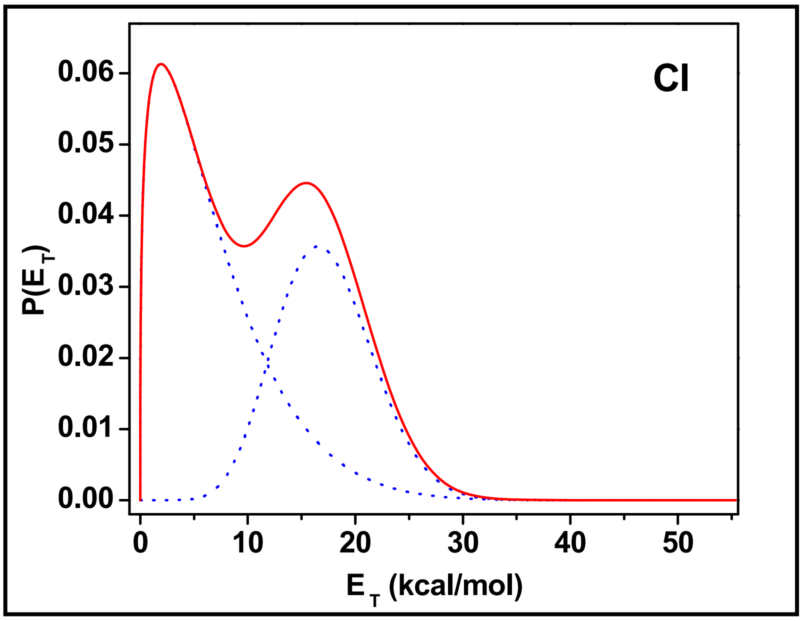

FIG. 3.4: *Photofragment center-of-mass translational energy distribution of chlorine atom Cl($^2P_{3/2}$) elimination channel for the 234 nm dissociation of halothane. The dashed lines indicate the energy distributions for the fast and slow component; the solid line shows the sum.*

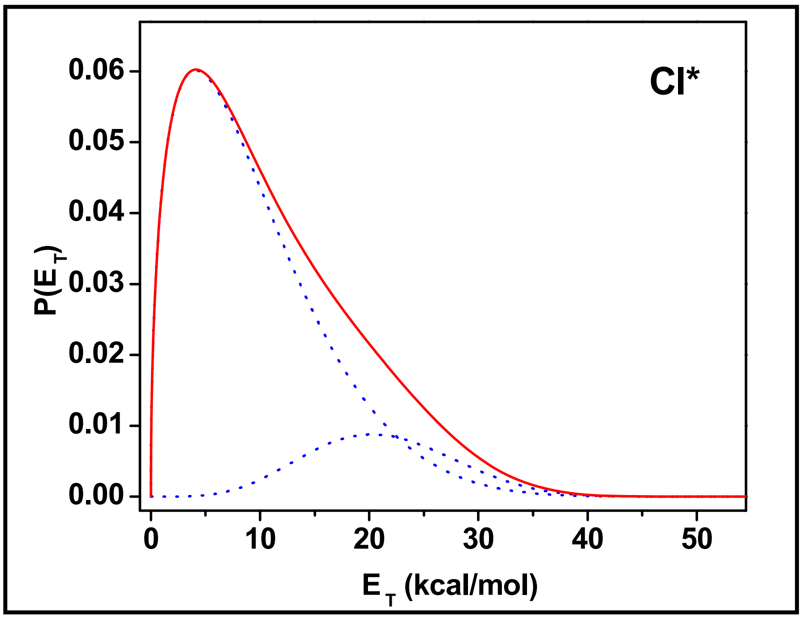

FIG. 3.5: *Photofragment center-of-mass translational energy distribution of chlorine atom Cl*($^2P_{1/2}$) elimination channel for the 234 nm dissociation of halothane. The dashed lines indicate the energy distributions for the fast and slow component; the solid line shows the sum.*

The $P(E_T)$ of Br and Br* with a single component are depicted in FIG. 3.3, whereas that of Cl and Cl* are bimodal, and shown in FIG. 3.4 and FIG. 3.5, respectively. The relative translational energies of Br and Br* channels are 10.5±1.0 and 8.5±0.9 kcal/mol, respectively. The relative translational energies for the fast (high energy) and slow (low energy) Cl channels are 17.5±2.0 and 7.5±1.0 kcal/mol, respectively. The fractions of the high and low translational energy components are determined to be 25% and 75%, respectively, for the Cl channel. Similarly, the average translational energies for the fast and slow Cl* channels are 21.0±2.0 and 9.5±1.0 kcal/mol, respectively. For the Cl* channel as well, the slow component contributes predominantly to the total yield, accounting for about 95%.

3.4.1.2 Relative quantum yields of the halogen atoms (X)

The spectral profiles of REMPI lines of Br and Br* were measured at 233.700 and 234.040 nm, respectively (shown in FIG. 3.6), and similarly that of Cl and Cl*

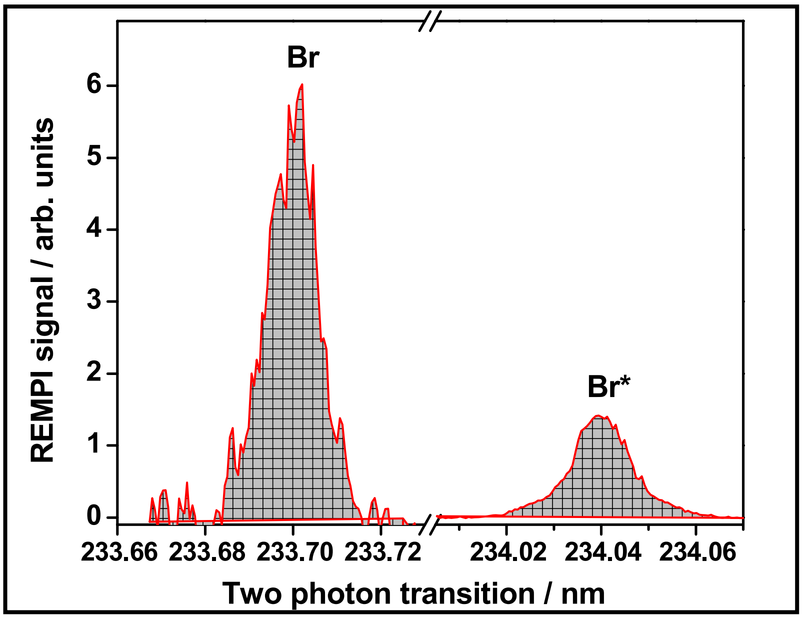

FIG. 3.6: *REMPI profiles of Br and Br* atoms produced in the 234 nm laser photolysis of halothane used for the determination of the spin-orbit ratio.*

were measured at 235.336 and 235.205 nm, respectively (shown in FIG. 3.7), to evaluate the relative quantum yields of X, Φ(X), and X*, Φ(X*). The relative quantum yields were evaluated using the integrated line intensities, I(X)/I(X*), which are directly proportional to the number density of X/X*, N(X)/N(X*), and can be expressed as in equation 3.1,

$$\frac{N(X^*)}{N(X)} = k\frac{I(X^*)}{I(X)}, \tag{3.1}$$

where the constant *k* is the relative ionization probability, i.e., the relative REMPI line strength of X as compared to that of X*. The values of *k* are taken to be 0.17±0.05 and 0.85±0.10 from literature for X=Br [65] and Cl [66], respectively.

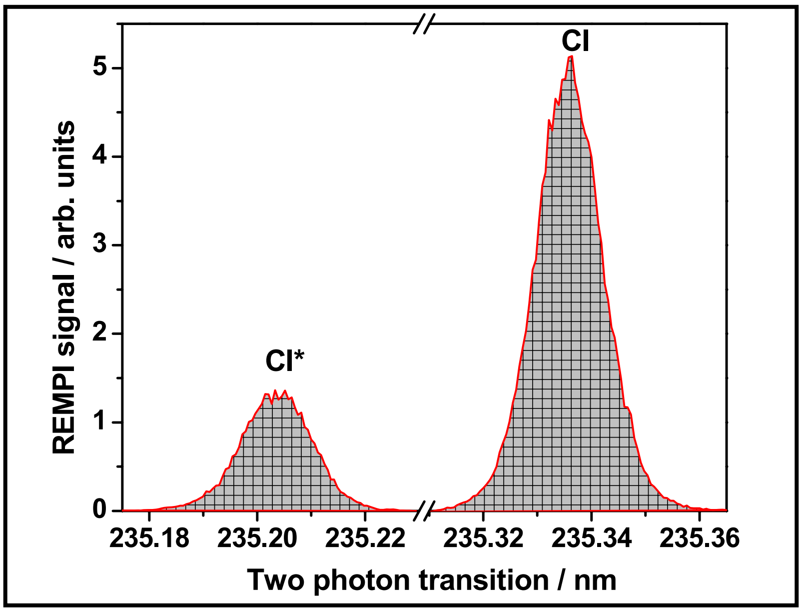

FIG. 3.7: *REMPI profiles of Cl and Cl* atoms produced in the 234 nm laser photolysis of halothane used for the determination of the spin-orbit ratio.*

The values of Φ(Br*) and Φ(Cl*) were calculated from the number density ratios to be 0.23 ± 0.05 and 0.22 ± 0.02, using following expressions,

$$\Phi(X^*) = \frac{N(X^*)}{N(X)+N(X^*)} \quad \text{and} \quad \Phi(X) = 1 - \Phi(X^*). \tag{3.2}$$

TABLE 3.1: *The dissociation energy of the C-X (X=Br, Cl) bond (D_0), available energy (E_{avl}), the average translational energy ($\langle E_T \rangle$), f_T values, the relative quantum yield (Φ) and the recoil anisotropy parameter (β) for photodissociation of halothane at 234 nm leading to Br and Cl fragments. Low energy Cl and Cl* channels are given in parenthesis. All energies are in kcal/mol.*

Reaction channels	hν[#]	D_0 (C-X)	E_{avl}	$<E_T>$	f_T value	Φ	β
CF_3-CHCl + Br	122	60.5	61.5	10.5±1.0	0.17	0.77±0.15	0.6±0.2
CF_3-CHCl + Br*	122	60.5	51.0	8.5±0.9	0.17	0.23±0.05	0.6±0.2
CF_3-CHBr + Cl	121	73.2	47.8	17.5±2.0 (7.5±1.0)	0.37 (0.16)	0.78±0.15	0.3±0.1
CF_3-CHBr + Cl*	121	73.2	45.4	21.0±2.0 (9.5±1.0)	0.46 (0.21)	0.22±0.02	0.3±0.1

[#] Excitation energy in kcal/mol

TABLE 3.2: *A comparison of the relative C-Br dissociation channel to the total C-Br and C-Cl dissociation channels in halothane and related compounds on excitation at different wavelengths.*

Compound	Br yield to the total Br and Cl yields from C-X bond scission at different wavelengths				
	267 nm	248 nm	234 nm	193 nm	157 nm
CH_2BrCl		~100% [68]		82% [68]	
CF_2BrCl			96% [57]	86% [69]	61% [30]
CF_3-CHBrCl (Halothane)	~ 100% [56]		~93%*	~72%# [47]	57% [29]
CF_2Br-CHClF					21% [58]

[*] Present work

[#] Based on Br yield from all the channels

These values are reported in Table 3.1. Similar relative yield of Cl* (0.18±0.02) has been reported in photodissociation of halothane at 193 nm [70]. In addition to the spin-orbit branching ratio, we have also sub-divided the chlorine product population distribution (including both Cl and Cl*) based on the relative amounts of the measured low and high kinetic energy components. The branching ratio of the low kinetic energy C-Cl bond scission to the high energy C-Cl bond scission is 0.65/0.35, considering both Cl and Cl* channels with their relative quantum yields. We have also estimated the branching ratio of the C-Br bond scission to the C-Cl bond scission channel in halothane on excitation at 234 nm to be ~13.0/1.0, by using the relative ionization probability of Cl to that of Br* as 1.24 ± 0.30 [71]. Thus, the C-Br bond rupture is the major C-X bond dissociation channel accounting for ~93% of the total X (Br and Cl) yields. Even on excitation at 193 nm, the major primary event for halothane is the C-Br bond rupture [70]. A comparison of the relative C-Br bond dissociation channel to the total C-Br and C-Cl dissociation channels in halothane and related alkyl halides, on excitation at different wavelengths, is given in Table 3.2.

3.5 Discussions

3.5.1 Excitation of halothane at ~234 nm

The UV absorption spectra [49,64,72] of halothane vapor, in the wavelength range of 200 to 315 nm, have a broad maximum at ~205 nm, with absorption almost exponentially decreasing to longer wavelengths and showing no absorption at 285 nm. The spectrum has no significant vibrational structure, suggesting that the electronic excited state is dissociative in nature. The spectrum suggests that irradiation of halothane at ~234 nm excites the red edge of this absorption with the absorption cross-section of ~1.0×10^{-19} cm^2 $molecule^{-1}$. Although absorption of this molecule at 234 nm has not been assigned to a specific electronic transition, this can be assigned to the σ*(C-Br)←n(Br) transition, based on our excited state calculations and the spectral information available on a related compound, CF_2BrCl [73,74]. Our excited state calculations predict the absorption features with maxima at 212.7 and 177.0 nm, the former corresponding to the experimentally observed features of 205 nm. We have assigned the low energy feature at 212.7 nm to the σ*(C-Br)←n(Br) transition. The high energy feature at 177 nm is assigned to a combination of σ*(C-Br)←n(Cl) and σ*(C-Cl)←n(Cl) transitions. Similar features have been reported in the absorption spectra of CF_2BrCl [73,74] as well. In addition to the 205 nm peak, another broad and unstructured absorption with maximum at 164 nm is observed for CF_2BrCl, and assigned to the σ*(C-Cl)←n(Cl) transition. Based on the absorption spectra of CF_2BrCl [73,74], Yokoyama et al. [29] have assigned the excitation of halothane at lower wavelength of 157 nm to the σ*(C-Cl)←n(Cl) transition.

3.5.2 Mechanism of bromine and chlorine atom formation

On photoexcitation of halothane at 234 nm, Br and Cl atoms are produced in both the ground and spin-orbit excited states, which are detected readily using REMPI technique.

3.5.2.1 Bromine atom

Since the excitation energy (122 kcal/mol) is greater than the bond dissociation energies of both the C-Br (60.5 kcal/mol) and C-Cl (73.2 kcal/mol) bonds of halothane [29], both the bonds can be cleaved on excitation at 234 nm. But, at this wavelength only the σ*(C-Br)←n(Br) transition of halothane is directly excited, and the direct C-Br bond dissociation can take place from the repulsive state to produce Br atoms in both the ground and spin-orbit excited states (reactions 3.3 and 3.4).

$CF_3\text{-}CHBrCl \rightarrow CF_3\text{-}CHCl + Br\ (^2P_{3/2})$ (3.3)

$\rightarrow CF_3\text{-}CHCl + Br^*\ (^2P_{1/2})$ (3.4)

The C-Br bond cleavage from the repulsive state should be characterized by an impulsive dissociation process, partitioning a greater fraction of the available energy in the relative translation of the products. In addition, the Br fragment is expected to have high recoil anisotropy, because of the fast C-Br bond dissociation event from a repulsive state. Our measurements on translational energy distribution and recoil anisotropy parameter (β) of Br and Br* validate the direct C-Br bond dissociation. Our results reveal a high fraction of the available energy going to the relative translation ($f_T = 0.17$) of the Br and Br* channels. The measured f_T value of 0.17 is in reasonably good agreement with the predicted value of 0.22 by a soft impulsive model [26] of energy partitioning. Even the value of the β parameter for both Br and Br* channels is high (0.6), as expected. A positive value of the β parameter implies that 234 nm excites roughly a parallel transition of halothane. Thus, the observed f_T and the β parameter values for the bromine atom channels suggest that these channels originate from direct C-Br bond dissociation, involving an impulsive mechanism.

The observed value of 0.6 for the β parameter is much reduced from the expected highest value of 2.0 for the β parameter for a parallel transition. One of the factors responsible for such reduction is the direction of the transition dipole moment with respect to the dissociating bond and this angle is denoted as θ_m. Our excited state calculations for the S_1 state give the value of θ_m as 32° and 44° for the Br and Cl fragments, respectively. The value of θ_m is related to recoil anisotropy parameter β as, $\beta = 3\cos^2\theta_m - 1$ (eq. 2.11, chapter 2). These θ_m values result in the values of β as 1.16

and 0.55 for Br and Cl, respectively. However, for the S_2 state the values of θ_m are calculated to be 43° and 52° for Br and Cl fragments, respectively, leading to the corresponding β values of 0.60 and 0.09. Thus, the simple geometry arguments are able to explain qualitatively the reduction in the β value of both bromine and chlorine atom channels. If we assume the excitation of halothane at 234 nm is mostly to the S_2 state (as our calculations predict), these arguments quantitatively explain reasonably well the measured β values. However, many times simple geometry arguments are not able to explain the value of β parameter, because of various factors [45,75], such as mixed initial transition with both parallel and perpendicular components, relatively longer dissociation lifetime, dissociation not from a single geometry rather from a range of geometries, excitation of multiple states, curve crossing of the states, etc. In the photodissociation of alkyl halides, in general, non-adiabatic coupling between $^3Q_0$ and $^1Q_1$ states, combined with excitation of both the parallel and perpendicular transitions, are mainly responsible for the observed β values of a halogen (X) fragment [41,54,76]. In the photodissociation of alkyl bromides at 234 nm, the β(Br*) values are close to the limiting value of the parallel transition (~2) [77]. In UV photodissociation of perfluorinated alkyl bromides also (including other halides), the β(Br*) values are close to 2. However, in allyl bromide the β(Br*) value is considerably small (0.37) due to the contribution of the $^1Q_1$ state (perpendicular transition) in the initial excitation of allyl bromide at 234 nm [78]. The β(Br*) values in photodissociation [79] of 3-bromo-1,1,1-trifluoro-2-propanol (BTFP) and 2-(bromomethyl) hexafluoro-2-propanol (BMHFP) at 234 nm are intermediate between that of alkyl bromides and allyl bromides, with an intermediate contribution of the perpendicular transition to initial excitation of BTFP and BMHFP. In bromochloroalkanes, for example in 1-bromo-2-chloroethane, β(Br) values are positive but β(Br*) values are negative. Thus, like other alkyl halides some contribution from the perpendicular transition and non-adiabatic curve crossing may be responsible for lower β values of the Br and Br* channels. Like in halothane, the excitation of CH_2BrI [2] at 234 nm, via the σ*(C-Br)←n(Br) transition, leads to the direct dissociation of the C-Br bond, producing bromine atom with the lower β value of 0.6.

3.5.2.2 Chlorine atom

Halothane produces chlorine atom in both the ground $Cl(^2P_{3/2})$ and the spin-orbit excited $Cl^*(^2P_{1/2})$ states on excitation at 234 nm. Two different, low and high kinetic energy, pathways for Cl and Cl* formation have been observed. The mechanism of Cl atom formation cannot involve direct C-Cl bond rupture, since the excitation at 234 nm leads to the σ*(C-Br)←n(Br) transition, and not the σ*(C-Cl)←n(Cl) transition of halothane. Although the C-Cl bond of halothane is not excited directly, it can get energy through intramolecular electronic energy transfer from the σ*(C-Br) state, leading to Cl formation through the C-Cl bond rupture. This interpretation is consistent with the polarization experiments, which show that both bond fission channels result from a dipole transition moment aligned roughly parallel to the breaking bonds with β values of 0.6 and 0.3 for the Br and Cl channels, respectively. Similar electronic energy transfer has also been observed in photodissociation of CF_2BrCl on excitation at 234 nm, resulting in formation of Cl besides Br [57]. On electronic excitation of halothane (2-bromo-2-chloro-1,1,1-trifluoroethane) [29] and 1-bromo-2-chloro-1,1,2-trifluoroethane [58] at 157 nm, which excites the σ*(C-Cl)←n(Cl) transition, the intramolecular electronic energy transfer has been observed from the nσ*(C-Cl) to the nσ*(C-Br) diabatic surfaces. Thus, they could explain the formation of Br from the C-Br bond rupture, in addition to the direct Cl formation.

Thus, on excitation of halothane at 234 nm, similar to CF_2BrCl, the locally excited nσ*(C-Br) surface can transfer energy to the nσ*(C-Cl) surface. The Cl atom can be produced impulsively through the C-Cl bond rupture from the repulsive nσ*(C-Cl) surface with a high translational energy and retention of some recoil anisotropy. This channel of Cl formation is responsible for the observed fast Cl and Cl* with the f_T values of 0.37 and 0.46, respectively, which can be explained by an impulsive mechanism of energy partitioning. The impulsive model is based on the assumption that the amount of available energy acts as a repulsive potential along the dissociating bond, i.e., the C-X bond in halothane. Then, the energy partitioned between fragments is determined by conservation of linear and angular momenta.

In the soft impulsive model, the energy is partitioned to both the rotation and vibration of the fragments (in addition to translation), whereas in the rigid model, the bond is assumed to be rigid, and the energy is partitioned to only rotation and not to vibration. The soft impulsive [26] and the rigid impulsive [80,81] models predict the f_T values of 0.31 and greater than or equal to 0.38, respectively, for the C-Cl bond dissociation channel. The fast chlorine atom channel can be explained by the rigid impulsive mechanism, whereas the slow Cl and Cl* channels with the f_T values of 0.16 and 0.21, respectively, can be due to the soft impulsive mechanism. The non-zero values of the β parameter (0.3±0.1) for the chlorine channels support the impulsive nature of even the slow chlorine atom channel. Moreover, the translational energy distributions of low energy Cl and Cl* with the observed f_T values of 0.16 and 0.21, respectively are much greater than the statistical value of ~0.07, calculated using formalism given by Muckermann [24] and Klots [25] (*vide infra*). The slow chlorine atom channel cannot be assigned to occur from the ground electronic state of halothane after fast internal conversion, or involving a secondary reaction because of following reasons. If halothane is relaxed to the ground electronic state and subsequently produces the slow chlorine atom channel, it should also generate slow bromine atom channel (the lowest energy pathway), showing a bimodal translational energy distribution for the bromine atom channel as well. However, we observed only one component for the bromine atom channel in the translational energy distribution. Moreover, the ground state dissociation of halothane, as in the infrared multiphoton dissociation (IRMPD) [82], is expected to produce the molecular product HCl, which is absent in the present work. In addition, the dissociation from the ground electronic state, after internal conversion from a repulsive surface, is expected to be a minor channel. However, in the present studies, the slow chlorine atom channel is a major channel. A secondary dissociation also cannot be responsible for the slow chlorine atom channel. Based on photodissociation mechanism of halothane at 157 nm [29], one can expect that the slow chlorine atom channel can originate from CF_3CHCl, a primary product along with Br from the C-Br bond scission (reactions 3.3 and 3.4). The formation of Cl from CF_3CHCl can involve first the 1,2-fluorine atom migration, followed by the C-Cl bond rupture (reaction 3.5),

$$CF_3\text{-}CHCl \rightarrow CF_2\text{-}CHClF \rightarrow CF_2{=}CHF + Cl. \qquad (3.5)$$

However, this Cl channel is difficult to be observed on excitation of halothane at 234 nm, since CF_3-CHCl will not have sufficient internal energy to undergo re-arrangement followed by the C-Cl bond dissociation. Moreover, this channel, involving re-arrangement of a primary channel followed by dissociation, is expected to be statistical in nature with isotropic distribution of the products. However, the translational energy distributions and the recoil anisotropy parameter (β) of low energy Cl and Cl* do not support a statistical dissociation mechanism. Thus, this pathway may not be responsible for the low energy channel of Cl and Cl*. Like halothane, in photodissociation of CF_2BrCl at 234 nm also [57], two different pathways of chlorine formation were observed, and the slow channel was assigned to an impulsive dissociation. However, the fast channel was assigned to a 2-photon dissociation process, in which the primary product CF_2Cl undergoes the C-Cl bond cleavage on its absorption of another photon of 234 nm, since the translational energy of this fast channel was observed to be greater than the available energy.

Thus, on excitation of halothane at 234 nm, its initially excited state mainly undergoes fast impulsive dissociation involving the C-Br bond rupture to produce high kinetic energy Br, else couples with the nσ*(C-Cl) surface to transfer energy to the C-Cl bond. Subsequently, the impulsive C-Cl bond scission produces both slow and fast chlorine atom pathways. We have attempted to support the proposed mechanism of the C-X bond rupture with the molecular orbital calculations.

3.5.3 Theoretical results

To understand the dynamics of the C-X (X=Cl, Br) bond cleavage, the potential energy (PE) curves of all the four singlet excited states of halothane were calculated as a function of the C-X bond length, employing TD-DFT theory with 6-311++G(d,p) basis sets. Since we could not optimize structures of the excited states at TD-DFT level of theory, we determined PE curves for a fixed length of the C-Cl bond by constraining the geometry of halothane to the equilibrium position of the ground state with only the distance of the C-Br bond varied in steps of 0.05 Å. Three sets of PE curves for the fixed C-Cl bond lengths of 1.8 (close to the equilibrium bond length of 1.78 Å), 2.0 and 2.2 Å are plotted in FIG. 3.8. The curves for the S_1 and S_2 states are nearly degenerate, and similar in all three cases. However, the PE curves for the S_3 and S_4 behave differently. Two avoided crossing regions can be seen with decreased energy and reduced energy separation between adiabatic curves with increasing C-Cl bond length from 1.8 to 2.2 Å. These avoided crossings result from coupling between the S_1 and S_3, and S_2 and S_4 diabatic PE surfaces, since these pairs of states involve

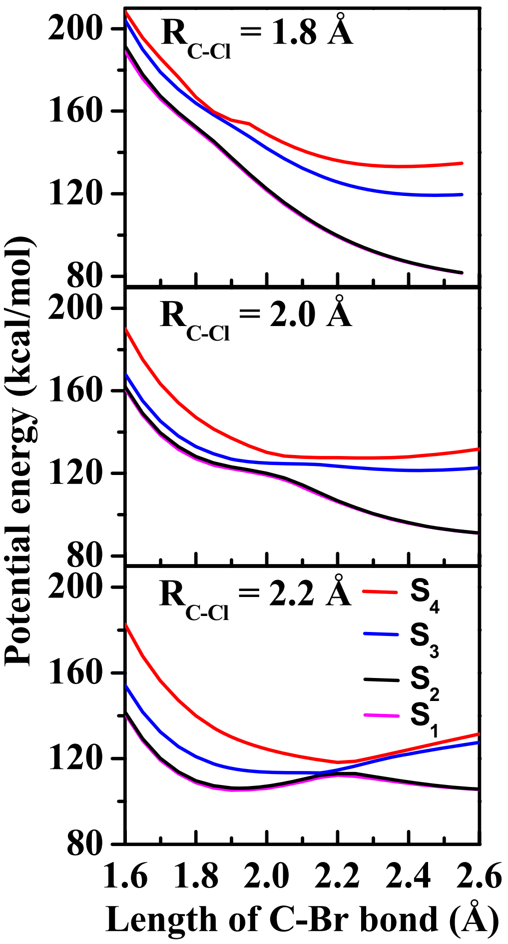

FIG. 3.8: The adiabatic potential energy curves of the four lowest states of halothane as a function of the C-Br bond length at the C-Cl bond lengths of 1.8, 2.0 and 2.2 Å.

non-bonding orbitals of similar nature (as mentioned earlier). The figure clearly demonstrates that the S_1 and S_2 states, with nσ*(C-Br) character, of halothane is excited at ~234 nm (~122 kcal/mol), and expected to directly lead to the C-Br bond fission to produce bromine atom. However because of avoided crossings, the C-Cl bond rupture is also observed. Thus, the excitation of halothane at ~234 nm leads to direct C-Br bond dissociation, and also populates the lower adiabatic state, on which the C-Cl bond cleaves.

The theoretically predicted two avoided crossing regions, with different energy separations between adiabatic states, can be responsible for bimodal translational energy distribution for the Cl product, and the explanation is based on that given in a theoretical study using wave packet propagation [30]. A smaller energy separation between adiabats S_1 and S_3 implies a weaker coupling, which gives a sharper PES in the avoided crossing region, leading to rapid dissociation on the lower adiabat. Thus, this avoided crossing is responsible for fast chlorine atom channel. In contrast, a larger energy separation between adiabats S_2 and S_4 implies a stronger coupling, which gives a flatter PES in the avoided crossing region, leading to slow dissociation on the lower adiabat. Thus, this avoided crossing is responsible for slow chlorine atom channel. Relative importance of these slow and fast chlorine atom channels can be explained considering the oscillator strengths of the transitions involved. The calculated oscillator strengths for transitions corresponding to the S_1 and S_3 states are much lower than that to the S_2 and S_4, respectively. Thus, the slow chlorine atom channel is the major component.

Similar PE curves have been calculated for CF_2BrCl as a function of the C-Cl bond lengths at fixed C-Br bond lengths considering the dominant transition alone

[30], to understand its dynamics of dissociation at 157 nm on excitation of the σ*(C-Cl)←n(Cl) transition. Their calculated avoided crossing region has qualitatively similar dependence, with respect to its location and the energy separation between adiabatic curves, as the present calculations for halothane. Unlike the Br channel, we observed two types of velocity distributions for the Cl channel. Thus, theoretical calculations in combination with the experimental results provide a better understanding of the C-X bond dissociation dynamics. These calculations assist in understanding the measured translational energy distributions of the C-Br and C-Cl bond dissociation channels, their relative importance and a possibility of simultaneous occurrence of these channels.

3.5.4 Translational energy distribution

The measured translational energy distribution in the photodissociation of halothane reveals that both the average and the maximum translational energies are nearly identical (within 2 kcal/mol) for Br and Br* channels, notwithstanding a 10.5 kcal/mol energy difference between these two spin-orbit states. The result suggests that the kinetic energy is released in the early part of the dissociation before the curve crossing takes place between the $^3Q_0$ and $^1Q_1$ states [56].

Since the available energy for the C-Br bond scission in halothane is about 12 kcal/mol greater than that for the C-Cl bond dissociation, the Br channel is expected to have greater translational energy, assuming that the same fraction of the energy is partitioned in both the cases. However, the average translational energies of Br (10.5 kcal/mol) and Br* (8.5 kcal/mol) are almost similar to that of Cl (10.0 kcal/mol) and Cl*(10.1 kcal/mol), respectively. Although the average translational energies of the bromine and chlorine channels are similar, that of fast Cl and Cl* channels are much greater than that of bromine channels. The fraction of the available energy going to the relative translation, f_T, of these channels is different. These f_T values of the Br and Br* (0.17) are somewhat lower than the predicted value of 0.22 by a soft impulsive model of energy partitioning [26]. The f_T value of the faster component of Cl (0.37) is in good agreement with a value of ~0.38, predicted by the rigid impulsive model, but that of Cl* (0.46) is somewhat greater than the predicted value. Thus, the measured f_T values support the conclusion that bromine and fast chlorine channels originate from repulsive surfaces of halothane. The f_T values of the slow components of Cl (0.16) and Cl* (0.21) are lower than that predicted values with the soft impulsive model of 0.31, but much greater than the statistically predicted values of 0.06 [25] and 0.08. [24] Although the measured f_T values are somewhat lower than the predicted values with the soft impulsive model, the slow chlorine atom channel is also assigned to an impulsive dissociation, based on our discussion in previous sections.

The difference in the f_T values of the bromine and fast chlorine channels can be explained by accessing different curvatures of two repulsive surfaces at 234 nm excitation [10]. The direct excitation is expected to sample a steep portion of the $n\sigma^*$(C-Br) surface, whereas after crossing it samples not so steep portion of the $n\sigma^*$(C-Cl) surface. For a steep repulsive surface, the impulsive force approximation is appropriate to explain the energy partitioning by the impulsive model (soft or rigid). The soft impulsive model predicted f_T value of 0.22, for the C-Br bond fission, is somewhat greater than the measured value of 0.17. However, for a less repulsive surface this approximation is not strictly valid, and the heavy Cl atom recoils away not only from the lighter carbon atom, but from the whole radical fragment, resulting in partitioning of a larger fraction of the available energy to translation [2]. This explains greater f_T values for the fast chlorine channel. However, lower f_T values for the slow chlorine atom channels have been observed. The greater translational energy in the chlorine channel in comparison to the bromine channel can also be explained reasonably well with another similar model based on the location of curve crossing [58]. The C-Br bond cleavage in halothane is direct, and the C-Cl bond rupture is due to energy transfer involving the [n(Br),σ*(C-Br)] and [n(Cl),σ*(C-Cl)] diabatic potential energy surfaces. The potential energy above the crossing is mainly partitioned to the relative translation of Br and its co-fragment, while the potential energy release below the crossing is primarily transferred to the relative translation of Cl and its co-fragment. Assuming the crossing point is close to the excitation energy at 234 nm, the direct reaction products, Br and its co-fragment, are expected to have relatively small amount of translational energy in comparison to the Cl and its co-fragment. The PE curves depicted in FIG. 3.8 justify the assumption, since the crossing point is at ~120 kcal/mol. Thus, one can expect that on excitation of halothane at higher excitation energies (photolysis at wavelengths lower than 235 nm), the average translational energy for the C-Br bond rupture should increase, but that for the C-Cl bond rupture should remain almost the same, as long as the excitation leads to the same transition σ*(C-Br)← n(Br).

The results imply that the co-fragments of Br and Br*, in comparison to that of Cl and Cl*, carry a relatively greater fraction of the available energy as internal energy. The Br and Br* channels can have relatively greater rotational energy, since the C-Br dissociation channel is expected to have a greater exit impact parameter than the C-Cl dissociation channel.

3.5.5 The C-Br versus C-Cl bond rupture

Photodissociation of halothane at 234 nm produces both Br and Cl atoms through the C-Br and C-Cl bond dissociation, respectively. To understand the relative importance of these two channels, we have roughly estimated the relative yield of the C-Br and C-Cl bond rupture to be ~13:1. The [n,σ*(C-Br)] surface of halothane is directly excited to produce Br; the Cl atom channel is possible due to the intramolecular energy transfer to the [n,σ*(C-Cl)] surface. Although the Cl atom channel is a minor pathway, its importance strongly depends on the excitation wavelength and the relative positions of the halogen atoms. The percent Br yields to the total Br and Cl yields of halothane and other related bromochloroalkanes on photolysis at different wavelengths are listed in Table 3.2. It is evident that the Br (Cl) elimination channel in an alkyl dihalide becomes more and more significant with increasing (decreasing) photolysis wavelengths. This observation is expected to be valid for any bromochloroalkane, including halothane, since with increasing wavelength mostly the [n,σ*(C-Br)] surface of the molecule is excited leading to the C-Br bond cleavage, and the decreasing excitation energy reduces the rupture of the stronger C-Cl bond. Our excited state calculations suggest that the crossing between these two diabatic states of halothane takes place at near 120 kcal/mol energy. Therefore, at lower excitation energies (greater than ~237 nm), the electronic energy transfer from the [n,σ*(C-Br)] to the [n,σ*(C-Cl)] surface is less probable, implying reduced Cl yield. In the photolysis of CF_2BrCl (whose PESs are expected to be similar as halothane) at 267 nm, the Cl channel was not detected, since it was expected to be negligibly small [56].

In addition to the photolysis wavelength, the relative positions of Br and Cl have a significant effect on the branching ratio of the C-Br and C-Cl bond dissociation in a bromochloroalkane. The photolysis at 157 nm leads to much greater Br yield (57%) in halothane (2-bromo-2-chloro-1,1,1-trifluoroethane) [29], with both Br and Cl atoms on the same carbon atom, than that in its isomer 1-bromo-2-chloro-1,1,2-trifluoroethane [58], with Br and Cl atoms on adjacent carbon atoms. This difference has been explained based on the coupling strength between the [n,σ*(C-Cl)] and [n,σ*(C-Br)] diabatic surfaces. In case of halothane, with both Cl and Br being located on the same C atom, the coupling between two chromophores is quite strong, since the coupling strength between two diabatic surfaces is directly dependent on the splitting between the adiabatic surfaces, originating due to the avoided crossing of the diabatic surfaces [29]. In 1-bromo-2-chloro-1,1,2-trifluoroethane the coupling strength is decreased significantly due to increased distance between Cl and Br, leading to inefficient energy transfer from the [n,σ*(C-Cl)] to the [n,σ*(C-Br)] diabatic surfaces. This results in a significantly lower yield of Br (21%) in comparison to halothane (57%). Similarly on photolysis at 234 nm, the Cl yield in halothane is expected to be greater than that in 1-bromo-2-chloro-1,1,2-trifluoroethane, since the energy transfer from the [n,σ*(C-Br)] to [n,σ*(C-Cl)] surface is more efficient in halothane. Similar dependence of intramolecular energy transfer on the distance between two chromophores has been observed in bromoacetyl and bromopropionyl chlorides, leading to different branching between C-Br and C-Cl bond rupture [68,69].

The relative branching ratios of the C-Br and C-Cl bond fission in halothane at different wavelengths are similar to that in CF_2BrCl (Table 3.2). This similarity is observed mainly because the electronic transitions are similar at a particular wavelength, and both Br and Cl are located on the same C atom in both the molecular systems. Thus, the strength of coupling between the [n,σ*(C-Br)] and [n,σ*(C-Cl)] diabatic surfaces is similar in both molecules.

3.5.6 Comparison with similar alkylhalides

The present studies on dissociation dynamics of halothane at 234 nm are very much different from its dissociation at 157 nm [29], mainly because of different excitations, σ*(C-Cl)←n(Cl) being in the latter case. At 157 nm the C-Cl bond rupture is the major channel with competing C-Br bond rupture channel. Each of these two channels has several pathways because of secondary reactions possible at high excitation energy. In addition, other channels, such as triple dissociation producing simultaneously Br and Cl, also have been reported. In contrast, dissociation of halothane at 234 nm in the present work leads to only primary Br and Cl atom channels, with only one pathway for the former and two pathways for the latter. Moreover, the three-body dissociation channel is not expected from excitation of halothane at 234 nm (122 kcal/mol), since the excitation energy is not sufficient to cleave simultaneously both the C-Br and C-Cl bonds.

In comparison to dissociation of CH_2BrCl at 234 nm [55] and CF_2BrCl at 267 nm [56] and 234 nm [57], with σ*(C-Br)←n(Br) transition, the dissociation of halothane at 234 nm is overall qualitatively similar to that of CF_2BrCl at 234 nm. We observed similar relative branching ratios of the C-Br and C-Cl bond fission in halothane and CF_2BrCl at different wavelengths. There exists only one channel for bromine, and two channels for chlorine formation. Even the slow chlorine channel has been assigned to the repulsive C-Cl bond rupture. Unlike in CF_2BrCl, in the halothane dissociation the fast channel is the minor chlorine channel. However, in halothane dissociation at 234 nm both Cl atom channels are assigned to the repulsive C-Cl bond rupture. In addition, the value of the β parameter is 1.05 and 1.60 for Br and Br* in CF_2BrCl, whereas 0.6 for both Br and Br* in halothane. In earlier studies of alkyl dihalides with Br and Cl, involving σ*(C-Br)←n(Br) excitation, the chlorine atom channel has not been investigated in detail, particularly its angular distribution. In the present work, in addition to the bromine channel, we have measured both translational energy distribution and the recoil anisotropy parameter β of the chlorine atom channel, and discussed its dynamics.

3.6 Conclusions

The UV photodissociation dynamics of halothane is investigated on excitation at ~234 nm to the n(Br)σ*(C-Br) surface. Both bromine and chlorine atoms are detected using (2+1) REMPI with TOF mass spectrometer. The C-Br bond rupture on the excited PES, which is repulsive along the C-Br bond, produces bromine atom in both the ground $Br(^2P_{3/2})$ and the spin-orbit excited $Br^*(^2P_{1/2})$ states, with the former accounting for 77% of the total bromine yield. Both Br and Br* are produced with anisotropic distributions, characterized by the recoil anisotropy parameter β value of 0.6±0.2. Using the measured translational energy distributions, we estimated the fraction of the available energy partitioned to the relative translation (f_T) to be 0.17 for both the Br and Br* channels, which is slightly lower than the predicted value of 0.22 by a soft impulsive model.

Like formation of the bromine atom, the chlorine atom also has two pathways producing Cl and Cl*, with the former accounting for 78% of the total chlorine yield. But unlike Br and Br*, Cl and Cl* have bimodal translational energy distributions, implying two different mechanisms of chlorine formation. The formation of chlorine atom involving the C-Cl bond rupture is not through the direct excitation of halothane. It is explained by an avoided crossing of the nσ*(C-Br) and the nσ*(C-Cl) diabatic potential energy surfaces near the excitation energy of ~122 kcal/mol above the ground electronic state, as predicted by our excited state calculations. Thus, the C-Cl bond rupture results due to the transition from the nσ*(C-Br) to the nσ*(C-Cl) surface. This impulsive C-Cl bond rupture is responsible for both the fast and slow Cl atom channels, and described reasonably well by rigid and soft impulsive models, respectively. Thus, the counter fragment of the fast and slow chlorine atom is expected to have no vibrational excitation and some vibrational excitation, respectively.

CHAPTER 4

UV-Photodissociation of tetrachloroethylene at 235 nm: A REMPI-TOF study

4.1 Introduction

The photodissociation dynamics of small halogenated polyatomic molecules containing a large number of Cl atoms, has been an area of extensive research both experimentally and theoretically because of their importance in surface etching [83,84] and atmospheric science [85,86]. The chlorine substituted ethylenes, such as vinyl chloride ($H_2C{=}CHCl$), trichloroethylene ($Cl_2C{=}CHCl$) and tetrachloroethylene ($Cl_2C{=}CCl_2$) plays a major role in contamination of surface and ground waters [87,88]. Among them trichloroethylene and tertrachloroethylene, which are used as industrial solvents, are produced in very large quantities worldwide [89]. Also, the anthropogenic contribution of organochlorine compounds to the environment is of great concern [90,91].

In atmosphere, chloroethylenes are mostly degraded by both direct UV photolysis and OH radical-induced oxidation, the latter initiates through OH attack on C=C double bond resulting the formation of an OH adduct. Chloroethylenes have strong absorption band around 200 nm, which is assigned to the $\pi^* \leftarrow \pi$ transition [92]. Trichloroethylene has an absorption band in the wavelength range of 180-250 nm, with the peak at ~200 nm. Similarly, tetrachloroethylene strongly absorbs in the wavelength range of 185-255 nm, with the peak at ~200 nm and a shoulder at ~235 nm [93]. In atmosphere, tetrachloroethylene undergoes direct photolysis in the above wavelength range and forms dichloroacetyl chloride as the major product, which is less degradable and more toxic than the parent molecule. In addition, it also produces phosgene, trichloroacetyl chloride, chloroform, and methylene chloride under atmospheric conditions [94].

The availability of several pathways in the UV photodissociation of chloroethylenes is interesting. These multiple pathways include simple bond cleavage, molecular eliminations and three body dissociation processes, depending on the excitation wavelength. The competition between these various dissociation channels has been the subject of numerous experimental and theoretical studies [95-99]. On UV excitation of chloroethylenes, halogen atom formation through the C–Cl bond fission and HCl elimination are the most important photodissociation channels. The branching ratio for the C–Cl bond fission and HCl elimination varies with the excitation wavelength and the number of halogen atom. In general, the dynamics of dissociation of a molecule is closely related to the properties of the initially prepared excited state. Additional effects are also seen in chloroethylenes due to the presence of chlorine atoms, mainly due to heavy chlorine atom effect in coupling the excited state with a dissociative state. Thus, intramolecular electronic and vibrational relaxations play an important role in chloroethylenes dynamics on photoexcitation. This manifests in the yields of several products, with different energy and angular distributions. In this regard, dynamical studies of chloroethylenes are very interesting, and some studies clearly illustrate the interactions of the potential energy surfaces in the excited state [100]. Detailed knowledge of the electronic states accessed in the initial photoexcitation, and their subsequent evolution is necessary to understand fully the photodissociation mechanism.

The photochemistry of chloroethylenes, especially in UV region, has been a subject of many investigations. In this context, a large number of theoretical and experimental studies, which include UV absorption and photodissociation dynamics studies, has been reported previously [93,101-106].To cite a few, an *ab initio* study by Nakatsuji and co-workers [107] reported the excitation energies and the oscillator strengths for the electronic transitions of dichloroethylenes (cis and trans) and tetrachloroethylene. For tetrachloroethylene, they assigned a $\pi^* \leftarrow \pi$ transition around 6.41 eV (~193 nm) as the optically bright state. Similarly, the vertical excitation energies for other transitions such as, σ^*(C-Cl)$\leftarrow\pi$, σ^*(C-Cl)$\leftarrow$n, $\pi^* \leftarrow$ n are reported as 5.76 (~215 nm), 7.91 (~157 nm), and 7.28 eV (~170 nm) respectively. A recent vacuum ultraviolet (VUV) absorption study by Eden *et al.* [93] on the photoabsorption spectrum of tetrachloroethylene over the range of 325 nm to 115 nm clearly shows these transitions. They identified the first low energy structure around 6.2 eV as mainly the singlet valence $\pi^* \leftarrow \pi$ transition. The low-energy shoulder appearing around 5.34 eV was assigned as a σ^*(C-Cl)$\leftarrow\pi$ transition. In the area of photodissociation dynamics, Umemoto *et al.* [108] measured the translational energy distribution of Cl and HCl following photoexcitation of mono- and dichloroethylenes at 193 nm via the $\pi^* \leftarrow \pi$ transition. They found that HCl products were formed in large abundance in monochloroethylene (vinyl chloride), which they attributed to internal conversion (IC) to a [π,σ^*(C-Cl)] state. In dichloroethlyene, they found a second Cl product channel and suggested its origin due to dissociation via an [n,σ^*(C-Cl)] state. Similarly, Tonokura *et al.* [106] measured the translational energy distribution as well as the angular dependence of the Cl products of mono- and dichloroethylenes and found two product channels. High translational energy products were formed with a large anisotropy parameter of 1.0 and a low translational energy channel was formed with a nearly isotropic, statistical distribution. They assigned the high and low translational energy channels to electronic relaxation and dissociation from the [π,σ*(C-Cl)] state and the ground state, respectively.

Very recently, Suits and co-workers [104] have studied the photodissociation of tetrachloroethylene near 235 and 202 nm using reduced-Doppler strategy with a direct current (DC) slice imaging technique. They have reported the translational energy distributions of both the spin-orbit excited states of chlorine atom produced in the photodissociation of tetrachloroethylene. However, these distributions overshoot the available energy, indicating some contribution from multiphotonic processes.

In the present work, the photodissociation dynamics of tetrachloroethylene (TCE) at 235 nm has been investigated by detecting the photofragment chlorine atom. The chlorine atoms formed on photodissociation of TCE were state selectively ionized, and detected by time-of-flight (TOF). We observed that chlorine atoms are produced in both the ground state Cl ($^2P_{3/2}$) and the spin orbit excited state Cl* ($^2P_{1/2}$), which lies only 882.4 cm^{-1} higher in energy [109]. The translational energy distributions and recoil anisotropies of the photoproducts were extracted from TOF profiles obtained with polarized laser beam. Likewise, the electronic branching ratio, defined as distribution of the photofragment chlorine atom over its electronic states, i.e., Cl($^2P_{3/2}$) and Cl*($^2P_{1/2}$), has been also measured during the course of the experiments. The experimentally obtained dynamical information was utilized to investigate the nature of the dissociative state, and to understand the interactions in the exit channels.

4.2 Experimental

The experiment was performed, using a molecular beam time–of–flight mass spectrometer system (MB–TOF–MS), as described in chapter 2. The TCE sample (>99% purity, Aldrich) was used, without further purification. Helium was bubbled through the sample, maintained at room temperature, and the mixture was expanded through the nozzle at a stagnation pressure of 1000 Torr. It was ensured that any interference to the measurements due to cluster photofragmentation was absent, or negligible, by operating at a low stagnation pressure, and using only the rising part of the molecular beam pulse. The power dependence measurements revealed a three photon dependency, which is consistent with one-photon dissociation of tetrachloroethylene, followed by (2+1) REMPI of the chlorine atoms, assuming that the ionization step is saturated.

4.3 Experimental results

Various dynamical parameters were determined from measured REMPI spectra and TOF profiles of Cl and Cl*, detailed procedure is discussed in chapters 2 and 3.

4.3.1 Spin-orbit branching ratio

The relative quantum yields for the chlorine atom fragments, formed in different spin-orbit states, were determined by normalizing the integrated intensity of the respective (2+1) REMPI transitions with respect to the laser intensity and the ratio of the two-photon absorption coefficients. From the measured integrated intensity ratio, one can easily obtain the product ratio, using equation 3.1, in which the relative ionization probability, k was taken to be 0.85±0.10, as reported by Liyanage *et al.* [66]. The relative quantum yield, Φ(Cl) and Φ(Cl*), can be determined from the product ratio using equation 3.2. The Φ(Cl*) obtained for tetrachloroethylene dissociation is found to be 0.22±0.04. However, the Φ(Cl*) obtained for trichloroethylene dissociation is found to be 0.37±0.06 [110]. The statistical limit for relative quantum yield, Φ(Cl*), is 0.33, which is defined as the ratio of the degeneracy of Cl* ($^2P_{1/2}$) to the sum of the degeneracies of both the fine structure states Cl ($^2P_{3/2}$) and Cl* ($^2P_{1/2}$). [66]

4.3.2 Translational energy distribution and anisotropy parameter

The TOF profiles were converted to the velocity domain for the Cl and Cl* atoms, shown in FIG. 4.1 for TCE. These profiles are given for the laser polarization only at the magic angle ~54.7°, since the angular distribution is isotropic. We analyzed the TOF data, using a forward convolution procedure, as described in chapter 2. The predicted TOF profiles were calculated for the experimental configurations, convoluted with the instrumental response function and compared with the experimental TOF profiles (shown as open circles). The calculated TOF profiles are displayed by the solid curve, with each component shown by a dotted curve (FIG. 4.1). The photofragment translational energy distributions, P(E_T), determined from the data in the FIG. 4.1, for the Cl and Cl*, are depicted in FIG. 4.2. For the Cl fragment, the faster component is centered at ~18 kcal/mol, consisting of 77±5% of the total fragments. The slower component peaks at around zero consisting of the remaining 23±5%. Similarly, for the Cl* fragment, the faster component is centered at ~14 kcal/mol, consisting of 92±5% of the total fragments, while the slower component is centered at ~2.7 kcal/mol, consisting of the remaining 8±5%. Similarly, in the

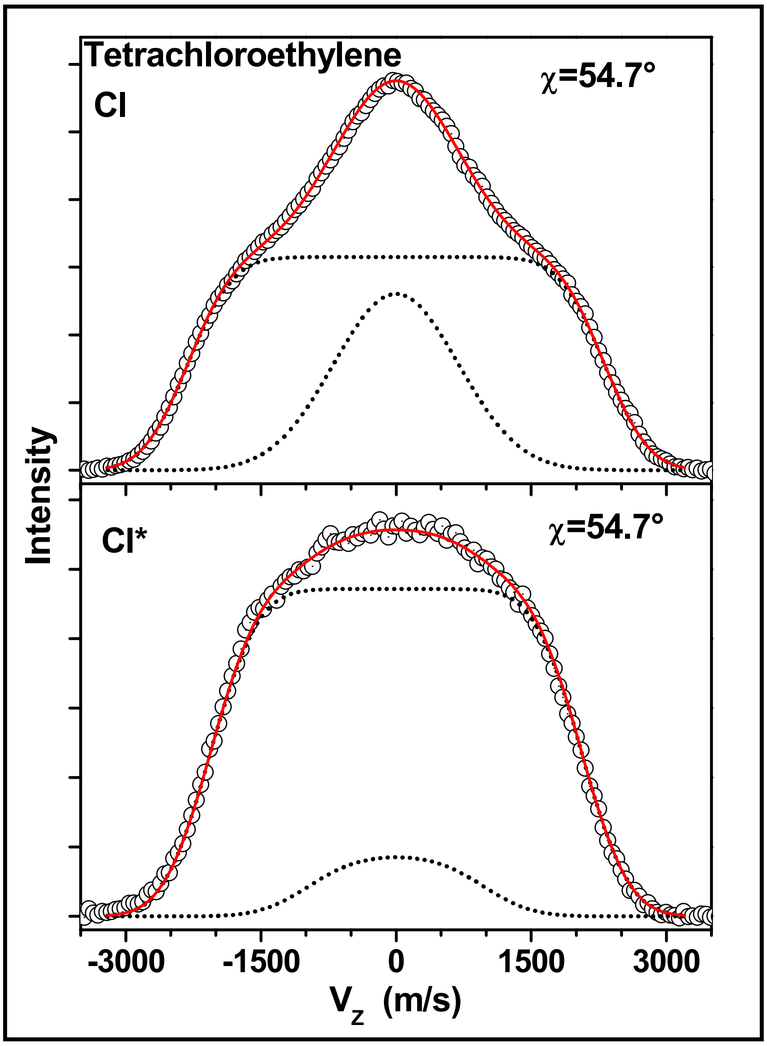

FIG. 4.1: *REMPI–TOF profiles of Cl ($^2P_{3/2}$) and Cl* ($^2P_{1/2}$) produced from the photodissociation of tetrachloroethylene at 235 nm. The circles are the experimental data, the dashed lines are forward convolution fit for two different channels and the solid red curve shows the sum.*

photolysis of trichloroethylene [110], for the Cl fragment, the faster component is centered at ~17 kcal/mol, consisting of 78±5% of the total fragments while the slower component is centered at ~2.5 kcal/mol, consisting of the remaining 22±5%. For the Cl* fragment, the faster component is centered at ~14 kcal/mol, consisting of 100±5% of the total fragments, while the slower component is absent. It was not possible to determine independently anisotropy parameters for the two components, and hence the

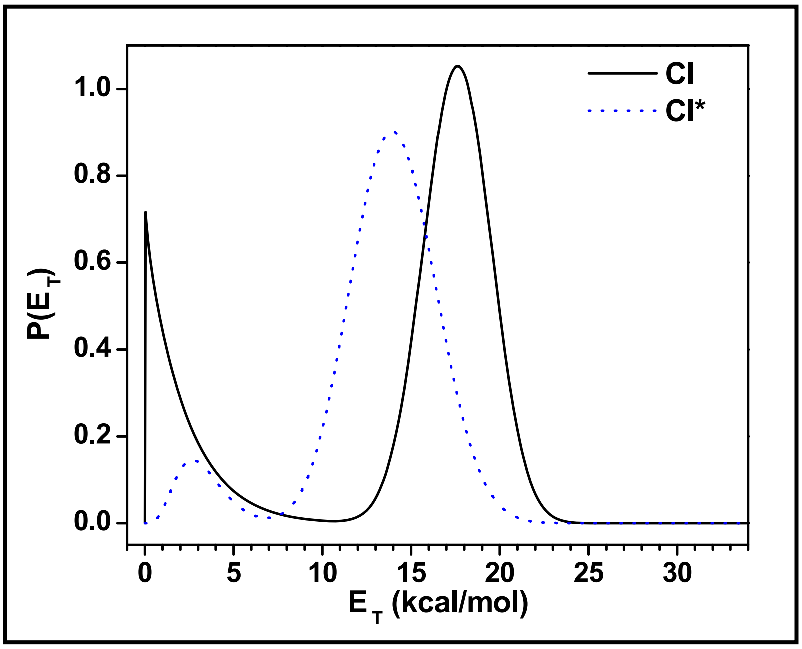

FIG. 4.2: *Photofragment center-of-mass translational energy distribution of Cl($^2P_{3/2}$) (black solid curve) and Cl*(blue dotted curve) elimination channel for the 235 nm dissociation of tetrachloroethylene.*

anisotropy was assumed to be the same for both the channels. The TOF profiles for both Cl and Cl* are independent of laser polarizations, implying the β parameter is well characterized by a value of 0.0, within the experimental uncertainties.

4.4 Discussion

4.4.1 Nature of excited states

Theoretical calculations were performed, to investigate the nature of the excited electronic states of both the chloroethylenes along with vinyl chloride. The geometry optimization for all the structures was done using Density Functional Theory (DFT) methods with MPW1PW91 correlation and exchange functionals using Gaussian suite of program [3]. The augmented correlation-consistent basis sets aug-cc-pVDZ were used for H, C, and Cl. Other higher basis sets such as aug-cc-pVTZ were also tried for geometry optimization; however, the optimized geometry using aug-cc-pVDZ was found to be closer to the experimental geometry. Hence, the basis

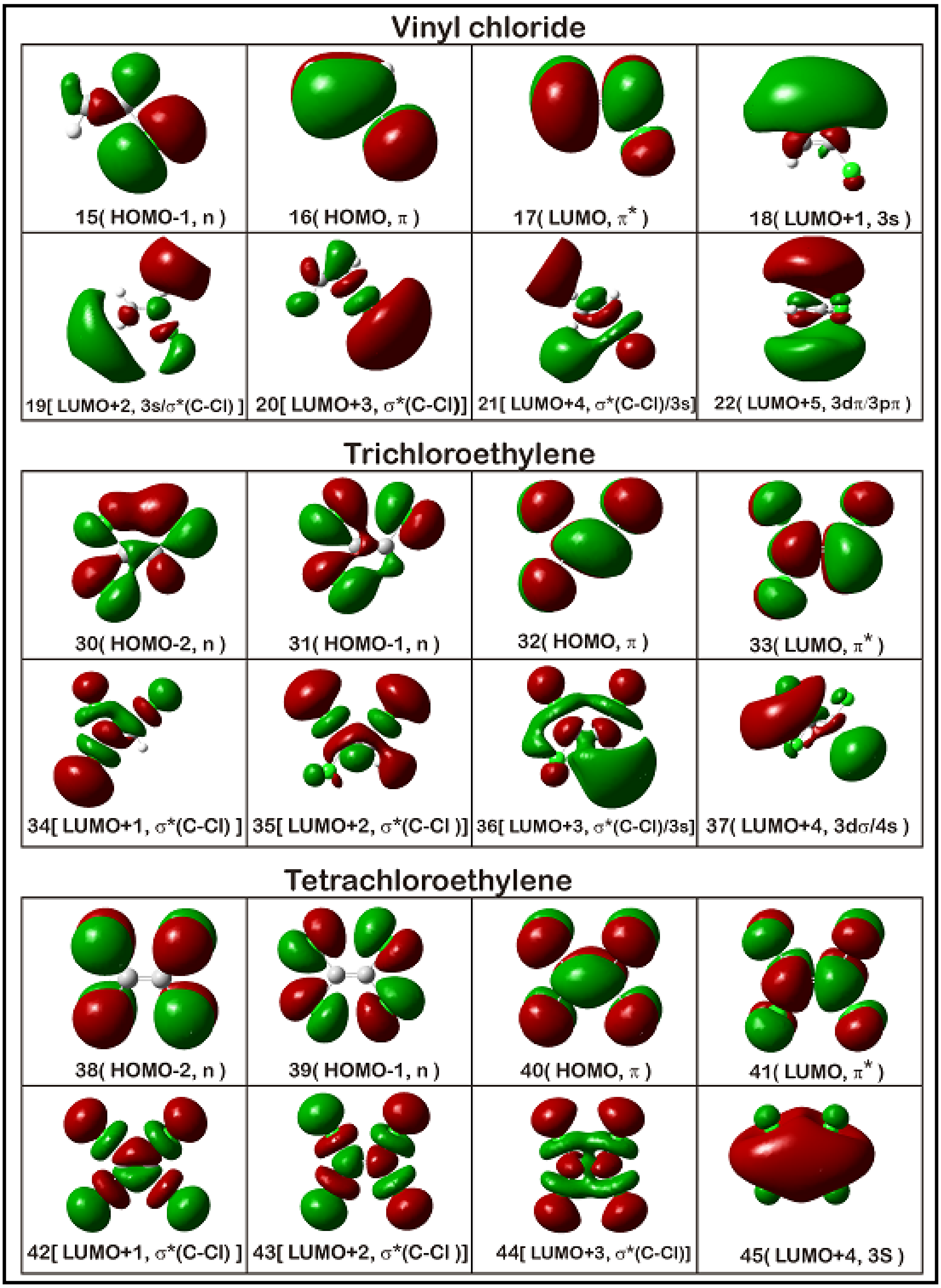

FIG. 4.3: *Computed HOMO, LUMO, along with other MOs involved in the transition of vinyl chloride, trichloroethylene and tetrachloroethylene.*

sets, aug-cc-pVDZ, were used for all the geometry optimization. Vertical excitation energies were obtained for various transitions, to understand the nature of the excited states. Although the calculated vertical excitation energies are not so accurate as compared to the experimental results, the nature of the transition and the orbitals involved are accurately predicted, using this method. The orbitals participating in the different electronic transitions were visualized for better understanding of the process, and are shown in FIG. 4.3. For determination of vertical excitation energies of various excited states, we carried out time-dependent density functional theory calculations (TD-DFT) at the UMPW1PW91/aug-cc-pVTZ level of theory. Several singlet excited states were found with significant oscillator strengths, consistent with previous studies. Theoretical calculations on all the above chloroethylenes show that the brightest state is a (π, π*) state with highest oscillator strength. Various low-lying singlet excited states along with their designation, nature of transition, and respective oscillator strengths are shown in Table 4.1 for vinyl chloride, trichloroethylene and tetrachloroethylene. In the following few paragraphs, we will now discuss the nature of these excited state potential energy surfaces (PESs) for all the three chloroethylenes studied.

For vinyl chloride in C_s symmetry, the lowest excited state is 1A″ which arises mainly from the 3s←π Rydberg transition along with a small contribution from σ*←π transition. The vertical excitation energy for this transition is calculated as 6.52 eV (190 nm) with oscillator strength of 0.0103. The next excited state is 2A′ which arises from a π*←π transition at 6.60 eV (188 nm) with oscillator strength of 0.2506. The π*←n transition is termed as 3A″, which is the fourth excited state and its vertical excitation energy is 6.96 eV (178 nm) with oscillator strength of 0.0006. Similarly, the seventh excited state, which is a σ*(C-Cl)←n transition, is termed as 3A′. The vertical excitation energy for this transition is calculated as 7.94 eV (156 nm) with oscillator

Table 4.1: *Vertical excitation energies in eV and in nm with their respective oscillator strengths (given in parentheses) of various low-lying singlet states along with symmetry designation and nature of transition for vinyl chloride, trichloroethylene and tetrachloroethylene. The point group symmetry for vinyl chloride and trichloroethylene is* C_s *while that for tetrachloroethylene is* D_{2h}.

	Vinyl chloride		Trichloroethylene		Tetrachloroethylene	
	State designation and nature of Transition	Vertical excitation energy with oscillator strength (in parenthesis)	State designation and nature of Transition	Vertical excitation energy with oscillator strength (in parenthesis)	State designation and nature of Transition	Vertical excitation energy with oscillator strength (in parenthesis)
1	$1A''$ 18, 21 ← 16 3s/σ*(C-Cl) ← π	6.52 eV, 190 nm (0.0103)	$1A''$ 34, 35 ← 32 σ*(C-Cl) ← π	5.58 eV, 222 nm (~0)	$1\ {}^1B_{1g}$ 42 ← 40 σ*(C-Cl) ← π	5.20 eV, 238 nm (~0)
2	$2A'$ 17 ← 16 π*←π	6.60 eV, 188 nm (0.2506)	$2A''$ 34, 35, 36 ← 32 σ*(C-Cl)/3s ← π	5.74 eV, 216 nm (0.0003)	$1\ {}^1B_{2g}$ 43 ← 40 σ*(C-Cl) ← π	5.64 eV, 220 nm (~0)
3	$2A''$ 20, 21← 16 σ*(C-Cl)/3s ← π	6.69 eV, 185 nm (0.0001)	$2A'$ 33 ← 32 π*←π	5.98 eV, 207 nm (0.3125)	$1\ {}^1B_{3u}$ 44 ← 40 σ*(C-Cl) ← π	5.65 eV, 220 nm (0.0005)
4	$3A''$ 17 ← 15 π*←n	6.96 eV, 178 nm (0.0006)	$3A''$ 36 ← 32 3s/σ*(C-Cl) ← π	6.34 eV, 195 nm (0.0042)	$1\ {}^1B_{1u}$ 41 ← 40 π*←π	5.83 eV, 213 nm (0.3669)
5	$4A''$ 19, 20, 21 ← 16 3s/σ*(C-Cl) ← π	7.07 eV, 175 nm (0.0011)	$4A''$ 33 ← 31 π*←n	6.72 eV, 185 nm (0.0001)	$2\ {}^1B_{1g}$ 41 ← 39 π*←n	6.33 eV, 196 nm (~0)
6	$5A''$ 21 ← 16 σ*(C-Cl)/3s ← π	7.30 eV, 170 nm (0.0137)	$5A''$ 37 ← 32 3s/σ*(C-Cl) ← π	7.02 eV, 177 nm (0.0158)	$2\ {}^1B_{3u}$ 45 ← 40 3s ← π	6.48 eV, 191 nm (0.0312)
7	$3A'$ 20, 21 ← 15 σ*(C-Cl) ← n	7.94 eV, 156 nm (0.0049)	# $3A'$ 34 ← 31 σ*(C-Cl) ← n	7.36 eV, 169 nm (0.0030)	$2\ {}^1B_{1u}$ 42 ← 39 σ*(C-Cl) ← n	7.01 eV, 177 nm (0.0179)

This state is ninth excited state for trichloroethylene. The seventh and eighth states are $6A''$ (π*←n) and $7A''$ [σ*(C-Cl)/4s←π] at 7.09 eV and 7.31 eV respectively, with the same oscillator strength of 0.0004.

strength of 0.0049. The above discussion clearly shows that the brightest state is a (π, π*) state. Also, the (n, π*) and (n, σ*) states lie much above the (π, π*) and [π, σ*(C-Cl)] states in the Franck-Condon region.

Similar to vinyl chloride, trichloroethylene also belongs to the C_s symmetry and the lowest excited state for this molecule is 1A″, which arises mainly from the σ*(C-Cl)←π transition. The vertical excitation energy for this transition is calculated as 5.58 eV (222 nm) with non-existent oscillator strength. The next excited state is 2A″ which arises mainly from the σ*(C-Cl)←π transition along with a small contribution from 3s←π Rydberg transition. The vertical excitation energy for this transition is calculated as 5.74 eV (216 nm) with the oscillator strength of 0.0003. The next excited state is 2A′, which arises exclusively from a π*←π transition at 5.98 eV (188 nm) with the oscillator strength of 0.3125. Similar to vinyl chloride, we found two states which arise mainly from 3s←π Rydberg transition along with a small contribution from σ*(C-Cl)←π transition. These states, namely, 3A″ and 5A″ are fourth and sixth excited state, respectively. The vertical excitation energies for these transitions are calculated as 6.34 eV (195 nm) and 7.02 eV (177 nm) with oscillator strengths of 0.0042 and 0.0158, respectively. The π*←n transition is termed as 4A″, which is fifth excited state and its vertical excitation energy is 6.72 eV (185 nm) with the oscillator strength of 0.0001. Similarly, the ninth excited state, which is a σ*(C-Cl)←n transition, is termed as 3A′. The vertical excitation energy for this transition is calculated as 7.36 eV (169 nm) with the oscillator strength of 0.0030. Similar to vinyl chloride, the brightest state in trichloroethylene is a (π, π*) state. Also, the (n, π*) and (n, σ*) states lie much above the (π, π*) and [π, σ*(C-Cl)] states in the Franck-Condon region.

Tetrachloroethylene belongs to D_{2h} symmetry and the lowest excited state for this molecule in this symmetry is $1\,^1\mathrm{B}_{1g}$, which arises mainly from a σ*(C-Cl)← π transition. The vertical excitation energy is calculated as 5.20 eV (238 nm) with non-existent oscillator strength. Similarly, the second excited state is termed as $1\,^1B_{2g}$, which also arises from a σ*(C-Cl)← π transition at 5.64 eV (220 nm) with missing oscillator strength. The third excited state also arises from a σ*(C-Cl)← π transition, which is termed as $1\,^1B_{3u}$ at 5.65 eV (220 nm). However, the oscillator strength for this transition is a non-zero value of 0.0005. The fourth excited state is termed as $1\,^1B_{1u}$ at 5.83 eV (213 nm) with an oscillator strength of 0.3669. This state arises mainly from a π*←π transition. The vertical excitation energy for π*←n transition in tetrachloroethylene is calculated as 6.33 eV (196 nm) with non-existent oscillator strength. This transition is fifth in series and termed as $2\,^1B_{1g}$. Similarly, for σ*(C-Cl)←n transition, the vertical excitation energy is calculated as 7.01 eV (177 nm) with relatively higher oscillator strength of 0.0179. This state is termed as $2\,^1B_{1u}$ and seventh in series.

Considering the corresponding wavelengths for vertical excitation energies and the respective oscillator strengths of the various transitions, it is evident that at 235 nm excitation, both trichloroethylene and tetrachloroethylene have a σ*(C-Cl)← π transition. At 235 nm, vinyl chloride does not absorb. Similarly, at 193 nm, all chloroethylenes have a π*←π transition. Since the excited (π, π*) state correlates only with highly excited photoproducts, which is not feasible in a single photon excitation in the present case, it is assumed that, in the above two compounds, the initially prepared (π, π*) states cross over to the nearby states, mostly (π, σ*) state and probably [π, σ*(C-Cl)] state to produce Cl atoms involving the C–Cl bond cleavages. Also, the initially prepared (π, π*) or [π, σ*(C-Cl)] state can undergo rapid internal conversion to the ground state, from where various other dissociation channels can occur, in addition to the above mentioned pathways. Details will be discussed *vide infra*.

4.4.2 Translational energy release and anisotropy parameter

The initial photodissociation process in tetrachloroethylene, with the absorption of one photon at 235 nm, is the generation of Cl atom as a primary product (reaction 4.1).

$$Cl_2C{=}CCl_2 \rightarrow Cl_2C{=}CCl + Cl \qquad \Delta H{=}90\ kcal/mol \qquad (4.1)$$

The chlorine atom can also be generated in secondary reactions (4.2-4.4) from the primary photoproduct $Cl_2C{=}CCl$ with subsequent absorption of another photon,

$$Cl_2C{=}CCl_2 \rightarrow Cl_2C{=}CCl + Cl \rightarrow ClC{\equiv}CCl + Cl + Cl \qquad \Delta H{=}119\ kcal/mol \qquad (4.2)$$

$$\rightarrow Cl_2C{=}CCl + Cl \rightarrow {}^3[Cl_2C{=}C{:}] + Cl + Cl \qquad \Delta H{=}198\ kcal/mol \qquad (4.3)$$

$$\rightarrow Cl_2C{=}CCl + Cl \rightarrow {}^1[Cl_2C{=}C{:}] + Cl + Cl \qquad \Delta H{=}165\ kcal/mol \qquad (4.4)$$

The heat of formation values for above reactions (4.1-4.4) are calculated at G3B3 level of theory using Gaussian suite of package [3].

The calculated ΔH values for all these reactions suggest that only reactions 4.1 & 4.2 are accessible by one photon absorption (122 kcal/mol). Although the reaction 4.2 is feasible energetically, the translational energy release in the Cl formation process will be negligible. However, other channels (reactions 4.3 & 4.4) can be initiated by multiphotonic processes. As discussed earlier, the power dependencies studies suggest single photon dissociation of chloroethylenes. So, the possibilities of reaction channels (4.4-4.6), in our present experimental conditions of monophotonic excitation, are ruled out energetically.

The partitioning of the available energy into various degrees of freedom of the fragments is mainly governed by the nature of the dissociative potential energy surface. As discussed in earlier section, the transition at 235 nm for tri- and tetrachloroethylene is σ*(C-Cl)←π in nature. It is understood that the energy partitioning for a dissociative event on a repulsive surface is well described by an impulsive model. Therefore, we have used an impulsive model [26], to calculate theoretically the translational energy released to the products of reaction 4.1. By using only conservation of momentum and energy, and the impulse assumption, one finds that the fraction of the available energy released as translational energy, E_T/E_{avl} (f_T), is given by

$$f_T = \frac{E_T}{E_{avl}} = \left(\frac{\mu_{C-Cl}}{\mu_{Cl_2C=CCl-Cl}} \right), \tag{4.5}$$

where μ_{C-Cl} is the reduced mass of the C and Cl atoms, $\mu_{Cl_2C=CCl\text{-}Cl}$ is the reduced mass of the $Cl_2C{=}CCl$ and Cl, and E_{avl} is the available energy. The f_T values in the case of tetrachloroethylene and trichloroethylene are calculated to be 0.32 and 0.35, respectively.

The available energy is estimated by,

$$E_{avl} = E_{h\nu} - D_0^0(Cl_2C{=}CCl{-}Cl) - E_{SO}, \tag{4.6}$$

where $E_{h\nu}$ is the photon energy (122 kcal/mol), $D_0^0(Cl_2C{=}C{-}Cl)$ is the C–Cl bond dissociation energy (90 kcal/mol), and E_{SO} is the spin–orbit energy of chlorine (2.4 kcal/mol). The internal energy of tetrachloroethylene is ignored as it is ~0 kcal/mol, for supersonically cooled sample. Thus, E_{avl} for the Cl and Cl* channels are 32.0 and 29.6 kcal/mol, respectively.

For tetrachloroethylene, the experimental average translational energy for the fast component is found to 17.6±1.9 and 14.0±1.7 kcal/mol, for Cl and Cl*, respectively, giving the corresponding f_T values of 0.55 and 0.47. These experimental

f_T values for Cl and Cl* are higher than that of value predicted by the impulsive model (0.32). Similar to tetrachloroethylene, the experimental f_T values for Cl and Cl* in trichloroethylene photolysis are found to be 0.52 and 0.47, respectively. In the present case, the experimental f_T value is comparatively higher than the value predicted using impulsive model. In another photolysis study of tetrachloroethylene, at 235 nm, using DC slicing imaging technique by Suits and co-workers [104], the experimental translational energies for Cl and Cl* are estimated to be 14.0 and 14.5 kcal/mol, respectively. In the same work, at 202 nm photolysis, the translational energy is estimated to be 13.8 and 15.7 kcal/mol for Cl and Cl* channels, respectively. The E_{avl} at 235 nm and 202 nm is 32 and 52 kcal/mol, respectively. The data on 235 nm and 202 nm photolysis of tetrachloroethylene clearly show that the translational energy released in the Cl elimination channel is almost identical, irrespective of a huge difference in the E_{avl}. A similar trend has been observed in the photolysis of trichloroethylene also. In our photolysis study of trichloroethylene at 235 nm [110], the translational energy released is estimated as 16.7±2.0 and 13.9±1.5 kcal/mol, for the Cl and Cl* channels, respectively. In separate studies at 193 nm photolysis of trichloroethylene, the average translational energy released into the Cl atom formation channel was estimated as, 19.4 kcal/mol [98] and 16.6 kcal/mol [111]. In trichloroethylene also, we can see that the increase in the E_{avl} energy has almost no effect on the translational energy released into the photofragments for the Cl atom formation channel. In other words, the amount of translational energy released is almost constant irrespective of the excitation wavelength or the available energy. This kind of behavior in translational energy release in any photodissociation process is typically for a dissociation process with an exit barrier. The above discussion on ineffectiveness of extra E_{avl} on the amount of translational energy released into the photofragments prompted us to think that there might be an exit barrier on the excited state PES. To further investigate this issue, we have mapped the potential energy (PE) curves for various excited states for the Cl atom elimination channel for three chloroethylenes, namely, vinyl chloride, trichloroethylene and tetrachloroethylene, using ab initio methods. The PE curves of various excited states along the C–Cl bond length were calculated. For this purpose, single point TD-DFT calculations on different C–Cl bond lengths were performed at UMPW1PW91/aug-cc-pVTZ level with all other internal coordinates kept at the ground-state values, which were optimized at UMPW1PW91/aug-cc-pVDZ level. For this purpose, the C–Cl bond lengths were varied from 1.7Å to 3.8Å, which is asymptote to its dissociation limit. The sanity of the present theoretical method adopted in this context is confirmed by comparing our results with that of Nakatsuji and co-workers [112] on vinyl chloride, carried out using symmetry-adapted cluster configuration interaction theory (SAC-CI). FIG. 4.4 shows various PESs, such as [π, σ*(C-Cl)], (π, π*), [n, σ*(C-Cl)], (n, π*) and for vinyl chloride. From this figure, we can easily see that the reported features of various PESs by Nakatsuji and co-workers are well reproduced using our computational method. So, we strongly believe that the present method can also accurately describe the Cl atom elimination channels in other chloroethylenes. Hence, we have applied this method to study the Cl atom elimination channel for trichloroethylene and tetrachloroethylene. PE curves for these chloroethylenes based on our calculations are shown in FIG. 4.5. These calculations on all the three chloroethylenes reveal that the (π, π*) state is a bound state, which correlates with the products in a higher electronic state. Similarly, the (n, π*) state is a bound state,

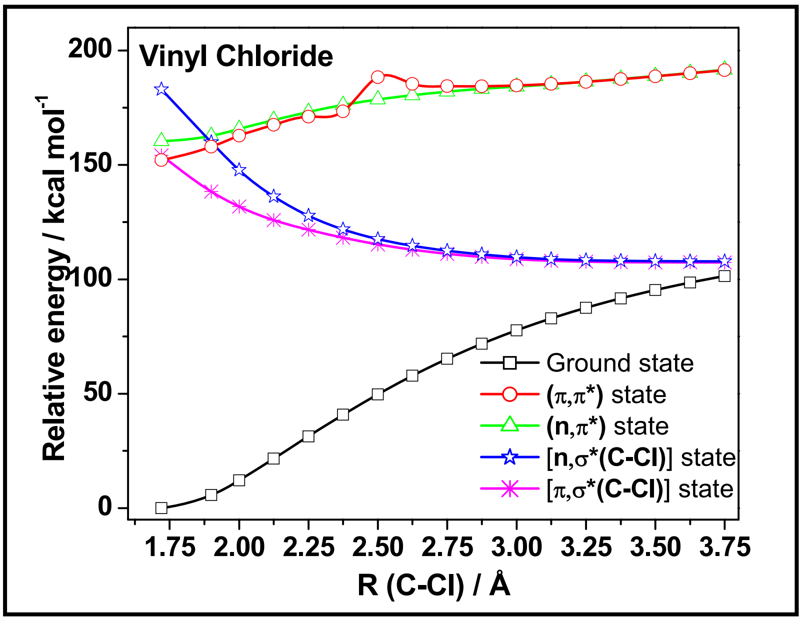

FIG. 4.4: *Various diabatic PESs calculated for vinyl chloride along the C–Cl bond.*

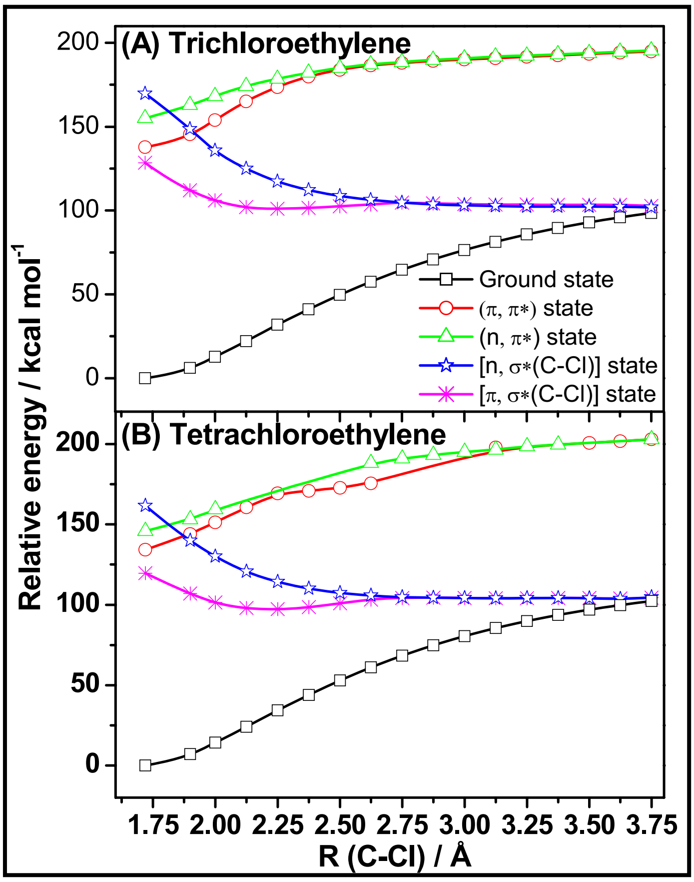

FIG. 4.5: *Various diabatic PESs calculated for (A) Trichloroethylene and (B) Tetrachloroethylene along the C–Cl bond.*

whereas the [n, σ*(C-Cl)] state is a repulsive state in all three chloroethylenes studied. The major interesting finding of our calculations is prediction of the bound nature of the [π, σ*(C-Cl)] state in both trichloroethylene and tetrachloroethylene, but purely repulsive in vinyl chloride. This comparison of PE curves for [π, σ*(C-Cl)] in three chloroethylenes can be seen in FIG. 4.6. The depth of the potential energy surface of the [π, σ*(C-Cl)] state is greater in tetrachloroethylene as compared to trichloroethylene. These results will be discussed further *vide infra*.

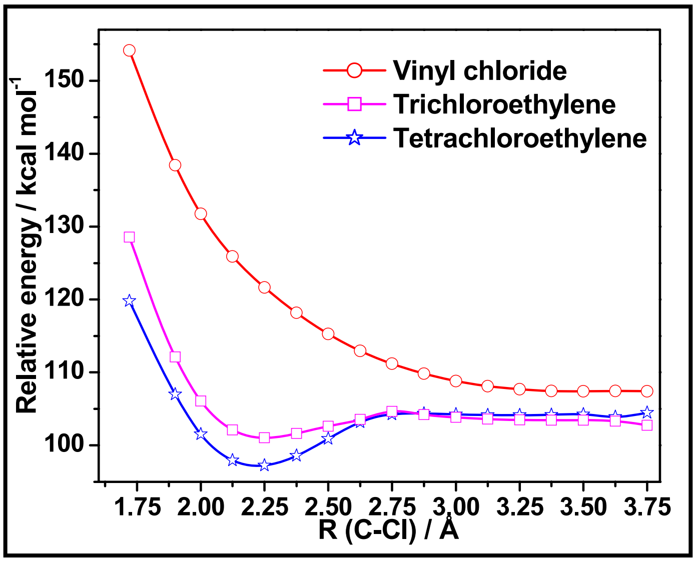

FIG. 4.6: *The diabatic PESs for the [π, σ*(C-Cl)] state involved in vinyl chloride, trichloroethylene and tetrachloroethylene.*

Now focusing on the slow component in the translational energy distribution, the average energies calculated are found to be 2.2±1.0 and 3.2±1.0 kcal/mol, with corresponding f_T values of 0.07 and 0.11 for Cl and Cl* channels, respectively. A statistical model has been used to understand the slow component of the translational energy distribution. A statistical dissociation process occurs predominantly, if the excess energy is partitioned statistically amongst the available degrees of freedom of the products. This is possible when a rapid internal conversion occurs to the long-lived ground electronic state, from which, subsequently, dissociation takes place without a barrier. A simple analytical expression, established by Klots [25], relating the mean translational energy release, E_T, and the E_{avl}, for a statistical barrierless dissociation process, is given as

$$E_{avl} = \frac{(r-1)}{2} E_T + E_T + \sum_i \frac{hv_i}{\exp(hv_i / E_T) - 1} \tag{4.7}$$

where r is the number of the rotational degrees of freedom, and $h\nu_i$ are the vibrational frequencies of the $Cl_2C{=}CCl$ product. In the present case of statistical calculation, the value E_T/E_{avl} comes out to be 1/11, i.e., ~0.09. Our measured E_T/E_{avl} values for slow components of Cl (0.07) and Cl* (0.11) are well described by the statistical model within the experimental uncertainty.

In the limit of an instantaneous dissociation process, the anisotropy parameter, β, is given by $\beta = 2\langle P_2(\cos\theta_m)\rangle$, where θ_m is the molecular frame angle between the molecular transition dipole moment and the photofragment recoil direction, and $P_2(\cos\theta_m)$ is the second order Legendre polynomial. Hence, for a parallel or a perpendicular transition, one would expect anisotropy of +2 or -1, respectively. The anisotropy measured in the present work is ~0.0, which indicates an isotropic dissociation process. Generally, an impulsive dissociation is accompanied with an anisotropic distribution of the photoproducts, since the dissociation lifetime is much shorter than the rotation period of the molecule. However, the anisotropy in an impulsive dissociation can be reduced or wiped out, due to several factors, such as mixed initial transition with parallel and perpendicular components, longer dissociation lifetime, dissociation not from a single geometry rather from a range of geometries etc. [75,113] The absence of recoil anisotropy in the present study is expected mainly due to the relatively longer dissociation lifetime, since the dissociation is from the bound [π, σ*(C-Cl)] state and the ground state for fast and slow component of chlorine atom, respectively, in case of trichloroethylene and tetrachloroethylene.

4.4.3 Mechanism of the dissociation process

We shall now present a complete picture of the dissociation process in the light of the above discussion in conjunction with the dynamics models for energy partitioning and the PESs calculation with the help of *ab initio* method. The TD-DFT calculation and the absorption spectra clearly show that the excitation of tri- and tetrachloroethylenes at 235 nm leads to the σ*(C-Cl)←π transition and not the π*←π transition. The σ*←π transition involves the initial excitation of the electron from the π orbital of the C=C double bond into the C–Cl antibonding orbital, resulting in the cleavage of the C–Cl bond. This process of the impulsive C–Cl bond cleavage leading to the formation of fast Cl atoms, allows with little internal excitation of the co-product. Thus, a sharp peak in the translational energy distribution is created as observed by Suits and co-workers [104] in case of tetrachloroethylene. At 235 nm photolysis of tetrachloroethylene, the f_T values for Cl and Cl* are estimated as 0.55 and 0.47, respectively. Similarly, in trichloroethylene photolysis the values are found to be 0.52 and 0.47 for Cl and Cl*, respectively. In both the cases, the experimental f_T values are comparatively higher than that of the value predicted using the impulsive model. Also, the anisotropy parameter for Cl atom formation channel in these chloroethylenes is nearly ~0.0. These results are in contrast to the results obtained in the photodissociation of vinyl chloride at 193 nm. These results on tri- and tetrachloroethylene are already explained in the light of the bound [π, σ*(C-Cl)] state in the earlier section. At 235 nm, these chloroethylenes are directly excited to the [π, σ*(C-Cl)] state and subsequently the dissociation process proceeds on the same PES with the formation of Cl atoms with large amount of translational energy. The bound nature of the [π, σ*(C-Cl)] state in both of these chloroethylenes is mainly responsible for the near zero anisotropy parameter as well a high translational energy release into the photofragments. At 235 nm photoexcitation, there is no cross-over from the initial [π, σ*(C-Cl)] state to any other repulsive state, such a [n, σ*(C-Cl)], near the Frank-Condon region. However, at longer C–Cl bond distance this type of cross-over may be possible; but again, this is ruled out in the light of PES calculation using TD-DFT methods as discussed earlier.

At 193 nm photolysis, the TD-DFT calculation on vertical excitation energies, their respective oscillator strengths and the absorption spectra clearly show that the initial excitation for all these chloroethylenes is mainly a π*←π transition. However, a small contribution from the σ*(C-Cl)←π transition is always present. In the absorption spectrum of vinyl chloride (VC), the shoulder due to the σ*(C-Cl)←π transition is not seen, although, it is clearly seen in that of tri- and tetrachloroethylene. This difference in absorption spectra is mainly attributed to the separation of the peaks due to σ*(C-Cl)←π and π*←π transition (Table 4.1). The separation for these two transitions for vinyl chloride is within 2 nm while that for tri- and tetrachloroethylene is almost 10 nm. Once these chloroethylenes are excited to the (π, π*) state, which is bound in nature, dissociation will occur from a lower-lying cross-over state which may be either a repulsive excited state or the ground state. If the crossing to a repulsive state happens in the vicinity of Franck-Condon region, the dynamics of dissociation will be just like a direct excitation to a repulsive state and most of the available energy will be partitioned into the translational degree of freedom. Therefore at 193 nm photoexcitation, the crossing between the (π, π*) state and the repulsive state is believed to be at much lower energy than the Franck-Condon region. In most of the studies of chloroethylenes, the lower lying repulsive excited state is thought to be the [π, σ*(C-Cl)] state, which is mainly responsible for high translation energy fragments. Using comparison with unsubstituted ethylene, the initial motion of the (π, π*) state is mostly expected to be in the C=C twisting and C=C stretching modes. However, the C=C twisting motion plays a crucial role in the dynamics, since it breaks the plane of symmetry and induces the coupling between the A′(π, π*) and A″[π, σ*(C-Cl)] states. Hence, the interaction between the (π, π*) state and the [π, σ*(C-Cl)] state increases along the out-of-plane coordinates. This coupling causes a highly efficient internal conversion from the initially pumped (π, π*) state to the low-lying [π, σ*(C-Cl)] states. Since the coupling of the (π, π*) state is allowed with the [n, σ*(C-Cl)] state in the twisted geometry, the repulsive [n, σ*(C-Cl)] state formed from cross-over, can also be associated with formation of high translational energy Cl atom fragment. However, based on our calculations, origin of the fast Cl atom fragment from the [n, σ*(C-Cl)] state is ruled out. Our TD-DFT calculations clearly show that the crossing point to the [n, σ*(C-Cl)] state lies far above the (π, π*) state in the Frank-Condon region. Neither the 193 nm (6.4 eV) nor 235 nm (5.3 eV) photoexcitation energy is sufficient to reach the crossing point of the (π, π*) and [n, σ*(C-Cl)] states. Thus, the [π, σ*(C-Cl)] state is solely responsible for the fast Cl atom elimination channel. These calculations are validated by the value of the β parameter, which is measured to be nearly zero, and is in line with the bound nature of [π, σ*(C-Cl)] state as explained in the earlier section. Moreover, the involvement of purely repulsive [n, σ*(C-Cl)] state should have given a non-zero value for the anisotropy parameter, whereas, the anisotropy parameter for tri- and tetrachloroethylene photolysis at 193 nm as well at 235 nm is almost zero. Unlike in tri- and tetrachloroethylenes, the [π, σ*(C-Cl)] state in vinyl chloride is repulsive in nature. Hence, the dissociation process in vinyl chloride has a non-zero value for anisotropy parameter, as expected. Also, work by Suits and co-workers [104] and our PES calculations for the C-Cl bond stretching clearly show that the coupling between (π, π*) and [n, σ*(C-Cl)] states create a barrier that is too large for either tri- or tetrachloroethylene to dissociate via the [n, σ*(C-Cl)] surface (see FIG. 4.5). With this discussion, we conclude that the dissociation is solely on the [π, σ*(C-Cl)] surface for all the chloroethylenes both at 235 nm and 193 nm photoexcitation. The remaining lower energy component is mainly due to internal conversion from the [π, σ*(C-Cl)] state to the ground state that dissociates statistically.

Another finding in the present theoretical study is about the relative depth of the bound [π, σ*(C-Cl)] states in tri- and tetrachloroethylenes. As seen in Fig. 4.6, the depth in the potential energy surface of the [π, σ*(C-Cl)] state is greater in tetrachloroethylene than that in trichloroethylene. The relative stability of this state can be explained considering the electronegative inductive effect of additional chlorine atoms. Both the (π, π*) and [π, σ*(C-Cl)] states are relatively more stabilized going from vinyl chloride to tri- and tetrachloroethylenes due to increasing inductive effect from increasing number of Cl atoms. Hence, the (π, π*) and [π, σ*(C-Cl)] states are lower in energy in tetrachloroethylene compared to that in trichloroethylene and vinyl chloride. Similarly, the stability of the chloroethylene radicals formed after the C-Cl bond cleavage can be explained with the help of this inductive effect. The relative depth of potential in the [π, σ*(C-Cl)] state can explain the measured ratio for the slow to fast chlorine atom. Since, the depth in [π, σ*(C-Cl)] PES of tetrachloroethylene is greater, the relative probability for internal conversion to the ground state is higher as compared to that in trichloroethylene resulting in the greater ratio of slow to fast chlorine atom in tetrachloroethylene. This proposition was confirmed experimentally. At 235 nm photolysis, the ratio of slow to fast chlorine atom, $Cl(^2P_{3/2})$, is determined to be 0.28 and 0.30 for tri- and tetrachloroethylene respectively. Similarly, for $Cl^*(^2P_{1/2})$, the corresponding ratio is found to be 0.01 and 0.08 for tri- and tetrachloroethylene. However, at 193 nm photoexcitation, the ratio of the fast and slow Cl atom may be slightly different, as the initial excited state is a (π, π*) state, and the internal conversion may occur from the initially prepared (π, π*) state as well.

4.5 Conclusions

The dynamics of the C–Cl bond dissociation in the photoexcitation of tetrachloroethylene has been studied at 235 nm using resonance-enhanced multiphoton ionization, coupled with a time-of-flight mass spectrometer. The excitation at 235 nm prepares the molecule in the [π, σ*(C-Cl)] state. We have determined the photofragment speed distribution, the anisotropy parameter, β, and the spin-orbit branching ratio, for chlorine atom elimination channels, to gain insights into dynamics of chlorine atom formation. Polarization-dependent and state-specific TOF profiles are utilized to get translational energy distributions, using a forward convolution method, taking into account the fragment anisotropies. The anisotropy parameters for both Cl and Cl* are the same, and equal to 0.0 ± 0.05. Bimodal nature of the relative translational energy distributions (E_T) for Cl and Cl* atoms, resulting from different potential energy surfaces, is observed in the dissociation process. The average translational energies for the Cl and Cl* channels for the fast component are 17.6±1.9 and 14.0±1.7 kcal/mol, while that for the slow component are 2.2±1.0 and 3.2±1.0 kcal/mol, respectively. Detailed theoretical calculations are performed using Time-dependent Density Functional Theory (TD-DFT) to understand the nature of the dissociative potential energy surface involved in the chlorine atom formation channel. In this article, we report the first theoretical study on the bound nature of the [π, σ*(C-Cl)] state in these chloroethylenes. Finally, we conclude that the high translational energy component of the chlorine atom formation is solely on the [π, σ*(C-Cl)] surface, for all the chloroethylenes both at 235 nm and 193 nm photoexcitation. The lower energy component is mainly due to internal conversion from the [π, σ*(C-Cl)] state to the ground state, that dissociates statistically.

CHAPTER 5

Photodissociation dynamics of 2-furoyl chloride and benzoyl chloride at 235 nm

5.1 Introduction

Photochemistry of acyl halides, particularly α,β-unsaturated compounds, has received considerable attention because of fundamental understanding and their importance in the medical, biological and environmental sciences. The α,β-acyl halides are building blocks for further functionalization by various reactions in organic chemistry. Oxygen-containing cyclic molecules, in general, are expected to be important combustion intermediates due to the heavy use of oxygenated fuel additives in gasoline in recent years [114]. These compounds have a widespread natural occurrence and roles in several areas such as air pollution, petroleum refining, and coal liquefaction and gasification processes. It is, therefore, of interest to study various reactions, particularly dissociation, involving these compounds. Moreover, α,β-acyl halides are potential source of halogen atoms after dissociation, and thus can have an impact on ozone depletion. They fall under the category of asymmetrically substituted carbonyl compounds. But, unlike aldehydes and ketones, these do not follow the well-known Norrish type I reactions, which lead to the preferential cleavage of the weaker of the two α C-C bonds to the carbonyl group. The weaker α C-C bond is preferentially cleaved in asymmetrically substituted ketones, as a result of rapid internal vibrational redistribution. This statistical dissociation behavior is not observed in acyl chlorides, their dissociation is dominated by the C–Cl bond rupture in gas phase, with a feature of non-statistical dissociation. Acetyl chloride, one of the simplest acyl halides, has been used extensively as a prototype for the photochemistry studies. The photodissociation of acetyl chloride at 248 nm [69,115,116]leads to the highly anisotropic angular distributions of Cl atoms. To explain the observation of the selective fission of the C–Cl bond over the nearly equivalent C–C bond in acetyl chloride, it is proposed that the C–Cl bond rupture is via the diabatic interaction between the ^{1}[n(O), π*(CO)] and ^{1}[n(Cl), σ*(C–Cl)] potential energy surfaces. Similar studies have been reported on its higher homologue, propionyl chloride (H_3CCH_2COCl) [117].

Photodissociation dynamics of α,β-unsaturated acyl halides has also been reported in literature. Acryloyl chloride ($H_2C{=}CHCOCl$), the simplest α,β-unsaturated acyl chloride, has been investigated both experimentally, on IR excitation from the ground electronic state [118] and UV excitation [119], and theoretically [120] in detail. It was suggested that the excitation of acryloyl chloride at 199 nm initially leads to a pre-dissociative state, from which the various dissociation channels were possible, and thus photodissociation did not proceed through a single direct dissociation mechanism. Photodissociation reactivity of acryloyl chloride was found to be different from its corresponding aldehyde ($H_2C{=}CHCHO$) and carboxylic acid ($H_2C{=}CHCOOH$) [120].

In general, the relaxation dynamics and the dissociation mechanism of an electronically excited aromatic carbonyl compound are different from that of an aliphatic carbonyl compound, because of a strong interaction between the aromatic ring and the carbonyl group [121]. This interaction affects the relative energies and reactivity of the (n,π*) and (π,π*) states of a carbonyl compound. In the present work, we have investigated photodissociation dynamics of 2-furoyl chloride and benzoyl chloride, a 5- and 6-membered aromatic compound, respectively on excitation at 235 nm, and compared the dynamics with that of similar α,β-unsaturated carbonyl chlorides, and other aliphatic acyl chlorides. We have detected the Cl fragment, in both the ground Cl($^2P_{3/2}$) and the spin-orbit excited Cl*($^2P_{1/2}$) states, employing resonance-enhanced multiphoton ionization on excitation of both the acyl chlorides. Each channel showed a bimodal velocity distribution of the Cl fragment, with an isotropic angular distribution. However, the HCl molecular product has been observed only in benzoyl chloride. We have focused on the dissociation mechanism of 2-furoyl chloride and benzoyl chloride to understand the dynamics of Cl and HCl generation.

5.2 Experimental

The photodissociation dynamics of 2-furoyl chloride and benzoyl chloride has been studied in a molecular beam (MB), using resonance-enhanced multiphoton ionization (REMPI) with time-of-flight (TOF) mass spectrometer, and the photoproducts Cl(3P $^2P_{3/2}$), Cl*(3P $^2P_{1/2}$) and HCl detected state-selectively. The experimental set-up has been discussed in detail in the experimental section of the thesis (Chapter 2). Briefly, a pulsed molecular beam of 2-furoyl chloride or benzoyl chloride (~5%) in He was generated, employing a solenoid valve (General valve), with 800 μm nozzle and 500 μs opening time, and a conical skimmer (1.9 mm diameter). A partially focused laser beam intercepts the molecular beam, and generates ions, which were detected using a detector system consisting of a two-stage Wiley–McLaren [38] TOF mass spectrometer, with extraction and acceleration regions. The detector system was mounted vertically, perpendicular to the horizontal MB. After passing through the acceleration region, the ion packet passed through a

1035 mm long field-free flight tube to the detector. Two deflector plates, placed perpendicular to the detector axis (*z* axis), guided translation of the ion packet in the (*x,y)* plane and at the center of 18 mm dual microchannel plates (MCP). A single compact voltage generator, having multiple output voltage ports, powered the TOF ion optics, the deflection plates and the MCP detector.

The 2-furoyl chloride (Alfa Aesar, 98% purity) and the benzoyl chloride (Fluka, >98% purity) sample were used as supplied, after degassing and purification by several freeze-pump-thaw cycles.

5.3 Theoretical methods

Ab initio molecular electronic structure theories were employed to investigate the Cl formation channels in 2-furoyl chloride, and Cl and HCl formation in benzoyl chloride on UV excitation, using Gaussian 03 program. [3] The ground state geometries of 2-furoyl chloride and benzoyl chloride, along with other expected products in the Cl and HCl channels, were optimized at the B3LYP/6-311+G(d,p) level of theory, and energies of these geometries were calculated at the Moller-Plesset MP4(sdq) level with the same basis sets. These energies are found to be within 3 kcal/mol of QCISD(T)/6-311G(d,p) energies. The harmonic vibrational frequencies and force constants were calculated, to ensure that the stationary points on the potential energy surface are true saddle points, and also for zero point energy correction. All the reported energy values are zero point energy corrected. The relative energies at MP4(sdq)/6-311+G(d,p) and QCISD/6-311G(d,p) levels gave the C-Cl bond dissociation energy in 2-furoyl chloride to be 76.0 and 73.3 kcal/mol, respectively. We have used an average value of 74.6 kcal/mol as the C-Cl bond dissociation energy in 2-furoyl chloride. The relative energies at MP4(sdq)/6-

311++G(d,p) level gave the C-Cl bond dissociation energy in benzoyl chloride to be 75.8 kcal/mol. The bond dissociation energy can be compared with the reported C-Cl bond dissociation energy in similar alkyl chlorides of 71.2 kcal/mol in allyl chloride [122] and 83.2 and 86.8 kcal/mol in acryloyl chloride [119,120]. The C-Cl bond dissociation energy of 71.2 kcal/mol in allyl chloride is lower than a typical C-Cl single bond dissociation enthalpy of ≥ 84 kcal/mol, due to the resonance stabilization of the allyl radical produced [122]. The bond dissociation energy in acryloyl chloride suggests almost no effect of the resonance stabilization of the acryloyl radical produced. But, an intermediate effect of the resonance stabilization on the C-Cl bond dissociation energy is observed in 2-furoyl chloride and benzoyl chloride, due to an extended conjugation of the ring π electrons in 2-furoyl and benzoyl radicals produced.

Excited electronic state calculations were performed at the time dependent density functional theory (TD-DFT) level, using cc-pVDZ and cc-pVTZ basis sets, and the electronic states of 2-furoyl chloride and benzoyl chloride, accessible at 235 nm, were predicted from the vertical excitation energies and the molecular orbital analysis. These calculations predict the excitation of 2-furoyl chloride and benzoyl chloride at 235 nm is to the S_2 and S_3 state, respectively, and both these states involve the π^*(ring, C=O)$\leftarrow\pi$(ring) transition. Structures of a few lower excited electronic states were optimized at the configuration interaction with single excitation (CIS) level, using 6-311+G basis sets for 2-furoyl chloride and 6-311+G(d) basis sets for benzoyl chloride. The larger basis sets could not be used, since the S_1 state could not be optimized with these basis sets. Any attempt to optimize the S_1 state of 2-furoyl chloride with larger basis sets led to a transition state (TS) structure with the C atom of the COCl group moving out of the molecular plane. We searched for the transition state structures for the C-Cl bond dissociation on the excited electronic states of 2-furoyl chloride and benzoyl chloride, and could locate the same only on the lowest singlet state, S_1 for both.

5.4 Results

2-Furoyl chloride and benzoyl chloride in molecular beams were irradiated at 235 nm to detect Cl in the former, and both Cl and HCl in the latter, using REMPI-TOF-MS. The observed TOF profiles of Cl and Cl* were analyzed, using a forward convolution method, which is described in detail in chapter 2, to extract the speed distribution g(v), translational energy distribution and the recoil anisotropy parameter (β).

5.4.1 Photodissociation of 2-furoyl chloride

Photodissociation of 2-furoyl chloride at 235 nm generates Cl, in both the ground ($^2P_{3/2}$) and the excited ($^2P_{1/2}$) spin orbit states. But, the (2+1) REMPI signal at *m/e*= 36(HCl) and MPI signal at *m/e*= 63(COCl) could not be detected under similar experimental conditions. The result suggests that HCl molecular elimination is either not taking place or it is a negligible channel.

5.4.1.1 REMPI detection of Cl

The chlorine atom fragment was detected using (2+1) REMPI and TOF mass spectrometry. A typical time-of-flight mass spectrum measured on photodissociation of 2-furoyl chloride at ~ 235 nm, resonant to the Cl REMPI line, is shown in FIG. 5.1. The laser power dependence of the REMPI intensity has a linear log-log plot with a slope of ~3.0 (one photon for photolysis and two for REMPI detection) in the range of laser power used. The result suggests (2+1) REMPI of chlorine atom, produced in a

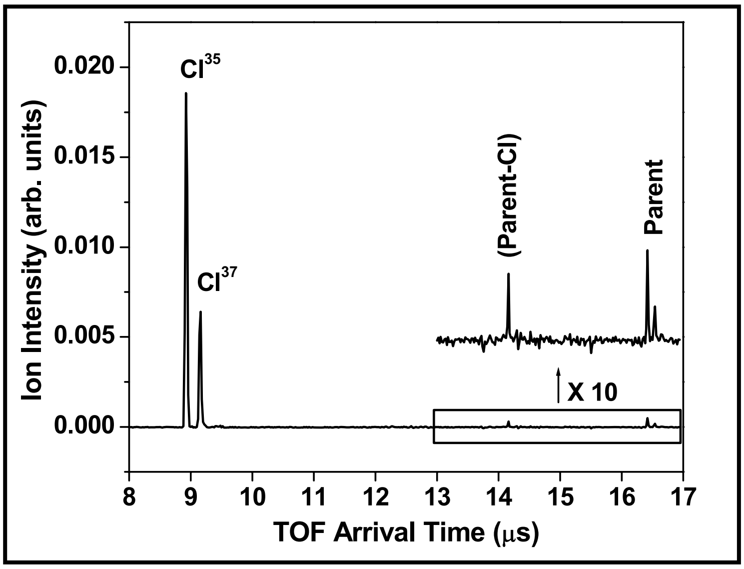

FIG. 5.1:*Time-of-flight mass spectra on photodissociation of 2-furoyl chloride on the Cl resonant line.*

single photon process, assuming that the ionization step is saturated. That Cl and Cl* are produced in a single photon process was validated by additional experiments. The shape and the width of TOF profiles of a halogen atom are systematically measured at various laser energies, and observed to be independent of laser energies. However, at high energy a slight increase in the width of the TOF profile was observed, implying a contribution from additional sources, such as secondary dissociation or multiphoton process. Hence, all the experiments were performed in the low energy region to ensure that the profiles remain the same, and the single photon condition is maintained.

5.4.1.1.1 Anisotropy parameters (β) and translational energy distributions of Cl and Cl*

The analysis of the measured time of flight profiles of Cl and Cl* (shown in FIG. 5.2) with different laser polarizations, at the χ values of 0°, 54.7° (the magic

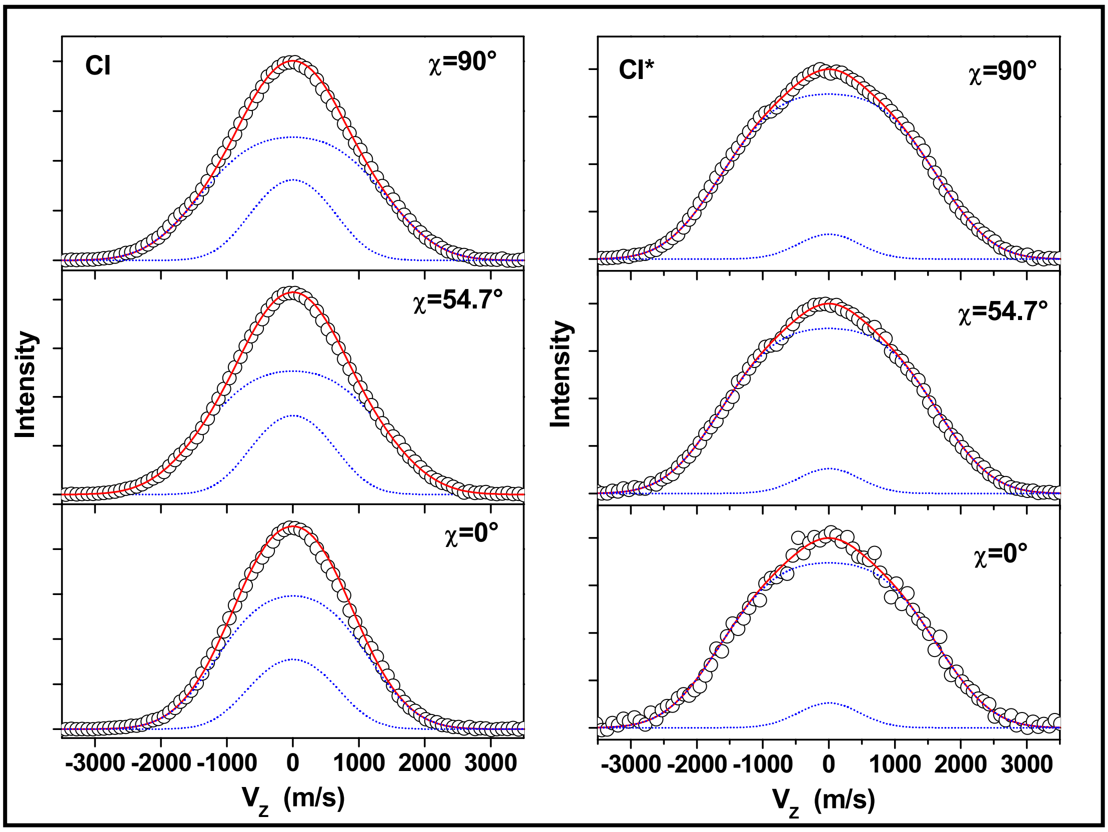

FIG. 5.2: *REMPI-TOF profiles of* $Cl(^2P_{3/2})$ *and* $Cl^*(^2P1_{/2})$ *produced from the 235 nm photodissociation of 2-furoyl chloride. The circles are the experimental data, dotted lines are two velocity components and the solid line is a forward convolution fit.*

Table 5.1: *The excitation energy (hν), dissociation energy of the C-Cl bond* (D_0), *available energy* (E_{avl}), *the average translational energy,* $\langle E_T \rangle$ *value, the relative quantum yield (Φ) and the recoil anisotropy parameter (β) for photodissociation of 2-furoyl chloride at 235 nm, leading to Cl and its co-fragment radical. All energies are in kcal/mol.*

Reaction channel	hν	D_0 (C-Cl)	E_{avl}	$\langle E_T \rangle$		Φ	β
				Fast	Slow		
c-C_4H_3O CO + Cl	122	74.6	47.4	7.0±2.0	1.5±0.5	0.85±0.11	0.0±0.2
c-C_4H_3O CO + Cl*	22	74.6	45.0	9.5±2.0	0.8±0.5	0.15±0.02	0.0±0.2

angle) and 90°, results in the β values of ~0 for both Cl and Cl* fragments. Thus, the TOF profiles of Cl and Cl*, in photodissociation of 2-furoyl chloride at 235 nm, are independent of the laser polarization. The β values, along with other observables, are given in Table 5.1. The β value of zero implies an isotropic angular distribution of the fragments, suggesting slow (with respect to the rotational period of 2-furoyl chloride) formation of Cl and Cl*. Thus, 2-furoyl chloride does not dissociate from an initially excited state to produce Cl and Cl*, rather it can dissociate from the ground state or an electronically excited state produced after non-radiative relaxation.

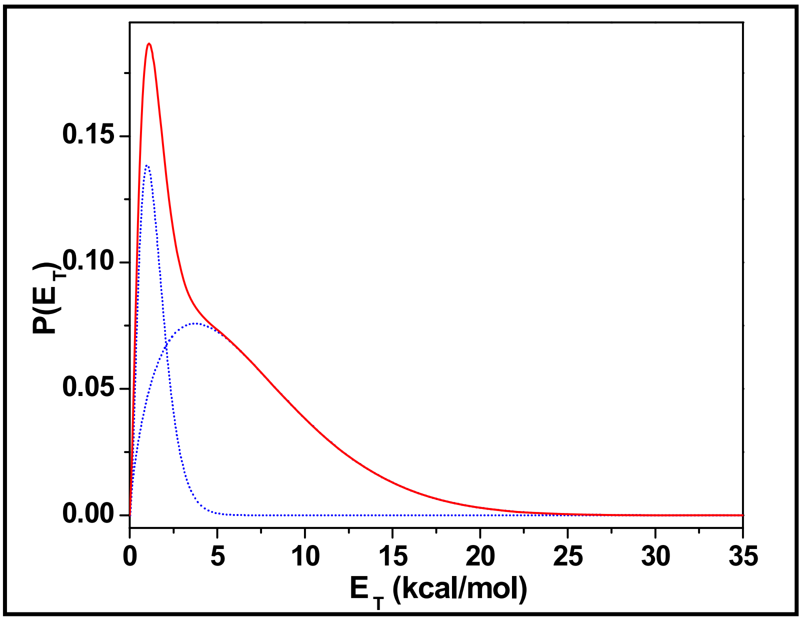

FIG. 5.3: *Center-of-mass recoil translational energy distribution for Cl($^2P_{3/2}$) in the photodissociation of 2-furoyl chloride at 235 nm. The dashed lines indicate the distributions for the slow and fast components of the chlorine atom formation channel; the solid line shows the sum.*

We also obtained photofragment speed distribution from the forward convolution analysis of the TOF profiles of Cl and Cl*. The analysis reveals two velocity components (fast and slow) in the distribution of both Cl and Cl* produced in

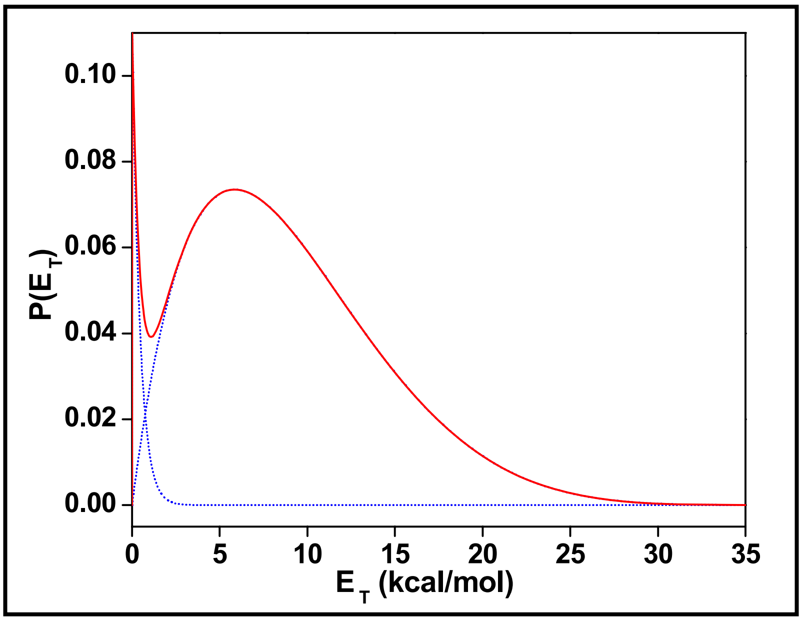

FIG. 5.4: *Center-of-mass recoil translational energy distribution for Cl*($^2P_{1/2}$) in the photodissociation of 2-furoyl chloride at 235 nm. The dashed lines indicate the distributions for the slow and fast components of the chlorine atom formation channel; the solid line shows the sum.*

photodissociation of 2-furoyl chloride at 235 nm. Thus, both Cl and Cl* originate from two different dissociation channels. Using the speed distributions, photofragment translational energy distributions of Cl and Cl* are determined, and depicted in FIG. 5.3 and 5.4, respectively. The relative translational energies for the fast (high energy) and slow (low energy) Cl channels are 7.0±2.0 and 1.5±0.5 kcal/mol, respectively. The fractions of the high and low translational energy components are determined to be 75% and 25%, respectively, for the Cl channel. Similarly, the average translational energies for the fast and slow Cl* channels are 9.5±2.0 and 0.8±0.5 kcal/mol, respectively. For the Cl* channel as well, the fast component contributes predominantly to the total yield, accounting for about 95%. This result is similar to that in photodissociation of acryloyl chloride at 235 nm, in which the majority of the translational energy distribution is contributed from fast Cl atoms [123]. The fraction of the available energy going to the relative translation, f_T, of the slow Cl(Cl*) channel is ~0.03(~0.02). These f_T values are explained well with the statistical models [24,25] of energy partitioning, which predict these values to be less than 6%. The statistical dissociation of the C-Cl bond, leading to slow Cl and Cl* channels, suggests that the slow fragments are produced from the ground electronic state of 2-furoyl chloride. However, the f_T values for the fast Cl and Cl* channels are higher, 0.15 and 0.21, respectively. These f_T values are underestimated by the statistical models, but overestimated by the soft impulsive model [26], which predicts the value to be 0.35. Thus, the fast Cl and Cl* channels do not originate from a repulsive surface of 2-furoyl chloride, rather these are expected to have exit barriers.

5.4.1.1.2 Relative quantum yields of the Cl and Cl* products

The spectral profiles of REMPI lines of Cl and Cl* were measured at 235.336 and 235.205 nm, respectively (shown in FIG. 5.5), and the relative quantum yields of

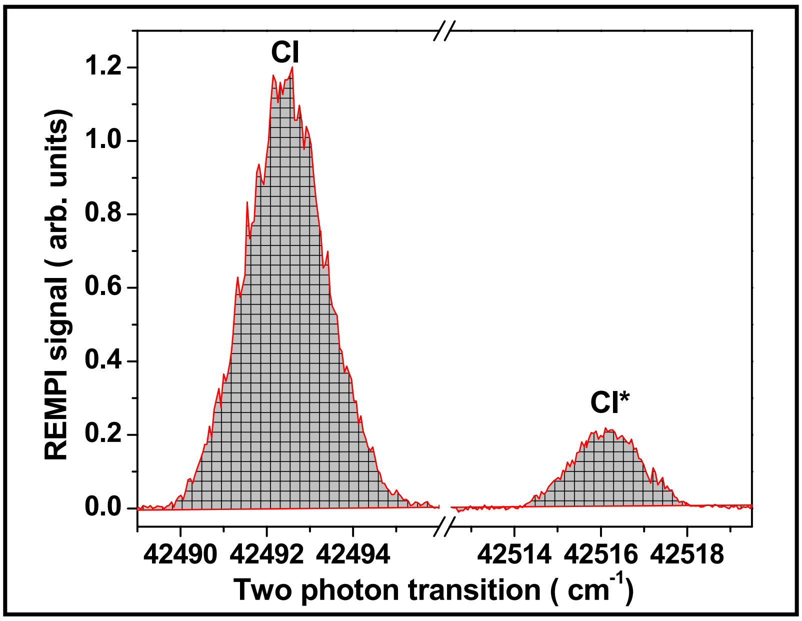

FIG. 5.5: *REMPI spectra of Cl and Cl* atoms produced in the 235 nm laser photolysis of 2-furoyl chloride.*

Cl, Φ(Cl), and Cl*, Φ(Cl*), were evaluated. The values of Φ(Cl*) and Φ(Cl) were extracted from the integrated line intensities, I(Cl)/I(Cl*), to be 0.15 ± 0.02 and 0.85± 0.05, respectively. These values are reported in Table 5.1. Similar relative yield of Cl* (0.19) has been reported in photodissociation of acryloyl chloride at 235 nm [123]. In addition to the spin-orbit branching ratio, the Cl product population distribution is also sub-divided based on the relative amounts of the measured low and high kinetic energy components. The branching ratio of the high kinetic energy C-Cl bond scission to the low energy C-Cl bond scission is 0.78/0.22.

5.4.1.2 Theoretical results

The optimized structures of the ground state of 2-furoyl chloride suggest two conformers, s-trans and s-syn with respect to the C-C single bond, of almost equal

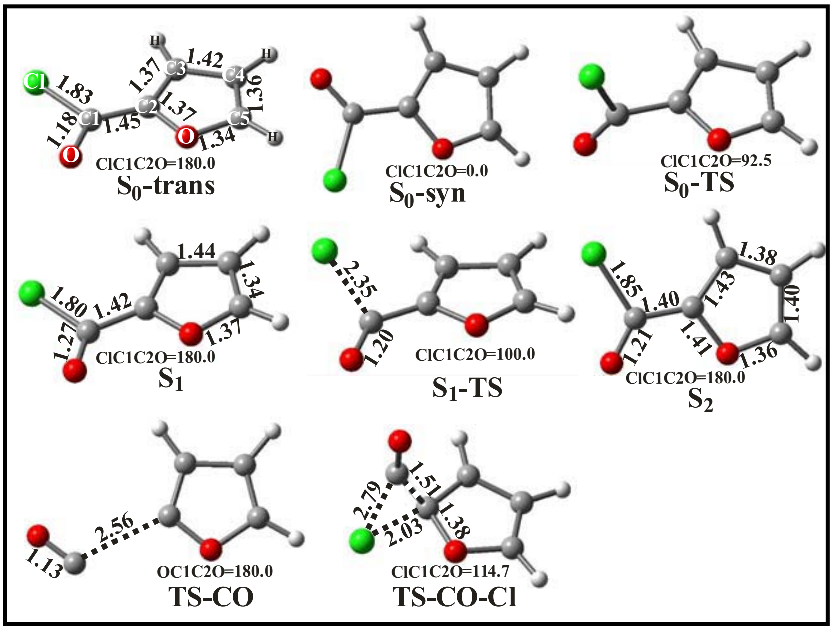

FIG. 5.6: *The optimized structures of the ground (first, showing two conformers with corresponding TS, and third, depicting TS for CO elimination, rows) and excited electronic (second row, showing S_1, TS for Cl formation from S_1, and S_2 states) states of 2-furoyl chloride, along with transition states. Details are given in the text. A few important bond lengths (in Å) and dihedral angles are marked on structures. Dissociating and forming bonds are depicted as dotted lines.*

stability (within 0.4 kcal/mol, with a greater stability for trans). Both syn and trans structures are planar (dihedral angle ClCCO of 0° and 180°, respectively) with the barrier of rotation to be 6.9 kcal/mol. These trans, syn and TS structures are depicted in FIG. 5.6 as S_0-trans, S_0-syn and S_0-TS, respectively.

Molecular orbital calculations predict that the S_1 and the T_2 states originate from the π^*(C=O, ring)$\leftarrow$n(Cl, O) excitation, involving the non-bonding electrons on mainly Cl or O atom of the COCl group to the antibonding π orbitals of C=O and the ring. The optimized S_1 geometry (structure marked as S_1 in FIG. 5.6) reveals an appreciable increase in the C=O bond length from 1.18 in S_0 to 1.27 Å. The angle ClCO is decreased from 120.3 to 113.4. These significant structural changes in the S_1 state suggest that the electronic excitation remains mostly localized to the C=O group of the COCl side-chain, and the furan ring remains almost unaffected. The nature of excitation of the T_2 state of 2-furoyl chloride is similar to that of its S_1 state.

MO calculations predict that both the S_2 and T_1 states originate from the π^*(C=O, ring)$\leftarrow\pi$(ring) excitation, with the excitation mostly localized in the ring. The S_2 structure (depicted as S_2 in FIG. 5.6) suggests that the C=C bond lengths of the ring are immensely affected, with the C2=C3 bond length (1.37 Å) of the ring, attached to the COCl group, acquiring a single bond character (1.43 Å) in the S_2 state. The structures of the S_2 and the T_1 states are almost similar.

Since the translational energy release predicts presence of exit barriers for fast Cl and Cl* channels, we attempted to locate corresponding TS structures on different PESs of 2-furoyl chloride, and located the same on only the S_1 state. The TS structure, optimized at CIS/6-311+G level of theory, has greatly extended C-Cl bond of 2.35 Å (shown as S_1-TS in FIG. 5.6) and reduced angle ClCO to 89.0° from 113.4° in the S_1

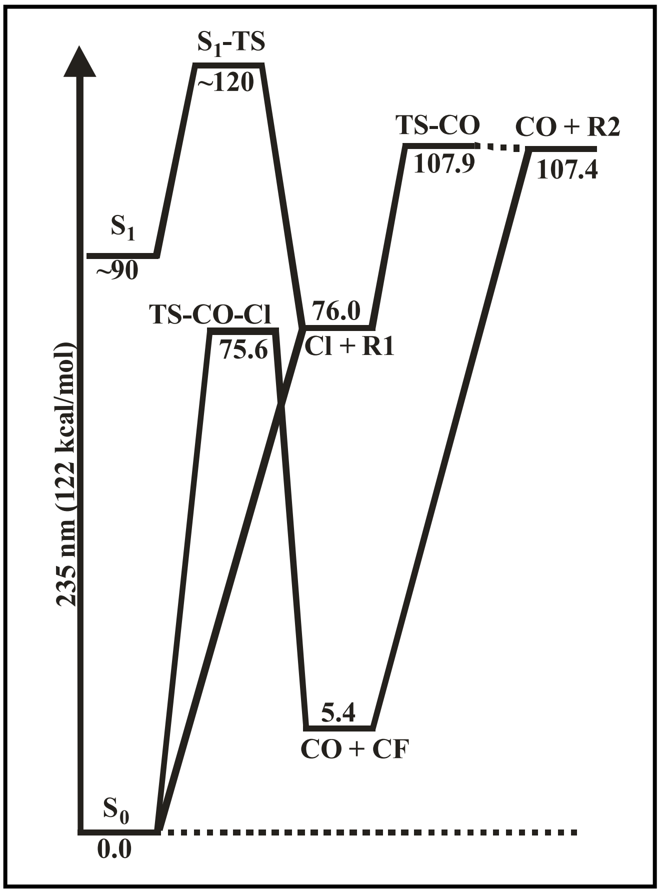

FIG. 5.7: *Relative potential energy diagrams for formation of Cl from the excited electronic state (S_1), and that of CO from the ground state of 2-furoyl chloride. Details are given in the text. All the energies are in kcal/mol.*

state. Although the TS structure is non-planar with the dihedral angle ClC1C2O of 100°, the planarity of the furan ring, including the C atom of the COCl group, is still retained. The TS for the C-Cl bond cleavage is predicted to have relative energies of ~30 and ~120 kcal/mol with respect to the S_1 and S_0 minima, respectively. These energies of the TS (shown in FIG. 5.7) are approximate, since theoretical calculations are at the CIS level with smaller basis sets. However, characterization of the TS for the C-Cl bond scission establishes presence of an exit barrier (~44 kcal/mol). The TS for the C-Cl bond cleavage is also expected on the T_2 surface, since the nature of the T_2 state is similar to that of the S_1 state. However, we failed to locate the TS on the T_2

surface. Higher level CASSCF calculations are required for prediction of accurate energies of TS, and to understand whether the C-Cl bond scission takes place only on the S_1 state of 2-furoyl chloride, or some other states are also involved.

5.4.2 Photodissociation of benzoyl chloride

Like in 2-furoyl chloride, both Cl and Cl* could be easily detected in benzoyl chloride. In addition, HCl was detected using (2+1) REMPI in the wavelength range 236-237 nm (shown in FIG 5.8) for the Q(J) branch of the V $^1\Sigma^+$ $(0^+)\leftarrow\leftarrow$ X $^1\Sigma^+$ (0^+) (12,0) band [124]. From the measured HCl REMPI spectrum, we have determined the

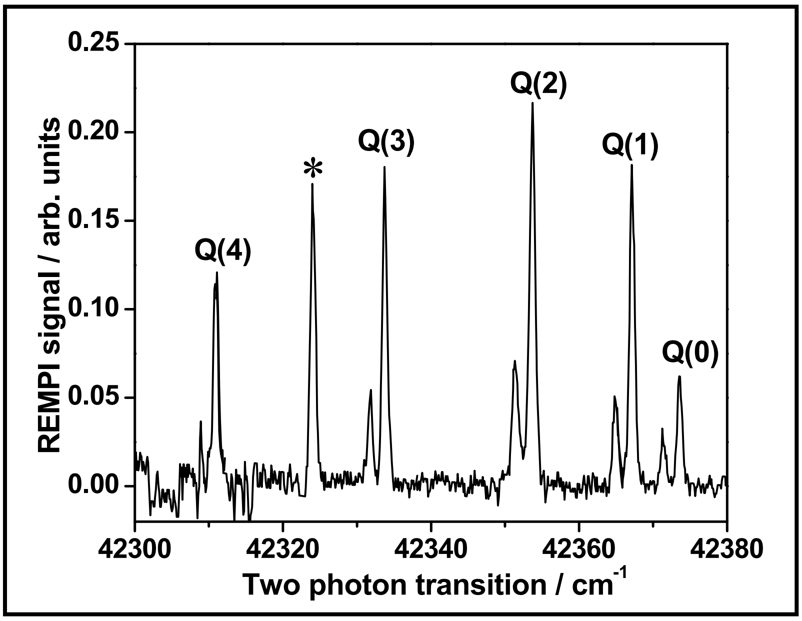

FIG. 5.8: *(2+1) REMPI spectra of $H^{35}Cl$ (stronger line of the doublets) and $H^{37}Cl$ (weaker line of the doublets), for the Q(J) branch of V $^1\Sigma^+$ $(0^+)\leftarrow\leftarrow$ X $^1\Sigma^+$ (0^+) (12,0) band, produced in the 235 nm laser photolysis of benzoyl chloride. The line marked with an asterisk (*) stands for a Cl line.*

rotational temperature for HCl (v″=0) to be 160±15 K. The FWHM of HCl TOF profile is comparable to that of the instrument response function. Thus, the dynamics of HCl formation is statistical, as expected from involvement of the ground state of benzoyl chloride. The HCl yield is comparable to the Cl yield. In the absence of relative ionization probability of HCl and Cl, we are unable to provide their relative branching ratio, which could have directly provided the competitiveness of these two channels. The dependence of the REMPI intensity of HCl on laser power shows a linear log-log plot with a slope of ~3.0 (one photon for photolysis and two for REMPI detection) in the range of laser power used. The result implies (2+1) REMPI detection of HCl, produced in a monophotonic process, with an assumption that the ionization step is saturated. The results suggest that HCl molecular elimination is taking place in addition to the Cl atom formation on UV excitation of benzoyl chloride at 235 nm. But, the C-C bond cleavage, producing COCl, is probably not a primary channel. However, this channel cannot be ruled out on the basis of our results.

5.4.2.1 REMPI detection of Cl

Photodissociation of benzoyl chloride at 235 nm generates Cl, in both the ground ($^2P_{3/2}$) and the excited ($^2P_{1/2}$) spin orbit states, which was detected using (2+1) REMPI and TOF mass spectrometry. Like HCl, the dependence of the REMPI intensity on laser power suggests (2+1) REMPI detection of chlorine atom, produced in a monophotonic process. Our additional experiments, like in 2-furoyl chloride, validate the result on Cl and Cl* being produced in a single photon process.

5.4.2.1.1 Anisotropy parameters (β) and translational energy distributions of Cl and Cl*

The time of flight profiles of Cl and Cl*, in photodissociation of benzoyl chloride at 235 nm, are almost independent of the laser polarization. The analyses of the measured TOF profiles of Cl and Cl* (shown in FIG. 5.9) with different laser polarizations, at the χ values of 0°, 54.7° (the magic angle) and 90°, provide the β values of zero for both Cl and Cl* fragments. The β values of zero suggest that

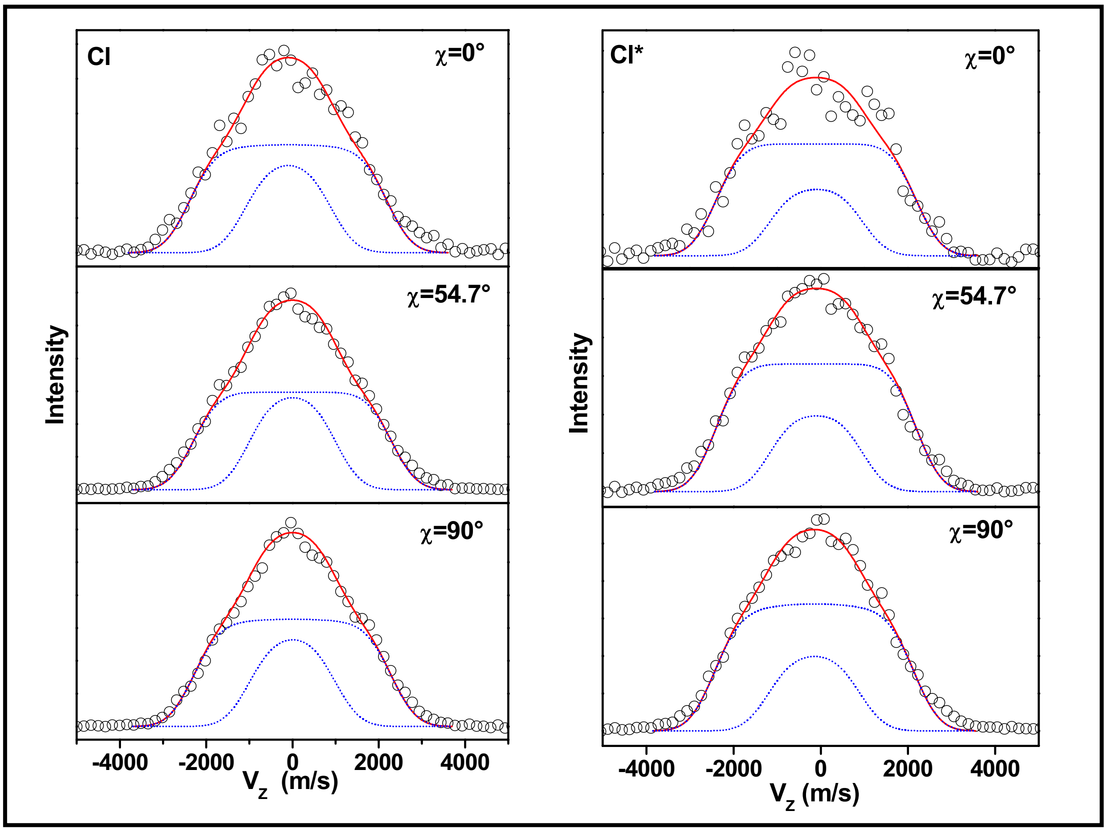

FIG. 5.9: *REMPI-TOF profiles of Cl($^2P_{3/2}$) and Cl*($^2P_{1/2}$) produced from the 235 nm photodissociation of benzoyl chloride. The circles are the experimental data, dotted lines are two velocity components and the solid line is a forward convolution fit.*

chlorine atoms are not produced from an initially excited state of benzoyl chloride, rather from the ground state or an electronically excited state produced after non-radiative relaxation. This fact is supported by our excited state calculations. These calculations suggest that the angle between the transition dipole moment and the dissociating C-Cl bond is ~150° and ~90° for the direct excitation to the S_3 and S_1 states, which correspond to the β parameter value of ~1.2 and ~-1.0, respectively (using equation 2.11). In general, several factors contribute to reduce [45,75] or even wash out [113] the initial anisotropy, such as longer dissociation lifetime than the rotational period, mixed initial transition both with parallel and perpendicular components, dissociation not from a single geometry rather from a range of geometries, etc. In the present case, the combined time taken for the relaxation and dissociation appears to be longer than the rotational period of the parent molecule, leading to washing out of the initial anisotropy.

We also obtained photofragment speed distributions of Cl and Cl* from the forward convolution analysis of their TOF profiles. These distributions are bimodal with two velocity components (fast and slow) for both Cl and Cl* produced in photodissociation of benzoyl chloride at 235 nm. Thus, both Cl and Cl* channels originate from two different dissociation pathways. These speed distributions are transformed into photofragment translational energy distributions of Cl and Cl*, and depicted in FIG. 5.10 and FIG. 5.11, respectively. The relative translational energies for the fast (high energy) and slow (low energy) Cl channels are 16.6±2.0 and 3.4±1.0 kcal/mol, respectively, with a predominant contribution from the former channel (~70%). Following a similar trend, the average translational energies for the fast and slow Cl* channels are 16.6±2.0 and 3.7±1.0 kcal/mol, respectively, and the fast component contributes predominantly (~78%) to the total yield. Similar results are obtained in photodissociation of 2-furoyl chloride and acryloyl chloride [123] at 235 nm, in which the majority of the chlorine atoms formed are fast chlorine atoms [123]. The fraction of the available energy going to the relative translation, f_T, of the slow Cl(Cl*) channel is measured to be ~0.07(~0.09) in photodissociation of benzoyl chloride. These f_T values are explained well with the statistical models of energy partitioning by Muckermann [24] and Klots [25], which predict these values to be about 8% and 3%, respectively. The statistical dissociation of the C-Cl bond, leading to slow Cl and Cl* channels, suggests that these channels operate mainly from the

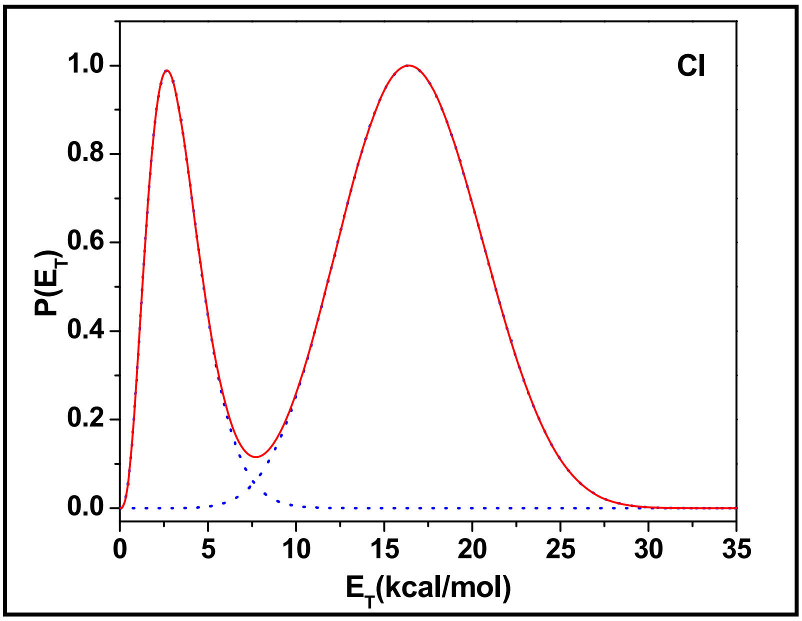

FIG. 5.10: *Center-of-mass recoil translational energy distribution for Cl($^2P_{3/2}$) in the photodissociation of benzoyl chloride at 235 nm. The dashed lines indicate the distributions for the slow and fast components of the chlorine atom formation channel; the solid line shows the sum.*

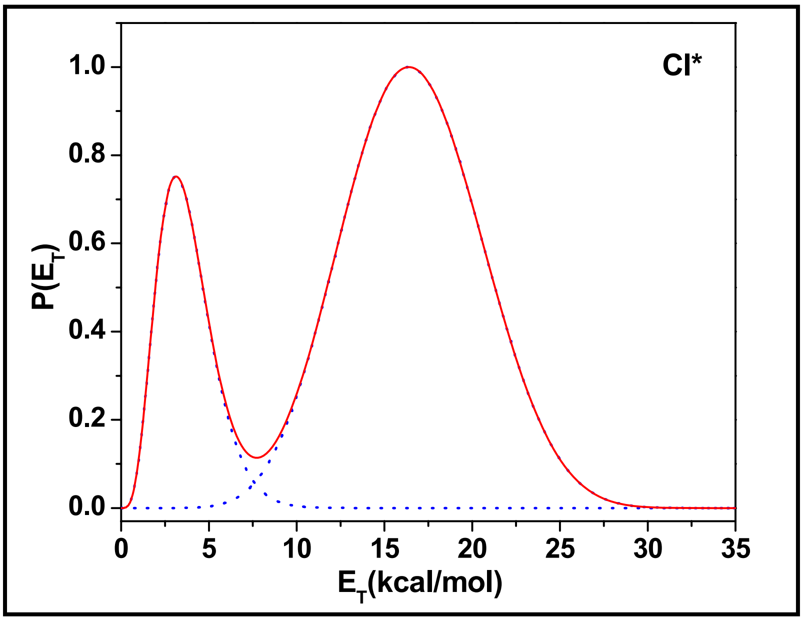

FIG. 5.11: *Center-of-mass recoil translational energy distribution for Cl*($^2P_{1/2}$) in the photodissociation of benzoyl chloride at 235 nm. The dashed lines indicate the distributions for the slow and fast components of the chlorine atom formation channel; the solid line shows the sum.*

ground electronic state of benzoyl chloride. In general, the presence of clusters can also be a potential source of slow Cl/Cl*. However, it is not expected to play a role in the present work. A small contribution to the slow chlorine atom channels from COCl (a primary product of probable C-COCl bond scission) dissociation cannot be ruled out from our experimental data. The measured f_T value of the fast Cl(Cl*) channel is much higher ~0.37(0.39), which is in a good agreement with a value of 0.34 predicted by the soft impulsive model [26] Thus, the fast Cl and Cl* channels either originate from a repulsive surface of benzoyl chloride, or have exit barriers. However, the measured β values of ~0 for both Cl and Cl* fragments suggest that the fast chlorine atoms cannot originate from a repulsive surface, as dissociation from a repulsive surface generally leads to an anisotropic distribution of the products with high non-zero β values, 2 and -1 in limiting conditions. Therefore, the fast chlorine atom channels in benzoyl chloride on excitation at 235 nm are expected to have exit barriers.

5.4.2.1.2 Relative quantum yields of the Cl and Cl* products

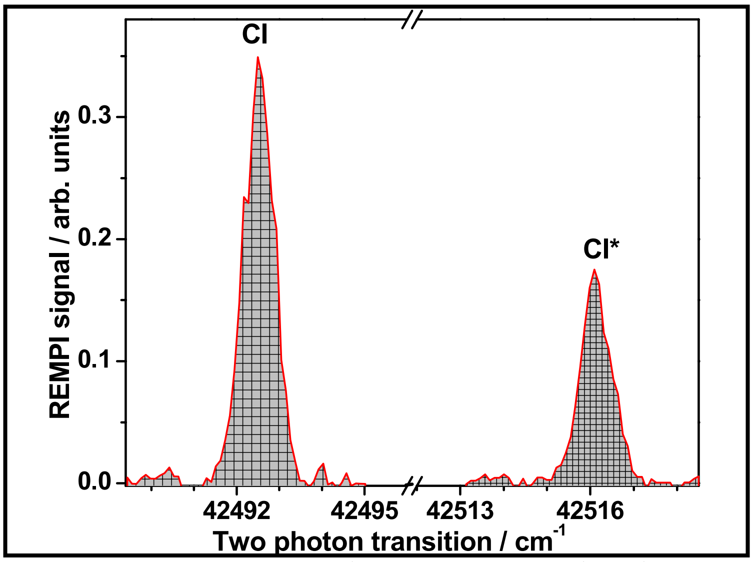

FIG. 5.12: *REMPI spectra of Cl and Cl* atoms produced in the 235 nm laser photolysis of benzoyl chloride.*

To measure the relative quantum yields, the spectral profiles of REMPI lines of Cl and Cl* were measured at 235.336 and 235.205 nm, respectively (shown in FIG. 5.12). The relative quantum yields of Cl, Φ(Cl), and Cl*, Φ(Cl*), are evaluated to be 0.70 ± 0.10 and 0.30 ± 0.05, respectively, from their measured relative intensities. These values are provided in Table 5.2. The value of Φ(Cl*) is in good agreement with its statistical value of 1/3, which is given as [J(Cl*)+0.5]/[J(Cl*)+J(Cl)+1]. Besides the spin-orbit branching ratio, we also sub-divided the Cl product population distribution, based on the relative values of the measured low and high kinetic energy components. The branching ratio of the high kinetic energy to the low kinetic energy C-Cl bond scission is measured to be 0.72/0.28.

Table 5.2: *The excitation energy (hv), dissociation energy of the C-Cl bond (D_0), available energy (E_{avl}), the average translational energy, ⟨E_T⟩ value, the relative quantum yield (Φ) and the recoil anisotropy parameter (β) for photodissociation of benzoyl chloride at 235 nm, leading to Cl and its co-fragment radical. The values in parentheses pertain to the slow chlorine atom channels. All energies are in kcal/mol.*

Reaction channels	hν	D_0 (C-X)	E_{avl}	$<E_T>$	f_T value	Φ	β
C_6H_5-CO + Cl	122	75.8	46.2	16.6±2.0 (3.4±1.0)	0.37 (0.07)	0.70±0.15	0.0±0.2
C_6H_5-CO+ Cl*	122	75.8	43.8	16.6±2.0 (3.7±1.0)	0.39 (0.09)	0.30±0.05	0.0±0.2

5.4.2.2 Theoretical results

Molecular orbital calculations predict that the S_1 state of benzoyl chloride originates mainly from the π*(C=O)←n(Cl, O) excitation, involving the non-bonding electrons on Cl or O atom (HOMO-2) to the antibonding π orbitals (LUMO) of C=O. The optimized S_1 geometry (structure marked as S_1 in FIG. 5.13) reveals an increase in the C=O bond length to 1.28 Å from 1.19 in S_0. The angle OC7Cl is decreased from 118.2° to 111.3°. The planarity of the benzene ring is retained in the excited state. These structural changes in the S_1 state suggest that the electronic excitation remains mostly localized to the C=O group of the COCl side-chain, with a small change in the bond lengths of the benzene ring.

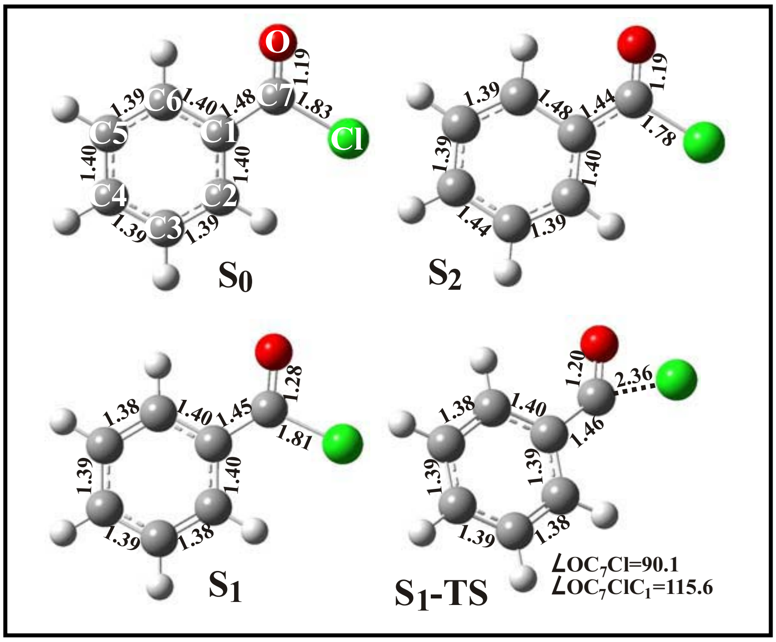

FIG. 5.13: *The optimized structures of the ground state (S_0), excited electronic states (S_1 and S_2) and TS (S_1-TS) for Cl formation from the S_1 state of benzoyl chloride. Details are given in the text. A few important bond lengths (in Å) and angles are marked on structures. Dissociating and forming bonds are depicted as dotted lines.*

The S_2 state originates mainly from the π*(ring)←π(ring) excitation, i.e. the excitation is mostly localized in the ring. This transition involves mainly HOMO and LUMO orbitals. The S_2 structure (depicted as S_2 in FIG. 5.13) suggests that the C=C bond lengths of the ring are immensely affected, with the two C=C bond lengths C1-C6 and C3-C4 (~1.39 Å) of the ring acquiring a single bond character (~1.46 Å) in the S_2 state. The C=O bond length remains unaffected. Similarly, the S_3 state originates primarily from the π*(ring)←π(ring) transition. The optimized geometry of this state is similar to that of the S_2 state.

The measured translational energy release and β values of ~0 for chlorine fragments suggest the presence of exit barriers for fast Cl and Cl* channels, as mentioned earlier. Since a simple bond cleavage from the ground electronic state of a stable molecule is generally barrier-less, fast chlorine atoms must be produced from an excited electronic state of benzoyl chloride and the reaction should have a well characterized transition state (TS). We attempted to locate corresponding TS structures on different PESs of benzoyl chloride, and located the same on the S_1 state. The TS structure, optimized at CIS/6-311+G(d) level of theory, on the S_1 surface has greatly extended C-Cl bond length of 2.36 Å (shown as S_1-TS in FIG. 5.13) and reduced angle OC_7Cl of 90.1° from 111.3° in the S_1 state. The TS structure is non-planar with the dihedral angle OC_7ClC_1 of 115.6°, but the benzene ring, including CO, is nearly planar. Thus, characterization of the TS for the C-Cl bond scission on the S_1 surface establishes presence of an exit barrier for fast chlorine channels. However, higher level of excited state calculations (such as CASSCF) are needed to estimate accurately the energies of the fast chlorine atom channels on the S_1 state, and to search for another possible excited state(s) of benzoyl chloride on which the C-Cl bond scission can takes place.

5.5 Discussion

5.5.1 Excitation of 2-furoyl chloride at 235 nm

2-Furoyl chloride is expected to have similar absorption spectra as that of benzoyl chloride or probably benzoic acid, since in both the cases π electrons of the ring are in conjugation with that of the C=O group of carboxylic acid or acid chloride.

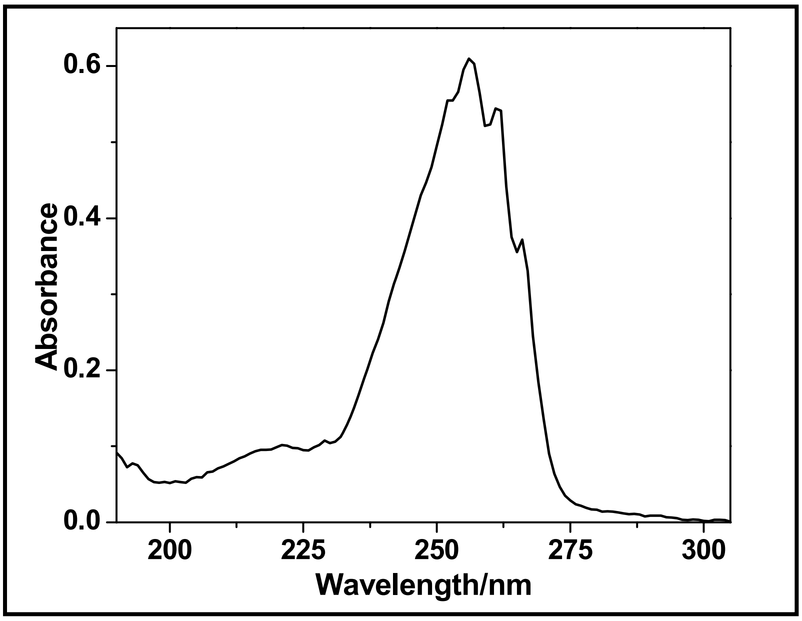

FIG. 5.14: *Gas phase UV absorption spectra of 2-furoyl chloride (0.6 Torr) recorded at room temperature.*

In carboxylic acid, the S_1 state arises from an electronic excitation located in the C=O group, and it is of nπ* character [125]. The S_2 state is stated to have ππ* character. Since the UV absorption spectra of 2-furoyl chloride in the vapor phase are not available in literature, the same have been measured (shown in FIG. 5.14). The room temperature absorption spectra are somewhat structured and show two bands. One band from 275 to ~230 nm with the maximum absorption at 256 nm, and the other weak band from ~230 nm to 200 nm with a broad maximum at 221 nm. In addition, very weak absorption is observed near 280 nm. In comparison to absorption spectra of benzoic acid, the absorption bands around 280 and 221 nm are very much reduced and the band at 256 nm is enhanced in 2-furoyl chloride absorption. These absorption features have been assigned based on molecular orbital (MO) calculations and compared with reported UV spectra of benzoic acid and acryloyl chloride.

Vertical excitation energies were calculated, employing time-dependent (TD) density functional theory (DFT), using the cc-pVDZ and cc-pVTZ basis sets for various electronic transitions of 2-furoyl chloride to understand the nature of excitation at 235 nm. Molecular orbitals participating in different electronic transitions were analyzed, and found that the S_1 state involves excitation of non-bonding electrons on Cl and O atoms of the COCl group to the antibonding π^* orbitals, mainly of the side-chain C=O group. However, the S_2 state involves the excitation of the π electrons of the ring to the antibonding π^* orbitals, mainly C=C of the ring. The characters of triplet T_1 ($^3\pi,\pi^*$) and T_2 ($^3n,\pi^*$) states are similar to that of S_2 ($^1\pi,\pi^*$) and S_1 ($^1n,\pi^*$) states, respectively. The calculated vertical excitation energies from the ground state to the S_1, S_2 and S_3 states with the cc-pVDZ basis sets are 106.4 (268.6 nm), 116.9 (244.6 nm) and 130.6 (218.9 nm) kcal/mol, respectively, along with their respective oscillator strengths of 0.0000, 0.37 and 0.0001. However, with the cc-pVTZ basis sets the calculated vertical excitation energies to the S_1, S_2 and S_3 states are 105.8 (270.1 nm), 114.5 (249.8 nm) and 129.6 (220.6 nm) kcal/mol, respectively, along with similar respective oscillator strengths. These calculated peak positions of 270.1, 249.8 and 220.6 nm, corresponding to S_1, S_2 and S_3 states respectively, with higher basis sets are in a relatively better agreement with the experimental values of 280, 256 and 221 nm. Although the S_1($^1n,\pi^*$) state (with oscillator strength of zero) in 2-furoyl chloride is not expected to be observed experimentally in the energy region below the S_2($^1\pi,\pi^*$) state, the observed weak shoulder at ~280 nm can be assigned to it. A non-zero transition probability for the S_1 state can be due to vibrational coupling. Thus, the excitation of 2-furoyl chloride at 235 nm (122 kcal/mol) is expected to lead the molecules mainly to the S_2 state ($^1\pi,\pi^*$). The nature and vertical excitation energies of the lower excited states of 2-furoyl chloride are similar to that reported for benzoic acid [125,126]. Electronic transitions in 2-furoyl chloride can also be compared to that in acryloyl chloride (H_2C=CHCOCl), since these are α,β-unsaturated carbonyl chlorides. Theoretical calculations [120] on acryloyl chloride predict that both S_1 and T_2 states originate from the C=O π*←n excitation, whereas the S_2 and T_1 states originate from the C=C π*←π excitation. Thus, the assignment of these four transitions is similar to that in 2-furoyl chloride.

5.5.2 Mechanism of Cl formation from 2-furoyl chloride

UV excitation of saturated alkyl chlorides generally leads to the C-Cl bond fission from a repulsive state σ*(C-Cl) with an impulsive mechanism, producing Cl and Cl* with an anisotropic angular distribution. However, the dynamics of the C-Cl bond fission in unsaturated alkyl chlorides involving a π*←π transition, such as allyl chloride [122], propargyl chloride [127] and 2-chloropropene [128] are different. In these cases, bimodal velocity distributions of Cl and Cl* are observed. In these two C-Cl bond scission channels, the high translational energy channel is assigned to originate from an electronic pre-dissociation, whereas the low energy channel operates from the ground electronic state, following internal conversion (IC), from an initially excited state. Even in unsaturated alkyl acid chlorides, such as fumaryl chloride [129] and acryloyl chloride [119], two similar C-Cl bond fission channels are observed on UV excitation.

2-Furoyl chloride (c-C_4H_3O COCl, with c- standing for cyclic) an unsaturated acid chloride, also has two C-Cl bond fission channels on excitation at 235 nm. But, what is the mechanism of Cl atom formation from 2-furoyl chloride? It can dissociate to produce Cl in broadly three possible pathways. The Cl fragment can be produced as a primary (reaction 5.1), or a secondary (reaction 5.2) product from the primary product COCl.

$$\text{c-}C_4H_3O\ COCl \rightarrow \text{c-}C_4H_3O\ CO\ (R1) + Cl(^2P_{3/2}, {}^2P_{1/2}) \qquad (5.1)$$

$$\text{c- }C_4H_3O\ COCl \rightarrow \text{c- }C_4H_3O\ (R2) + COCl \qquad (5.2a)$$

$$COCl \rightarrow CO + Cl(^2P_{3/2}, {}^2P_{1/2}) \qquad (5.2b)$$

These two dissociation channels involve only the side-chain without ring-opening. The third possible mechanism can involve first the ring-opening by a C-O bond cleavage, and the primary biradical can subsequently undergo dissociation or isomerization, followed by dissociation to produce Cl in one or more pathways. Our calculations at MP4(sdq)/6-311+G(d,p)//B3LYP)/6-311+G(d,p) level predict that reactions 5.1 and 5.2a are endothermic by 76.0 and 107.7 kcal/mol, respectively. Similarly, the ring-opening of 2-furoyl chloride involving the C-O bond cleavage is endothermic by 81.1 kcal/mol. Thus, present calculations suggest that Cl formation is more feasible energetically as a primary product (reaction 5.1). Another source of Cl (secondary) involving the C–COCl fission (reaction 5.2) is a higher energy channel and can proceed with much difficulty, because of the conjugation interaction [120]. Thus, although Cl formation involves a side-chain reaction, the furan ring cleavage in 2-furoyl chloride is expected to be a high energy channel.

The proposed mechanism of Cl formation from 2-furoyl chloride cannot be compared with literature, since no information is available on photodissociation of 2-furoyl chloride or even furancarboxylic acids. However, the dissociation mechanism can be compared to dissociative electron capture (DEC) of 2-furancarboxylic acid, in which only two primary processes are centered at the carboxylic acid group, and the ring does not open up. These processes involve COO-H and CO-OH bond cleavage, producing H and OH, respectively, along with their co-fragment ions [130]. Even the carboxylic acid group is not detached from the furan ring. It is not surprising since the bond between the ring carbon to the carboxylic carbon is strengthened (acquires a double bond character), because of resonance between the furan O atom and the COOH group through the ring. Similar resonance is possible between the furan O atom and the COCl group of 2-furoyl chloride, and thus rendering the COCl elimination, as a primary product (reaction 5.2a), difficult energetically on excitation of 2-furoyl chloride at 235 nm. Even the bonds of the ring-carbon with hydrogen, carbon, fluorine and chlorine atoms in substituted furans are unusually strong, and the ring-carbon–H bonds in alkylfurans are among the strongest ever C–H bonds recorded [131]. It appears that the photodissociation of 2-furoyl chloride is grossly similar to the dissociation of 2-furancarboxylic acid in DEC. However, the dissociation dynamics of 2-furancarboxylic acid induced by UV light can differ from that by electrons.

The photodissociation of 2-furoyl chloride can also be compared to that of benzoic acid [125,126,132], since the furan ring in the former is also aromatic, like the benzene ring in the latter. The photodissociation of benzoic acid at 248 and 193 nm also involves the carboxylic group only, and the ring remains intact. Two channels are observed at 248 nm: the C-OH bond cleavage, generating OH along with its co-fragment, and the decarboxylation with molecular CO_2 elimination [126]. At higher energy, on excitation of benzoic acid at 193 nm, an additional channel, leading to formation of COOH and its co-fragment, opens up. It is suggested that many electronic states of benzoic acid are involved in the photodissociation processes. Thus, similar to the photodissociation of benzoic acid that of 2-furoyl chloride also involves reactions mainly at the side-chain. It appears that the photodissociation of benzoyl chloride also should lead to the side-chain reaction alone, leaving the ring uncleaved. As expected, we did observe side-chain reaction on photoexcitation of benzoyl chloride at 235 nm (*vide infra*).

Thus, our experimental results combined with theoretical calculations suggest that reaction 5.1 (primary reaction involving C-Cl bond dissociation) is responsible for Cl formation on excitation of 2-furoyl chloride at 235 nm, with corresponding TS in the S_1 state. Since the C-Cl dissociation channel in the S_1 state has an exit barrier, this can be responsible for the fast Cl and Cl* formation. A fraction of 2-furoyl chloride in the S_1 state can escape dissociation, and undergo non-radiative relaxation to the ground electronic state, from which slow Cl and Cl* can be produced. The scheme for Cl and Cl* formation from 2-furoyl chloride on excitation at 235 nm can be given as follows:

$$\begin{tikzcd} \mathbf{S_0} \arrow[r, "\mathbf{h\nu}"] & \mathbf{S_2(^1\pi\pi^*)} \arrow[r, "\mathbf{IC}"] & \mathbf{S_1(^1n\pi^*)} \arrow[r, "\mathbf{IC}"] \arrow[d] & \mathbf{S_0} \arrow[r] & \mathbf{Cl / Cl^*(slow)} \\ & & \mathbf{Cl / Cl^*(fast)} & & \end{tikzcd}$$

The branching ratio of the high kinetic energy (fast) to the low energy (slow) C-Cl bond scission is measured to be 0.78/0.22, implying, at least, 78% yield of the S_1 state of 2-furoyl chloride dissociates to produce mainly Cl and Cl*. Thus, relaxation of the S_1 state to the S_0 state by internal conversion is a minor process in 2-furoyl chloride. Unlike in 2-furoyl chloride, dissociation in cyclic ethers is initiated by the ring cleavage involving the C-O bond cleavage, because the C-O bond cleavage energy in cyclic ethers, such as tetrahydrofuran (74.6/74.8 kcal/mol) [133,134], is lower. Therefore, the thermal and photochemistry of cyclic ethers give rise to unsaturated hydrocarbons and carbonyl compounds. The ultraviolet photolysis of cyclic ethers has been interpreted to involve the cleavage of the carbon-oxygen bond as the major primary process [135].

In acryloyl chloride also, the C-Cl bond cleavage is predicted to take place in the S_1 and T_2 states on UV excitation [120], and reported to be a primary dissociation channel [119,123]. The C–OH bond (analogous to the C–Cl bond of an acid chloride) dissociation is also the major channel from benzoic acid on excitation at 248 nm [126], and predicted to occur in the T_2 state after IC from S_2 to S_1 followed by ISC [125]. The C–COOH bond (analogous to the C–COCl bond of an acid chloride) dissociation could be observed in benzoic acid at higher excitation energy of 193 nm irradiation, predictably from the T_1 state. The role of the S_0 state of benzoic acid in photodissociation of the C–OH and C–COOH bonds is stated to be negligible.

5.5.3 Mechanism of CO formation from 2-furoyl chloride

In addition to the nascent Cl product, detected by REMPI, stable CO and C_2H_2 products were detected by FT-IR absorption. The minor product C_2H_2 is expected to be produced, as a secondary product, from the furan ring cleavage. We have not investigated the mechanism of its formation. The other stable product CO can be produced as a secondary product (reaction 5.3) from the primary product c-C_4H_3O CO (R1 produced in reaction 5.1), or COCl (reaction 5.2a) through reaction 5.2b.

$$\text{c-}C_4H_3O\ CO\ (R1) \rightarrow \text{c-}C_4H_3O\ (R2) + CO \qquad (5.3)$$

Since in the previous section, it is pointed out that reaction 5.2a cannot compete energetically with reaction 5.1, the formation of CO involving reaction 5.2a cannot be considered. Thus, the radical c-C_4H_3O CO (R1) can undergo the C-O bond cleavage via a TS (marked as TS-CO in FIG. 5.6) to produce CO. The TS has a planar geometry with the C-CO bond stretched to 2.56 Å. The activation barrier and the endoergicity of the reaction are predicted to be 31.9 and 31.4 kcal/mol, respectively. The predicted energy of TS being very close to the endoergicity of the reaction, suggests a loose TS with the saddle point lying in the exit channel. This barrier for CO elimination in 2-furoyl chloride (31.9 kcal/mol) is higher than that in acryloyl chloride (23.0 kcal/mol) [123] with a similar dissociation mechanism.

The CO product can also be generated as a primary product through reaction 5.4, involving a TS, shown as TS-CO-Cl in FIG. 5.6, with concerted Cl migration to the ring and CO elimination,

$$\text{c-}C_4H_3O\ COCl \rightarrow \text{c-}C_4H_3O\ Cl\ (CF) + CO. \qquad (5.4)$$

In the TS the COCl group is not in the plane of the furan ring. The activation barrier and endoergicity of the reaction (shown in FIG. 5.7) are calculated to be 75.6 and 5.4 kcal/mol, respectively. Thus, energetics suggests this mechanism of CO production to be more plausible.

5.5.4 Excitation of benzoyl chloride at 235 nm

The experimental UV absorption spectra of benzoyl chloride in vapor phase are reported to have absorption maxima at 278, 265 and <245 nm with absorption cross-section of $3.6\text{x}10^{-18}$, $2.5\text{x}10^{-18}$ and $>7.5\text{x}10^{-1}8$ cm^2 $molecule^{-1}$, respectively [136]. Our calculated vertical excitation energies of the lower singlet excited states S_1, S_2 and S_3 of benzoyl chloride are 4.45 eV (278.7 nm), 4.66 eV (265.9 nm) and 5.14 eV (241.0 nm) with the oscillator strengths of 0.0, 0.0196 and 0.2684, respectively (given in Table 5.3). The reported experimental UV absorption maxima of benzoyl chloride match very well with our calculated VEEs. Although TD-DFT estimates the peak positions reasonably well, an excellent agreement in the present work is a co-incidence. This theory is reasonably good enough to predict the nature of excitation. But, the calculated oscillator strengths are not fully consistent with the reported absorption cross-section of benzoyl chloride. The major issue is that the calculations predict zero oscillator strength for the S_1 state, but this transition is observed experimentally.

Table 5.3: *A comparison between experimental UV absorption and theoretically calculated vertical excitation energy (VEE), oscillator strengths (OS) and characters of lower singlet excited electronic states of benzoyl chloride, 2-furoyl chloride and benzoic acid.*

Compound	Experimental (λ_{max} in nm)	Theoretical		
		VEE (nm)	OS	Electronic States (Characters)
Benzoyl chloride[#] [136]	278 265 <245	278.7 265.9 241.0	0.0 0.0196 0.2684	S_1 [n(Cl,CO),π*(CO)] S_2 [π(ring),π*(ring)] S_3 [π(ring),π*(ring)]
Furoyl chloride[#]	280 256 221	270.1 249.8 220.6	0.0 0.369 0.0001	S_1 [n(Cl,CO),π*(ring,CO)] S_2 [π(ring,CO),π*(ring,CO)] S_3 [n(Cl),π*(ring,CO)]
Benzoic acid [125,126]	278 273 220	252.6 244.2 219.1	0.0002 0.015 0.18	S_1 [n(CO),π*(CO)] S_2 [π(ring),π*(ring)]

[#] Present work

In fact, the absorption due to the S_1 state at 278 nm is measured to be stronger than that due to the S_2 state at 265 nm. The calculated zero oscillator strength for the S_1 state indicates a role of vibrational mixing in allowing observed absorption due to this state. Such a discrepancy can be observed at this level of calculations. The UV absorption spectra of benzoyl chloride can be compared with that of 2-furoyl chloride and benzoic acid, since in all three cases π electrons of the ring are in conjugation with that of the C=O group of carboxylic acid or acid chloride. In carboxylic acid, the S_1 state arises from an electronic excitation located in the C=O group, and it is of the nπ* character [125]. The S_2 state is assigned to have ππ* character. The experimental room temperature UV absorption spectra of 2-furoyl chloride in the vapor phase are somewhat structured, showing two bands with the maximum absorption of the stronger band at 256 nm (275 to ~230 nm) and that of the weak band at 221 nm (~230 to 200 nm). In addition, very weak absorption is observed near 280 nm. The nature of the two lower energy bands in benzoyl chloride, 2-furoyl chloride and benzoic acid is similar (shown in Table 5.3). However, the nature of the third band at higher energy is different in benzoyl and 2-furoyl chlorides.

The excitation of benzoyl chloride at 235 nm (~122 kcal/mol) is expected to lead the molecules mainly to the S_3 state ($^1\pi,\pi^*$), which has the highest oscillator strength in the excitation region. Unlike excitation of benzoyl chloride, the excitation of 2-furoyl chloride at 235 nm is to the S_2 state, but with the same character ($^1\pi,\pi^*$).

5.5.5 Mechanism of Cl formation for benzoyl chloride

Similar to 2-furoyl chloride, benzoyl chloride (C_6H_5COCl), a 6-membered unsaturated cyclic acid chloride, also has two C-Cl bond fission channels on excitation at 235 nm. It can dissociate to produce Cl in broadly two possible pathways. Chlorine atom can be formed as a primary (reaction 5.5), or a secondary (reaction 5.6) product from the primary product COCl.

$$C_6H_5COCl \rightarrow C_6H_5CO + Cl(^2P_{3/2}, {}^2P_{1/2}) \qquad (5.5)$$

$$C_6H_5COCl \rightarrow C_6H_5 + COCl \qquad (5.6a)$$

$$COCl \rightarrow CO + Cl(^2P_{3/2}, {}^2P_{1/2}) \qquad (5.6b)$$

These two dissociation channels involve only the side-chain and not opening of the ring. Our calculations at MP4(sdq)/6-311++G(d,p)//B3LYP)/6-311++G(d,p) level predict that reactions 5.5 and 5.6a are endothermic by 75.8 and 102.3 kcal/mol, respectively. Thus, present calculations suggest that Cl formation is more feasible energetically as a primary product (reaction 5.5). Another source of Cl, secondary reaction from higher energy channel involving the C–COCl fission (reaction 5.6), is difficult to proceed because of the conjugation interaction [120]. Thus, in benzoyl chloride, similar to 2-furoyl chloride, Cl formation involves a side-chain reaction, and the ring cleavage is expected to be a high energy channel. As discussed earlier, even in photodissociation of benzoic acid [125,126,132] at 248 and 193 and dissociative electron capture (DEC) of furancarboxylic acids [130] reactions occur at the side-chains only, leaving the rings uncleaved.

Thus, our experimental results combined with theoretical calculations suggest that the reaction 5.5 (primary reaction involving C-Cl bond dissociation) is responsible for Cl formation on excitation of benzoyl chloride at 235 nm, with the corresponding TS in the S_1 state. Since the C-Cl dissociation channel in the S_1 state has an exit barrier, this will lead to a high fraction of available energy in the relative translation. Thus, the C-Cl bond dissociation from the S_1 state can be responsible for the fast Cl and Cl* formation. A fraction of benzoyl chloride in the S_1 state can escape dissociation, and undergo non-radiative relaxation to the ground electronic state, from which slow Cl and Cl* can be produced. Formation of slow Cl atom channel from the ground electronic state of benzoyl chloride is vindicated by the detection of molecular HCl among the products. The scheme for chlorine atom and HCl channels on excitation of benzoyl chloride at 235 nm can be given as follows:

$$\begin{tikzcd}
\mathbf{S_0} \arrow[r, "h\nu"] & \mathbf{S_3(^1\pi\pi^*)} \arrow[r] & {} \arrow[r] & \mathbf{S_1(^1n\pi^*)} \arrow[r] \arrow[d] & \mathbf{S_0} \arrow[r] \arrow[d] & \mathbf{HCl} \\
 & & & \mathbf{Cl / Cl^*(fast)} & \mathbf{Cl / Cl^*(slow)} &
\end{tikzcd}$$

The branching ratio of the high kinetic energy (fast) to the low energy (slow) C-Cl bond scission is measured to be 0.72/0.28, implying about 72% of benzoyl chloride in the S_1 state dissociates to produce mainly chlorine atoms. Thus, like in 2-furoyl chloride, relaxation of the S_1 state to the S_0 state by internal conversion is a minor process in benzoyl chloride.

5.5.6 Mechanism of HCl formation for benzoyl chloride

Along with chlorine atom channels, HCl channel was also observed on excitation of benzoyl chloride at 235 nm. We have calculated energetically possible pathways for formation of HCl from the ground electronic state of benzoyl chloride. All optimized structures of stable and transition states are shown in FIG. 5.15, and corresponding energies in FIG. 5.16. Assuming 1,3-HCl molecular elimination on the ground electronic state of benzoyl chloride, we searched for the corresponding TS. Our all efforts to locate this TS failed, and instead these led to the TS (structure shown as TS1 in FIG. 5.15) involving 1,3-Cl migration, with a four-membered cyclic structure, to the ring. The cyclic structure of the TS is non-planar with the dihedral angle CCCCl of 52.3°. The stable molecule (Stab1) formed subsequently lacks the aromaticity of the benzene ring, and it eliminates either CO through a TS (TS2) with a non-planar structure or HCl through a TS (TS2-C) with a planar structure. The co-fragment of HCl channel (pathway C) is a bicyclic stable compound, bicyclo[4.1.0]hepta-1,3,5-trien-7-one (BCHTO), having a planar geometry. But, the co-fragment of CO is a carbene, with a non-planar structure (Stab2), which re-arranges in two different pathways, designated as A and B. The pathway A involves formation of a complex between benzyne and HCl (Comp-A), having stability of ~2 kcal/mol, through a TS (TS3-A). The TS structure is non-planar with the angle ClHC=

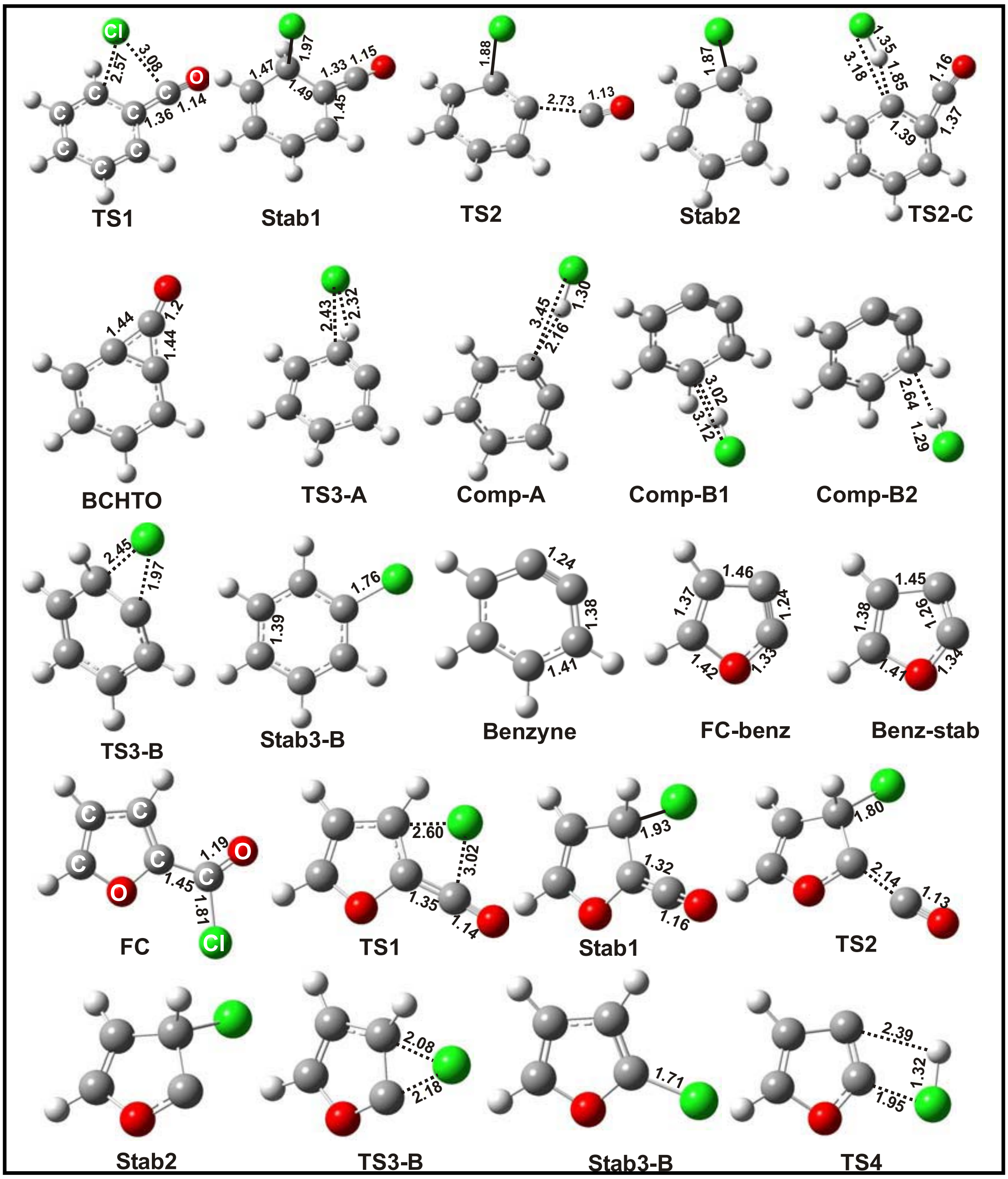

FIG. 5.15: The optimized structures of all the molecular structures, including TS, produced during formation of HCl from the ground electronic states of benzoyl and 2-furoyl chlorides. Details are given in the text. A few important bond lengths (in Å) are marked on structures. Dissociating and forming bonds are depicted as dotted lines.

82.5°, whereas the structure of the complex (Comp-A) is perfectly planar, with the angle ClHC widening to 168.9°. The lower energy pathway B involves 1,2-Cl migration via TS (TS3-B), which has a non-planar ring structure, to produce chlorobenzene (Stab3-B). This chlorobenzene intermediate does not produce the molecular HCl product through a concerted process, since we failed to optimize the corresponding TS structure for 1,2-HCl elimination. Instead chlorobenzene dissociates forming a complex between benzyne and HCl (Comp-B), but with a different structure than the complex in the pathway A (Comp-A). Unlike Comp-A, comp-B has a non-planar geometry, and the H-Cl bond length is slightly shorter with the HCl molecule oriented perpendicular to the planar ring, and H atom pointing towards a ring carbon atom. Two different structures of Comp-B (Comp-B1 and Comp-B2) have been optimized. In Comp-B1, the HCl molecule is the closest (C-HCl bond length = 3.02Å) to the β–carbon atom, with respect to the C≡C triple bond of the ring. However, in Comp-B2 the HCl molecule is the closest (C-HCl bond length = 2.64Å) to the α–carbon atom. Comp-B2 is more stable than Comp-B1 and even Comp-A by about 5 and 1 kcal/mol, respectively. Thus, Comp-B2 is the most stable structure among various complex structures. Both pathways A and B, with the minimum energy requirement of 117.5 and 102.8 kcal/mol, respectively, are energetically feasible for HCl formation on excitation of benzoyl chloride at 235 nm (~122 kcal/mol). Thus, there exist three different pathways A, B and C for HCl formation from benzoyl chloride. However, based on the calculated energies, mainly the pathway C is expected to contribute to HCl formation.

Unlike in UV dissociation of benzoyl chloride at 235 nm, the HCl product was not detected in that of 2-furoyl chloride, mainly because this chain of reactions is not feasible energetically in the latter. We attempted to calculate the energies of the same sequence of the reactions (as in benzoyl chloride) in 2-furoyl chloride as well; all the optimized structures are shown in FIG. 5.15 and the energies in FIG. 5.16. We could

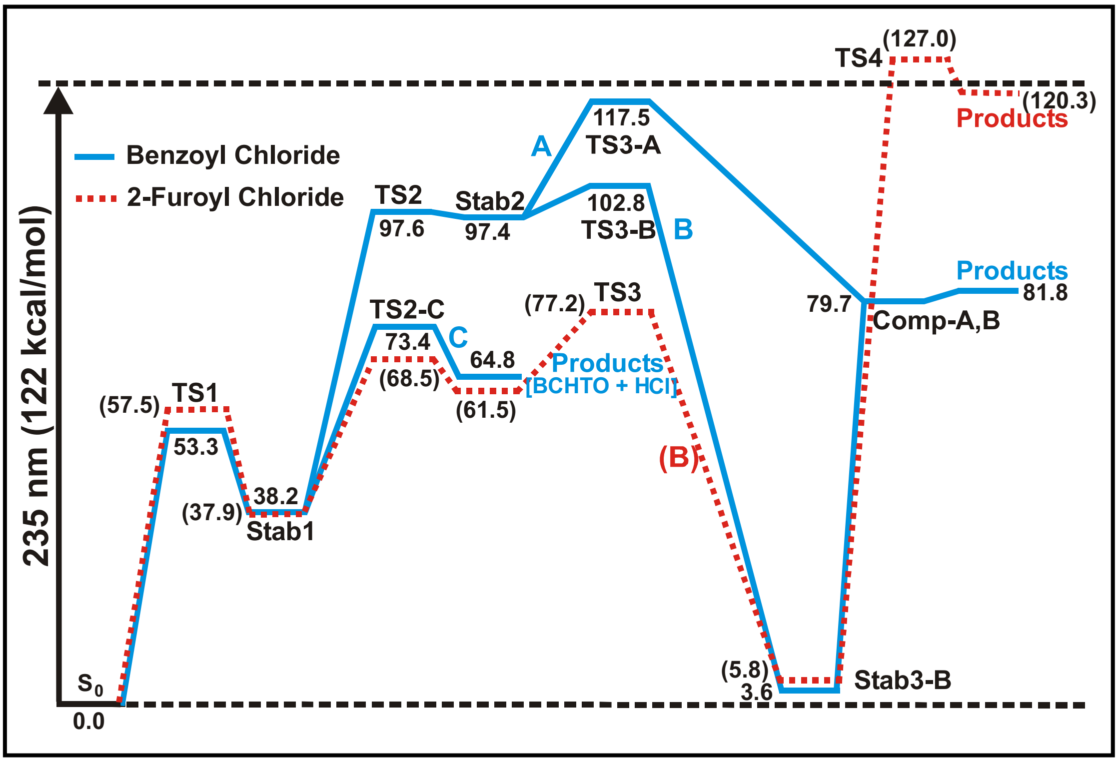

FIG. 5.16: Relative potential energy diagrams for formation of HCl from the ground electronic state (S_0) of benzoyl chloride (solid line) and 2-furoyl chloride (dotted line). Energies in parentheses pertain to 2-furoyl chloride, and all the energies are in kcal/mol. Three different HCl pathways are depicted as A, B and C. Details are given in the text.

not optimize the pathway A for HCl formation from 2-furoyl chloride, since we could not obtain a corresponding TS structure (TS3-A) for isomerization of carbene (Stab2) leading to formation of a complex between HCl and benzyne-type specie. The carbene follows only the pathway B, i.e. 1,2-migration of Cl, producing chlorofuran (Stab3-B). But, even chlorofuran does not form a complex between HCl and benzyne-type specie enroute HCl formation. However, unlike similar reaction in benzoyl chloride, chlorofuran can undergo concerted 1,2-HCl elimination with a higher energy barrier of 127 kcal/mol (TS4). In the HCl channel, the co-fragment is produced with a non-planar structure (Benz-stab), which is different from a benzyne-like structure (FC-benz). In Benz-stab structure, one C-O bond acquires a double bond character. A benzyne-like planar structure (FC-benz) is also characterized with energy similar (within 1.0 kcal/mol) to Benz-stab. However, FC-benz has a negative vibrational frequency, implying this structure to be a TS. Similarly, we could not optimize a TS for HCl formation to the pathway C of benzoyl chloride. Thus, photoexcitation of 2-furoyl chloride at 235 nm (~122 kcal/mol) does not produce HCl due to an energy constraint. But, HCl formation on excitation of benzoyl chloride at 235 nm is energetically allowed. Moreover, detection of the HCl product in benzoyl chloride is further aided by its relatively higher absorption cross-section at 235 nm, and the efficient relaxation of its initially excited state to the ground electronic state, probably due to higher number of vibrational modes in benzoyl chloride.

In addition to benzoyl chloride, the HCl product is also observed from other acyl chloride on UV excitation. Unlike in benzoyl chloride, HCl elimination is reported as a primary product, involving 1,2-elimination, in UV photodissociation of the gaseous acryloyl chloride [119] at 193 nm. Similar mechanism of the 1,2-HCl elimination is also proposed in its thermal dissociation, using IR laser-powered homogeneous pyrolysis [118]. But the mechanism of HCl formation from photolysis of acryloyl chloride at ≥230 nm in argon matrix is different [137]. It involves first the 1,3-Cl migration, followed by either CO elimination or 1,2-HCl elimination in the second step, leading to formation of a carbene or a dienone, respectively. The mechanism of HCl formation in benzoyl chloride is somewhat similar to that in acryloyl chloride at ≥230 nm. The second step of molecular CO and HCl elimination is also observed in benzoyl chloride. But, the HCl formation involves 1,1 elimination process, and leads to a bicyclic co-fragment (BCHTO). The CO elimination is followed by the 1,1-HCl elimination, which proceeds via a complex of HCl and benzyne.

5.5.7 Comparison of Cl formation in 2-furoyl chloride and benzoyl chloride with other α,β-unsaturated chlorides

The chlorine atom formation dynamics in photodissociation of 2-furoyl chloride and benzoyl chloride (which can be considered as α,β-unsaturated chlorides) has several similar features as that of α,β-unsaturated chlorides, such as allyl, propargyl, acryloyl chloride and fumaryl chloride. In these chlorides, the C-Cl bond scission is a primary channel, and both high and low kinetic energy Cl and Cl* are produced, with predominance of the former. In 2-furoyl chloride, the low energy component contributes to 25% and 5% only to the Cl and Cl* channels, respectively. In benzoyl chloride, the low energy component contributes to 30% and 22% to the Cl and Cl* channels, respectively. But, in allyl [138], propargyl [127], and acryloyl [123] chlorides, the slow component of the Cl* channel is too small to be detected. However, it could be detected in fumaryl chloride [129] to be 13%. The observed branching ratio of the high to low energy chlorine component in benzoyl chloride (0.72/0.28) is same as that in fumaryl chloride. But, this branching ratio in benzoyl chloride is slightly different in 2-furoyl chloride (0.78/0.22), implying that the low energy component is slightly greater in the former. The result suggests that the electronic relaxation to the vibrationally excited ground state in benzoyl chloride is more efficient than that in 2-furoyl chloride. The relative quantum yields of Cl and Cl* in 2-furoyl chloride (0.85, 0.15) and benzoyl chloride (0.70, 0.30) are comparable to that in fumaryl chloride (0.76, 0.24) [129] and acryloyl chloride (0.81, 0.19) [123];

the agreement of benzoyl chloride is very good even with allyl chloride (0.67, 0.33) [78,138]. In these chlorides, isotropic angular distributions of Cl and Cl* are observed, with the anisotropy parameter β value close to zero. An isotropic distribution of chlorine atom channel in these chlorides suggests their slow dissociation.

Dissociation reaction in both 2-furoyl chloride and benzoyl chloride takes place only in the side chain, and the excited molecules relax to the S_1 ($^1n\pi^*$) state, from the S_2 state in the former and the S_3 state in the latter, to produce the high kinetic energy Cl channel. Even in other chlorides, the high kinetic energy chlorine channels are major, and originate from an excited state(s). But, the low energy chlorine channels are minor, and either operate from the ground electronic state or are secondary reactions. In acryloyl chloride, the C-Cl bond cleavage is predicted to take place in the S_1 and T_2 states on UV excitation [120], and reported to be a primary dissociation channel [119,123]. The C–OH bond (analogous to the C–Cl bond of an acid chloride) dissociation is also the major channel from benzoic acid on excitation at 248 nm [126], and predicted to occur in the T_2 state after IC from S_2 to S_1 followed by intersystem crossing (ISC) [125]. The C–COOH bond (analogous to the C–COCl bond of an acid chloride) dissociation could not be observed. However, on excitation of benzoic acid at higher energy of 193 nm, the C-COOH bond cleavage could be observed, predictably from the T_1 state. The role of the S_0 state of benzoic acid in photodissociation of the C–OH and C–COOH bonds is stated to be negligible. But, the S_0 state of benzoyl chloride and 2-furoyl chloride plays an important role in formation of low kinetic energy chlorine atom channels.

Since acetyl chloride also dissociates from the $^1n\pi^*$ state to produce the Cl channel [116,139], it is worth discussing dynamics of Cl formation in 2-furoyl chloride and benzoyl chloride relative to that in acetyl chloride on excitation at 235 nm. In acetyl chloride also [139,140], a bimodal distribution of $Cl(^2P_{3/2})$ is observed, with a minor contribution from the low kinetic energy component. However, in contrast to 2-furoyl chloride and benzoyl chloride, acetyl chloride produces anisotropic Cl and Cl* distributions, indicating a prompt dissociation relative to the molecular rotation. Isotropic distributions of Cl in 2-furoyl chloride and benzoyl chloride suggest their slow dissociation. This difference probably arises because of different excitation of these acyl chlorides at 235 nm. The excitation populates the $^1(\pi\pi^*)$ state of both 2-furoyl chloride and benzoyl chloride, which subsequently relaxes to the $^1(n\pi^*)$ state before dissociation to produce chlorine. But, the excitation of acetyl chloride directly populates the $^1(n\pi^*)$ state.

5.6 Conclusions

The photodissociation dynamics of 2-furoyl chloride and benzoyl chloride has been investigated, on excitation at 235 nm to its S_2 and S_3 states, respectively, with $^1(\pi,\pi^*)$ character, using resonance-enhanced multiphoton ionization (REMPI) and time-of-flight mass spectrometry. The C-Cl bond dissociation dynamics in these acyl chlorides are similar. The atomic Cl fragments, detected by (2+1) REMPI, are produced in both the spin-orbit ground $Cl(^2P_{3/2})$ and excited $Cl^*(^2P_{1/2})$ states, with relative quantum yields of 0.85 and 0.15 in 2-furoyl chloride and 0.70 and 0.30 in benzoyl chloride. The Cl and Cl* fragments are primary products, produced from the C-Cl bond scission of the COCl side-chain, and show bimodal translational energy distributions with the average high (low) kinetic energy of 7.0 (1.5) and 9.5 (0.8) kcal/mol in 2-furoyl chloride and 16.6 (3.4) and 16.6 (3.7) kcal/mol in benzoyl chloride. The high kinetic energy channel is the dominant one (78% and 70% in 2-

furoyl chloride and benzoyl chloride, respectively), and expected to have an exit barrier, since the observed relative translational energies are much greater than the statistical limit and smaller than the impulsive limit of the energy partitioning models. The presence of an exit barrier for the high kinetic pathway of the C-Cl bond scission in these acyl chlorides is vindicated by excited state MO calculations, through which corresponding transition state was located in the S_1 state, with the $^1(n,\pi^*)$ character. The minor low kinetic energy C-Cl bond fission channels in both 2-furoyl chloride and benzoyl chloride result from the ground electronic state, subsequent to non-radiative relaxation of the initially excited states, and are explained well with the statistical mechanism. Similarly, the HCl molecular channel originates from the ground electronic state of benzoyl chloride, after non-radiative relaxation of the initially excited state. The angular distributions of both $Cl(^2P_{3/2})$ and $Cl^*(^2P_{1/2})$ are nearly isotropic with the recoil anisotropy parameter (β) value close to zero. Thus, the combined time of relaxation of initially excited benzoyl chloride to the S_1 state, and subsequent C-Cl bond fragmentation of the fast chlorine atom is slower than the molecular rotation period of the parent molecules, leading to washing out of the initial anisotropy. The C-Cl bond fission dynamics in acyl chlorides is grossly similar to that in acryloyl chloride, since these are α,β-unsaturated carbonyl chlorides with similar electronic excitation. However, like in acryloyl chloride the HCl product is observed in only benzoyl chloride.

CHAPTER 6

UV-Photodissociation of 2-bromo-2-nitropropane: Dynamics of OH and Br formation

6.1 Introduction

Photodissociation of nitro compounds [141-146] is investigated extensively, since these are important as prototypical molecules for combustion and decomposition of energetic materials. In addition, several different products, such as NO_2, NO, O and HONO are energetically accessible in these compounds. In our recent studies on photodissociation of nitrotoluenes at 193 nm [147], we detected OH from o-nitrotoluene after intramolecular re-arrangement involving H transfer from the methyl group to an oxygen atom of the NO_2 group. Similar studies on nitroalkanes [148], such as nitromethane, nitroethane, 2-nitropropane and 2-methyl-2-nitropropane, also at 193 and 248 nm reveal OH as a dissociation product. Although the mechanism of OH formation from these nitroalkanes involves H transfer to the NO_2 group, it is different in nitromethane from other higher nitroalkanes. In nitromethane (H_3CNO_2), OH is produced from a re-arranged structure, $H_2CN(O)OH$ of the parent molecule, whereas in other nitroalkanes it is mainly produced from dissociation of HONO, a primary product of concerted molecular elimination. Unlike in nitrotoluene, UV-visible emission was observed in nitroalkanes.

Studies on photodissociation dynamics of 2-bromo-2-nitropropane (BNP) at 193 nm were undertaken to investigate the effects of Br atom on the dynamics of OH formation. The presence of a halogen atom can significantly alter the dynamics of dissociation of a polyatomic organic molecule by changing the nature of excitation of the molecule and providing various low energy dissociation pathways. For an example, photodissociation of saturated alcohols at 193 nm does not generate or generates a negligibly small yield of OH, since the C-OH bond cleavage reaction does not compete with the CO-H bond cleavage in saturated alcohols [149-151]. But, brominated saturated alcohols, such as bromoethanol [113,152-155], and 3-bromo-1,1,1-trifluoro-2-propanol (BTFP) [79], readily generate OH on excitation at 193 nm involving a different dissociation mechanism. Unlike in saturated alcohols with $\sigma^*\leftarrow n_O$ excitation, in these brominated saturated alcohols, $\sigma^*(\text{C-Br})\leftarrow n(\text{Br})$ transition leads to prompt impulsive Br elimination involving the C-Br bond dissociation, and subsequently the co-fragment of Br undergoes the C-OH bond scission to produce OH. Thus, the presence of Br plays a significant role in altering the yield of the OH channel in saturated alcohols. Has Br any role to play in the BNP dissociation as well, with regard to OH formation? Although nitroalkanes [141,143,144,148] are known to produce OH on excitation at 193 nm, does BNP also generate OH? If OH is produced from BNP, is the mechanism of OH formation similar to that in nitroalkanes or brominated saturated alcohols? It will be interesting to address these queries on photodissociation of BNP at 193 nm. Like other nitroalkanes we did detect OH on UV-photodissociation of BNP employing laser-induced fluorescence (LIF), and measured partitioning of the available energy to understand the dynamics of dissociation. We have also measured the Br radical product, using resonance-enhanced multiphoton ionization (REMPI) technique, for a better understanding of the dynamics of dissociation of BNP.

6.2 Experimental

Photodissociation studies of BNP for LIF measurements have been carried out in a flow reactor. In these studies, the BNP sample pressure was maintained at mTorr level in the flow cell to study photodissociation dynamics, using the laser photolysis-laser induced fluorescence (LP-LIF) setup. The vapor of the compound flowed through the reaction chamber at a flow velocity of approximately 10 cm/s, and was photolyzed by ArF and KrF lasers at 193 and 248 nm, respectively. The OH fragment was probed state selectively by exciting the $A^2\Sigma^+ \leftarrow X^2\Pi$ (0,0) transition of OH (306-309 nm), and monitoring the subsequent A→X fluorescence. Similarly, the product OH ($v''=1,J''$) was detected by exciting the A-X(1,1) transition.

Excitation of BNP at 193 nm leads to UV-visible emission, which was dispersed with a monochromator (Jarrell Ash, model 82-410; resolution ~3 nm) and detected with the PMT. The signal was averaged for 64 shots at each wavelength and stored in a digital oscilloscope (LeCroy, 9350A) for further processing.

The photodissociation dynamics experiments to detect Br were performed in a molecular beam environment by combining resonance-enhanced multiphoton ionization (REMPI) and time-of-flight (TOF) mass spectrometer to state-selectively monitor the photoproducts $Br(^2P_{3/2})$ and $Br^*(^2P_{1/2})$ atoms. The detail of both the experimental setup (LIF and REMPI) is discussed chapter 2. The BNP sample (Aldrich, 97% purity) was used as supplied after degassing and purification by several freeze-pump-thaw cycles.

6.3 Theoretical calculations

Ab initio molecular electronic structure theories were employed to investigate the potential energy surface (PES) for the OH dissociation channel of BNP on UV excitation, using Gaussian suit package [3]. The ground-state full geometry optimization was carried out at the B3LYP level of theory with 6-311+G(d,p) basis sets, and energies of the optimized geometries were calculated at the Moller-Plesset MP4(sdq) level with the same basis sets. Excited electronic state calculations were performed at the configuration interaction with single electronic excitation (CIS) level and the excited states of BNP accessible using ArF laser at 193 nm were predicted from the vertical excitation energies. The harmonic vibrational frequencies and force constants were calculated to ensure that the stationary points on the potential energy surface are true saddle points. The molecular orbitals participating in the electronic transitions were assigned for each of the low lying excited states.

6.4 Results and analysis

6.4.1 Photodissociation at 193 nm

BNP is expected to undergo several dissociation pathways from the ground and the excited electronic states on UV excitation. Four low energy primary dissociation/isomerization channels (reactions 6.1-6.4) are expected for BNP. The C-N (reaction 6.1) and the C-Br (reaction 6.2) bond scission will produce NO_2 and Br, respectively. In addition to these radical pathways, two molecular pathways from BNP are elimination of HONO (reaction 6.3) and isomerization of BNP (reaction 6.4) from the nitro to the nitrite form. The nitrite form can also lead to molecular elimination of HONO (reaction 6.5). We investigated dynamics of OH formation from BNP at 193 and 248 nm. Since BNP is devoid of any OH group, its formation should include intramolecular isomerization, which involves one H transfer to one of the O atoms of the NO_2 group, and simultaneous or subsequent cleavage of the N-OH bond. Our calculations (*vide infra*) suggest that the simultaneous N-OH bond cleavage is energetically not possible. Instead the intramolecular H atom transfer to O atom and the C-NO_2 bond cleavage are simultaneous, leading to formation of HONO (reactions 6.3 and 6.5), which can subsequently undergo the N-OH bond cleavage to produce OH (reaction 6.6).

$$H_3C\text{-}C(Br)(NO_2)\text{-}CH_3 \rightarrow H_3C\text{-}C(Br)\text{-}CH_3 + NO_2 \tag{6.1}$$

$$\rightarrow H_3C\text{-}C(NO_2)\text{-}CH_3 + Br \tag{6.2}$$

$$\rightarrow H_3C\text{-}C(Br){=}CH_2 + HONO \tag{6.3}$$

$$\rightarrow H_3C\text{-}C(Br)(ONO)\text{-}CH_3 \tag{6.4}$$

$$H_3C\text{-}C(Br)(ONO)\text{-}CH_3 \rightarrow H_3C\text{-}C(Br){=}CH_2 + HONO \tag{6.5}$$

$$HONO \rightarrow OH + NO \tag{6.6}$$

Alternatively, the $H_3C\text{-}C(NO_2)\text{-}CH_3$ radical (produced in reaction 6.2) can undergo an intramolecular re-arrangement (reaction 6.7a) involving H atom transfer to O atom of NO_2. The intermediate can produce OH through the N-OH bond cleavage (reaction 6.7b).

$$H_3C\text{-}C(NO_2)\text{-}CH_3 \rightarrow H_3C\text{-}C(NO\text{-}OH){=}CH_2 \tag{6.7 a}$$

$$H_3C\text{-}C(NO\text{-}OH){=}CH_2 \rightarrow H_3C\text{-}C(NO){=}CH_2 + OH \tag{6.7 b}$$

Our experimental and theoretical results suggest this mechanism of OH formation operates at 193 nm excitation of BNP. Our experimental work includes measurements on the partitioning of the available energy in translation, rotation and vibration of the OH product.

6.4.1.1 Nascent OH distribution

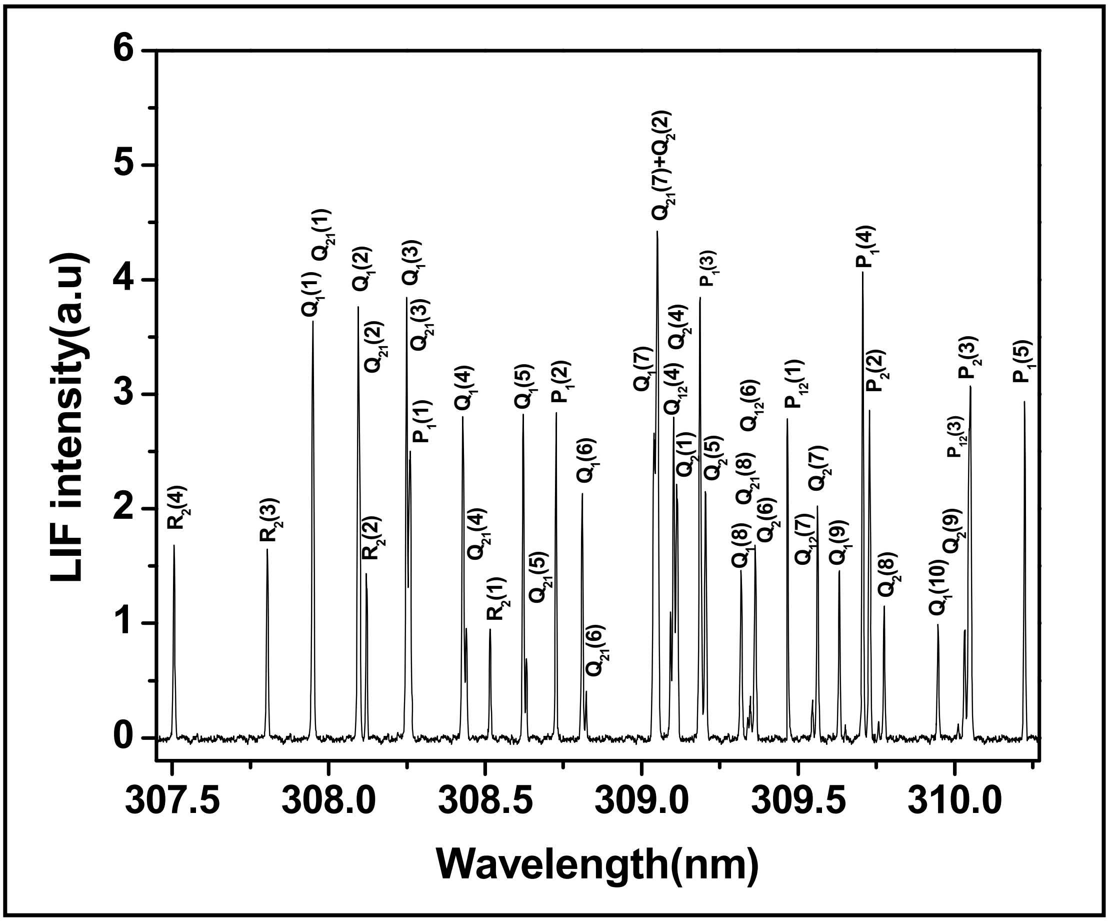

Fig. 6.1: *LIF excitation spectrum of the (0,0) band of the* $A^2\Sigma^+ \leftarrow X^2\Pi$ *system of the nascent OH product from photodissociation of BNP (50 mTorr) at 193 nm.*

The nascent photoproduct OH(v'',J$''$) was detected by LIF on excitation of BNP at 248 or 193 nm. At 193 nm, OH is produced in both v''=0 and 1. But at 248 nm, the OH(v''=1) yield was negligibly small. FIG. 6.1 shows the fluorescence excitation spectrum of the (0,0) band of the A $^2\Sigma^+$-X $^2\Pi$ system of OH from BNP on excitation at 193 nm. We use the standard notation ΔJ(N'') for the transition and denote transitions associated with the spin-orbit states X $^2\Pi_{3/2}$ and A $^2\Pi_{1/2}$ with subscripts "1" and "2", respectively. Line intensity was normalized appropriately to extract information on the internal state distribution of the OH fragment.

6.4.1.1.1 Rotational temperature

The rotational lines of the (0,0) and (1,1) bands of the nascent OH product were measured up to $N'' = 12$ and 6, respectively, on excitation of BNP at 193 nm. Each rotational line was fitted to a Gaussian function and its area was evaluated. The measured area was corrected for the Einstein absorption coefficients [36], and energies of the photolysis and the probe lasers. The rotational population at J'', $P(J'')$, is proportional to the corrected line intensity, and is given by the Boltzmann equation as given in equation 2.3, $\ln(P(J'')/(2J''+1)) = -\varepsilon hc/kT_R$ + constant. Plots of this equation for both $v''=0$ and 1 are straight lines, whose slopes give the rotational

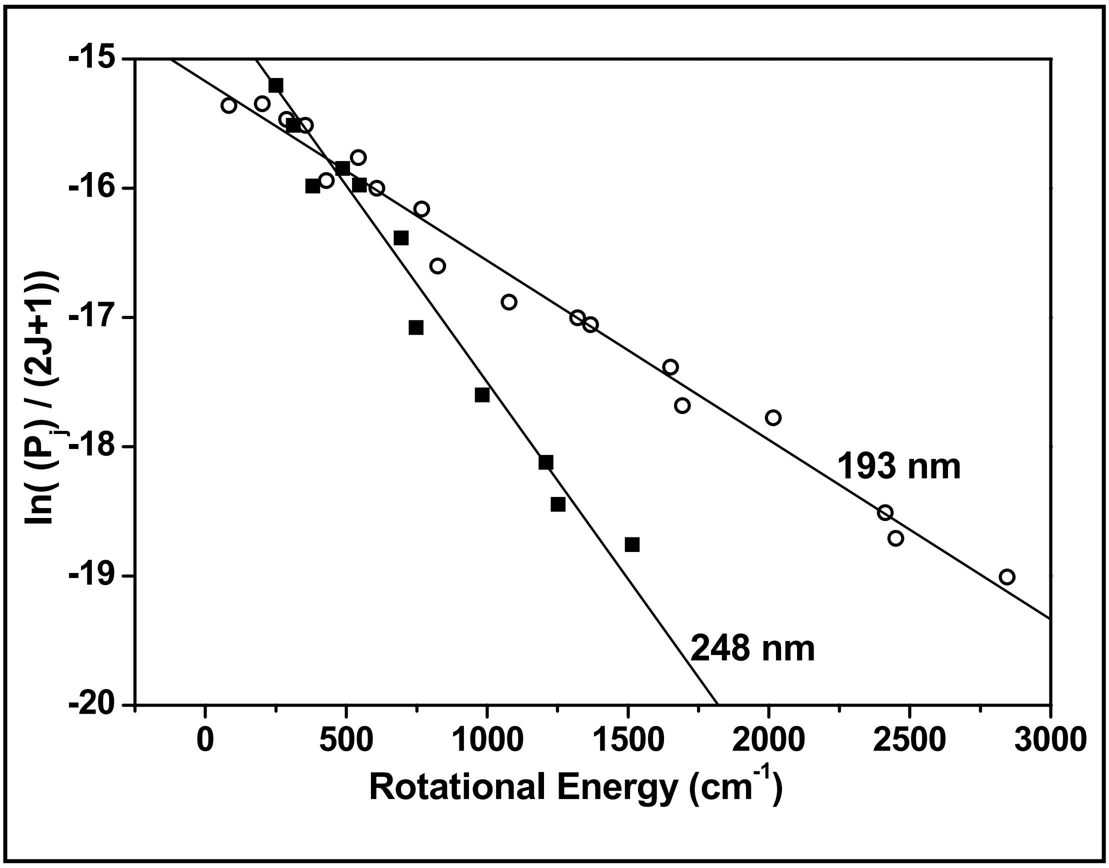

FIG. 6.2: *Boltzmann plots of rotational state population against energy of rotational states of OH (v″= 0) generated in dissociation of BNP at 248 and 193 nm.*

temperatures, T_R = 925±100 K and 620±60 K, respectively. All the measured rotational lines were used for calculating T_R. At all the N'' values, the lines are a good fit, implying the measured rotational populations can be described well by Boltzmann distributions. FIG. 6.2 depicts the Boltzmann plots for the rotational population distribution of OH(v''=0) produced at 193 and 248 nm.

6.4.1.1.2 Vibrational temperature

Assuming a Boltzmann distribution, a vibrational temperature can be obtained from the ratio of the LIF intensities of the same rotational line of the (0,0) and (1,1) transitions by using the relation as given by equation 2.4, $I(R_{1,2}(N'');v''=1)\ /\ I(R_{1,2}(N'');v''=0) = \exp(-\Delta\varepsilon_v hc/kT_V)$, where $\Delta\varepsilon_v$ is the energy difference between v'' = 1 and v'' = 0 for a given spin-orbit state and N'', and T_V is the vibrational temperature. The constants h, c, and k have their usual meanings. Intensities of a few rotational lines $P_1(2)$, $Q_1(1)$, $Q_1(2)$, $Q_1(3)$, $Q_1(4)$, $R_2(3)$ and $R_2(4)$ were used to estimate T_V, and its average value was found to be 1870 ± 150 K.

6.4.1.1.3 Translational temperature

The average translational energy of the photoproduct OH can be estimated using widths of Doppler-broadened rotational lines. The width depends on the fragment molecular velocity, laser line width, and the thermal motion of the parent molecule. The line width was de-convoluted with the instrumental function (0.24 cm^{-1}), which was measured by the line width of thermalized OH at high pressure (50 Torr of 0.1% BNP in Ar) and longer delay time (115 μs). A typical Doppler-broadened line of OH on excitation of BNP at 193 nm is shown in FIG. 6.3. A few rotational lines were fitted to a Gaussian function, and their widths (fwhm, Δν), after de-convolution, were used to calculate the translational temperature T_T using the Doppler relation [14],

$$\Delta \nu = \frac{2\nu_0}{c}\sqrt{\frac{2kT_T \ln 2}{m}} \tag{6.8}$$

where m is the mass of the fragment OH, and ν_0 is the frequency at the center of the line. The average translational energy channeled into OH was estimated to be 17.2 kcal/mol, using the average T_T, on photodissociation of BNP at 193 nm.

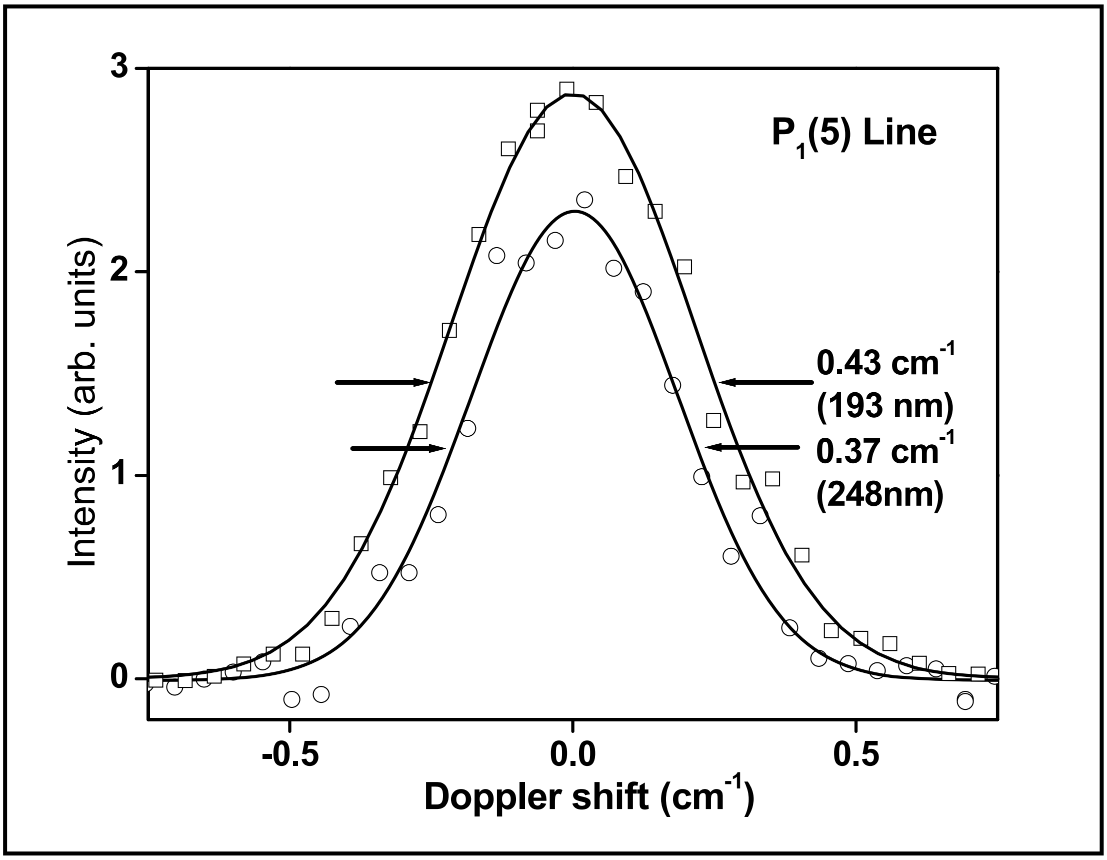

FIG. 6.3: *Doppler profiles of $P_1(5)$ line of the $A^2\Sigma^+ \leftarrow X^2\Pi$ (0,0) system of the OH radical produced in dissociation of BNP at 248 and 193 nm.*

6.4.1.1.4 Spin-orbit and Λ-doublet population

The ground electronic state of OH being $^2\Pi$, there are two spin-orbit components $^2\Pi_{3/2}$ and $^2\Pi_{1/2}$ (chapter 2). The relative populations, after proper correction, of $^2\Pi_{3/2}$ and $^2\Pi_{1/2}$ states of the product OH are plotted against N''(depicted

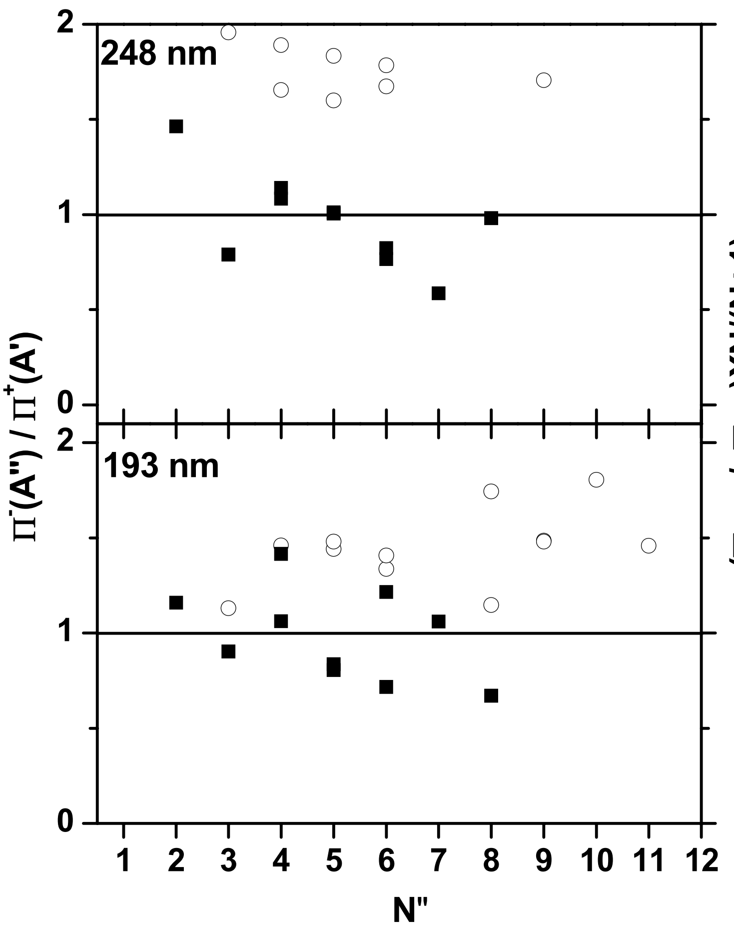

FIG. 6.4: Plots of Λ-doublet (left y-axis, points marked as solid squares) and the spin-orbit state population ratio (right y-axis, points marked as open circles) against rotational quantum number N″ for the nascent OH formed in laser-induced photodissociation of BNP at 248 nm (upper plot) and 193 nm (lower plot).

in FIG. 6.4). The LIF intensities of $P_{1,2}(N'')$ and $Q_{1,2}(N'')$ lines are used to obtain the spin-orbit population. The figure shows the distribution of the OH population in two spin-orbit states is non-statistical (ratio ~ 1.5) with a slight preference for the $^2\Pi_{3/2}$ state, which suggests probably the initially excited state of BNP interacts with some other states before dissociation to produce OH.

The Λ-doublets arise due to different orientations of the π lobes with respect to the rotational plane of the molecule (chapter 2). When the ratio of the corrected intensities of *P* and *Q* lines was plotted for each rotational quantum number (N″), it was found that the values were close to unity (FIG. 6.4). Hence, we can conclude that both the Λ-doublets states of the nascent OH radical are equally populated.

6.4.1.2 Electronically excited NO_2

On photoexcitation of BNP at 193 nm, strong UV-visible emission was detected between 310 and 760 nm (FIG. 6.5) with a broad peak at ~540 nm. This emission is assigned due to the electronically excited NO_2 photoproduct [143]. This product can be produced involving the simple C-N bond scission, with our calculated bond dissociation energy of 50.4 kcal/mol, which is smaller than the C-N bond dissociation energy in nitroethane, 2-nitropropane and 2-methyl-2-nitropropane [148],

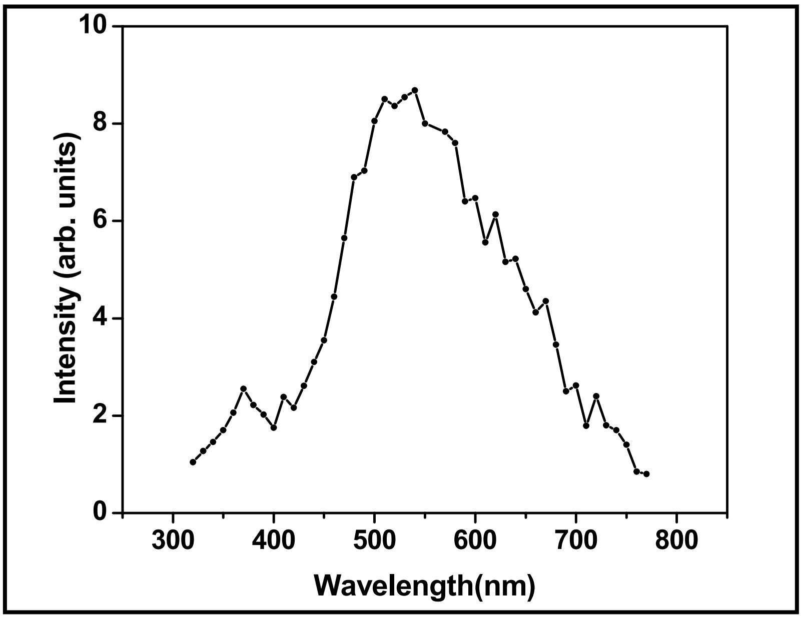

FIG. 6.5: *The dispersed fluorescence spectrum at 150 ns time delay from the pump laser pulse with a broad peak at ~540 nm, resulting from the photoexcitation of BNP at 193 nm.*

mainly because of the stability provided to the radical fragment by the electron withdrawing effect of Br. This small value of the bond dissociation energy results into a high value of 97.6 (148.0 – 50.4) kcal/mol as the available energy in the products after NO_2 formation on excitation of BNP at 193 nm. Since NO_2 is generated involving a simple bond scission, only a small fraction of the available energy is expected to released in the relative translation of the products, with a significant fraction in the internal states. Thus, the NO_2 product is expected to be produced electronically excited, and to emit in the observed wavelength region.

The decay of fluorescence at the peak wavelength 540 nm is a single exponential. The pressure dependence of the temporal profile of the emission at 540 nm was investigated to measure the radiative lifetime of the emitter and the quenching rate coefficient of the fluorescence by the parent molecules. FIG. 6.6 shows a typical temporal profile of fluorescence at 540 nm on irradiation of BNP (175 mTorr) at 193 nm with a single-exponential decay fit. A plot of pseudo first order rate coefficient of emission against the number density of BNP is a straight line (shown in the inset) with the intercept and slope of 3.9×10^{5} s^{-1} and 1.4×10^{10} $molecules^{-1}$ cm^{3} s^{-1}, respectively. Thus the radiative lifetime of the emitter is 2.6 μs, and the fluorescence quenching by BNP is quite efficient as inferred from the observed high quenching rate coefficients of 1.4×10^{10} $molecules^{-1}$ cm^{3} s^{-1}. This radiative lifetime of NO_2 is quite reasonable, considering variation in its measured lifetime (1.0 to 6.0 μs) from various precursors [145,148]. However, these lifetimes are lower than the reported radiative lifetime (~35 μs) [143,156] of the $^{2}B_{2}$ state of NO_2. One plausible reason for differences in measured lifetimes of NO_2 can be origin of fluorescence from its different states with

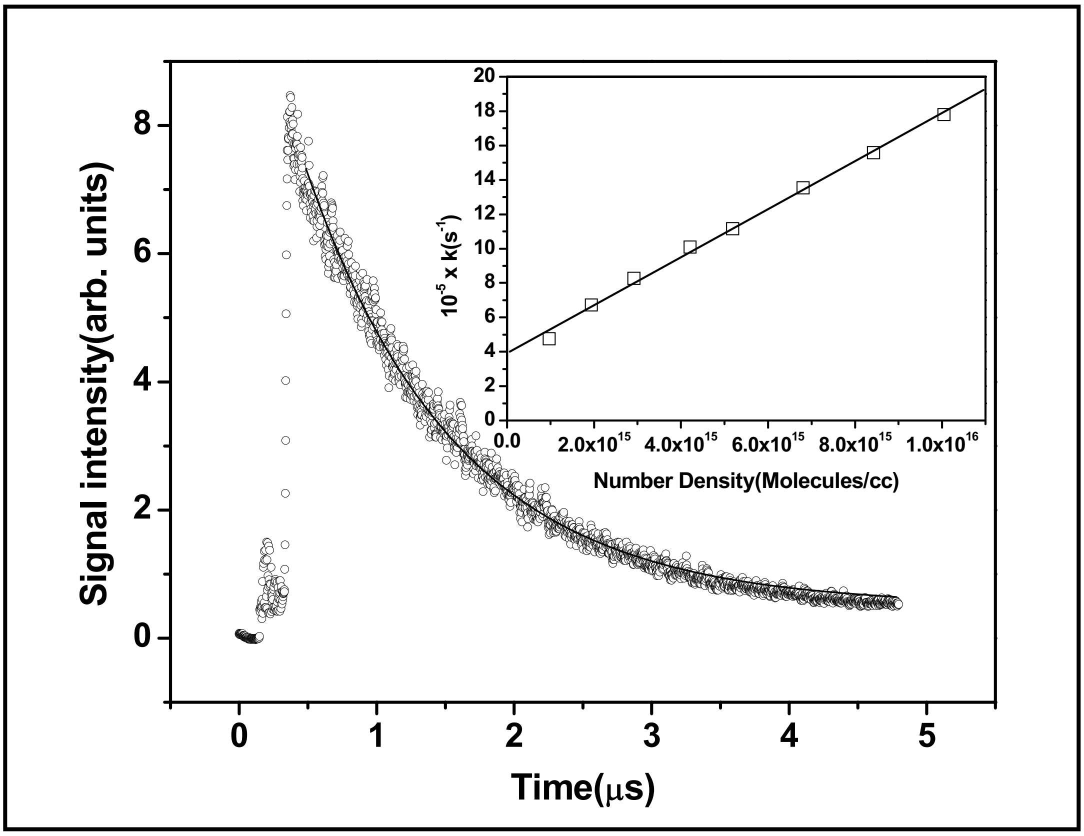

FIG. 6.6: *A typical observed fluorescence temporal profile (experimental points shown as open circles) at 540 nm after irradiation of BNP (175 mTorr) at 193 nm with a single-exponential fit (solid line) of its decay. The plot in the inset depicts the linear dependence of the fluorescence decay rates on varied pressures of BNP.*

different upper state vibrational character. Secondly, emission from other species, such as NO, can also contribute to the total emission.

6.4.2 Photodissociation at 248 nm

Similar to 193 nm excitation, BNP produces OH(v''=0, J$''$) on excitation at 248 nm. However, the LIF intensity from OH(v''=0) is lower than that at 193 nm excitation of BNP, with a negligibly small yield for OH(v''=1). Similar analysis as that in the case of photodissociation at 193 nm shows that the translational energy released in the OH fragment is 10.8 kcal/mol. The rotational population distribution (shown in FIG. 6.2) of the OH (v''=0, J$''$) product is characterized by a rotational temperature of

550±50 K. Unlike dissociation of BNP at 193 nm, OH is produced mostly vibrationally cold at 248 nm. The FIG. 6.4 shows the distribution of the OH population in two spin-orbit states is non-statistical (ratio ~ 1.7) with a slight preference for the $^2\Pi_{3/2}$ state. Both the Λ-doublets states of the nascent OH radical are equally populated (shown in FIG. 6.4).

On photoexcitation of BNP at 248 nm, negligibly small fluorescence yield could be observed, mainly due to small available energy of 64.6 (115.0-50.4) kcal/mol. Since the energy released to the internal states of NO_2 on excitation at 248 nm is expected to be lower than that at 193 nm, only weak fluorescence could be observed in the former. The results suggest that BNP on excitation at 248 nm produces OH with probably a different mechanism than at 193 nm (discussed later). At 248 nm, OH is produced from spontaneous dissociation (reaction 6.6) of the primary product HONO, produced in reaction 6.3.

6.4.3 REMPI detection of Br on photodissociation of BNP at 234 nm

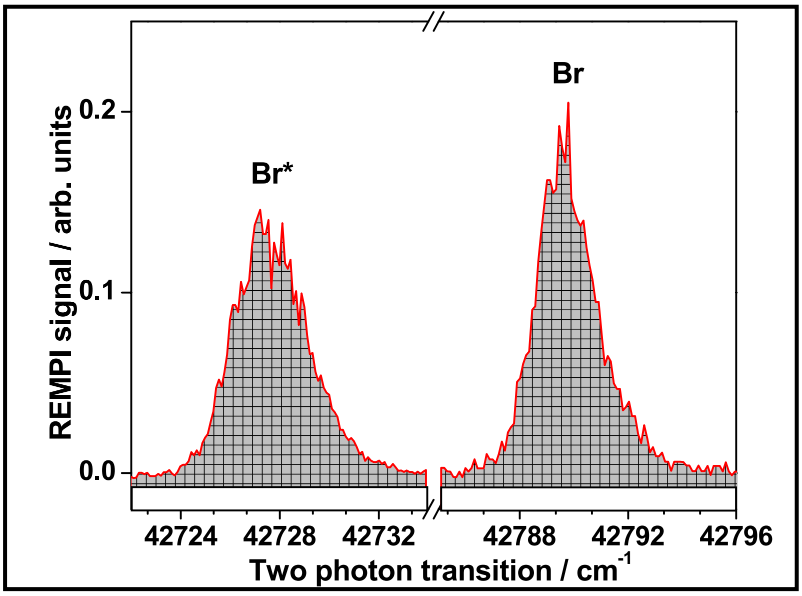

FIG. 6.7: Corrected REMPI spectral profiles of Br and Br atoms produced in the 234 nm laser photolysis of BNP.*

Photodissociation of BNP at 234 nm generates Br, in both the ground ($^2P_{3/2}$) and the excited ($^2P_{1/2}$) spin orbit states, which was detected with (2+1) REMPI scheme. The REMPI spectral profiles of Br and Br* are shown in FIG. 6.7. The laser power dependence of the REMPI intensity suggests that production of Br and Br* is a single photon process. The measured TOF profiles of Br and Br* were analyzed using a forward convolution technique, which is described in detail in chapter 2 to extract the speed distribution g(v), translational energy distribution and the recoil anisotropy (β).

6.4.3.1 Translational energy distribution of Br

We measured the time of flight profiles of Br($^2P_{3/2}$) and Br*($^2P_{1/2}$) with different laser polarizations at the χ values of 0°, 54.7° (the magic angle) and 90°. These TOF profiles for Br($^2P_{3/2}$) and Br*($^2P_{1/2}$), depicted in FIG. 6.8, have been analyzed by a forward convolution method. The analysis suggests that recoil anisotropies for both Br and Br* are the same, and equal to almost zero, implying independence of the TOF profiles on the laser polarization. The observed polarization independence of the TOF profiles of Br and Br* implies that dissociation of BNP leading to Br is slow, and does not occur from its initially excited state. Thus, BNP molecules probably come to the ground state after initial excitation, which is centered at NO_2 part, before undergo dissociation. We did not obtain any evidence for origin of Br from an excited state of BNP.

We also obtained photofragment speed distribution (shown in FIG. 6.9) from the forward convolution analysis of the TOF profiles of Br and Br*. The analysis reveals only one velocity component in the distribution of both Br and Br*, and the relative translational energy of 5.0±1.0 and 6.0±1.5 kcal/mol, respectively.

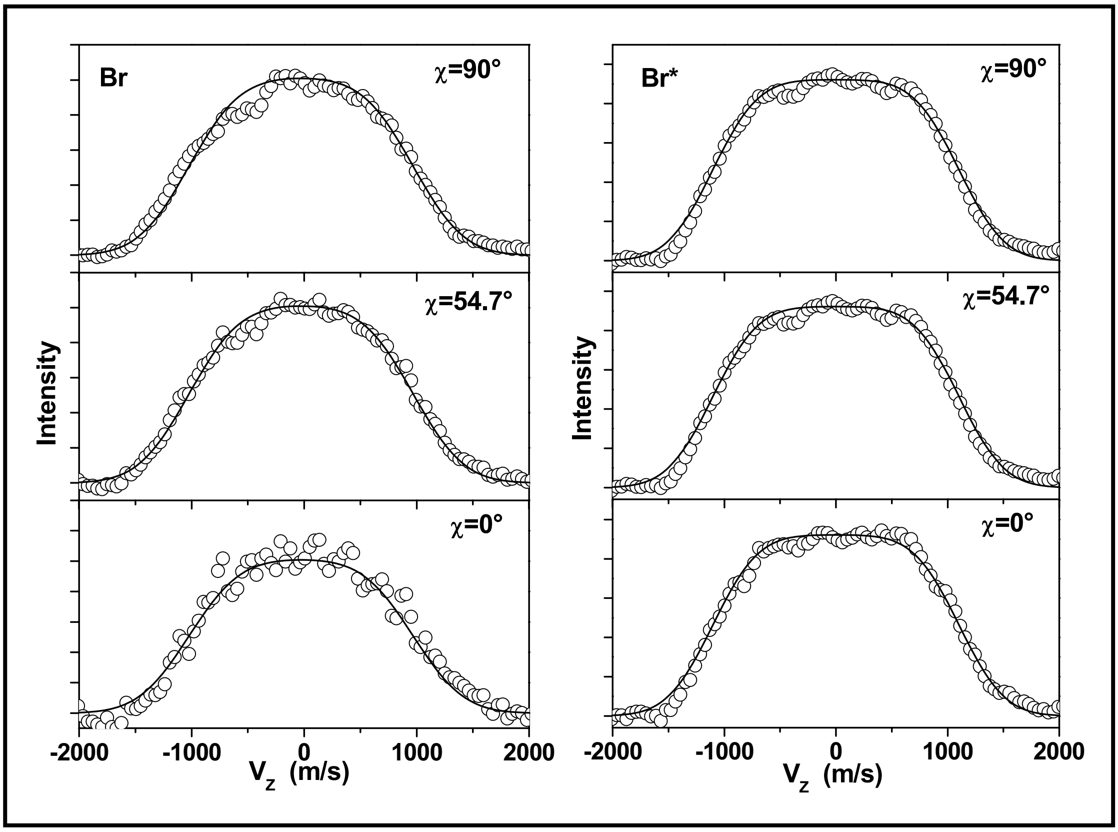

FIG. 6.8: *REMPI-TOF profiles of Br($^2P_{3/2}$) and Br*($^2P_{1/2}$) produced from the 234 nm photodissociation of BNP. The circles are the experimental data and the solid line is a forward convolution fit.*

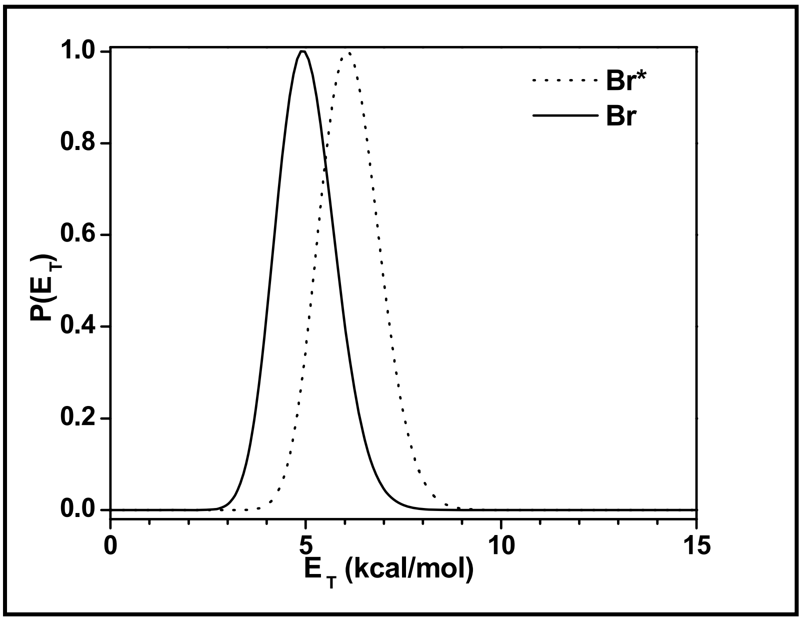

Fig. 6.9: *Photofragment translational energy distribution of Br($^2P_{3/2}$) and Br*($^2P_{1/2}$) for the 234 nm dissociation of BNP.*

6.4.3.2 Spin-orbit ratio of the Br product

The spectral profiles of REMPI lines of Br($^2P_{3/2}$) and Br*($^2P_{1/2}$) were measured at 42789.9 and 42727.7 cm^{-1}, respectively (shown in FIG. 6.7) to evaluate the relative spin-orbit population of Br. The relative quantum yields of Br and Br* were extracted from the integrated intensities of these lines. The number density, N(N*), of Br(Br*) produced is directly proportional to the integrated intensity I(I*) of the REMPI line corresponding to Br(Br*), given by equation 3.1. The relative quantum yields, Φ(Br) and Φ(Br*), can be determined from the number density ratio, and the value of Φ(Br*) has been determined to be 0.49 ± 0.15 using the equation 3.2. The measured value of Φ(Br*) is somewhat higher than the statistical limit of 0.33, based on the degeneracy of both the states, which indicates that the excited state is more strongly coupled with the repulsive state which leads to Br* [106].

6.4.4 Theoretical results

The excited state calculations have predicted that an initially excited state of nitromethane undergoes fast radiationless decay, through conical intersections, to the lower/ground electronic states before dissociation [157,158]. It is also reported that in nitromethane, the dissociation of the C-N bond leads to formation of electronically excited NO_2 as the major channel and formation of the ground/lower electronic state of NO_2 as a minor channel. Thus, it can be assumed that all other competing dissociation and re-arrangement channels from nitromethane occur from the ground electronic state. Extending this assumption of dissociation from the ground electronic state to other nitroalkanes (NE, NP, and MNP), we have carried out the ground electronic state *ab initio* molecular orbital calculations to propose a plausible mechanism of OH formation on excitation of these nitroalkanes at 193 nm. Our theoretical calculations, combined with the experimental results, suggest that in nitroethane and higher nitroalkanes [148], OH is formed from dissociation of HONO, the product of concerted molecular elimination, whereas in nitromethane, it is formed from a re-arranged structure (aci form) of the parent molecule, $CH_2N(O)OH$. Similar calculations have been carried out in the present study to explore various possibilities of OH formation from BNP, in addition to NO_2 and Br radical channels, and compare their energetics.

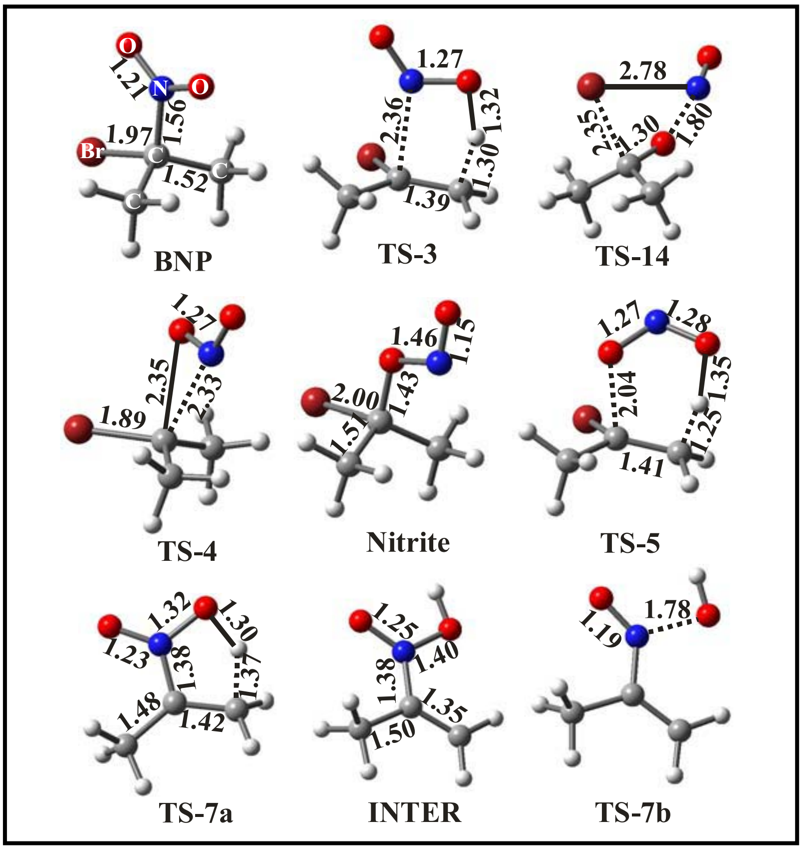

FIG. 6.10: *The optimized structures of the ground electronic state of BNP and transition states of probable reactions producing OH. Details are given in the text. All structures are optimized at the B3LYP/6-311+G(d,p) level of theory. Dissociating bonds are depicted as dotted lines. Each TS structure is marked as TS-n, where n represents the reaction number (6.n).*

The ground state geometries of BNP and various products, including transition states have been calculated. These optimized structures at the B3LYP/6-311+G(d,p) level of theory are depicted in FIG. 6.10, and their relative energies at MP4(sdq)/6-311+G(d,p) level are given in FIG. 6.11 and 6.12. The most stable ground electronic state geometry of BNP reveals that both NO_2 and Br are in the same plane. Like all nitroalkanes, BNP is expected to undergo the C-NO_2 bond scission to produce NO_2 and its co-fragment $(CH_3)_2CBr$ (reaction 6.1) with calculated MP4(sdq) bond dissociation energy of 50.4 kcal/mol. An additional radical channel in BNP has been calculated to be the C-Br bond scission (reaction 6.2) with the dissociation energy of 56.7 kcal/mol. BNP undergoes concerted dissociation to produce HONO and H_3C-C(Br)=CH_2 (reaction 6.3) involving a five-centered TS, in which the five atoms of the ring are almost planar. The TS structure shows that one of the H atoms of a CH_3 group is being transferred to an O atom of the NO_2 group with the extended C-H bond length of 1.30 Å and the new H-O bond length of 1.32 Å. This intramolecular re-arrangement is facilitated by rotation of the NO_2 group, and thus lifting the planarity of NO_2 and Br (dihedral angle ONOBr = 145.0^o in the TS) in BNP and bringing the H atom being transferred in the same plane as the NO_2 group in TS (dihedral angle ONOH = 179.7^o). The dissociating C-N bond gets extended from 1.56 to 2.36 Å in TS. The activation barrier (E_b) and the energy change for this reaction is calculated to be 45.6 and 13.0 kcal/mol, respectively.

BNP molecules can also isomerize to its nitrite form H_3C-C(Br)(ONO)-CH_3 (reaction 6.4) involving a three-centered TS with the dissociating C-N and the forming new C-O bond lengths of 2.33 and 2.35 Å, respectively. The E_b value and the energy change for this isomerization reaction are 65.1 and -5.3 kcal/mol, respectively. The nitrite form of BNP, more stable than its nitro form by 5.3kcal/mol, can also dissociate, like the nitro form, to produce HONO involving a six-centered TS (reaction 6.5), which has a distorted chair structure. The breaking C-H and emerging H-O bond lengths in the TS structure are 1.25 and 1.35 Å, respectively. The dissociating C-O bond is greatly extended from 1.43 Å in the nitrite form to 2.04 Å in the TS structure. The E_b value and the energy change for HONO formation are 59.3 and 18.3 kcal/mol, respectively. HONO produced can undergo the simple HO-NO bond cleavage to produce OH and NO (reaction 6.6) with the E_b value of 38.2 kcal/mol, which is smaller than the reported value [159]. In this case, the MP4 energy has a better agreement than the MP4(sdq) energy [148].

We have also attempted to understand the mechanism of Br formation on excitation of BNP at 234 nm with the help of theoretical calculations, and the same is discussed in a later section.

6.5 Discussion

6.5.1 OH Channel

On photoexcitation of BNP at 248 and 193 nm, OH is readily detected using LIF. Since electronic absorption spectra of BNP are not available in literature, it is not known which transitions are excited at these wavelengths. In general, nitroalkanes have broad absorption in the UV region with peaks around 200 nm (strong) and 280 nm (weak) due to $\pi^* \leftarrow \pi$ and $\pi^* \leftarrow n$ transitions, respectively, localized on the NO_2 chromophore [160]. In another work, the weaker band at 280 nm was assigned to the $\pi^* \leftarrow \sigma(C\text{-}NO_2)$ instead of $\pi^* \leftarrow n$ transition [157]. The presence of Br in BNP can change the nature of electronic transitions. Introduction of Br into the α-position with reference to the nitro group exerts a small bathochromic effect with a slight increase in the absorption cross-section between these two absorption bands at 280 and ~200 nm [161]. This effect gets magnified with increased number of nitro groups or halogen atoms, mainly because of some contributions of these groups to the 200 nm band.

Our excited state calculations of BNP at the CIS level suggests that the excitation at 248 nm leads to mainly $\pi^*(NO_2)\leftarrow n(Br/O)$ transition and that at 193 nm to the $\sigma^*(C\text{-}Br)\leftarrow n(Br)$ transition. The excitation of BNP at 234 nm is similar to that at 248 nm, and involves the $\pi^*(NO_2)\leftarrow n(Br/O)$ transition. Hence, photodissociation behavior of BNP at 234 and 248 nm is expected to be similar. Thus, the presence of Br atom in BNP modifies the nature of transitions to $\pi^*\leftarrow n$ and $\sigma^*\leftarrow n$ from $\pi^*\leftarrow n/\sigma$ and $\pi^*\leftarrow \pi$, respectively.

6.5.1.1 Mechanism of OH formation at 248 nm

On excitation of BNP at 248 nm, the $\pi^*(NO_2)\leftarrow n(Br/O)$ transition is excited, and hence some photochemical reactions involving the NO_2 group is expected. Since BNP is devoid of any OH group, for OH formation the first step should involve an intramolecular H transfer from one of the CH_3 groups to an oxygen atom of the NO_2 group. We searched for corresponding TS (shown as TS-3 in FIG. 6.10) on the ground electronic state of BNP employing MO theory, and found that the H atom transfer and the C-N bond cleavage occur simultaneously in a concerted pathway producing 2-bromopropene and HONO (reaction 6.3), with the E_b value of 45.6 kcal/mol (given in FIG. 6.11). The nascent HONO has sufficient internal energy to undergo dissociation to produce OH, involving the HO-NO bond cleavage (reaction 6.6). In addition, a small contribution from the H-ONO bond cleavage (higher energy channel producing NO_2 and H) is reported from HONO dissociation on excitation at 193 nm [159]. In the present case of chemically excited HONO with small internal energy, the HO-NO bond scission, producing OH and NO, is expected energetically to be the exclusive dissociation channel. This proposed mechanism of OH formation in BNP is similar to that in 2-nitropropane and 2-methyl-2-nitropropane [148]. Since like 2-methyl-2-nitropropane, BNP is devoid of any H atom on the C atom, which is attached to the

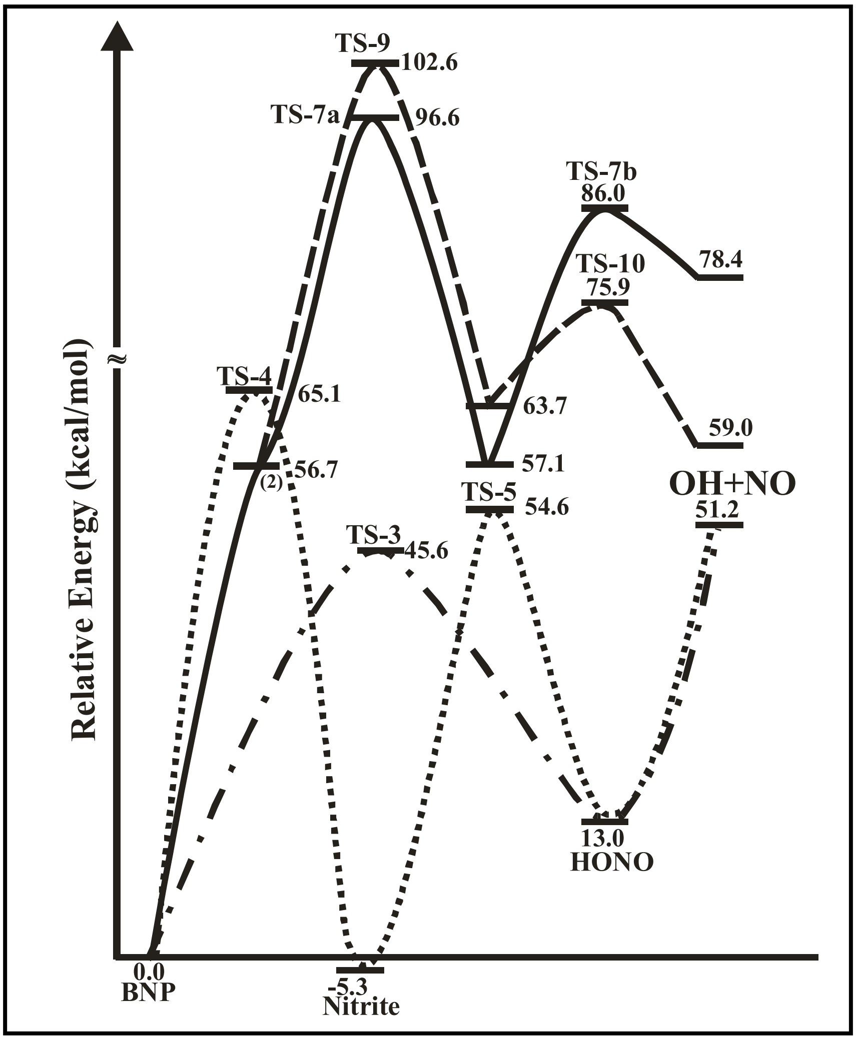

Fig. 6.11: *Relative potential energy diagrams for formation of OH from the ground electronic state of BNP. All energies (in kcal/mol) are at MP2/6-311+G(d,p) level of theory. Each TS is marked as TS-n, where n represents the reaction number (6.n). A number n in parenthesis also stands for a reaction (6.n). The curves in bold, dashed-dot and dot represent mechanism for OH formation at 193 nm, 248 nm and through nitrite form of BNP, respectively. The dashed curves represent a possible* NO_2 *formation channel.*

NO_2 group, another possible mechanism of OH formation via aci-form is ruled out. OH formation from BNP through HONO involving the nitrite form (marked as nitrite in FIG. 6.10), which is more stable than nitro form by 5.3 kcal/mol, is also likely. The corresponding TS structure has been calculated, and shown as TS4 in FIG. 6.10. The nitrite form, like the nitro form of BNP, can undergo intramolecular H transfer involving a TS (shown as TS-5 in FIG. 6.10) to produce HONO along with its co-fragment. Subsequently, energetic HONO can dissociate to produce OH. Since the E_b value for BNP isomerization to nitrite is relatively high (65.1 kcal/mol, FIG. 6.11), this reaction channel is not expected to compete with lower energy HONO elimination channel directly from BNP. We also searched for OH as a three-body fragmentation product of BNP. However, we failed to locate the corresponding TS for this reaction. Even if the TS exists, the value of E_b is expected to be higher. Thus, theoretical calculations suggest that energetically the most probable OH channel is from HONO, formed directly from BNP.

6.5.1.2 Mechanism of OH formation at 193 nm

Photochemistry of BNP at 193 nm, leading to OH formation, can be more complex than that at 248 nm. At 193 nm excitation of BNP, mainly the σ^*(C-Br)←n(Br) transition is excited, with a small contribution from the $\pi^* \leftarrow \pi$ transition. Thus, the photochemistry of BNP is expected to be initiated mainly by an impulsive C-Br bond cleavage from a repulsive state to produce the Br radical and its co-fragment, which can produce OH after intramolecular re-arrangement with H migration to the NO_2 group (reaction 6.7). The dissociation energy of the C-Br bond is calculated to be 56.7 kcal/mol. We could locate the TS structure for an intramolecular H transfer to the O atom of the NO_2 group in the co-fragment (depicted as TS-7a in

FIG. 6.10), producing an aci-form intermediate (shown as INTER in FIG. 6.10). The value of E_b for this reaction is calculated to be 39.9 kcal/mol. Subsequently, the N-OH bond cleavage in this aci-form intermediate leads to the formation of OH, the endothermicity of the process being 21.3 kcal/mol. We could locate the TS structure for the OH formation channel at the HF/6-311+G(d,p) level (shown as TS_7b in FIG. 6.10), but not at B3LYP/6-311+G(d,p). Therefore, the MP4(sdq)/6-311+G(d,p) energy (FIG. 6.11) for this TS is given for the HF/6-311+G(d,p) optimized structure. The mechanism of the intramolecular H transfer in the radical fragment is not accompanied by simultaneous cleavage of the C-N bond, and, thus, the mechanism is different from that in BNP on excitation at 248 nm. In the latter TS structure, the H transfer and the C-N bond scission take place in a concerted manner, leading to formation of HONO, which undergoes the HO-NO bond scission to produce OH. Thus, like halogenated alcohols and halogenated alkanes, the first step in photodissociation of BNP at 193 nm is expected to be the C-Br bond dissociation. Other primary reactions, such as the H atom transfer to the O atom of the NO_2 group and NO_2 elimination are not likely to compete with the fast C-Br bond cleavage from a repulsive state.

If the C-Br bond dissociation is the only primary channel on excitation of BNP at 193 nm, how the observed NO_2 product is formed? Similar to the OH channel, the NO_2 channel can originate from the co-fragment radical of Br after 1,2-H migration (reaction 6.9), followed by the C-N bond cleavage (reaction 6.10).

$$H_3C\text{-}C(NO_2)\text{-}CH_3 \rightarrow H_2C\text{-}CH(NO_2)\text{-}CH_3 \qquad (6.9)$$

$$H_2C\text{-}CH(NO_2)\text{-}CH_3 \rightarrow H_2C{=}CH\text{-}CH_3 + NO_2 \qquad (6.10)$$

The barrier for the co-fragment radical to undergo the 1,2-H migration is calculated to be 45.9 kcal/mol. The isomer radical H_2C-$CH(NO_2)$-CH_3 can produce NO_2 and H_2C=CH-CH_3, involving the C-N bond scission with the reaction barrier of 12.2 kcal/mol. The potential energy diagram of this reaction channel is shown as a dashed curve in FIG. 6.11. This reaction channel is energetically possible to generate NO_2 in the ground electronic state, but may not have sufficient energy to produce electronically excited NO_2. Another possible NO_2 channel can result from the $\pi^* \leftarrow \pi$ transition, a minor component of BNP excitation at 193 nm. The excited BNP molecules can relax to the ground electronic state, and subsequently these can undergo the C-N bond dissociation, like other nitroalkanes, to produce electronically excited NO_2 as a primary product. Thus, on excitation of BNP at 193 nm, the $\sigma^* \leftarrow n$ transition can be responsible for Br and OH products, whereas the $\pi^* \leftarrow \pi$ transition has to be involved to explain the observed electronically excited NO_2 product. If the NO_2 formation as a primary product from BNP, on excitation at 193 nm, is possible, we cannot rule out the possibility of OH formation via HONO, a similar mechanism as that proposed for 248 nm dissociation of BNP. This possibility is supported by the fact that the measured dynamical features of the OH channel from BNP at 193 nm are not significantly different from that at 248 nm.

Our experimental and theoretical results do not unambiguously validate one of the two proposed mechanisms of OH formation, via HONO from the ground electronic state or via Br elimination from a repulsive state followed by an intramolecular re-arrangement, from BNP on excitation at 193 nm. We could not get any direct or indirect evidence from literature, whether Br is produced from a repulsive surface of BNP. To the best of our knowledge, UV photodissociation of halonitrohydrocarbons in the gas phase is not reported in literature. An electron attachment followed by dissociation of chloronitrobenzene is reported to produce Cl and NO_2 anions [162]. To validate the OH formation mechanism via Br elimination reaction, high level excited state calculations on BNP and the detection of Br as a primary product on excitation of BNP at 193 nm are required. We could not carry out the Br detection from BNP on excitation at 193 and 248 nm employing REMPI, because of some experimental constraints. We could investigate the formation dynamics of Br from BNP on excitation at only 234 nm. Our REMPI-TOF measurements of Br and Br* products on excitation of BNP at 234 nm, suggest the statistical dissociation from the ground electronic state and not an impulsive dissociation from a repulsive state. Thus, the dissociation mechanism of BNP at 193 nm can be different from that at 234 nm, as expected because of different electronic excitations of BNP at these wavelengths. However, the dissociation dynamics of BNP at 234 nm is expected to be similar to that at 248 nm, because of the similar nature of the electronic excitations of BNP at these wavelengths.

6.5.1.3 Partitioning of the available energy

The translational energies released in OH are measured to be 10.8 and 17.2 kcal/mol from photodissociation of BNP at 248 and 193 nm, respectively. The greater value of the measured translational energy at 193 is more than what can be accounted for by greater photon energy. Different mechanisms of OH formation on excitation of BNP at 193 nm should reflect in the partitioning of the available energy in the fragments. Since the first step in OH formation from BNP on excitation at 193 nm involves an impulsive dissociation, all the products, including OH, at 193 nm are expected to have higher translational energy. Similarly, the rotational energy in the OH produced at 193 nm is greater than that at 248 nm.

Energy released in rotation of OH is given by

$$\langle E_{rot}\rangle = \sum\langle E_{rot}\rangle_{V"} = \sum P_{V"}(J")E_{rot}(J"), \tag{6.11}$$

where $P_{v''}$(J″) is the state distribution and E_{rot}(J″) is the energy of a given rotational state J″ in v''= 0 or 1. Thus, the rotational energy in the OH fragment is estimated to be 1.3 and 2.4 kcal/mol in photodissociation of BNP at 248 and 193 nm, respectively. To estimate the vibrational temperature T_{V} of the OH product, we could not construct a Boltzmann's plot, since we could measure the population of OH only in v''=0 and 1. Assuming the Boltzmann distribution of the OH vibrational populations in these two levels, the average value for T_{V} was calculated to be 1870 ± 100 K. In both these cases of photodissociation at 248 and 193 nm, the Λ-doublets and spin-orbit populations of OH are similar.

6.5.2 Br channel

The UV excitation of a halogenated hydrocarbon generally leads to an impulsive dissociation of the C-X bond in a primary reaction channel from a repulsive state. Our investigation on photodissociation of BNP at 193 nm suggests a similar mechanism. But, our REMPI measurements on Br, produced from 234 nm photodissociation of BNP, suggest that it is not produced from a repulsive state, rather from the ground electronic state.

6.5.2.1 Mechanism of Br formation

Photodissociation of BNP at 234 nm produces Br and Br*, which can be generated as primary products (reaction 6.2), or as secondary products in reactions 6.12, 6.13 and 6.14, respectively, from $H_3C\text{-}C(Br)\text{-}CH_3$ (product of reaction 6.1),

$H_3C\text{-}C(Br)\text{=}CH_2$ (product of reactions 6.3 and 6.5) or $H_3C\text{-}C(Br)(ONO)\text{-}CH_3$ (product of reaction 6.4).

$$H_3C\text{-}C(Br)\text{-}CH_3 \rightarrow H_3C\text{-}C\text{-}CH_3\ (\text{singlet}) + Br \quad (6.12a)$$

$$\rightarrow H_3C\text{-}C\text{-}CH_3\ (\text{triplet}) + Br \quad (6.12b)$$

$$H_3C\text{-}C(Br)\text{=}CH_2 \rightarrow H_3C\text{-}C\text{=}CH_2 + Br \quad (6.13)$$

$$H_3C\text{-}C(Br)(ONO)\text{-}CH_3 \rightarrow H_3C\text{-}C(\text{=}O)\text{-}CH_3 + BrNO \quad (6.14)$$

Since Br and Br* are produced with only one velocity component in the distribution, and with the same recoil anisotropy (β) values of about zero, these products are generated in a single and common reaction channel, which is not impulsive. Thus, only one of the five possible channels for formation of Br and Br* is operative from BNP on excitation at 234 nm. Energetically the most favorable Br/Br* channel on photoexcitation of BNP at 234 nm is the primary reaction (6.2) with the endothermicity of 56.7 kcal/mol (FIG. 6.12). Another pathway has the lowest E_b (45.6 kcal/mol) for the primary reaction (6.3), but higher for the subsequent reaction (6.13). This Br channel is difficult energetically, since the Br generation reaction (6.13) requires at least 76.4 kcal/mol of energy. Assuming a statistical distribution [80] of the available energy (122.1 - 13.0 kcal/mol = 109.1 kcal/mol) in the primary reaction (reaction 6.3), the internal energy in the $H_3C\text{-}C(Br)\text{=}CH_2$ fragment is estimated to be 74.0 kcal/mol, which is barely sufficient to cleave the C-Br bond of the fragment to produce Br. Moreover, the value of this estimated internal energy is an upper limit, since the reaction has an exit barrier and the statistical model overestimates the internal energies in the fragments for such reactions.

The potential energy curves of all possible Br formation channels from the ground electronic state of BNP are shown in FIG. 6.12. The secondary channel via the

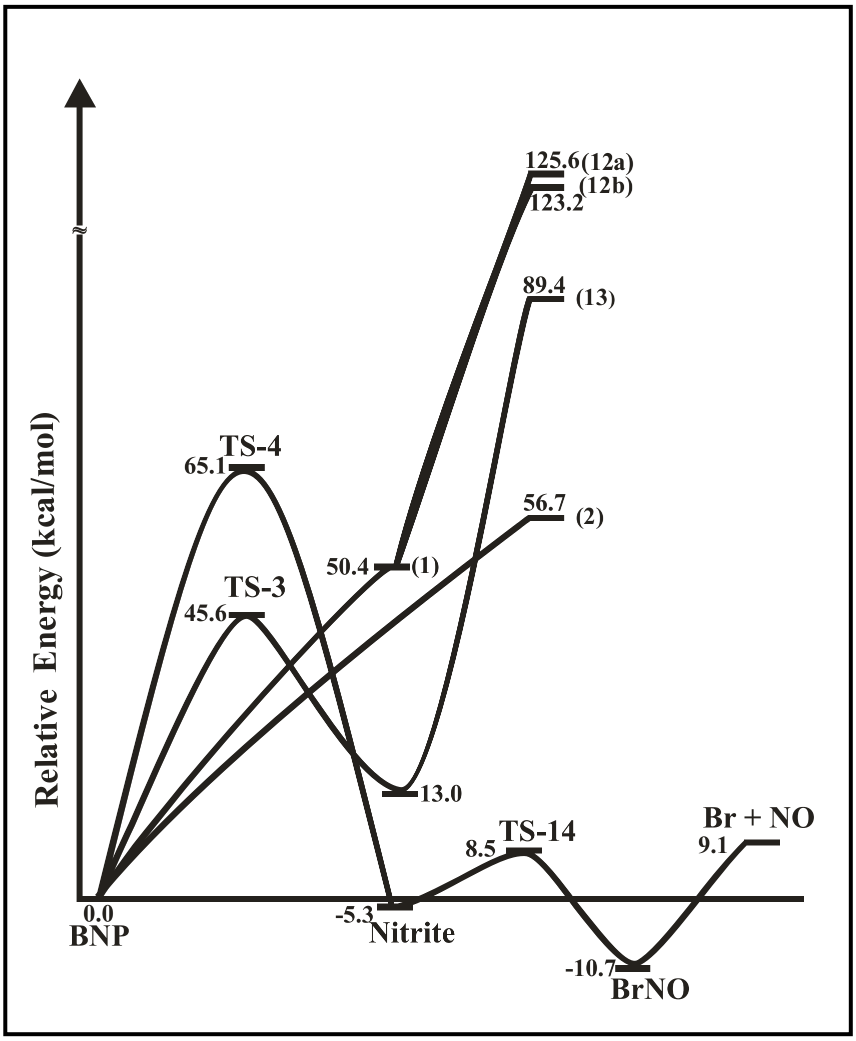

Fig. 6.12: Relative potential energy diagrams for formation of Br from the ground electronic state of BNP. All energies (in kcal/mol) are at MP2/6-311+G(d,p) level of theory. Each TS is marked as TS-n, where n represents the reaction number (6.n). A number n in parenthesis also stands for the corresponding reaction (6.n).

nitrite form of BNP (reaction 6.14) is energetically feasible, but not expected to compete with other lower energy Br channels. On UV irradiation of nitromethane as well, it is shown that the nitrite channel does not compete with other channels [163]. Other mentioned secondary channels (reactions 6.12a and b) are not possible energetically, but these are feasible only in a two photon process, in which Br/Br* can be generated from the second photon excitation of the primary product H_3C-C(Br)-

CH_3. Since our studies on power dependence of Br/Br* suggest their production through a monophotonic dissociation process, the contributions of these secondary channels in the yields of Br and Br* are negligible.

6.5.2.2 Partitioning of the available energy in the Br channel

The C-Br bond cleavage of BNP on excitation at 234 nm generates the Br radical and its co-fragment, $H_3C\text{-}C(NO_2)\text{-}CH_3$. The available energy, E_{avl}, of the reaction is partitioned in the relative translation of the fragments, and the internal energy of the co-fragment. The values of the available energies are calculated to be 65.4 and 54.9 kcal/mol for the Br and Br* channels, using

$$E_{avl} = h\nu - D_0 - E_{SO}, \tag{6.15}$$

where hν, D_0 and E_{SO} are the photon energy corresponding to 234 nm (122.1 kcal/mol), dissociation energy of the C-Br bond (our calculated value of 56.7 kcal/mol) and the spin-orbit energy of Br (10.5 kcal/mol), respectively. The internal energy of BNP is ignored as it is ~0 kcal/mol, for supersonically cooled BNP. The average relative translational energies in Br and Br* channels are measured to be 5.0±1.0 and 6.0±1.5 kcal/mol, respectively. If Br and Br* are produced from the same precursor with similar dynamics, the latter is expected to have a lower translational energy because of lower available energy. However, both the values are similar within the experimental error. The fraction of the available energy being partitioned to the relative translation, f_T, is estimated by the ratio $\langle E_T \rangle / E_{avl}$, and these values are 0.08 and 0.12 for the Br and Br* channels, respectively. The measured values of f_T are compared with a statistical [24] and a soft impulsive model [26] of energy partitioning, which estimate these values to be ~0.06 and 0.25, respectively. The soft impulsive model underestimates the measured f_T values, which are in close agreement with the statistical dissociation of BNP leading to Br and Br* products.

On UV photoexcitation of alkyl halides (RX), the C-X bond cleavage is a primary dissociation channel taking place from a repulsive state with an appreciable amount of the available energy in the relative translation. Photodissociation of CH_2BrCl [41] at 248 nm produces Br and Br* from a repulsive state with the f_T values of 0.48 and 0.54, respectively. Even in haloalcohols, the C-X bond dissociation is direct and takes place from a repulsive state. For an example, the excitation of 2-bromoethanol [113] at 193 nm produces Br/Br* (Br and Br* were unresolved) from the repulsive state $\sigma^*_{C\text{-}Br}$, with the f_T value of 0.42. In the present experiment on BNP, the f_T values for the Br and Br* channels (~0.10) are much lower than those observed for an impulsive dissociation, suggesting Br formation is not from a repulsive state, rather from the ground electronic state of BNP. This statement is further supported by the absence of recoil anisotropies for Br and Br*. An impulsive dissociation is generally accompanied with anisotropic distribution of products, since the dissociation lifetime is much shorter in comparison to the rotation period. However, the anisotropy in an impulsive dissociation can be reduced [45,75] and even sometimes wiped out [113], due to several factors, such as mixed initial transition both with parallel and perpendicular components, relatively longer dissociation lifetime, dissociation not from a single geometry rather from a range of geometries, etc. The absence of recoil anisotropies in the present studies is not due to washing out effects, since relatively lower values of f_T are observed, and may be attributed to a non-direct dissociation of BNP with longer lifetime.

6.6 Conclusions

Photodissociation of 2-bromo-2-nitropropane (BNP) at 248 and 193 nm generates OH as detected by laser-induced fluorescence spectroscopy. At 248 nm, the OH fragment is produced mostly vibrationally cold (v''=0, J″) with the rotational population characterized by a temperature of 550±50 K. The spin-orbit components of the OH fragment are not in equilibrium, and the population ratio (~1.7) has a slight preference for the $^2\Pi_{3/2}$ state. But, the Λ-doublets are almost in equilibrium, suggesting no preference for its π lobe with respect to the plane of rotation. The OH fragment is produced translationally hot with the translational energy of 10.8 and 17.2 kcal/mol at 248 and 193 nm photodissociation, respectively. However, photodissociation of BNP at 193 nm leads to production of vibrationally excited OH(v''=1), with a vibrational temperature of 1870±150 K. The rotational populations of OH in v''=0 and 1 are characterized by temperatures of 925±100 K and 620±50 K, respectively. Like photodissociation of BNP at 248 nm, at 193 nm also the spin-orbit components of OH are not in equilibrium, but the Λ-doublets are almost in equilibrium. Thus, the partitioning of energy in translation, rotation and vibration of the OH product at 193 nm dissociation of BNP is similar to that at 248 nm, with differences in quantities arising from higher photon energy of 193 nm. A plausible mechanism of OH formation is discussed based on both the experimental and the theoretical results. Overall dynamics of OH formation from BNP on excitation at 248 or 193 nm appear to be similar. The NO_2 product is produced electronically excited, as detected by measuring UV-visible fluorescence, at 193 nm and mostly in the ground electronic state at 248 nm.

The Br product is measured using REMPI-TOF technique on photoexcitation of BNP at 234 nm, and obtained translational energy distributions and anisotropy parameters for both Br($^2P_{3/2}$) and Br*($^2P_{1/2}$). The f_T values for the Br and Br* channels are 0.08 and 0.12, respectively, and explained reasonably well with the statistical dissociation ($f_T \sim 0.06$). The absence of recoil anisotropies for these products validates the statistical dissociation of BNP. The experimental results, in combination with the theoretical calculations, suggest that the electronically excited BNP molecules relax to the ground state on UV excitation at 248 and 234 nm, and subsequently dissociate to produce OH and Br through different channels. The mechanism of OH formation from BNP on excitation at 193 nm is not clearly understood. The initially excited BNP molecules can undergo the C-Br bond scission from a repulsive state, and subsequently the co-fragment of Br can dissociate producing OH after intramolecular re-arrangement. Alternatively, the mechanism of OH formation can remain similar as that proposed for the dissociation of BNP at 248 nm excitation.

CHAPTER 7

Summary and future direction

This thesis presents the studies on UV-photodissociation dynamics of different polyatomic halogenated molecules in gas phase. The aim of this work is to investigate the OH and halogen atom (Cl and Br) formation dynamics from different chemical environments. We have employed highly sensitive and selective techniques of LIF and REMPI for these studies, and selected several polyatomic halogenated molecules with different functional groups. The experimental findings are discussed in four chapters in this thesis. Chapters 3, 4 and 5 deal with the halogen atom formation dynamics from halothane (saturated haloalkane), tetrachloroethylene (haloalkene), and 2-furoyl and benzoyl chlorides (aromatic acyl chlorides), respectively. Chapter 6 describes both OH and Br formation dynamics on UV excitation of 2-bromo-2-nitropropne (BNP) at two different wavelengths. The OH and halogen atom (Cl and Br) with HCl are probed using Laser Photolysis-Laser Induced Fluorescence (LP-LIF) and Molecular Beam-Resonance Enhanced Multiphoton Ionization-Time of Flight-Mass Spectrometry (MB-REMPI-TOF-MS) techniques, respectively. Various scalar and vector quantities of dissociation have been measured, and corroborated by theoretical modelling and molecular orbital calculations, to get a holistic picture of the dissociation process. This concluding chapter summarizes all the results obtained from experimental and theoretical work carried out, and a future direction to this work to acquire assistive knowledge.

The first chapter is an introductory chapter, giving a general overview on photodissociation dynamics and its importance. The journey of a polyatomic molecule, starting from its absorption of a photon to dissociation into multiple fragments is discussed. The principles of various experimental techniques along with other important aspects of photodissociation process, which are keys in understanding the dynamics of the event, are also discussed in this chapter. The 2nd chapter deals with the experimental details, employed in this thesis. The analysis of the experimentally obtained data to get dynamical information also discussed briefly in this chapter.

Chapter 3 gives the details on photodissociation dynamics of 2-bromo-2-chloro-1,1,1-trifluoroethane (halothane), a saturated haloalkane, near 234 nm. Both bromine and chlorine atoms are detected in both the ground and spin-orbit excited states. The C-Br bond scission is observed predominantly due to direct σ*(C-Br)←n(Br) transition, with translational energy distribution described with a soft impulsive model. The recoil anisotropy parameter (β) of 0.6±0.2 for this channel vindicates the impulsive nature of dissociation. The diabatic crossing from the [n,σ*(C-Br)] surface to the [n,σ*(C-Cl)] diabatic surface is responsible for an unexpected chlorine formation via the stronger C-Cl bond fission, which is supported by the excited state molecular orbital calculations. The velocity distribution of bromine atom has one component, however, that of chlorine atom is bimodal. Both fast and slow chlorine atom channels are associated with β value of 0.3±0.1, and are produced impulsively from the [n,σ*(C-Cl)] repulsive surface. Thus, the presence of the bromine atom has a pronounced effect on the C-Cl bond dissociation dynamics. Moreover, the energy transfer between the two modes is fast enough to produce anisotropic distribution of the chlorine atoms. The bromine dissociation channel is found to be more abundant one, with a relative yield of 13:1 for the C-Br to the C-Cl bond rupture. The C-Br bond dissociation channel being major is explained based on the initial transition of σ*(C-Br)←n(Br) at 234 nm. In this chapter a comparison of dissociation dynamics with some reported data on similar alkyl halides is also made. The abundance of Cl atom channel is found to be strongly dependent on the excitation wavelength and the relative positions of the halogen atoms. The Cl elimination channel in an alkyl dihalide becomes more and more significant with decreasing photolysis wavelengths. Similarly, when both Cl and Br are located on the same C atom, like in case of halothane, the coupling between the two chromophores becomes the strongest, resulting in more efficient energy transfer from the [n,σ*(C-Br)] to the [n,σ*(C-Cl)] diabatic surfaces and relatively greater chlorine atom yield.

The next system discussed in chapter 4 is the dissociation dynamics of tetrachloroethylene, an unsaturated halogenated compound, at 235 nm. In this molecule, the presence of unsaturation modifies the initial transition at 235 nm to the [π,σ*(C-Cl)] state. From where, a fast chlorine atom channel operates but with an isotropic angular photofragment distribution (β ~ 0). This result is exactly opposite to that obtained in case of halothane, and indicates that even the faster chlorine atom formation channel in tetrachloroethylene is slow with respect to the rotational time period of the parent molecule. In addition to undergoing dissociation to generate the fast chlorine atom channel, the initial excited state relaxes to the ground electronic state, after fast internal conversion, to produce a slow chlorine atom channel. Both these fast and slow channels are observed for the chlorine atom fragment produced in its ground (Cl) and spin orbit excited (Cl*) states. The average translational energies for the Cl and Cl* channels for the fast components are 17.6±1.9 and 14.0±1.7 kcal/mol, while that for the slow components are 2.2±1.0 and 3.2±1.0 kcal/mol, respectively. To understand the nature of the dissociative potential energy surface involved in the chlorine atom formation channel, detailed theoretical calculations are performed using Time-dependent Density Functional Theory (TD-DFT) method. The results obtained in this study are compared with other chloroethylenes, to get a complete picture of the effect of unsaturation on the C-X dissociation dynamics. Our calculations suggest a bound nature of the [π,σ*(C-Cl)] state in case of tetrachloroethylene and trichloroethylene, but a pure repulsive nature in case of vinyl chloride. The depth of the potential energy surface of the [π,σ*(C-Cl)] state is greater in tetrachloroethylene as compared to trichloroethylene. Thus, with increase in the number of chlorine substituent in the vicinity of the unsaturation there is an increase in the stability of the [π,σ*(C-Cl)] state, and this bound nature of the [π,σ*(C-Cl)] state is mainly responsible for near zero anisotropy and high translational energy associated with the chlorine atom channel. Thus, this chapter clearly demonstrates how presence of unsaturation and the substituents associated with it can modify the nature of the excited state, which in turn, modifies the overall dynamics of dissociation.

In chapter 5 the UV-photodissociation dynamics of two aromatic acyl chloride, benzoyl and 2-furoyl chlorides, has been discussed in detail. These molecules have a carbonyl moiety and an extended conjugation in the vicinity of the halogen atom. The nature of excitation at 235 nm in these chlorides is different from that in two systems discussed in chapters 3 and 4. However, the halogen atom formation dynamics in these acyl chlorides is somewhat similar to that in tetrachloroethylene. For both benzoyl and 2-furoyl chlorides the chlorine fragments formed in their spin orbit ground Cl($^2P_{3/2}$) and excited Cl*($^2P_{1/2}$) states, with isotropic angular distribution and bimodal translational energy distributions. In all these cases the fast chlorine atom channel is found to be the major one. In case of tetrachloroethylene the chlorine atom channel associated with high kinetic energy, is attributed to the dissociation from the initial prepared [π, σ*(C-Cl)] state. However, for both benzoyl and 2-furoyl chlorides, the initial excitation at 235 nm is localized in the carbonyl group, and leads to the S_3 ($^1\pi,\pi^*$) and S_2 ($^1\pi,\pi^*$) state, respectively. A major fraction of this initial state relaxes to the S_1 ($^1n\pi^*$) state to produce the high kinetic energy chlorine atom channel, and a minor fraction relaxes to the ground (S_0) state to produce the slow chlorine atom channel. The observed branching ratio of the high to low energy chlorine component in 2-furoyl chloride (0.78/0.22) is slightly different from that in benzoyl chloride (0.72/0.28). The results suggest that the electronic relaxation to the vibrationally excited ground state in benzoyl chloride is more efficient than that in 2-furoyl chloride. The overall dissociation dynamics found to be similar in these two aromatic acyl halides, notwithstanding different ring size. This is mainly due to the fact that the ring does not take part in the photodissociation, and the chlorine elimination mechanism is localized in the side chain only. However, we could detect an additional HCl elimination channel in case of benzoyl chloride, and not in 2-furoyl chloride. The mechanism of HCl elimination is discussed in this chapter in detail. The energy constraint and participation of the aromatic ring are found to play a major role in dictating the difference in dynamics between benzoyl and 2-furoyl chlorides with respect to the HCl elimination channel.

The work discussed in chapters 3, 4 and 5 are focused on the dynamics of halogen atom formation on UV excitation of different halogenated molecules. The overall dynamics of the C-X bond dissociation is controlled by the nature of initial excited states and that of the functional group associated with the halogen atom. The presence of a heavier halogen atom, like Br, can significantly alter the dynamics of dissociation of a polyatomic organic molecule by changing the nature of excitation of the molecule, and providing different low energy dissociation pathways. In chapter 6 the details of UV-photodissociation of 2-bromo-2-nitropropane (BNP) is discussed at two different wavelengths, with emphasis on the effect of a halogen (Br) substituent and nature of the initial excited state, on the dissociation dynamics of a nitrocompound. Photoexcitation of BNP at 248 and 193 nm is found to generate OH, Br and NO_2 among other products. At both 248 and 193 nm, the OH fragment is produced with high kinetic energy of 10.8 and 17.2 kcal/mol, respectively. However, at 248 nm it is produced vibrationally cold ($v''=0$), and at 193 nm vibrationally excited ($v''=1$) with a vibrational temperature of 1870±150 K. The rotational populations of OH ($v''=0$) being characterized by a temperature of 550±50 and 925±100 K at 248 and 193 nm excitation of BNP, respectively. The NO_2 product is produced mostly in the ground electronic state at 248 nm, but in electronically excited state at 193 nm, and it was detected by measuring UV-visible fluorescence. The Br photoproduct is detected at 234 nm dissociation, using REMPI-TOF technique. The average translational energies associated with the Br and Br* channels are 5.0±1.0 and 6.0±1.5 kcal/mol, respectively, and no recoil anisotropies were observed for these products. The low translational energy and isotropic distribution of the bromine photofragment suggest a statistical dissociation mechanism. Most plausible mechanisms of OH and Br formation are discussed based on both the experimental and the theoretical results. The nature of initial excited state is similar at 248 and 234 nm involving

$\pi(NO_2)\leftarrow n(Br/O)$ transition, whereas at 193 nm the transition is mainly the σ^*(C-Br)$\leftarrow$n(Br) transition, with a small contribution from the $\pi^*\leftarrow\pi$ transition. On excitation of BNP at 248 nm, the $\pi(NO_2)\leftarrow n(Br/O)$ transition is excited, and hence some photochemical reactions involving the NO_2 group is expected. The mechanism OH formation at 248 nm involves an intramolecular H transfer from one of the CH_3 groups to an oxygen atom of the NO_2 group to generate an intermediate HONO, which subsequently dissociates to give the OH radical. Thus the electronically excited BNP molecules relax to the ground state on UV excitation at 248 and 234 nm, and subsequently dissociate to produce OH and Br through different channels. The mechanism of OH formation from BNP on excitation at 193 nm is not clearly understood. However, as the nature of excitation has mostly a σ^*(C-Br)$\leftarrow$n(Br) character, the first step of the dissociation of BNP at 193 nm is likely to involve the impulsive C-Br bond scission, and subsequently the co-fragment of Br can dissociate producing OH after intramolecular re-arrangement. Alternatively, the mechanism of OH formation can remain similar as that proposed for the dissociation of BNP at 248 nm excitation. Thus, like other higher nitroalkanes, with an α-hydrogen atom, the mechanism of OH formation at 248 nm takes place via HONO from the ground electronic state with an exit barrier. However, the presence of the Br atom modifies the nature of excitation to σ^*(C-Br)$\leftarrow$n(Br) at 193 nm, and OH formation seems to follow an entirely different pathway.

In brief, on UV excitation a saturated alkyl halide, for example halothane, is excited to a repulsive [n(Br),σ^*(C-Br)] state, and undergoes fast C-Br bond cleavage, leading to Br and Br* with anisotropic angular distribution. Generally, other dissociation channels do not compete with this impulsive C-X bond cleavage.

However, in halothane the stronger C-Cl bond also cleaves due to the energy transfer from the initially excited [n,σ*(C-Br)] state to the [n,σ*(C-Cl)] state. The energy transfer between these two modes is fast enough to compete with the fast C-Br bond dissociation to produce anisotropic distribution of even chlorine atoms. However, the presence of unsaturation in a halogenated molecule, for example in tetrachloroethylene, modifies the initial transition at 235 nm from [n,σ*(C-Cl)] to the [π,σ*(C-Cl)] state, from where fast chlorine is produced. The dissociation being slow, a fast non-radiative process competes with dissociation and relaxes the molecule to the ground electronic state to produce slow chlorine atom channel. In acyl halides of benzoyl and 2-furoyl chlorides, with carbonyl group and extended conjugation, the initial excitation at ~235 nm is now changed to the ($^1\pi,\pi^*$) state. The initial excited state relaxes by the competing C-Cl bond dissociation to generate Cl atom with high translational energy, and by non-radiative processes to the ground electronic state to produce the slow chlorine atom channel, and molecular HCl elimination channel (only in benzoyl chloride). For a halogenated molecule with a nitro group, such as 2-bromo-2-nitropropane (BNP), the dynamics of dissociation becomes complicated generating OH along with Br.

The work reported in the thesis employing REMPI technique has been carried out using a single laser beam. However, experiments at different frequencies of the pump laser, and using velocity map imaging, can provide better information about the excited PESs, and their mutual interactions. For example, REMPI detection of Br on photodissociation of BNP at 193 nm could have given direct credence to the proposed mechanism of OH formation. In addition, we mainly focused on measuring the scalar dynamical quantities like, internal energy distribution, spin-orbit ratio, Λ-doublet ratio, etc. associated with OH formation for understanding its formation dynamics in photodissociation of polyatomic molecules. One may obtain additional information on the dynamics by performing polarization experiments and detecting the vector quantities, like angular distribution of the OH photofragment etc. However, we could measure recoil anisotropy parameter for the C-X (X=Cl, Br) bond dissociation channel.

To get more insights into dynamics of dissociation of a polyatomic molecule, we have carried out theoretical calculations on molecular structures and energies, and also done modeling of the partitioning of the available energy, and have explained satisfactorily our experimental results. However, theoretical calculations have not been performed at higher level, particularly excited state calculations, because of computation resource constraints. The associated error level in energy calculations can be further reduced by performing calculations at higher level with larger basis sets.

References

[1] R. Schinke: Photodissociation Dynamics, Cambridge University press, 2006.
[2] L. J. Butler, E. J. Hintsa, S. F. Shane, Y. T. Lee, J. Chem. Phys. 86 (1987) 2051.
[3] M. J. Frisch, G. W. Trucks, H. B. Schlegel, et al. Gaussian 03, Revision B.04; Gaussian Inc., Pittsburg PA, (2003).
[4] A. Saha, M. N. Kawade, H. P. Upadhyaya, A. Kumar, P. D. Naik, Chem. Phys. 416 (2013) 1.
[5] A. Saha, H. P. Upadhyaya, A. Kumar, P. D. Naik, Chem. Phys. 428 (2014) 127.
[6] A. Saha, H. P. Upadhyaya, A. Kumar, P. D. Naik, P. N. Bajaj, Chem. Phys. 402 (2012) 74.
[7] A. Saha, M. Kawade, S. Sengupta, H. P. Upadhyaya, A. Kumar, P. D. Naik, J. Phys. Chem. A 118 (2014) 1185.
[8] A. Saha, M. Kawade, H. P. Upadhyaya, A. Kumar, P. D. Naik, J. Chem. Phys. 134 (2011) 044316.
[9] J. I. Steinfeld, J. S. Francisco, W. L. Hase: Chemical Kinetics and Dynamics, Prentice-Hall, Inc., New Jersey, 1999.
[10] S. J. Singer, K. F. Freed, Y. B. Band, Adv. Chem. Phys. 61 (1985) 1.
[11] J. T. Moseley, Adv. Chem. Phys. 60 (1985) 245.
[12] C. Wentrup: Reactive Molecules. The Neutral Reactive Intermediates in Organic Chemistry, Wiley, 1984.
[13] K. K. Rohatgi-Mukherjee: Fundamentals of Photochemistry, New Age International(P) Ltd., Delhi, 1986.
[14] W. Demtroder: Laser Spectroscopy, Springer, Verlag Berlin Heidelberg, 2008.
[15] R. D. Levine, R.B. Bernstein, Oxford University Press, New York, 1987.
[16] H. Sato, Chem. Rev. 101 (2001) 2687.
[17] R. N. Zare, P. J. Dagdigian, Science 185 (1974) 739.
[18] J. L. Kinsey, Annu. Rev. Phys. Chem. 28 (1977) 349.
[19] J. J. Valentini: Spectrometric Techniques, Academic, London, 1985.
[20] M. N. R. Ashfold, J. D. Howe, Annu. Rev. Phys. Chem. 45 (1994) 57.
[21] P. J. Dagdigian, H. W. Cruse, A. Schultz, R. N. Zare, J. Chem. Phys. 61 (1974) 4450.
[22] D. B. Galloway, T. G. Meyer, J. A. Bartz, L. G. Huey, F. F. Crim, J. Chem. Phys. 100 (1994) 1946.
[23] R. D. Levine, J. L. Kinsey, in R.B. Bernstein (Ed.). Plenum Press, New York, 1979.
[24] J. T. Muckerman, J. Phys. Chem. 93 (1989) 179.
[25] C. E. Klots, J. Chem. Phys. 58 (1973) 5364.
[26] A. F. Tuck, J. Chem. Soc. Faraday Trans. 2 73 (1977) 689.
[27] S. W. North, D. A. Blank, J. D. Gezelter, C. A. Longfellow, Y. T. Lee, J. Chem. Phys. 102 (1995) 4447.
[28] G. C. G. Waschewsky, P. W. Kash, T. L. Myers, D. C. Kitchen, L. J. Butler, J. Chem. Soc. Faraday Trans. 90 (1994) 1581.
[29] A. Yokoyama, K. Yokoyama, T. Takayanagi, J. Phys. Chem. A 101 (1997) 6647.
[30] K. Yokoyama, A. Yokoyama, T. Takayanagi, J. Chem. Phys. 114 (2001) 1624.
[31] E. P. Wigner, E. E. Witmer, Z. Phys. 51 (1928) 859.
[32] P. L. Houston, J. Phys. Chem. 91 (1987) 5388.
[33] C. H. Greene, R. N. Zare, J. Chem. Phys. 78 (1983) 6741.
[34] R. J. Van Brunt, R. N. Zare, J. Chem. Phys. 48 (1968) 4304.
[35] G. H. Dieke, H. M. Crosswhite, J. Quant. Spectrosc. Radiat. Transfer 2 (1961) 97.
[36] I. L. Chidsey, D. R. Crosley, J. Quant. Spectrosc. Radiat. Transfer 23 (1980) 187.

[37] D. M. Lubman, R. M. Jordan, Rev. Sci. Instrum. 56 (1985) 373.
[38] W. C. Wiley, I. H. McLaren, Rev. Sci. Instrum. 26 (1955) 1150.
[39] J. A. Syage, J. Chem. Phys. 105 (1996) 1007.
[40] K. Bergmann, R. T. Carter, G. E. Hall, J. R. Huber, J. Chem. Phys. 109 (1998) 474.
[41] W. S. McGivern, R. Li, P. Zou, S. W. North, J. Chem. Phys. 111 (1999) 5771.
[42] R. Vasudev, R. N. Zare, R. N. Dixon, J. Chem. Phys. 80 (1984) 4863.
[43] M. Dubs, U. Bruhlmann, J. R. Huber, J. Chem. Phys. 84 (1986) 3106.
[44] H. P. Upadhyaya, A. Saha, A. Kumar, T. Bandyopadhyay, P. D. Naik, P. N. Bajaj, J. Phys. Chem. A 114 (2010) 5271.
[45] R. J. Wilson, J. A. Mueller, P. L. Houston, J. Phys. Chem. A 101 (1997) 7593.
[46] A. S. Bracker, E. R. Wouters, A. G. Suits, Y. T. Lee, O. S. Vasyutinskii, Phys. Rev. Lett. 80 (1998) 1626.
[47] A. S. Bracker, S. W. North, A. G. Suits, Y. T. Lee, J. Chem. Phys. 109 (1998) 7238.
[48] S. W. North, A. J. Marr, A. Furlan, G. E. Hall, J. Phys. Chem. A 101 (1997) 9224.
[49] M. Bilde, T. J. Wallington, C. Ferronato, J. J. Orlando, G. S. Tyndall, E. Estupinan, S. Haberkorn, J. Phys. Chem. A 102 (1998) 1976.
[50] S. C. Wofsy, M. B. McElroy, Y. L. Yung, Geophys. Res. Lett. 2 (1975) 215.
[51] F. S. Rowland, Annu. Rev. Phys. Chem. 42 (1991) 731.
[52] K. Q. Lao, M. D. Person, P. Xayariboun, L. J. Butler, J. Chem. Phys. 92 (1990) 823.
[53] Y. Amatatsu, S. Yabushita, K. Morokuma, J. Chem. Phys. 104 (1996) 9783.
[54] V. Blanchet, P. C. Samartzis, A. M. Wodke, J. Chem. Phys. 130 (2009) 034304.
[55] S.-H. Lee, Y.-J. Jung, K.-H. Jung, Chem. Phys. 260 (2000) 143.
[56] J. Huang, D. Xu, J. S. Francisco, W. M. Jackson, J. Chem. Phys. 119 (2003) 3661.
[57] S.-H. Lee, K.-H. Lee, Chem. Phys. Lett. 350 (2001) 306.
[58] A. Yokoyama, T. Takayanagi, G. Fujisawa, J. Chem. Phys. 103 (1995) 1710.
[59] V. L. Orkin, V. G. Khamaganov, J. Atmos. Chem. 16 (1993) 169.
[60] W. Dmowski, J. Fluorine Chem. 132 (2011) 504.
[61] W. Dmowski, Z. Urbanczyk-Lipkowska, D. Wojcik, J. Fluorine Chem. 130 (2009) 509.
[62] J. M. Neuberger, Drug Saf. 5 (1990) 28.
[63] L. R. Goldfrank: Goldfrank's Toxicologic Emergencies., McGraw-Hill, New York, 2002.
[64] T. Langbein, H. Sonntag, D. Trapp, A. Hoffmann, W. Malms, E.-P. Roth, V. Mors, R. Zellner, Br. J. Anaesth. 82 (1999) 66.
[65] K. C. Lau, Y. Liu, L. J. Butler, J. Chem. Phys. 125 (2006) 144312.
[66] R. Liyanage, Y. A. Yang, S. Hashimoto, R. Gordon, R. W. Field, J. Chem. Phys. 103 (1995) 6811.
[67] D. F. McMillen, D. M. Golden, Annu. Rev. Phys. Chem. 33 (1982) 493.
[68] P. W. Kash, G. C. G. Waschewsky, L. J. Butler, M. M. Francl, J. Chem. Phys. 99 (1993) 4479.
[69] L. J. Butler, Annu. Rev. Phys. Chem. 49 (1998) 125.
[70] F. Taketani, K. Takahashi, Y. Matsumi, J. Phys. Chem. A 109 (2005) 2855.
[71] M. S. Park, Y. J. Jung, S. H. Lee, D. C. Kim, K.-H. Jung, Chem. Phys. Lett. 322 (2000) 429.
[72] V. L. Orkin, E. E. Kasimovskaya, J. Atmos. Chem. 21 (1995) 1.
[73] J. Doucet, R. Gilbert, P. Sauvageau, C. Sandorfy, J. Chem. Phys. 62 (1975) 366.
[74] J. Burkholder, R. R. Wilson, T. Gierczak, R. Talukdar, S. A. Mckeen, J. J. Orlando, G. L. Vaghjiani, A. R. Ravishankara, J. Geophys. Res. 96 (1991) 5025.
[75] R. T. Carter, A. Hallou, J. R. Huber, Chem. Phys. Lett. 310 (1999) 166.
[76] M. D. Person, P. W. Kash, L. J. Butler, J. Chem. Phys. 94 (1991) 2557.
[77] T. Gougousi, P. C. Samatzis, T. N. Kitsopoulos, J. Chem. Phys. 108 (1998) 5742.

[78] M. S. Park, K. W. Lee, K.-H. Jung, J. Chem. Phys. 114 (2001) 10368.

[79] Y. N. Indulkar, H. P. Upadhyaya, A. Kumar, S. B. Waghmode, P. D. Naik, J. Phys. Chem. A 113 (2009) 8462.

[80] A. H. H. Chang, D. W. Hwang, X.-M. Yang, A. M. Mebel, S. -H. Lin, Y. -T. Lee, J. Chem. Phys. 110 (1999) 10810.

[81] G. E. Busch, K. R. Wilson, J. Chem. Phys. 56 (1972) 3626.

[82] K. K. Pushpa, A. Kumar, R. K. Vatsa, P. D. Naik, K. A. Rao, J. P. Mittal, V. Parthasarathy, S. K. Sarkar, Chem. Phys. Lett. 249 (1996) 167.

[83] J. J. Ritsko, F. Ho, J. Hurst, Appl. Phys. Lett. 53 (1988) 78.

[84] D. A. Danner, D. W. Hess, J. Appl. Phys. 59 (1986) 940.

[85] F. S. Rowland, M. J. Molina, Rev. Geophys. Space Phys. 13 (1975) 1.

[86] J. Park, Y. Lee, G. W. Flynn, Chem. Phys. Lett. 186 (1991) 441.

[87] E. P. Olaguer, Environ. Sci. Poll. Res. 9 (2002) 175.

[88] I. J. Simpson, S. Meinardi, N. J. Blake, F. S. Rowland, D. R. Blake, Geophys. Res. Lett. 31 (2004) L08108-1.

[89] S. Yamazaki-Nishida, S. Cervera-March, K. Nagano, M. A. Anderson, K. Hori, J. Phys. Chem. 99 (1995) 15814.

[90] J. R. Haas, E. L. Shock, Geochim. Cosmochim. Acta 63 (1999) 3429.

[91] G. W. Gribble, Environ. Sci. Technol. 28 (1994) 310A.

[92] M. J. Berry, J. Chem. Phys. 61 (1974) 3114.

[93] S. Eden, B. Barc, N. J. Mason, S. V. Hoffmann, Y. Nunes, P. Limão-Vieira, Chem. Phys. 356 (2009) 150.

[94] D. J. Mark, W. R. Haag, P. G. Blystone, Destruction of Organic Contaminants in Air Using Advanced Ultraviolet Flash Lamps, Final Report on EPA Contract CR 8188209-01-0 (1992).

[95] Y. Huang, Y.-A. Yang, G. He, S. Hashimoto, R. J. Gordon, J. Chem. Phys. 103 (1995) 5476.

[96] Y. Huang, Y.-A. Yang, G.-X. He, R. J. Gordon, J. Chem. Phys. 99 (1993) 2752.

[97] Y. Huang, G. He, Y. Yang, S. Hashimoto, R. J. Gordon, Chem. Phys. Lett. 229 (1994) 621.

[98] K. Sato, S. Tsunashima, T. Takayanagi, G. Fujisawa, A. Yokoyama, J. Chem. Phys. 106 (1997) 10123.

[99] D. A. Blank, W. Sun, A. G. Suits, Y. -T. Lee, S. W. North, G. E. Hall, J. Chem. Phys. 108 (1998) 5414.

[100] Y. Mo, K. Tonokura, Y. Matsumi, M. Kawasaki, T. Sato, T. Arikawa, P. T. A. Reilly, Y. Y. Xie, Y. Yang, Y. Huang, R. J. Gordon, J. Chem. Phys. 97 (1992) 4815.

[101] S. Arulmozhiraja, M. Ehara, H. Nakatsuji, J. Chem. Phys. 129 (2008) 174506.

[102] J.-L. Chang, J. Chem. Phys. 122 (2005) 194321.

[103] J.-L. Chang, Y.-T. Chen, J. Chem. Phys. 116 (2002) 7518.

[104] N. Herath, M. L. Hause, A. G. Suits, J. Chem. Phys. 134 (2011) 164301.

[105] M. Umemoto, K. Seki, H. Shinohara, U. Nagashima, N. Nishi, M. Kinoshita, R. Shimada, J. Chem. Phys. 83 (1985) 1657.

[106] K. Tonokura, L. B. Daniels, T. Suzuki, K. Yamashita, J. Phys. Chem. A 101 (1997) 7754.

[107] S. Arulmozhiraja, M. Ehara, H. Nakatsuji, J. Chem. Phys. 129 (2008) 174506.

[108] M. Umemoto, K. Seki, H. Shinohara, U. Nagashima, N. Nishi, M. Kinoshita, R. Shimada, J. Chem. Phys. 83 (1985) 1657.

[109] L. J. Radziemski Jr., V. Kaufman, J. Opt. Soc. Am. 64 (1974) 366.

[110] H. P. Upadhyaya, A. Saha, A. Kumar, P. D. Naik, Indian J. Phys. 86 (2012) 165.

[111] Y.-J. Lee, Y.-R. Lee, C.-C. Chou, S.-M. Lin, J. Chem. Phys. 109 (1998) 346.

[112] S. Arulmozhiraja, R. Fukuda, M. Ehara, H. Nakatsuji, J. Chem. Phys. 124 (2006) 034312.

[113] E. J. Hintsa, X. Zhao, Y. -T. Lee, J. Chem. Phys. 92 (1990) 2280.

[114] K. Owen: Gasoline and Diesel Fuel Additives, Wiley, New York, 1989.

[115] M. D. Person, P. W. Kash, L. J. Butler, J. Chem. Phys. 96 (1992) 2021.

[116] M. D. Person, P. W. Kash, L. J. Butler, J. Chem. Phys. 97 (1992) 355.

[117] Z.-R. Wei, X.-P. Zhang, W.-B. Lee, B. Zhang, K.-C. Lin, J. Chem. Phys. 130 (2009) 14307.

[118] G. R. Allen, D. K. Russel, New J. Chemistry 28 (2004) 1107.

[119] D. E. Szpunar, J. L. Miller, L. J. Butler, F. Qi, J. Chem. Phys. 120 (2004) 4223.

[120] G.-L. Cui, Q.-S. Li, F. Zhang, W.-H. Fang, J.-G. Yu, J. Phys. Chem. A 110 (2006) 11839.

[121] W.-H. Fang, Acc. Chem. Res. 41 (2008) 452.

[122] M. L. Morton, L. J. Butler, T. A. Stephenson, F. Qi, J. Chem. Phys. 116 (2002) 2763.

[123] K.-C. Lau, Y. Liu, L. J. Butler, J. Chem. Phys. 123 (2005) 054322-1.

[124] D. S. Green, G. A. Bickel, S. C. Wallace, J. Mol. Spectrosc. 150 (1991) 303.

[125] J. Li, F. Zhang, W. H. Fang, J. Phys. Chem. A 109 (2005) 7718.

[126] Y. A. Dyakov, A. Bagchi, Y. T. Lee, C.-K. Ni, J. Chem. Phys. 132 (2010) 14305-1.

[127] L. R. McCunn, D. I. G. Bennett, L. J. Butler, H. Fan, F. Aguirre, S. T. Pratt, J. Phys. Chem. A 110 (2006) 843.

[128] J. A. Mueller, B. F. Parsons, L. J. Butler, F. Qi, O. Sorkhabi, A. G. Suits, J. Chem. Phys. 114 (2001) 4505.

[129] M. Kawade, A. Saha, H. P. Upadhyaya, A. Kumar, P. D. Naik, P. N. Bajaj, J. Phys. Chem. A 115 (2011) 1538.

[130] V. V. Takhistov, M. V. Muftakhov, A. A. Krivoruchko, V. A. Mazunov, Izv. Akad. Nauk SSSR, Ser. Khim., No. 9 (1991) 2049.

[131] J. M. Simmie, H. J. Curran, J. Phys. Chem. A 113 (2009) 5128.

[132] Q. Wei, J. L. Sun, X. F. Yue, S. B. Cheng, C. H. Zhou, H. M. Yin, K. L. Han, J. Phys. Chem. A 112 (2008) 4727.

[133] S. SenGupta, H. P. Upadhyaya, A. Kumar, P. D. Naik, P. N. Bajaj, J. Chem. Phys. 122 (2005) 124309.

[134] J. Kramer, J. Phys. Chem. 86 (1982) 26.

[135] A. A. Scala, E. W.-G. Diau, Z. H. Kim, A. H. Zewail, J. Chem. Phys. 108 (1998) 7933.

[136] F. Caralp, V. Foucher, R. Lesclaux, T. J. Wallington, M. D. Hurley, Phys. Chem. Chem. Phys. 1 (1999) 3509.

[137] N. Pietri, M. Monnier, J.-P. Aycard, J. Org. Chem. 63 (1998) 2462.

[138] Y. Liu, L. J. Butler, J. Chem. Phys. 121 (2004) 11016.

[139] S. Deshmukh, J. D. Myers, S. S. Xantheas, W. P. Hess, J. Phys. Chem. 98 (1994) 12535.

[140] X. Tang, B. J. Ratliff, B. L. FitzPatrick, L. J. Butler, J. Phys. Chem. B 112 (2008) 16050.

[141] G. Radhakrishnan, T. Parr, C. Wittig, Chem. Phys. Lett. 111 (1984) 25.

[142] X. Yue, J. Sun, Q. Wei, H. Yin, K. Han, Chin. J. Chem. Phys. 20 (2007) 401.

[143] L. J. Butler, D. Krajnovich, Y. -T. Lee, G. Ondrey, R. Bersohn, J. Chem. Phys. 79 (1983) 1708.

[144] G. D. Greenblatt, H. Zuckerman, Y. Haas, Chem. Phys. Lett. 134 (1986) 593.

[145] J. C. Mialocq, J. C. Stephenson, Chem. Phys. 106 (1986) 281.

[146] W. M. Kwok, M. S. Hung, D. L. Phillips, Mol. Phys. 88 (1996) 517.

[147] S. Sengupta, H. P. Upadhyaya, A. Kumar, S. Dhanya, P. D. Naik, P. N. Bajaj, Chem. Phys. Lett. 452 (2008) 239.

[148] S. Sengupta, Y. Indulkar, A. Kumar, S. Dhanya, P. D. Naik, P. N. Bajaj, J. Phys. Chem. A 112 (2008) 12572.

[149] S. Harich, J. J. Lin, Y. -T. Lee, X. Yang, J. Phys. Chem. A 103 (1999) 10324.
[150] K. Xu, G. Amaral, J. Zhang, J. Chem. Phys. 111 (1999) 6271.
[151] W. Zhou, Y. Yuan, J. Zhang, J. Chem. Phys. 119 (2003) 7179.
[152] D. W. Chandler, J. W. Thoman, W. P. Hess, Inst. Phys. Conf. Ser., No. 114, (1990) 355.
[153] S. P. Sapers, W. P. Hess, J. Chem. Phys. 97 (1992) 3126.
[154] L. W. Edwards, M. Ryazanov, H. Reisler, S. J. Klippenstein, J. Phys. Chem. A 114 (2010) 5453.
[155] B. J. Ratliff, C. C. Womack, X. N. Tang, W. M. Landau, L. J. Butler, D. E. Szpunar, J. Phys. Chem. A 114 (2010) 4934.
[156] K. Q. Lao, E. Jensen, P. W. Kash, L. J. Butler, J. Chem. Phys. 93 (1990) 3958.
[157] J. F. Arenas, J. C. Otero, D. Pelaez, J. Soto, J. Chem. Phys. 129 (2003) 7814.
[158] J. F. Arenas, J. C. Otero, D. Pelaez, J. Soto, J. Chem. Phys. 122 (2005) 84324.
[159] G. Amaral, K. Xu, J. Zhang, J. Phys. Chem. A 105 (2001) 1465.
[160] C. Mijoule, S. Odiot, S. Fliszar, J. M. Schnur, THEOCHEM 149 (1987) 311.
[161] V. I. Slovetskii, A. A. Fainzilberg, V. I. Gulevskaya, S. S. Novikov, Izvest. Akad. Nauk SSSR (1961) 683.
[162] I. Dabkowska, M. Orzol, I. Bald, J. Langer, E. Illenberger, Chem. Phys. Lett. 455 (2008) 139.
[163] R. S. Zhu, M. C. Lin, Chem. Phys. Lett. 478 (2009) 11.